Department of Engineering Design and Production

Microstructures of nickel-base alloy dissimilar metal welds

Roman Mouginot and Hannu Hänninen

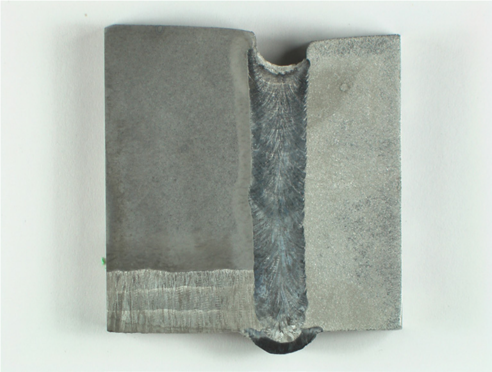

Aalto University

SCIENCE +
TECHNOLOGY

RESEARCH REPORT

Aalto University publication series
SCIENCE + TECHNOLOGY 5/2013

Microstructures of nickel-base alloy dissimilar metal welds

Roman Mouginot and Hannu Hänninen

Aalto University
School of Engineering
Department of Engineering Design and Production
Engineering Materials

Aalto University publication series
SCIENCE + **TECHNOLOGY** 5/2013

ISBN 978-952-60-5065-2 (printed)
ISBN 978-952-60-5066-9 (pdf)
ISSN-L 1799-4896
ISSN 1799-4896 (printed)
ISSN 1799-490X (pdf)
http://urn.fi/URN:ISBN:978-952-60-5066-9

Unigrafia Oy
Helsinki 2013

Finland

NORDIC ECOLABEL
441 697
Printed matter

Preface

This work is part of the “Structural integrity of Ni-base alloy welds” (SINI) project, which includes Aalto University, VTT and Finnish and Swedish power companies. It is also part of the “Environmental influence on cracking susceptibility and ageing on nuclear materials” (ENVIS) project, which is a project in the Finnish Research Programme on Nuclear Power Plant Safety 2011 – 2014 SAFIR 2014 and includes VTT, VYR (State Nuclear Waste Management Fund) and Finnish and Swedish power companies. It has been conducted in the Laboratory of Engineering Materials of Aalto University’s School of Engineering in the Department of Engineering Design and Production.

Abstract

Dissimilar metal welds (DMWs) between low-alloy steels (LAS), stainless steels (SS) and nickel-base alloys are very important in the design of conventional and nuclear power plants (NPPs). They help to reach better performances for high temperature environment but they can promote premature failure of components. Failure is often related to cracking in the heat affected zone of base materials.

In this study, a literature review was conducted concerning the behavior of Inconel Ni-base alloys and LAS in DMWs for nuclear applications. It was centered on the metallurgical changes occurring with post-weld heat treatment (PWHT) at the interface of ferritic/austenitic DMWs, on the weldability of Inconel filler metals and on the narrow-gap welding (NGW) technique emerging in the NPP design. The aim was to characterize a NGW present in modern pressurized water reactor (PWR) design, which uses an Inconel filler metal to join the reactor pressure vessel nozzle to its safe-end. In addition, the behavior of Alloy 690 was studied.

Eight samples were characterized. A narrow-gap Alloy 52 mock-up manufactured in the SINI project was studied in the as-welded condition and after PWHT. It showed that PWHT resulted in increased carbon depletion in the LAS side and in an extensive chromium carbide precipitation in the weld metal. It was responsible for a sharp hardness peak in the weld metal. Samples from EPRI (Electric Power Research Institute) were characterized for ENVIS project, showing different weld configurations involving Alloy 690 as base metal and Inconel 52, 152 and 52M as filler metals. Differences in the behavior of the filler metals were observed. Higher hardness was found in Inconel 52M, followed by Inconel 152 and 52, respectively. Inconel 152 showed different behavior than Inconel 52 concerning carbon migration. The microstructure of Alloy 690 was characterized and was found to correspond to the literature review.

Keywords: Dissimilar metal weld, nuclear power plant, Alloy 690, Inconel 52, Inconel 152, Inconel 52M, SA 508, SA 533 Gr.B, narrow gap weld, safe-end, interface, metallurgical changes, hardness.

Contents

Introduction 1

1. Materials in Nuclear Power Plants 3
   - 1.1. Design 3
   - 1.2. Environment 6
     - 1.2.1. BWR water chemistry 6
     - 1.2.2. PWR water chemistry 6
     - 1.2.3. Radiation fields 7
   - 1.3. Materials 8
     - 1.3.1. Main material selection 8
     - 1.3.2. Ferritic low alloy steels 12
     - 1.3.3. Austenitic stainless steels 14
     - 1.3.4. Nickel-base alloys 16
2. Dissimilar metal welds 20
   - 2.1. Overview 20
   - 2.2. Microstructural zones 22
     - 2.2.1. Homogeneous welds 25
     - 2.2.2. Particularities of DMWs 28
   - 2.3. General issues with DMWs in power plants 29
     - 2.3.1. Residual stresses 30
     - 2.3.2. Metallurgical changes at interfaces 31
     - 2.3.3. Creep 33
     - 2.3.4. Variations of electrochemical properties 34
     - 2.3.5. Aging mechanisms 34
3. Developments in DMWs 35
   - 3.1. Heat treatments 36
     - 3.1.1. Annealing 36
     - 3.1.2. Tempering 36
     - 3.1.3. Stress relieving 37
   - 3.2. New materials 38
   - 3.3. Narrow-gap welding 41
4. Metallurgy of typical ferritic-austenitic DMW 45
   - 4.1. Overview 45
   - 4.2. Ferritic/austenitic interface 47

4.2.1. Ferritic HAZ 47
4.2.2. Formation of hard and soft zones at the interface 51
4.2.3. Effect of diffusion barriers 60
4.3. Austenitic-austenitic interface 61
4.3.1. Weldability of Ni-base alloys 62
4.3.2. Microstructures 68
4.3.3. Long-term behavior of Ni-base alloys 77
4.3.4. Grain boundary engineering 85
5. Experimental research work 87
5.1. Microstructural characterization 87
5.2. Hardness measurements 88
5.3. Sample presentation 93
5.3.1. Alloy 52 mock-up 93
5.3.2. EPRI samples 96
5.4. Sample preparation 105
6. Results 106
6.1. Alloy 52 mock-up AW sample 1 106
6.1.1. Microstructures 106
6.1.2. Microhardness 110
6.1.3. Nanoindentation 111
6.2. Alloy 52 mock-up HT sample 3 113
6.2.1. Microstructures 113
6.2.2. Microhardness 117
6.2.3. Nanoindentation 120
6.3. CIEMAT GTAW 122
6.3.1. Microstructures 122
6.3.2. Microhardness 127
6.4. CIEMAT SMAW 128
6.4.1. Microstructures 128
6.4.2. Microhardness 131
6.5. MHI plate 132
6.5.1. Microstructures 132
6.5.2. Microhardness 136
6.6. GTAW 19508A 141

6.6.1. Microstructures 141
6.6.2. Microhardness 143
6.7. ENSA weld mock-up 145
6.7.1. Microstructures 145
6.7.2. Microhardness 149
6.8. PG&E mock-up 152
6.8.1. Microstructures 152
6.8.2. Microhardness 160
6.9. Discussion 162
6.9.1. LAS HAZ and interface with Ni-base weld metal 163
6.9.2. Ni-base weld metals and buttering layers 164
6.9.3. Alloy 690 165
Conclusions 166
References 168

Introduction

Welding in nuclear power engineering is an extensive field that is both time consuming and expensive. It has a fundamental impact on nuclear safety and economic viability of the whole process. Service experience shows that the life of components is governed by the behavior of welds: premature failures indicate the detrimental effects of welding on structural integrity.

Of major interest are the welds between different metals, called dissimilar metal welds (DMW), due to the huge variety of joints involving carbon steel, stainless steel, nickel-base alloy, and overlaying welding that are necessary in the plant. The use of DMWs helps reducing the constructional cost of components while meeting better performances for applications requiring high temperature, corrosive environment and high pressure. However, DMWs have several fabrication and metallurgical issues: they involve both conventional welding issues and the interaction between materials with different properties. It can lead to in-service failures.

In addition to good mechanical and corrosion resistance, nickel-base filler metals have a coefficient of thermal expansion (CTE) that is intermediate between ferritic and austenitic steels. Thus, they are frequently used in applications requiring dissimilar metal welding. Typically, Inconel 82 and 182 have been used as filler metals for dissimilar metal welds involving low alloy steels (LAS), stainless steels (SS) and Inconel 600 as base metals for boiling water reactors (BWR) and pressurized water reactors (PWR).

The susceptibility of Inconel 600 to stress corrosion cracking (SCC) and the cracking observed in Inconel 82 and 182 have led to the use of alloys with higher chromium content. Such alloys are Alloy 690 and filler metals Inconel 52 and 152. These alloys have first been used for repairs and replacements, but are now directly involved in the construction of new plants. In addition to these new materials, narrow-gap welding has been developed to weld thick sections more economically, and is now an emerging technology in nuclear power plant designs.

As a consequence, a large number of new types of DMWs involving new alloys and/or new welding designs are currently used in the nuclear power plants. There is little knowledge available concerning their behavior. An understanding of their physical and structural properties is therefore required to make decisions with lacking in-service experience and better comprehend possible long-term implications. This is especially true when the average age of the existing nuclear power plants is constantly extending.

This study is part of the SINI project (Structural Integrity of Ni-base Alloy Welds) which aim is mainly to develop reliable research methods for the measurement, evaluation and design of dissimilar metal joints for new materials. The project is funded by the main Finnish and Swedish energy companies and involves Aalto University School of Engineering and VTT for the research work.

In this study, several samples from mock-up welds provided by EPRI (Electric Power Research Institute) representing different types of Alloy 690 DMWs present in nuclear power plants were studied. In addition, samples from a mock-up weld manufactured in the project simulating a dissimilar metal narrow-gap weld were characterized.

1. Materials in Nuclear Power Plants

1.1. Design

As conventional power plants, nuclear power plants (NPP) are designed to create steam from water. The steam then activates a turbine, which is bound to a generator. This generator will transform the kinetic energy into electricity.

The major difference with NPP is that it uses nuclear fission to heat the water. The nuclear reaction takes place in the nuclear reactor (Fig. 1).

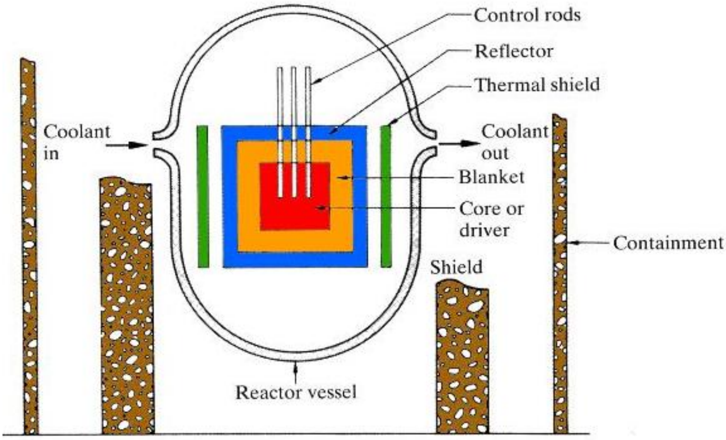

Fig. 1 Cut of a nuclear reactor and main constituents. Of major importance are the RPV nozzles by which enters and leaves the coolant. ***(Aalto University, 2012)***

The reactor is basically made of three parts:

- The reactor pressure vessel (RPV), in which occurs the nuclear reaction.
- The shield, within the plant, that protects from radiation.
- The containment, which is supposed to isolate the plant in case of accident.

The reactor pressure vessel contains also: the core (nuclear fuel and coolant), the moderator (a light material aimed at slowing down neutrons), the reflector (reflects the escaping neutrons), the control rods (they strongly absorb neutrons and they are used to control the intensity or stop the reaction), the thermal shield (it absorbs gamma rays and protects the reactor pressure vessel).

The two conventional and most used types of NPPs are boiling water reactors (BWR, 94 units in 2010) and pressurized water reactors (PWR, 268 units in 2010).

As shown in Figure 2, the main difference is that in BWRs, the steam is produced directly in the reactor pressure vessel and goes to the turbine. In PWRs, a first circuit of water is heated in the reactor pressure vessel. This primary circuit is then used as a heat source to vaporize water in a secondary circuit. The secondary circuit activates the turbine.

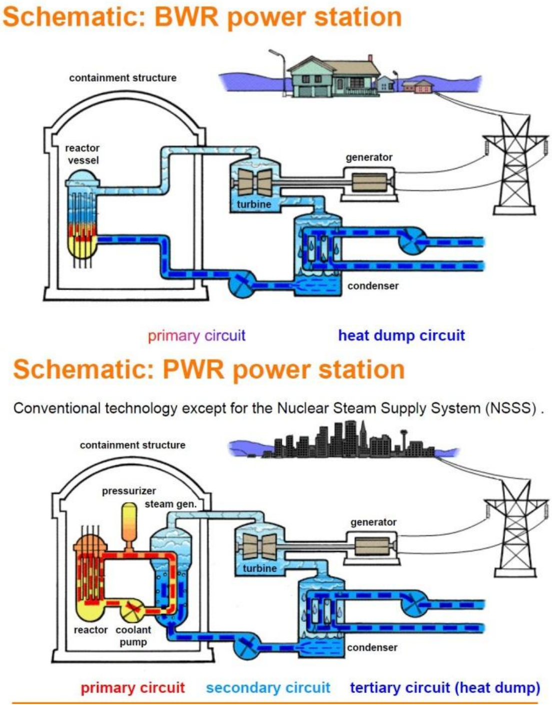

Fig. 2 Difference of principle between BWR and PWR. In BWR, the water heated in the RPV directly enters the turbine. In PWR, it is used to heat a secondary circuit. ***(Aalto University, 2012)***

The design of nuclear reactors has evolved through several generations since the first prototypes of commercial power plants of the 50s. The generation II refers to the first commercial plants of the 70/80s, mostly BWRs, PWRs and RBMK in Russia.

Generation III consists of advanced designs such as ABWR and APWR. They improve the existing designs and are more efficient, more economical and safer. In addition, the generation III+ refers to the further development of the 90s concerning economy and safety, such as the EPR. A new generation IV is expected for 2030.

The EPR (Fig. 3) is the first generation III+ reactor to be built (in Olkiluoto 3, Finland). It is an APWR design, developed by Areva and Siemens, with superior safety and efficiency. The material selection has been made according to the PWR operation experience. The piping welds are made using NG-GTAW.

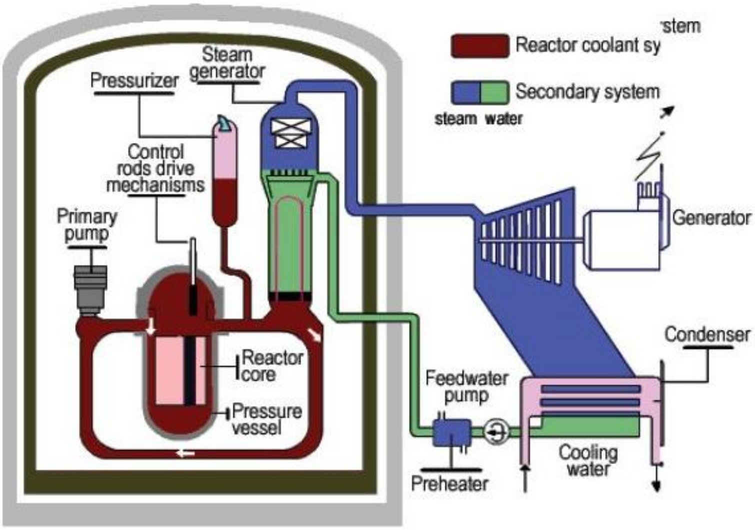

Fig. 3 Cut of the EPR design. ***(Aalto University, 2012)***

When selecting the materials for each NPP design, factors will be cost, stress and environment. The particularity of NPPs among conventional power plants is the nature of the environment that materials have to sustain. It will change according to the design and the location within the plant. Another factor is the temperature. The reactor design determines the maximum operating temperature of the reactor pressure vessel. Thus, it determines the vessel materials in compliance with the design codes and with an acceptable lifetime. **(Shankar et al. 2006)**

1.2. Environment

A specific aspect of NPPs is the water chemistry. Material degradation has to be minimized while fuel performance is kept high. Apart from the fuel performance affected by the water of the primary circuit, the corrosion of alloys all along the different water circuits is one of the major concerns regarding the integrity of the plant. Of major interest are the impurities in the water, the oxygen and additive content and the temperature. The operating temperatures inside water-cooled NPPs are generally lower than for conventional power plants (around 300°C for BWRs and PWRs).

1.2.1. BWR water chemistry

In BWRs, the typical pressure is 70-90 bar and the steam temperature 290°C. High-purity water must be preserved in all the coolant systems. The oxygen content (200 ppb) makes the environment oxidizing **(Hänninen, 2009)**. IGSCC of pipe welds is the major issue. It can happen in all grades of SS and nickel-base alloys depending on the water chemistry, temperature and electrochemical corrosion potential (ECP). For common BWR water chemistry, the ECP is mainly influenced by the content of oxidizing radiolysis products, O_2 and H_2O_2, dissolved in the water at high temperatures. When associated with other metallurgical factors such as sensitization at GBs, cold work and residual stress, these environmental factors can lead to IGSCC. The main oxidant is hydrogen peroxide, which decomposes into oxygen when leaving the radiation field. Another factor is the presence of impurities such as sulphate and chloride.

1.2.2. PWR water chemistry

In PWRs, the reactor pressure is around 140-160 bar, and the temperature of the coolant is generally 290-330°C. The oxygen content is kept around 0 ppb, promoting a reducing environment **(Hänninen, 2009)**. In the primary circuit, boric acid is used as a chemical shim, coordinated with LiOH to maintain a constant pH. Hydrogen is added to prevent heavy crud of corrosion products from forming on fuel cladding surface. In the secondary circuit, corrosion is mainly due to the impurities in the boiling regions. The integrity of steam generators has been a major concern, even with control of impurities, pH and oxidizing corrosion potential. Inconel 600 tubing has proved to corrode severely in both primary and secondary circuit sides. The main parameters influencing SCC in PWR primary circuit water are temperature, hydrogen concentration, Li content, pH and presence of zinc. Hydrogen has a considerable impact on the crack growth rate of Inconel 600, 182 and 132 alloys. The temperature has a considerable effect on the PWSCC. Crack growth rate increases significantly with temperature. Resistance to cracking increases with decreasing hydrogen content. In the normal range of hydrogen content in PWRs (25-55 cc/kg), the influence of hydrogen on crack initiation is small. There are certain differences between initiation and propagation of cracks due to hydrogen. There is a strong effect of corrosion potential near the Ni/NiO oxide stability. Extended fuel cycles imply operation at higher Li contents. Increase of Li can reduce the crack initiation time, but there is broadly little influence of Li on crack initiation. In addition to limit the activity buildup, zinc can have beneficial effects on the initiation of PWSCC, but little effect on crack propagation. There are contradictions between crack initiation and propagation data.

1.2.3. Radiation fields

A specific condition in NPPs is radiation. About 20 MeV/fission goes in all the structures of the reactor pressure vessel and has the potential for radiation damages. The austenitic SS used for the structures of BWR and PWR reactor pressure vessels are intended for the full life of the plant and can be exposed to high dose of radiation. The material microstructure and mechanical properties can change considerably. Thus, the SCC susceptibility is also affected. Irradiation assisted stress corrosion cracking (IASCC) is an important ageing mechanism. Austenitic SS such as 304, 316L and 347 are affected by IASCC. Neutron irradiation causes cascade of atom displacements from the equilibrium crystallographic location, creating vacancies and interstitials. This leads to diffusion of point defects to GBs, dislocations and surfaces, changing significantly the microstructures. High temperatures can be generated by gamma heating in thick sections. Also, neutrons can induce transmutation reactions, thus changes in composition. For highly irradiated austenitic SS, intergranular cracking has been observed even in an inert environment. Dissolved hydrogen can play a role in IASCC susceptibility through hydrogen embrittlement. **(IAEA, 2011)**

1.3. Materials

1.3.1. Main material selection

Due to the numerous environments present in the different types and different circuits of LWRs, the material selection in NPPs is wide (see for BWRs Fig. 4 and for PWRs Fig. 5). In addition, the materials used differ from one constructor to another (see Fig. 6).

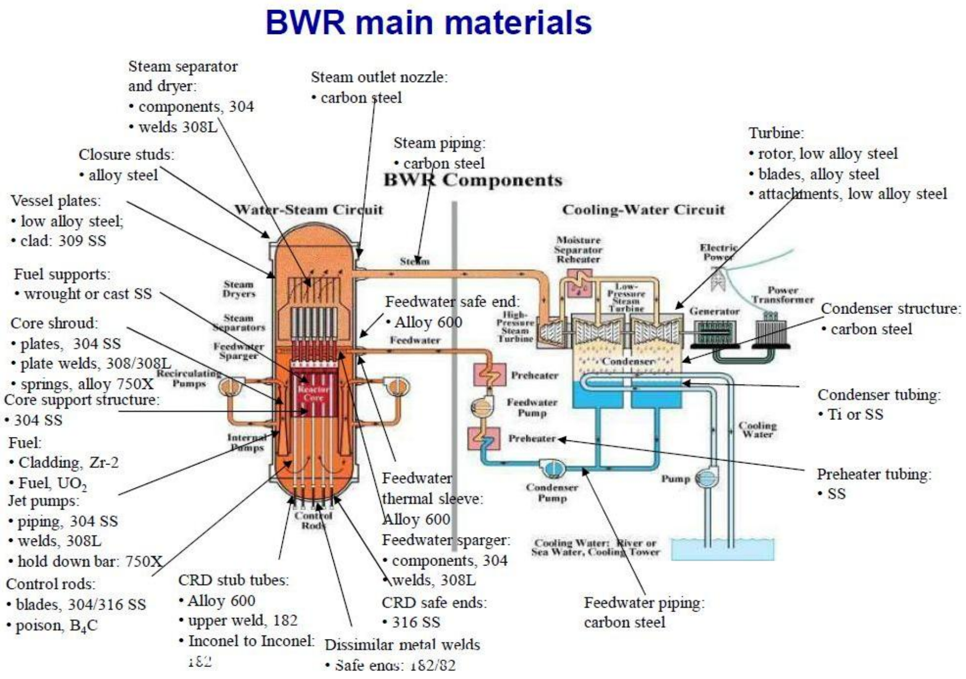

Fig. 4 Material selection for BWR. ***(Aalto University, 2012)***

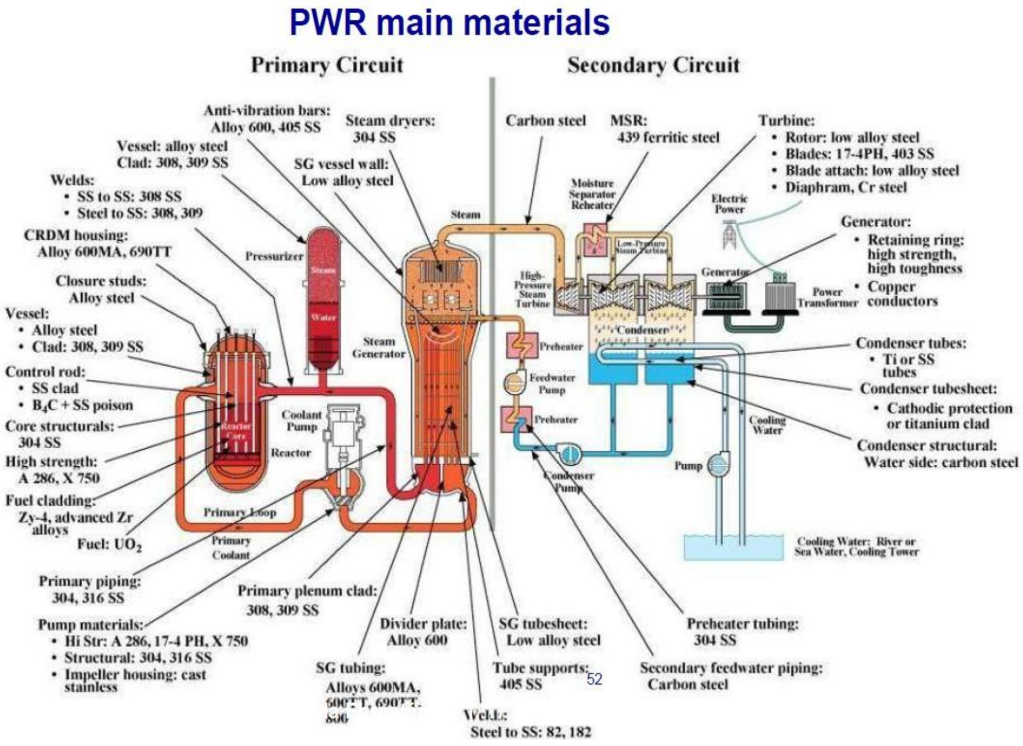

Fig. 5 Material selection for PWR. ***(Aalto University, 2012)***

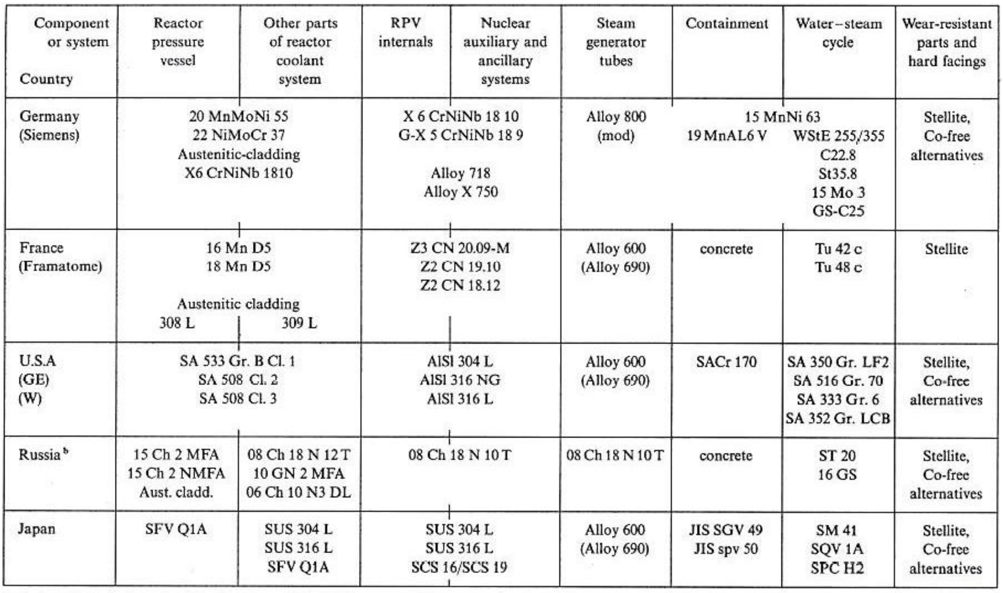

Component or system Country	Reactor pressure vessel	Other parts of reactor coolant system	RPV internals	Nuclear auxiliary and ancillary systems	Steam generator tubes	Containment	Water–steam cycle	Wear-resistant parts and hard facings
Germany (Siemens)	20 MnMoNi 55 22 NiMoCr 37 Austenitic-cladding X6 CrNiNb 1810		X 6 CrNiNb 18 10 G-X 5 CrNiNb 18 9 Alloy 718 Alloy X 750		Alloy 800 (mod)	15 MnNi 63 19 MnAL6 V	WStE 255/355 C22.8 St35.8 15 Mo 3 GS-C25	Stellite, Co-free alternatives
France (Framatome)	16 Mn D5 18 Mn D5 Austenitic cladding 308 L	309 L	Z3 CN 20.09-M Z2 CN 19.10 Z2 CN 18.12		Alloy 600 (Alloy 690)	concrete	Tu 42 c Tu 48 c	Stellite
U.S.A (GE) (W)	SA 533 Gr. B Cl. 1 SA 508 Cl. 2 SA 508 Cl. 3		AISI 304 L AISI 316 NG AISI 316 L		Alloy 600 (Alloy 690)	SACr 170	SA 350 Gr. LF2 SA 516 Gr. 70 SA 333 Gr. 6 SA 352 Gr. LCB	Stellite, Co-free alternatives
Russia[b]	15 Ch 2 MFA 15 Ch 2 NMFA Aust. cladd.	08 Ch 18 N 12 T 10 GN 2 MFA 06 Ch 10 N3 DL	08 Ch 18 N 10 T		08 Ch 18 N 10 T	concrete	ST 20 16 GS	Stellite, Co-free alternatives
Japan	SFV Q1A	SUS 304 L SUS 316 L SFV Q1A	SUS 304 L SUS 316 L SCS 16/SCS 19		Alloy 600 (Alloy 690)	JIS SGV 49 JIS spv 50	SM 41 SQV 1A SPC H2	Stellite, Co-free alternatives

[a] Designations of the national codes are used; [b] WWR types (RBMK-type with fuel channels similar to the Candu NPPs).

Fig. 6 Material selection depending on the constructor. ***(Aalto University, 2012)***

However, the primary materials used in all advanced NPPs are LAS, SS and nickel-base alloys (Fig. 7).

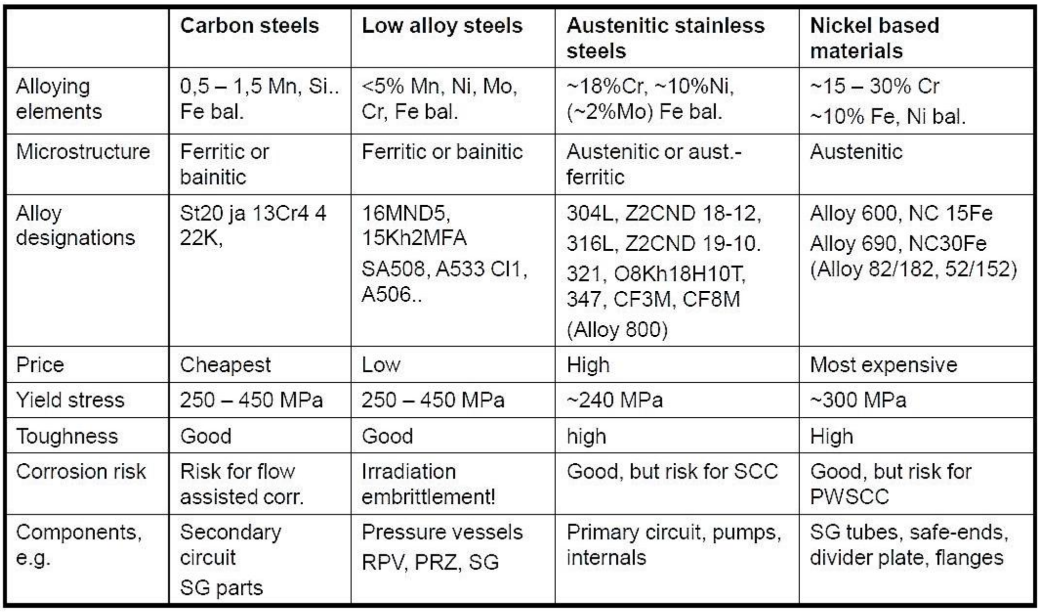

	Carbon steels	Low alloy steels	Austenitic stainless steels	Nickel based materials
Alloying elements	0,5 – 1,5 Mn, Si.. Fe bal.	<5% Mn, Ni, Mo, Cr, Fe bal.	~18%Cr, ~10%Ni, (~2%Mo) Fe bal.	~15 – 30% Cr ~10% Fe, Ni bal.
Microstructure	Ferritic or bainitic	Ferritic or bainitic	Austenitic or aust.-ferritic	Austenitic
Alloy designations	St20 ja 13Cr4 4 22K,	16MND5, 15Kh2MFA SA508, A533 Cl1, A506..	304L, Z2CND 18-12, 316L, Z2CND 19-10. 321, O8Kh18H10T, 347, CF3M, CF8M (Alloy 800)	Alloy 600, NC 15Fe Alloy 690, NC30Fe (Alloy 82/182, 52/152)
Price	Cheapest	Low	High	Most expensive
Yield stress	250 – 450 MPa	250 – 450 MPa	~240 MPa	~300 MPa
Toughness	Good	Good	high	High
Corrosion risk	Risk for flow assisted corr.	Irradiation embrittlement!	Good, but risk for SCC	Good, but risk for PWSCC
Components, e.g.	Secondary circuit SG parts	Pressure vessels RPV, PRZ, SG	Primary circuit, pumps, internals	SG tubes, safe-ends, divider plate, flanges

Fig. 7 Main materials in LWRs: carbon steels, LAS, austenitic SS and Ni-base alloys. ***(Aalto University, 2012)***

The material selection has evolved regarding the service experience. The major trend is the observation of environmental degradation of Inconel 600 and associated weld metals Inconel 82 and 182. These alloys are mainly used for the steam generator (SG) tubing and the reactor pressure vessel nozzle safe end (see Figs. 4, 5, 6). They are now replaced by Alloy 690 and weld metals Inconel 52 and 152, especially in PWRs. **(Shankar et al. 2006)**

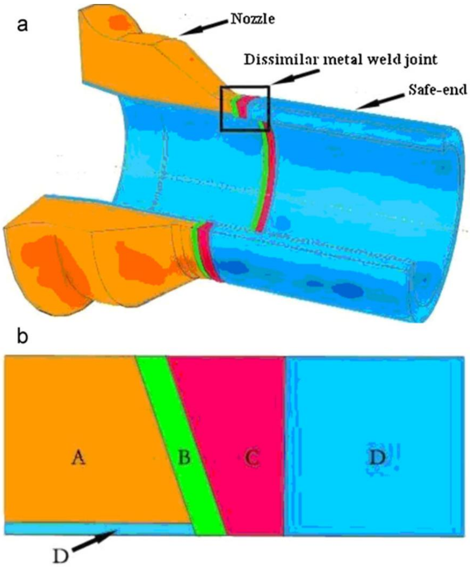

Fig. 8 Scheme of a RPV safe-end (a) and the four materials composing the DMW (b):

- *A- ferritic LAS SA508,*
- *B- buttering alloy Inconel 82,*
- *C- weld alloy Inconel 182,*
- *D- austenitic stainless steel 316L or alloy Inconel 600.* ***(Wang et al. 2011)***

A typical and critical DMW intervenes where the pipe lines connect to the RPV through its nozzle (see Fig. 8). To facilitate the assembly, transition pieces called safe-ends are used. They are made of SS or nickel-base alloy. Their main purpose is to enable the joint between the ferritic steel and the austenitic steel to be welded at the manufacturer, while the easier joint between the austenitic stainless steels of the safe-end and the pipe line is made by the constructor

1.3.2. Ferritic low alloy steels

The material selection for the reactor pressure vessel is the key parameter, as it is the component that broadly sets the lifespan of the nuclear power plant. It is subject to neutron irradiation embrittlement and its replacement is difficult. Due to the severe service conditions, the materials used for RPVs require good strength and toughness to prevent failure. **(Lee et al. 2011)**

Ferritic LAS such as SA533 or SA508 are key materials in the structure of nuclear power plants. They are manganese–nickel–molybdenum low-alloy steels (see Fig. 9). They have sufficient strength to withstand internal pressure from the RPV and high fracture toughness to ensure safety in case of accidental thermal shock **(Hong et al. 2001)**. SA 508 Class 1, 2 and 3 are approved for use up to 371°C under the ASME Code. For consideration of this material for RPVs where the temperature could exceed 371°C, depending on the design, creep-fatigue response and thermal stability become important factors. There is limited data available on the thermal aging effects on their mechanical properties. **(Shankar et al. 2006)**

Investigations have revealed that LAS (if excessive hardness is avoided) has a very high resistance to SCC growth in chloride-free BWR environment up to very high stress intensity **(Seifert et al. 2005)**. However, microstructural changes occur in the LAS HAZ, such as grain coarsening, carbide precipitation and martensite formation. They have deleterious effects on toughness and they sensitize the material to brittle fracture **(Hong et al. 2000)**.

It is possible to improve the mechanical properties of current SA508 Gr.3 Mn-Mo-Ni LAS by controlling their heat treatment and chemical composition. Another solution is to develop new materials with higher strength and toughness, such as the SA508 Gr.4N Ni–Cr–Mo low alloy steel, with higher Ni and Cr contents **(Lee et al. 2011)**. However, strength and toughness are usually opposed. It is difficult to improve both at the same time. In addition, RPV manufacturing usually involves welding. Thus, LAS must keep excellent mechanical properties in the welded regions **(Hong et al. 2001)**. Because of the medium carbon level, they can be difficult to weld. Thus, when they are used for welding applications, lower carbon content has to be used to increase the weldability, while maintaining the strength.

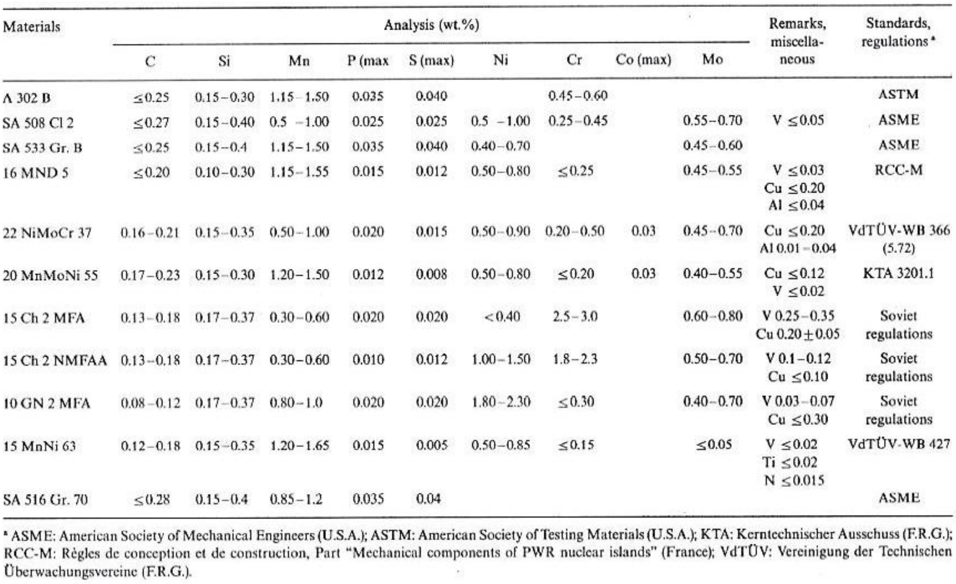

Materials	Analysis (wt.%)									Remarks, miscella-neous	Standards, regulations[a]
	C	Si	Mn	P (max	S (max)	Ni	Cr	Co (max)	Mo		
A 302 B	≤0.25	0.15–0.30	1.15–1.50	0.035	0.040		0.45–0.60				ASTM
SA 508 Cl 2	≤0.27	0.15–0.40	0.5 –1.00	0.025	0.025	0.5 –1.00	0.25–0.45		0.55–0.70	V ≤0.05	ASME
SA 533 Gr. B	≤0.25	0.15–0.4	1.15–1.50	0.035	0.040	0.40–0.70			0.45–0.60		ASME
16 MND 5	≤0.20	0.10–0.30	1.15–1.55	0.015	0.012	0.50–0.80	≤0.25		0.45–0.55	V ≤0.03 Cu ≤0.20 Al ≤0.04	RCC-M
22 NiMoCr 37	0.16–0.21	0.15–0.35	0.50–1.00	0.020	0.015	0.50–0.90	0.20–0.50	0.03	0.45–0.70	Cu ≤0.20 Al 0.01–0.04	VdTÜV-WB 366 (5.72)
20 MnMoNi 55	0.17–0.23	0.15–0.30	1.20–1.50	0.012	0.008	0.50–0.80	≤0.20	0.03	0.40–0.55	Cu ≤0.12 V ≤0.02	KTA 3201.1
15 Ch 2 MFA	0.13–0.18	0.17–0.37	0.30–0.60	0.020	0.020	<0.40	2.5–3.0		0.60–0.80	V 0.25–0.35 Cu 0.20±0.05	Soviet regulations
15 Ch 2 NMFAA	0.13–0.18	0.17–0.37	0.30–0.60	0.010	0.012	1.00–1.50	1.8–2.3		0.50–0.70	V 0.1–0.12 Cu ≤0.10	Soviet regulations
10 GN 2 MFA	0.08–0.12	0.17–0.37	0.80–1.0	0.020	0.020	1.80–2.30	≤0.30		0.40–0.70	V 0.03–0.07 Cu ≤0.30	Soviet regulations
15 MnNi 63	0.12–0.18	0.15–0.35	1.20–1.65	0.015	0.005	0.50–0.85	≤0.15		≤0.05	V ≤0.02 Ti ≤0.02 N ≤0.015	VdTÜV-WB 427
SA 516 Gr. 70	≤0.28	0.15–0.4	0.85–1.2	0.035	0.04						ASME

[a] ASME: American Society of Mechanical Engineers (U.S.A.); ASTM: American Society of Testing Materials (U.S.A.); KTA: Kerntechnischer Ausschuss (F.R.G.); RCC-M: Règles de conception et de construction, Part "Mechanical components of PWR nuclear islands" (France); VdTÜV: Vereinigung der Technischen Überwachungsvereine (F.R.G.).

Fig. 9 LAS compositions for nuclear applications. Among them, it is worth noting SA 302 B, SA 508 CL.2 and SA 533 Gr.B. ***(Aalto University, 2012)***

Fifty-three of the 73 PWR reactor pressure vessels operating in 1994 were fabricated using formed steel plates of either SA302 Grade B (SA302B) steel for earliest vessels or SA533 Grade B Class 1 (SA533 Gr.B-1) steel for the other vessels. Nickel-modified SA302B is the early equivalent of SA533 Gr.B-1. Twenty of the later reactor pressure vessels were fabricated using ring forgings of SA508 Class 2 or SA508 Class 3 rather than plates. The nozzles are all forgings of SA508 Cl2 or SA508 Cl3. **(Shah et al. 2006)**

Irradiation embrittlement is the major issue for the RPV LAS structure. It increases the ductile-to-brittle transition temperature and brittle fracture may initiate. Welds are particularly susceptible. Irradiation embrittlement can be minimized by restricting the P, Cu, Ni content. **(Hänninen, 2009)**

1.3.3. Austenitic stainless steels

With more than 12% Cr, steel becomes stainless. The formation of a passive layer of Cr_2O_3 increases drastically the corrosion resistance. The three main types of stainless steels are austenitic, ferritic, and martensitic. These three types of steels are identified by their predominant crystal structure: ferritic, austenitic and martensitic.

Since Cr is a ferrite stabilizer, steels containing large amounts of Cr are usually ferritic. They have good mechanical properties, bur their corrosion resistance may need to be improved.

Austenitic SS contain both Cr and Ni. Nickel will stabilize the FCC austenitic phase at room temperature. Nickel will also increase the ductility of the alloy. The FCC austenitic phase is more ductile and can be worked easily. The most common austenitic SS are grades 304 and 316. They are structured around the grade 302 composition (Fe, 18wt% Cr, 8wt% Ni). Common grades of austenitic SS used in NPPs are listed in Figure 10.

Special properties, including corrosion resistance, oxidation resistance, and strength at high temperatures, can be incorporated into austenitic stainless steels by adding other alloying elements like chromium, nickel, molybdenum, nitrogen, titanium, and niobium. Carbon can add strength at high temperatures, but it reduces corrosion resistance by forming chromium carbides. In addition, depending on the presence of other ferrite and austenite stabilizing elements and cooling rate, a variety of microstructures can result. In welding, Schaeffler diagrams are used to predict the resulting microstructure around SS considering the nickel and chromium equivalents for the alloy composition. Austenitic SS offer good weldability, but have to be stabilized by additions of about 1% Nb or Ti in order to avoid chrome carbide $Cr_{23}C_6$ precipitation in the HAZ. Worth noting is that austenitic SS do not harden in the weld HAZ. However, cold work can produce martensite from the austenite.

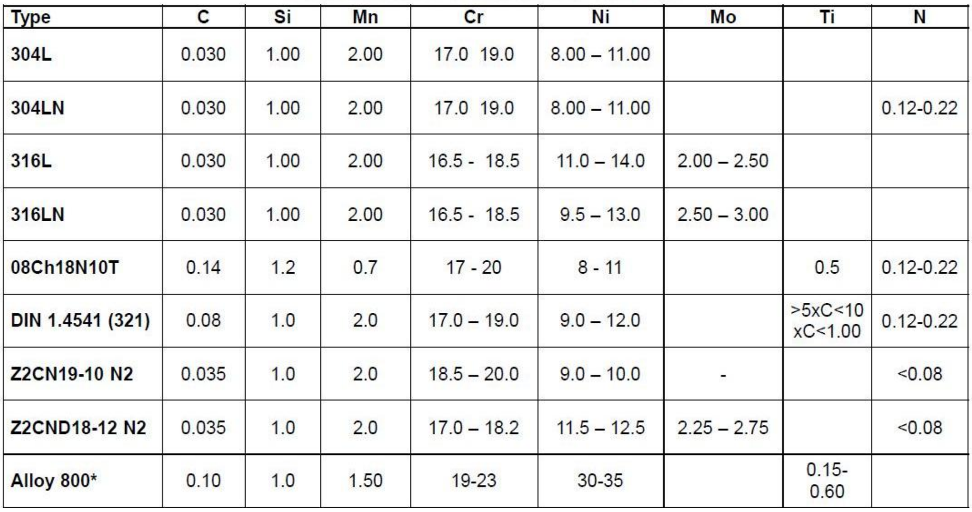

Type	C	Si	Mn	Cr	Ni	Mo	Ti	N
304L	0.030	1.00	2.00	17.0 19.0	8.00 – 11.00			
304LN	0.030	1.00	2.00	17.0 19.0	8.00 – 11.00			0.12-0.22
316L	0.030	1.00	2.00	16.5 - 18.5	11.0 – 14.0	2.00 – 2.50		
316LN	0.030	1.00	2.00	16.5 - 18.5	9.5 – 13.0	2.50 – 3.00		
08Ch18N10T	0.14	1.2	0.7	17 - 20	8 - 11		0.5	0.12-0.22
DIN 1.4541 (321)	0.08	1.0	2.0	17.0 – 19.0	9.0 – 12.0		>5xC<10 xC<1.00	0.12-0.22
Z2CN19-10 N2	0.035	1.0	2.0	18.5 – 20.0	9.0 – 10.0	-		<0.08
Z2CND18-12 N2	0.035	1.0	2.0	17.0 – 18.2	11.5 – 12.5	2.25 – 2.75		<0.08
Alloy 800*	0.10	1.0	1.50	19-23	30-35		0.15- 0.60	

Fig. 10 Austenitic SS grades, among which the common grades 304L and 316L. Incoloy 800 is given as a comparison. ***(Aalto University, 2012)***

The inside of the reactor pressure vessel is clad with stainless steel to inhibit general corrosive attack. Grades 308 and 309 SS are generally weld-deposited using an SAW process whenever possible, and a stress relief heat treatment is applied after that. Some older vessels were clad on the inside surface with grade 304. **(Shah et al. 2006)**

Super-austenitic SS are also commonly used, with higher Ni, Mo and N content to ensure better corrosion resistance. Also, other alloys with lower carbon content such as 304L and 316L offer the same corrosion resistance properties and are less expensive. However, when higher anti-corrosion and high temperature properties are needed, nickel-base alloys are used.

As for LAS, irradiation will have effects on austenitic SS. It can cause material hardening and GB segregation, which reduces corrosion resistance. With higher neutron fluence voids develop at GBs, that probably affect the susceptibility to IASCC. **(Hänninen, 2009)**

1.3.4. Nickel-base alloys

A large number of industrially important materials are derived from nickel–iron–chromium alloys. These alloys are within the gamma austenitic range of the ternary Ni–Fe–Cr phase diagram. They are known for good resistance to corrosion and oxidation and good elevated temperature strength.

Examples are the Inconel alloys (INCONEL is a trademark of INCO Alloys International, Inc., Huntington, WV). They are based on the Inconel alloy 600 composition. Alloy 600 is a solid solution strengthened alloy with good strength and toughness even at high temperatures. It has good oxidation and corrosion resistance in many environments. In addition, the alloy is easily fabricated and joined. Many modifications of alloy 600 have been made to produce alloys with different characteristics:

- Inconel alloy 601 contains aluminum for improved high temperature oxidation resistance.
- Inconel alloy 625 contains molybdenum and niobium in solid solution for better strength.
- Inconel alloy 690, with further additions of chromium, was developed for use in the nuclear industry and is particularly noted for its resistance to corrosion in high purity water. It has an austenitic microstructure with many intra- and intergranular carbides.

Figure 11 shows the composition of the two major Ni-base base metals used in this study, Inconel 600 and 690.

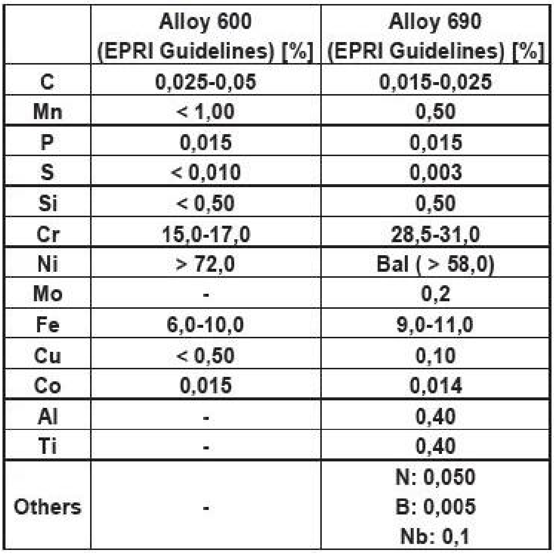

	Alloy 600 (EPRI Guidelines) [%]	Alloy 690 (EPRI Guidelines) [%]
C	0,025-0,05	0,015-0,025
Mn	< 1,00	0,50
P	0,015	0,015
S	< 0,010	0,003
Si	< 0,50	0,50
Cr	15,0-17,0	28,5-31,0
Ni	> 72,0	Bal (> 58,0)
Mo	-	0,2
Fe	6,0-10,0	9,0-11,0
Cu	< 0,50	0,10
Co	0,015	0,014
Al	-	0,40
Ti	-	0,40
Others	-	N: 0,050 B: 0,005 Nb: 0,1

Fig. 11 Composition of Inconel 600 and Alloy 690. Alloy 690 has higher Cr and Fe contents. ***(Staehle et al. 2003)***

Other alloys have been developed for use in particular corrosion environments at high temperatures. Several of these are age-hardenable alloys, which contain additions of aluminum and titanium:

- Inconel alloys 718 and X-750 have higher strength and better creep and stress rupture properties than alloy 600. They have also the same good corrosion and oxidation resistance. Alloy 718 exhibits excellent stress rupture properties up to 705°C as well as good oxidation resistance up to 980°C. It is widely used in gas turbines and other aerospace applications, and for pumps, nuclear reactor parts, and tooling.

The INCOLOY alloys are other examples of nickel–iron–chromium alloys:

- Incoloy 800 is resistant to hot corrosion, oxidation, and carburization and has good elevated-temperature strength.
- Incoloy 801contains more titanium, which, with appropriate heat treatments, can age-harden the alloy and provide increased resistance to intergranular corrosion.
- Incoloy 802 contains more carbon which provides improved high temperature strength through carbide strengthening.
- Incoloy G-3 contains molybdenum, copper, and other additions and is exceptionally resistant to attack by aggressive corrosion environments.

The corrosion- and heat-resistant alloys, e.g., alloys 600 and 800, are used extensively in heat-treating equipment, nuclear and fossil-fuel steam generators. Alloys 625 and 825 are used in chemical processing, aircraft turbines and nuclear waste-handling systems. The age-hardened Inconel and Incoloy alloys are used in gas turbines, high temperature springs and bolts, nuclear reactors and waste management. There are also nickel–iron–chromium alloys used as welding electrode and filler metals. Such alloys are Inconel 82, 182, 52, 152, and 617. The compositions of the most common Ni-base filler metals used in this study are listed in Figure 12 and their main mechanical properties are given in Figure 13. **(Kirk-Othmer Encyclopedia of Chemical Technology, 2005)**

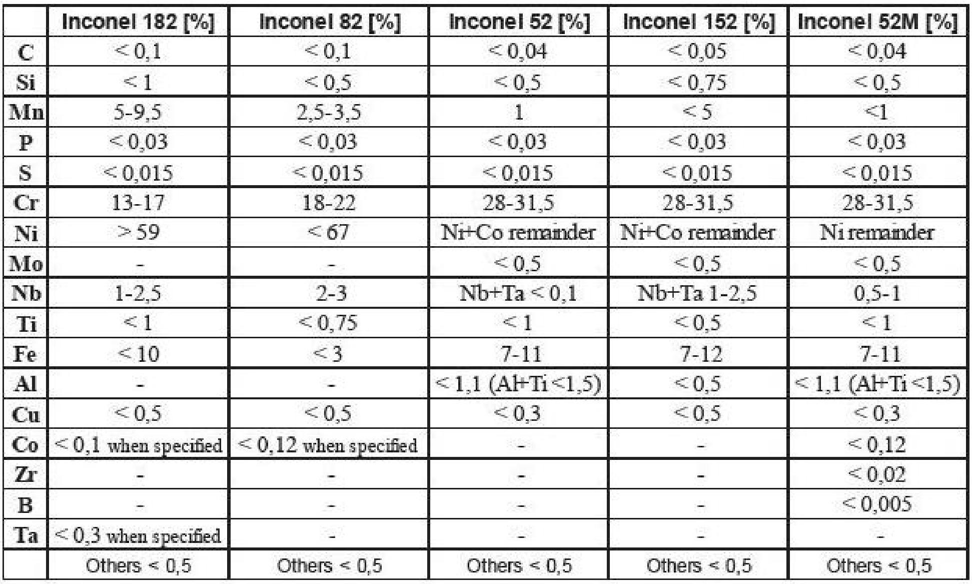

	Inconel 182 [%]	Inconel 82 [%]	Inconel 52 [%]	Inconel 152 [%]	Inconel 52M [%]
C	< 0,1	< 0,1	< 0,04	< 0,05	< 0,04
Si	< 1	< 0,5	< 0,5	< 0,75	< 0,5
Mn	5-9,5	2,5-3,5	1	< 5	<1
P	< 0,03	< 0,03	< 0,03	< 0,03	< 0,03
S	< 0,015	< 0,015	< 0,015	< 0,015	< 0,015
Cr	13-17	18-22	28-31,5	28-31,5	28-31,5
Ni	> 59	< 67	Ni+Co remainder	Ni+Co remainder	Ni remainder
Mo	-	-	< 0,5	< 0,5	< 0,5
Nb	1-2,5	2-3	Nb+Ta < 0,1	Nb+Ta 1-2,5	0,5-1
Ti	< 1	< 0,75	< 1	< 0,5	< 1
Fe	< 10	< 3	7-11	7-12	7-11
Al	-	-	< 1,1 (Al+Ti <1,5)	< 0,5	< 1,1 (Al+Ti <1,5)
Cu	< 0,5	< 0,5	< 0,3	< 0,5	< 0,3
Co	< 0,1 when specified	< 0,12 when specified	-	-	< 0,12
Zr	-	-	-	-	< 0,02
B	-	-	-	-	< 0,005
Ta	< 0,3 when specified	-	-	-	-
	Others < 0,5	Others < 0,5	Others < 0,5	Others < 0,5	Others < 0,5

Fig. 12 Composition of Ni-base filler metals. Inconel 52,152 and 52M have higher Cr and Fe contents. Inconel 52M has additions of boron and zirconium. ***(Aalto University, 2012)***

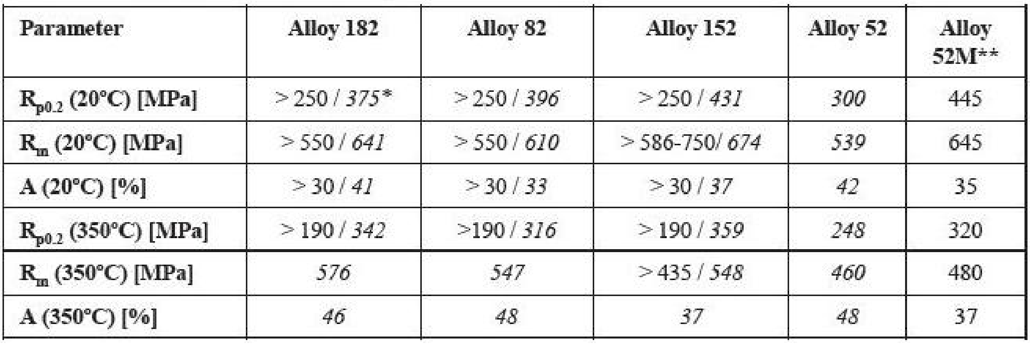

Parameter	Alloy 182	Alloy 82	Alloy 152	Alloy 52	Alloy 52M**
$R_{p0.2}$ (20°C) [MPa]	> 250 / 375*	> 250 / 396	> 250 / 431	300	445
R_m (20°C) [MPa]	> 550 / 641	> 550 / 610	> 586-750/ 674	539	645
A (20°C) [%]	> 30 / 41	> 30 / 33	> 30 / 37	42	35
$R_{p0.2}$ (350°C) [MPa]	> 190 / 342	>190 / 316	> 190 / 359	248	320
R_m (350°C) [MPa]	576	547	> 435 / 548	460	480
A (350°C) [%]	46	48	37	48	37

Fig. 13 Mechanical properties of Ni-base filler metals, at room temperature and usual in-service temperature. ***(Boursier et al. 2004)***

In practice, Ni-base alloys are more difficult to weld than the SS fillers. They are subject to ductility dip cracking (DDC), hot cracking and reheat cracking. Especially, Inconel 52 was developed for its better SCC resistance, but it is more difficult to weld than Inconel 82 and 182. Figure 14 shows the composition of some high-strength alloys mentioned before.

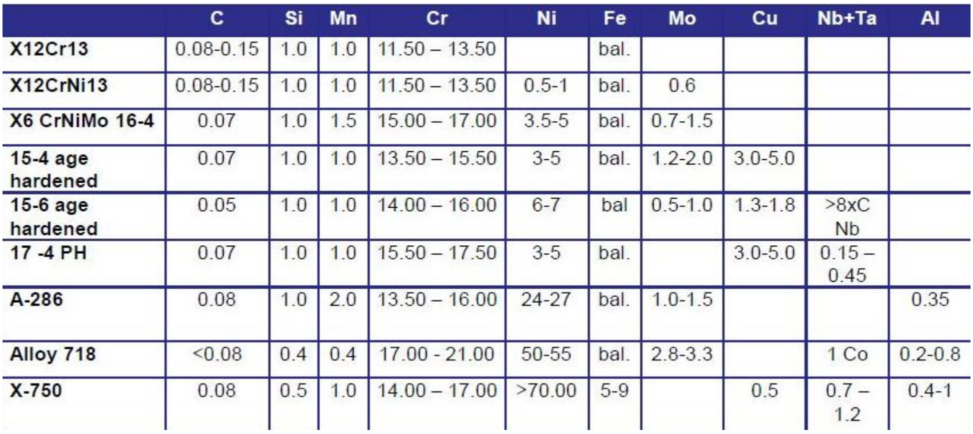

	C	Si	Mn	Cr	Ni	Fe	Mo	Cu	Nb+Ta	Al
X12Cr13	0.08-0.15	1.0	1.0	11.50 – 13.50		bal.				
X12CrNi13	0.08-0.15	1.0	1.0	11.50 – 13.50	0.5-1	bal.	0.6			
X6 CrNiMo 16-4	0.07	1.0	1.5	15.00 – 17.00	3.5-5	bal.	0.7-1.5			
15-4 age hardened	0.07	1.0	1.0	13.50 – 15.50	3-5	bal.	1.2-2.0	3.0-5.0		
15-6 age hardened	0.05	1.0	1.0	14.00 – 16.00	6-7	bal	0.5-1.0	1.3-1.8	>8xC Nb	
17 -4 PH	0.07	1.0	1.0	15.50 – 17.50	3-5	bal.		3.0-5.0	0.15 – 0.45	
A-286	0.08	1.0	2.0	13.50 – 16.00	24-27	bal.	1.0-1.5			0.35
Alloy 718	<0.08	0.4	0.4	17.00 - 21.00	50-55	bal.	2.8-3.3		1 Co	0.2-0.8
X-750	0.08	0.5	1.0	14.00 – 17.00	>70.00	5-9		0.5	0.7 – 1.2	0.4-1

Fig. 14 Composition of some high-strength alloys, among which Inconel 718 and X-750. ***(Aalto University, 2012)***

To be noted is also the development of the ferritic-martensitic highly-alloyed steels for boiler and turbine materials, and for steam generators of NPPs. They are based on ferritic Cr-Mo steels. They were not considered originally for fission reactor because of high temperature strength considerations. They became of great interest because of their swelling resistance compared to austenitic SS. New research about making of the low-activation ferritic and martensitic steels is conducted in relation to fusion reactors. **(Klueh et al. 2001)**

To conclude, the joint between the RPV nozzle and its safe-end is a typical example of DMW. It is also one of the most important concerning the structural integrity of the NPP. In both BWR and PWR, the failure mechanism will be mainly SCC and irradiation-assisted stress corrosion cracking (IASCC), the main failure locations being the heat-affected zones (HAZ) of the welds. **(Hänninen, 2009)**

2. Dissimilar metal welds

2.1. Overview

There are many applications where different properties are required for different parts of the same weldment. These weldments are then made from metals of different compositions. They are called dissimilar metal welds (DMWs) and their importance has increased greatly over the past two decades. Applications of DMWs include cladding for corrosion resistance and joining base metals that exhibit large differences in structure and properties **(Lippold et al. 1999)**.

There are two types of DMWs:

- Joining of two base metals of different composition, usually using a different filler metal.
- Joining of two base metals of similar composition, but using a different filler metal. **(Karlsson, 1995)**

Typically, ferritic LAS joined to austenitic nickel-base alloy and using a nickel-base filler metal are of the former type. Joining of two pieces of austenitic nickel-base alloy using another nickel-base filler metal belongs to the latter type.

Figure 15 shows the typical aspects of DMWs found in nuclear power plants.

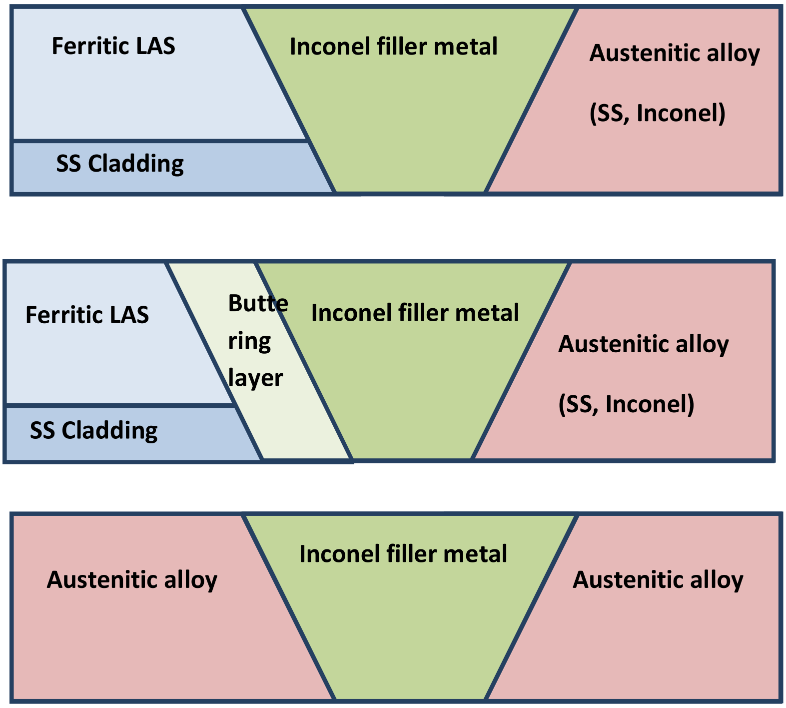

Fig. 15 Typical DMW designs in NPPs. The second is usual for a weld between a RPV nozzle and its safe-end.

It is to be noted that when the solubility or the coefficients of thermal expansion of the materials to be welded do not match, the only way to make a successful joint is to use a transition material between the two dissimilar metals. It can be done by using an intermediate piece in between, or by using a buttering layer (a deposit of several layers of a transition metal on one of the base metals). In addition, this buttering layer is often used as a diffusion barrier preventing dilution from base to weld metals to have deleterious effects on the microstructures **(Anand et al. 2008).** This will be addressed more in detail in the next chapters.

The most common question in DMWs is that of filler metal selection. It is fundamental to minimize the risk of weld failures. The filler metal must accept dilution from the base metals without cracking or forming undesirable phases. It must also have enough strength, ductility and corrosion resistance for service **(Karlsson, 1995)**. Most applications require matching tensile and yield strength. If welding a lower strength material to a higher strength one, it is better to match the filler metal to the lower strength one, as it will allow greater ductility and decrease the risk of cracking. **(Bundy, 2012)**

Ni-base filler metals have a number of advantages:

- they are resistant to dilution without the formation of martensite,
- their CTE is close to that of LAS, resulting in little thermal fatigue,
- their yield strength is low,
- they are not subject to brittle sigma phase formation during HT,
- they reduce carbon migration.

Nickel-base alloys have increased the service life of ferritic/austenitic welds by 5 by reducing the carbon migration and differential expansion strains. However, they are susceptible to hot cracking. **(Karlsson, 1995)**

2.2. Microstructural zones

A DMW will generally present at least two fusion lines, that is, between the filler metal and the base metals or buttering layer. As shown in Fig. 16, these interfaces will generally consist of four distinct microstructural zones:

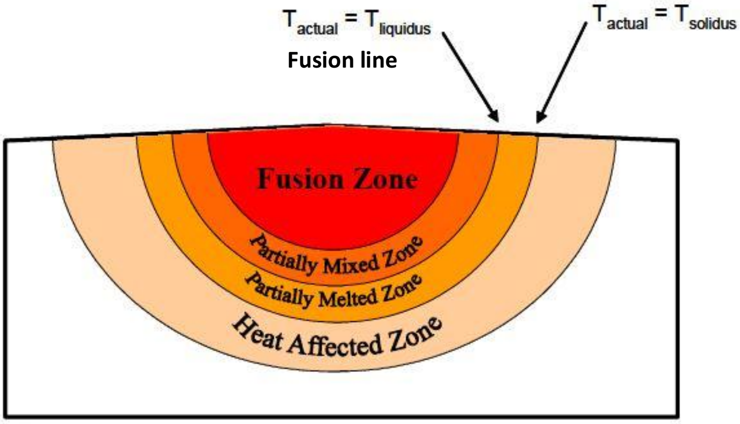

Fig. 16 Schematic illustration of four distinct microstructural zones existing in DMWs: fusion zone (FZ), unmixed zone (UMZ), partially melted zone (PMZ) and heat affected zone (HAZ). ***(DuPont et al. 2010)***

- The fusion zone (FZ) or composite zone (CZ) is the region of weld with complete melting and re-solidification. There is a complete mixing between the base metal and the filler metal. The metals are uniformly diluted due to the fluid flow that occurs in the weld metal in the liquid state. The composition within this FZ is macroscopically uniform due to this mixing.

The partially mixed zone (PMZ) or unmixed zone (UMZ) (see Fig. 17) is a stagnant boundary layer formed by complete melting and re-solidification of base metal, where mixing between the base metal and filler metal is incomplete. This is due to friction at the interface between the liquid metal and the base metal. A composition gradient is generally observed here between the fusion zone and the base metal. This composition gradient is very important in terms of microstructure and performance. It is possible to eliminate the formation of the UMZ in DMWs by increasing the weld pool convection. One technique is the use of electromagnetic force. **(David, 2005)**

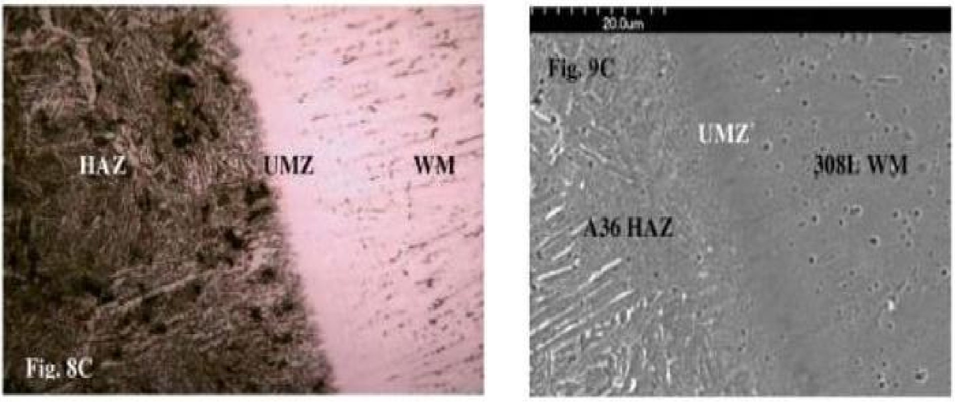

Fig. 17 Optical and SEM image of UMZ at the interface between A36 HAZ and 308L weld metal. ***(Gandhi et al. 2005)***

- The partially melted zone (PMZ) is a transition region in base metal where the temperature was between the liquidus and solidus of the base metal during welding. Different amounts of liquation can often be observed in this region. It can have huge influence on the microstructure: liquation at GBs, localized melting of secondary phases, constitutional liquation of certain particles or carbide dissolution. No mixing occurs with the filler metal, so the composition in this region is identical to the base metal.

- The heat affected zone (HAZ) is an un-melted region of the base metal, but where temperature remains high enough for solid-state transformations to occur: carbide dissolution or grain growth. It is thus affected by the heating and cooling weld cycles. **(DuPont et al. 2010)**

The characterization and control of the HAZ and the PMZ is of particular concern. It is in these zones that most of the in-service failures occur for the ferritic steels, notably because of their reduced creep resistance **(Coleman et al. 1993)** and for nickel-base alloys because of their tendency to liquation cracking in the PMZ, especially after post-weld heat treating (PWHT) **(Soares et al. 2007)**. The classification of microstructural zones can become more complex in the case of weld repairs such as overlays, resulting in a weld with an increased number of materials and zones: aged and new base metals, aged and new weld metal, aged and new HAZ. **(Hyde et al. 2001)**

As shown in Figure 18, the different microstructural zones are related to the solidification temperature range and to the several phases that will solidify during cooling.

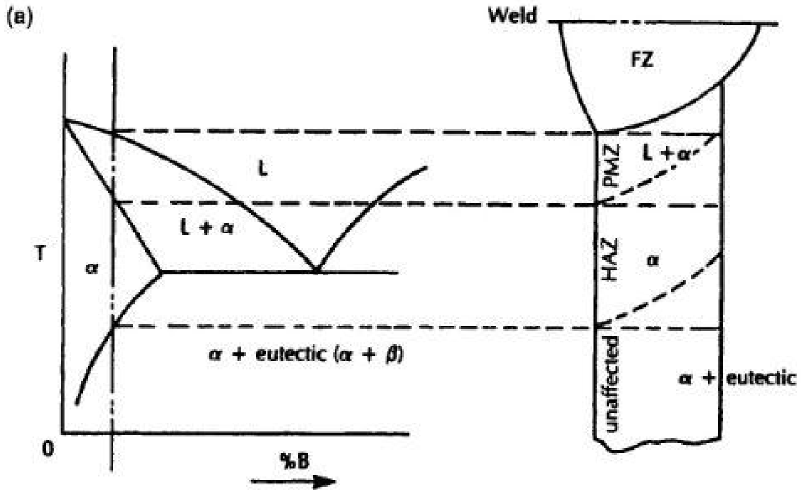

Fig. 18 Illustration showing the correlation between the various zones in a fusion weld in an alloy and the corresponding equilibrium phase diagram. ***(Messler, 1993)***

2.2.1. Homogeneous welds

During fusion welding, the weld becomes both more homogeneous because of convection in the weld metal and more heterogeneous mainly because of solute redistribution during solidification.

When welding two metals, a filler metal is added, either of the same composition as the base metals (homogeneous welding) or of different composition (heterogeneous welding). Homogeneous welding has numerous advantages concerning matching: perfect compatibility of base and weld metals, uniform chemical and mechanical properties of base and weld metals.

The main form of nucleation in the fusion zone is heterogeneous nucleation. The numerous nucleating agents present during welding bring new surfaces on which nucleation is possible. This reduces the interfacial energy, thus, the critical nuclei radius needed for nuclei to persist. As a consequence, only a small undercooling is needed for nucleation to occur.

In welding, the partially-melted base metal surface will act as a nucleating surface for the liquid weld metal. The interfacial energy depends on the wetting angle between the base metal and the weld metal. It is assumed that for similar weld where base and weld metals are the same, the wetting is perfect and so the nucleation barrier is low. It can already be seen that DMWs will act differently.

After the nucleation, the grain growth is first epitaxial, that is to say using the pre-existing grains of the base metal and solidifying from them without changing the crystallographic orientation. It explains the continuity of grain boundaries in similar welds.

As shown in Fig. 19, the grains continue to grow following a competitive-growth mechanism. The grains which easy-growth crystallographic direction is similar to the temperature gradient will grow faster than others. The easy growth direction in BCC and FCC materials is the <100>. Competitive growth will produce a cube-on-cube (<100>//<100>, {100}// {100}) orientation relationship between the HAZ and weld metal grains along the fusion boundary and a weak <100> fiber texture toward the centerline of the welds in cubic metals **(Lippold et al. 1999)**.

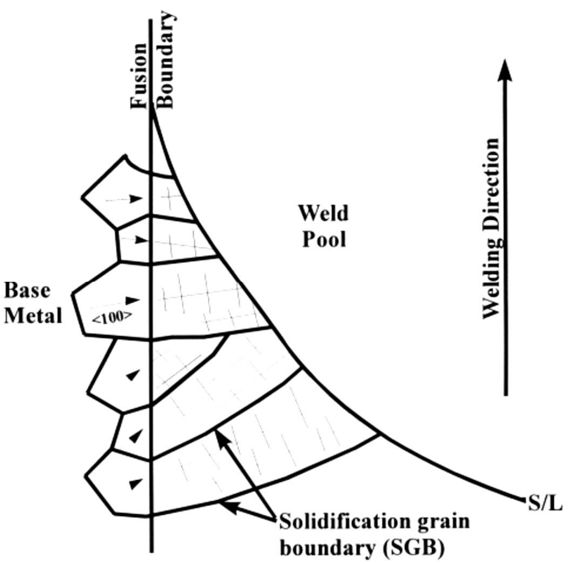

Fig. 19 Epitaxial grain growth mechanism for a homogeneous weld. The continuity across the fusion line is clearly visible. ***(Lippold et al. 1999)***

However, the fusion line microstructure in DMWs possesses unique features. Notably, in DMWs between ferritic and austenitic metals, another type of boundary exists, called Type II boundary. It is parallel to the fusion line and it has no continuity across the fusion line **(Lippold et al. 1999)**.

Other mechanisms can also intervene in the solidification structure, and can explain the presence of equi-axed dendrites. These are unlikely to occur in most welds, but they can contribute to the weld metal microstructures often observed in DMWs:

- Dendrite fragmentation: the fragile tips of dendrites are broken by convective flow and serve as heterogeneous nuclei for growth of equi-axed dendrites.
- Grain detachment: the convective flow detaches grains of the partially melted base metal, which in turn acts as sites for heterogeneous nucleation of equi-axed dendrites.
- Heterogeneous nucleation: from foreign solid particles in the weld pool (such as pieces of welding torch, particles of unmelted flux, impurities).
- Surface nucleation: air cooling at the surface of a weld pool.

Even with homogeneous welds, heterogeneities appear during the solidification: the rejection of solute from a molten alloy is a consequence of solute partitioning between solid and liquid phases of an alloy. Under equilibrium, the final weld should be completely homogeneous, but weld solidification takes place under non-equilibrium conditions, resulting in incomplete solute redistribution in the final weld. The consequences are microsegregation across cells or dendrite arms and banding **(Kou, 2003)**:

- Microsegregation causes composition gradients between dendrite cores and arms, which can have huge effects on the solidification cracking susceptibility of the weld metal.
- Banding is the result of a fluctuating growth rate, resulting in fluctuating solute rejection at the solidification line. It makes layers of solid of different properties to form, perturbing the solidification structure.

However, heterogeneous welding is often needed and always present (by definition) for DMWs: different base metals require different filler metals. Even similar base metal can need a different weld metal, often more alloyed. As it will be explained in this study, the use of dissimilar metals brings particular issues.

2.2.2. Particularities of DMWs

Based on the solidification theory of alloys, welding of similar metals is well understood. But the understanding of DMW solidification is difficult because the interaction of new factors, related to the differences between base and filler metals. Mostly, the region near the fusion line often differs from the bulk weld metal in composition, microstructure and properties. **(Chatterjee et al. 2006)**

- Difference in the crystal structures: In DMWs with different crystal structures, the wetting between base and weld metals may not be perfect, bringing a greater free energy barrier. Thus, nucleation of solid weld metal occurs on heterogeneous sites on the partially melted HAZ grain at the fusion boundary. Because these nuclei form at heterogeneous sites on the HAZ interface, they may or may not exhibit those preferred orientation relationships observed in SMWs. As a result, the fusion boundary exhibits random misorientation between base and weld metal grains. This is of great importance for the subsequent cooling transformations, notably the formation of Type II boundaries which promote cracking **(Lippold et al. 1999)**.
- Difference in the lattice parameter.
- Difference between the thermo-mechanical properties of the base metals, which influence the heat transfer during welding.
- Varying composition across the weld pool and consequent multiple liquidus isotherm defining the solid-liquid interface. Of major importance is the segregation-driven composition profile at the interface, caused by the rejection of alloying elements into the liquid by the solidifying weld metal. It has a major role in issues related to DMWs **(Kou, 2003)**.
- Nucleation of intermetallic compounds when present in the phase diagram.
- Natural convection when the base metal densities are different.

In addition, microsegregation occurs in all welds, but another particular concern with DMWs is macrosegregation, which refers to composition gradients bigger than the dendrite or grain width. Macrosegregation in DMWs can occur if the mixing is insufficient. It is more severe for thick sections welded with multiple passes. As a result, there can be differences in composition between the passes. It can affect, for example, the ferrite content and thus the resistance to SCC. **(Turner et al. 1964; Messler, 1999)**

Inhomogeneity in the region along the fusion boundary has been reported to cause many problems, including hydrogen cracking, corrosion and stress corrosion cracking. The composition transition zone is often in the martensitic range (as it can be seen in the Schaeffler diagram) **(Kou, 2003)**. The consequences of UMZ and PMZ are changes in composition resulting in formation of undesirable phases, hydrogen-induced cracking or preferential corrosive attack **(Messler, 1999)**.

These phenomena are related either to the solidification of the fusion zone, to the formation of heterogeneous zones or to the evolution of heat-affected materials. They contribute to the general issues concerning DMWs.

2.3. General issues with DMWs in power plants

A DMW should be as strong as the weaker of the two base metals, that is to say, it should possess enough tensile strength and ductility so that the joint will not fail in the weld metal.

However, it has been shown that the DMWs fail before the components reach their expected service life. It has been the reason for numerous studies **(Celik et al. 1999)**, the main issue being the use of structural components in a high temperature environment or exposed to thermal fatigue as a result of the temperature change during the different operations of NPP. The majority of problems with high temperature components in power plants are related to cracking in welds. Cracking associated with DMWs has been a persistent and costly problem over the last four decades. It is directly influenced by the stress state and the local structure properties.

The problem of DMWs relates to the intermetallic compounds formed in the transition zone between the metals, which microstructures have to be investigated to determine their ductility and susceptibility to cracking and corrosion. Cracking in welds usually occurs along grain boundaries. This includes weld solidification cracking, weld metal liquation cracking, HAZ liquation cracking, stress relief heat treatment and strain-age cracking, and ductility dip cracking **(Lippold et al. 2000)**. The general problems that are encountered with DMWs are related to residual stress, creep behavior and metallurgical changes across the interfaces and the HAZ. All these factors combine in the aging mechanisms that occur in the welds.

2.3.1. Residual stresses

A residual stress is a stress present in a body without external constraints. It is due to elastic accommodation of plastic deformations during machining or heating. For example, heat input during welding can cause local expansion. During cooling, depending on the material, some parts can contract more than others. High tensile residual stresses are a major factor of SCC in welds.

There are three types of residual stresses **(Aalto University, 2012)**, depending on their characteristic scale. They influence structural integrity in different ways:

- Type I: Macroscopic structural stress (over the whole structure). They influence crack growth and failure.
- Type II: Microscopic internal stress (over 3-10 grains). They influence short crack growth.
- Type III: Microscopic intragranular stress (inside one grain). They contribute to crack initiation.

The residual stresses are the major causes of cracking in welds and HAZ regions during service in power plants. They are influenced by the process parameters, which include the employed welding process type, arc traveling speed, voltage and current. For multi-pass welds, the different locations are submitted to different thermal cycle and restraint condition, thus the strain-hardening magnitude is also different. In addition, the grain size and the phase content and distribution are also heterogeneous over the weld, resulting in different yield stress which has significant effects on the final welding residual stress especially in the weld zone **(Deng et al. 2008)**. Other structural parameters can affect the residual stresses, such as the weld groove shape, weld joint type, thickness and geometry type **(Akbari et al. 2012)**.

Residual stresses in DMWs are also mainly due to the difference in the coefficient of thermal expansion of the materials. If these are very different, internal stresses will appear in the intermetallic zone during any temperature change across the different regions of the weldment **(Srinivasan et al. 2006)**. This is of particular importance during temperature fluctuations **(Kotecki et al. 1997)** that will cause thermal fatigue cracking to happen, especially if brittle phases have appeared in the transition zones. The difference in melting temperatures in DMWs is also to be considered, since one metal will be molten before the other when subjected to the same heat source. When metals of different melting temperatures and thermal expansion coefficients are welded, the welding process with a high heat input that will make the weld quickly has an advantage.

Several parameters may affect the magnitude and distribution of the residual stresses. Especially, the welding process parameters, material properties and structural factors have significant influences on welding residual stress magnitude and distribution. **(Akbari et al. 2012)**

2.3.2. Metallurgical changes at interfaces

2.3.2.1. Carbon migration

Carbon migration from the higher carbon containing alloy to the lower alloy steels, especially those which are highly alloyed, is one of the main issue of DMWs **(Srinivasan et al. 2006)**. It leads to carbon depleted layers where creep is promoted, and it is the main contributor to all other metallurgical changes such as carbide precipitation and formation of martensite.

2.3.2.2. Precipitation of carbides

Undesirable precipitation at elevated temperatures can occur in DMWs. It is a particular issue during post-weld heat treatments (PWHTs) **(Srinivasan et al. 2006)**. Carbides act as stress concentrators or brittle elements, and their formation at high temperature contributes to the thermal stresses **(Klueh et al. 1982)**. It often occurs at grain boundaries **(Albert et al. 1997)**. In addition, carbides are responsible of sensitization as their formation causes the diffusion and depletion of elements needed for corrosion resistance. The formation of chromium carbides on grain boundaries and the related depletion of chromium in the adjacent zones of the grains reduce the corrosion resistance. In austenitic stainless steels subjected to temperatures between 500–800°C, for times between few seconds to many hours, depending on the carbon content, it gives rise to a reduction in passivity and a susceptibility to IGSCC (**IAEA, 2011).**

2.3.2.3. Type II boundary

They are grain boundaries close to the fusion line. Unlike Type I boundaries which result from the competitive growth and are perpendicular to the fusion line, these Type II boundaries are parallel to the fusion line, typically less than 100 µm away in the weld metal. Studies have shown that they are due to the differences in crystal structure between the materials. Cracking in DMWs typically occurs near the fusion boundary either along the martensitic transition zone immediately adjacent to the fusion boundary or along the Type II boundary in the weld metal **(Lippold et al. 1999)**. The narrow zones between the fusion line and the Type II boundaries are of particular concern when considering the constituents involved in failures.

2.3.2.4. Formation of soft and hard zone at the weld interface

The effect of hardness changes on mechanical properties of the DMWs is a major concern, especially when welding two metals of different carbon content **(Lundin et al. 1990; Zumelzu et al. 1996; Ryder et al. 1990)**. The formation of hard and soft zone is the result of all other parameters of DMWs: the differences in chemical composition, the morphology and distribution of hard micro-constituents in the narrow zone between the fusion boundary and the Type II boundaries, due to the carbon migration from the higher carbon content alloy. The development of a brittle martensitic layer close to the fusion boundary has been the subject of numerous studies, as well as the formation of chromium/molybdenum carbides in the region close to the Type II boundary leading to higher hardness. **(Srinivasan et al. 2006)**

2.3.3. Creep

The high operating temperatures in conventional and nuclear power plants are sufficient to activate creep deformation. The rate of accumulation of damage may be significantly higher in the weld metal than in other parts **(Becker et al. 2001)** and failure experiences indicate that in the majority of cases where creep cracking occurs, defects predominate in the welds. Studies show the significant influence of material mismatch **(Segle et al. 1998; Tu et al. 1999)**. Creep crack growth (CCG) has been studied in DMWs, where zones exhibit different material properties, leading to dissimilar creep behaviors and thus to a complex creep behavior of the complete weld **(Segle et al. 2004)**. The problems are usually associated to the HAZ, where the creep behavior varies markedly due to the local variations in temperature and cooling rates during welding. DMW can be considered to be made of several narrow regions, which have different creep strengths. This leads to a complex stress redistribution which has a great influence on the accumulation of creep damage and, thus, on the failure of the weldment.

Of particular concern is Type IV creep cracking, which occurs at the interface between the HAZ and the base material in ferritic steel welds **(Perrin et al. 1999)**. The cracking is attributed to the formation and growth of creep voids with arrays of carbide precipitates in the ferritic steel close to the weld interface. The resulting cracking can be relatively rapid. The crack can be regarded as 'unzipping' of an already creep-damaged zone **(Sireesha et al. 2000)**.

2.3.4. Variations of electrochemical properties

Joining two metals of different electrochemical properties is an issue as the difference of the metals on the electrochemical series is an indication of their susceptibility to corrosion at the intermetallic zone. Corrosion can become serious if the difference is large. Studies show that electrochemical property variations in the weld can increase the environmentally assisted corrosion **(Srinivasan et al. 2006)**. In addition, the intergranular precipitation of carbides can create a chromium depleted zone near the grain boundaries, which reduces the local resistance to intergranular corrosion and increases the susceptibility to IGSCC **(Sahlaoui et al. 2002)**.

2.3.5. Aging mechanisms

The combination in a high-temperature environment of residual stress, metallurgical changes, creep behavior and corrosion susceptibility result in ageing mechanisms, the specific processes that gradually change characteristics of a component with time and use. They mainly consist of **(IAEA, 2005):**

- Embrittlement
- Fatigue
- Stress corrosion cracking
- General corrosion
- Erosion/corrosion
- Mechanical wear

Stress corrosion cracking (SCC) is one of the most important ageing mechanisms in BWRs and PWRs **(Kaneshima et al. 2005)**. It intervenes notably in the failure of reactor pressure vessels after long-term services **(Horn et al. 2002)**. SCC has caused many NPPs to replace piping or SGs. SCC and corrosion fatigue of DMWs have become the major concern in the nuclear industry, and many studies have been done on the SCC of DMWs **(Vaillant et al. 2007)**.

SCC occurs in virtually any alloy when it is simultaneously subject to a tensile stress and a corrosive environment. The important factors affecting SCC are temperature, environment, material composition, microstructure, residual stresses and applied stresses, making SCC of particular concern when considering DMWs. Crack propagation can be either transgranular or intergranular. Intergranular stress corrosion cracking (IGSCC) can occur even though the alloy is insensitive to intergranular corrosion. Residual tensile stresses can accelerate the corrosion cracking, especially along sensitized grain boundaries **(Brooks et al. 1993)**. Studies show that the weld interface and transition regions play a key role in SCC susceptibility, especially due to the formation of hard layers **(Seifert et al. 2008; Roberts et al. 1985)**. Transgranular (TGSCC) and irradiation-assisted (IASCC) are also forms of environmentally assisted cracking (EAC), and the mechanisms have been studied extensively.

For austenitic alloys such as stainless steels or nickel-base alloys, the SCC mechanism in high-temperature water is based mainly on the slip-dissolution/film-rupture model **(Rebak et al. 1996)**. The repeated formation and destruction of oxide layers are thought to cause deteriorated SCC resistance of the material.

3. Developments in DMWs

Austenitic alloys have good mechanical properties and corrosion resistance. Thus, stainless steels 304 and 316 have been chosen for pipe material in nuclear power plants. However, thermal sensitization may occur in the HAZ of austenitic alloys during both welding and post-weld heat treatments. SCC failures due to sensitized stainless steels have been reported in BWRs since the 1960s. **(Lee et al. 2009)**

Besides the control of water chemistry, fabrication methods and the use of corrosion resistant cladding, the solutions have been the design of new annealing heat treatments and the development of substitute materials: the thermally sensitized materials were first replaced by low-carbon grades and stabilized grades.

3.1. Heat treatments

Heat treatment is the controlled heating and cooling of metals to modify their physical and mechanical properties without changing the product shape**.** It can be done on purpose or be the result of manufacturing processes such as welding. It has two main aims: i) softening, to reduce the strength or hardness, remove residual stresses**,** improve toughness and restore ductility, ii) hardening, to increase the strength and wear properties**.** The most common softening heat treatments are annealing and tempering.

3.1.1. Annealing

It is a softening heat treatment done by heating to above a critical temperature (austenitization temperature for steels), maintaining in temperature and cooling. It is made of three stages: recovery, recrystallization and grain growth. Recovery will soften the metal through rearranging and removal of dislocations. In recrystallization, new grains nucleate and grow in the high-strain zones. If annealing continues after recrystallization is completed, then grain growth can occur and the microstructure coarsens. Different types of annealing processes can be found:

- Full annealing: the material is cooled slowly in a temperature-controlled furnace so that the equilibrium microstructure is obtained.
- Normalizing: the material is cooled at room temperature under natural convection. This process is considerably cheaper than full annealing. However, depending on the part geometry, the cooling is non-uniform resulting in non-uniform material properties across the part.
- Process annealing: it is used to treat work-hardened parts. It restores some of the ductility, allowing the parts to undergo further cold working without fracturing. The material stays in the same phase throughout the process.

3.1.2. Tempering

It is used to increase the toughness of iron-based alloys. It removes the brittleness caused by a predominance of martensite. After cooling, the steel is reheated to a temperature of 150 to 400 ºC. Gradual heating is important to avoid cracking. After reaching the desired temperature, the parts are held at that temperature for about 2 hours, and then cooled in still air. For steels that have been welded, the HAZ can be as hard as quenched steels. Moreover, uneven heating and cooling can create internal stresses. Tempering is sometimes used in place of stress relieving to reduce the internal stresses and to decrease the brittleness around the weld.

3.1.3. Stress relieving

It is done to minimize the manufacturing-induced stress by subjecting the parts to a temperature of about 650 ºC for an extended time (about 1 h or more), until the whole part reaches the temperature, and then cooling it in still air. Alloy steels are stress relieved at higher temperatures. The parts that usually benefit from stress relieving heat treatments are large and complex weldments, castings with a lot of machining and parts with small dimensional tolerances.

For nickel-base alloys, heat treatments are generally i) annealing at temperatures between 700 and 1200°C depending on the composition, ii) stress relieving at temperatures between 430 and 870°C, iii) stress equalizing, iv) solution treating and v) age hardening. (**Rajan et al. 2004)**

Two main heat treatments were developed for Inconel X-750. The first is called equalized and aged (EQA): the material has a two-step thermal treatment: the first at 885°C for about 24 h followed by ageing at 704°C for 20 h. The second heat treatment is high temperature annealing (HTA). It involves a single step ageing at 704°C for about 20 h after solution annealing at 1093°C for one to two hours. The main goal of HTA treatment is to precipitate the strengthening gamma prime phase, Ni_3Al, together with a fine, dense $M_{23}C_6$ carbide distribution at grain boundaries. HTA is more resistant to IGSCC **(IAEA, 2011)**.

In the late 1970s, Alloy 600 tubes were subjected to a high-temperature treatment to improve the resistance to corrosion. Improved manufacturing processes and PWHT have been developed (e.g., solution annealing: 1050°C for 30 min). They will keep the levels of residual tensile stresses below critical levels and dissolve any $Cr_{23}C_6$ that may be present, returning the chromium to the matrix level of the alloy composition, thereby restoring its corrosion resistance. **(Tipping, 2011)**

To be considered is the ability to produce a favorable microstructure. There must be sufficient carbon in solid solution to precipitate as carbides. A high annealing temperature favors the precipitation of intergranular carbides and produces the desired microstructure. Low annealing temperature results in an insufficient supply of carbon for intergranular precipitation. In addition, subsequent thermal treatments may not significantly modify the microstructure and SCC resistance in this case. For Alloy 690, the usual heat treatment consists of two steps: solution annealing for carbide dissolution and thermal treatment for carbide precipitation **(Hong et al. 2005)**. It is however not always sufficient to remove totally the effects of cold work and the residual stresses.

The difficulty in DMWs is that the different alloys can react differently to a heat treatment. PWHT of 500-700°C are often used for ferritic steels. But it may cause sensitization of an austenitic steel or weld metal (especially for unstabilized alloy with high carbon content). Also, embrittlement due to sigma phase formation is possible, especially for weld metals with high ferrite contents. A possible solution is the use of a suitable austenitic buttering layer. It enables to heat-treat the ferritic part before the actual welding. **(Karlsson, 1995)**

3.2. New materials

After the grades 304 and 316, the new alloys have lower carbon content such as 304L stainless steel, 316L stainless steel and nickel-base alloy 600. The bulk carbon content is limited to $C \leq 0.03\%$. They have replaced 304 and 316 stainless steel as second generation nuclear piping materials. The low carbon content results in less chromium carbide precipitation at grain boundary during heating and reduces the chromium depletion. The thermal and mechanical response of alloy 600 and 304L are similar, but alloy 600 has a better SCC resistance in chloride solutions **(Page et al. 1983)**. Stabilized alloys like 347 and 321 stainless steels are also used, where carbon is bound by a strong carbide former such as niobium or titanium. Alloys 600 and 182 have also been modified with niobium additions. Combining both low carbon content and high stabilization is appropriate **(IAEA, 2011)**. As for weld metals, austenitic stainless steel welding consumables were used at the beginning, but studies showed that considerable improvement can be achieved by using nickel-base filler materials such as Inconel 82 and 182. They have a CTE between those of the ferritic and austenitic base metals. In addition, the low carbon activity gradient between ferritic steel and nickel-base alloy weld metal, and the low diffusivity of carbon in the nickel-based alloy, result in reduced carbon diffusion. **(Sireesha et al. 2000)**

However, despite the use of low carbon and stabilized materials, IGSCC still has occurred in BWRs. Studies have shown that it is due to cold work induced during fabrication, resulting in high hardness levels, residual stresses and deformation-induced phase transformation such as martensite. X-750 is a precipitation-hardened alloy with similar nickel and chromium contents as solid-solution strengthened alloy 600, and it has been used for high strength applications **(IAEA, 2011)**.

Moreover, inspections since the 80s have revealed the presence of cracks and leaks due to intergranular corrosion in alloy 600 tubes of PWRs and also later in BWRs due to intergranular stress corrosion cracking (IGSCC). More generally, nickel-base alloys such as alloys 600, 132 and 182, have shown susceptibility to intergranular stress corrosion cracking in normal PWR primary water systems. Mostly, cracks initiated in the HAZ of Inconel 182 and 82 welded to base metal Inconel 600. This is due to the presence of corrosion environment, residual stress, and material sensitization effects **(Hickling et al. 2004; Danko, 1992)**. Thus, a major concern rose regarding the suitability of Alloy 600 and Alloy 82/182. Investigations have shown that Alloys 600, 182 and 82 are particularly susceptible to SCC and IGSCC in the HAZ **(King et al. 2003; Bamford et al. 2005)**. These alloys were designed to reduce sensitization issues, but SCC and IGSCC of alloys 600, 82 and 182 are still related to sensitization. This is especially true when using welding processes with high heat input such as SMAW and GTAW. Chromium carbides such as $Cr_{23}C_6$ and Cr_7C_3 can precipitate at the GBs in the HAZ during cooling. It leads to chromium depletion near the GBs **(Scott, 2007)**. The PWSCC susceptibility of alloy 600 is related to the carbide morphology, and also cold work. Due to the low carbon solubility in nickel-base alloys, carbon in solid solution combines with chromium in alloy 600 to form chromium carbides during cooling. It seems that carbides on the grain boundary increase the resistance to PWSCC, whereas intragranular carbides increase the susceptibility. The mechanisms proposed are either the blunting of cracks by boundary carbides acting as dislocation sources at the crack tip, or reducing the corrosion by acting as oxygen sinks and hinders for diffusion. The role of carbon is, however, not so clear for alloy 182 and 82 weld metals. It is known that the precipitate is mainly niobium carbide **(IAEA, 2011)**. **(Lee et al. 2009)**

Alloy 690 is a replacement for alloy 600. It is characterized by significantly higher chromium content (approximately 30 wt% compared to 16 wt% for Inconel 600). It is more SCC resistant, as the high chromium content reduces sensitization due to chromium depletion during carbide precipitation at GBs **(Yu et al. 1990)**. The high chromium content also increases resistance to corrosion due to chemical solutions, whereas the high nickel content (approximately 60 wt%) increases resistance to sodium hydroxide and chloride SCC. In addition, Alloy 690 is more resistant than Inconel 600 concerning IGSCC and surface corrosion **(Crum et al. 1982)**. Alloy 690 is especially resistant to IGSCC. Many filler metals like Inconel 82 and 182 are still compatible with alloy 690. However, the high SCC and IGSCC susceptibility has led to a research for other materials. Thus, filler metals with higher chromium content, Inconel 52 and 152, have been developed. They exhibit both high IGSCC and surface corrosion resistance **(Page et al. 1988)**. No cracking has been reported to date in these materials **(IAEA, 2011)**. Also, many studies have confirmed the high PWSCC resistance of alloys 690, 52 and 152 at temperatures up to 360°C. Other alloys still in use are alloys X-750 and 718 for high-strength applications in PWRs, and gamma-prime strengthened stainless steel alloy 286 **(IAEA, 2011)**.

However, alloy 690 weldments can still crack severely. This is mostly due to weld designs. A cause of cracks is the rapid cooling from high temperature. It leads to segregation of elements and heterogeneous distribution of thermal stresses **(Kerr et al. 1987)**. In addition to their intrinsic properties, studies have also investigated the matching of Inconel 52, 152, 82 and 182 with Alloy 690 welding. They showed that Inconel 82 has a greater hot cracking susceptibility than Inconel 52 and that most cracks follow GBs resulting in intergranular fractures. Also, Inconel 82 has a lower melting point and a wider solidification range, resulting in higher solidification cracking susceptibility **(Wu et al. 1999)**. Despite the fact that they are used commercially for the welding of alloy 690, there are few papers available in the literature regarding the characteristics of these weld metals. **(Kuo et al. 2002)**

After the discovery in the 90s of the ductility dip cracking (DDC) phenomenon, new alloy Inconel 52M was developed with increased amount of boron and zirconium at the GBs. However, due to the new composition, its susceptibility to hot cracking was increased. Thus, Inconel 52MSS was developed with increased resistance to both hot cracking and DDC.

Also to be noted is the research concerning the entirely new alloy EPRI P87. It has a CTE as good as the existing Ni-base fillers, even closer to that of ferritic steels. It also has a carbon content matching that of the ferritic steels P91 and 92, thus, eliminating the main driving force of carbon diffusion. Thus, this alloy is specially developed to address the two main issues leading to premature failure in DMWs: mismatch of CTE and carbon migration. **(Siefert et al. 2011)**

To conclude, the repair and replacement of damaged components in NPPs are now done with Alloy 690 as base metal and Inconel 52 and 152 as weld metals **(Frederick et al. 2006)**. They show all good SCC and IGSCC resistance. However, the susceptibility of welds to SCC, IGSCC and PWSCCs depends not only on the nature of base and weld metals, but also on the microstructural changes which take place during the welding process. Such changes are mostly related to the heating and cooling rates. Thus, they depend on the choice of welding technique. **(Ahluwalia et al. 2007)**

3.3. Narrow-gap welding

Among the available welding procedure, narrow-gap welding (NGW) is a new choice for welding thick-section component in NPPs. It is used in the primary cooling system in PWR modern designs. It relates to an automatic or semi-automatic process for welding thick plate materials separated by very narrow groove (see Fig.

20). It is known since the 60s. Narrow-gap welding is an important technique for increasing productivity in the manufacture of thick-walled components.

Manual Weld
Material: Austenit
Thickness: 12 mm

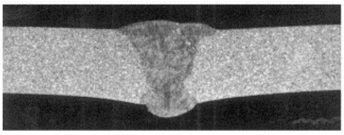

Conventional Narrow-Gap Weld
Material: Austenit
Thickness: 12 mm

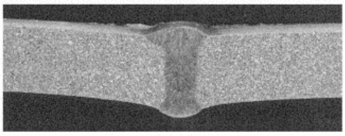

Optimized Narrow-Gap Weld
Material: Austenit
Thickness: 12 mm

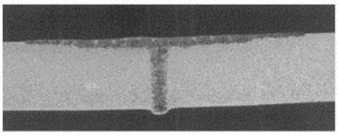

Fig. 20 Geometrical comparison between NGW and conventional welding. Optimized NGW reduces greatly the amount of weld metal. ***(Engelhard et al. 2000)***

Thick plate structures are conventionally welded with a V, or double V, edge preparation. The included angles are from 30 to 60 degree. The use of a double V for thick sections allows welding to be performed on both sides of the work piece at once. The pieces are welded together by starting at the root and gradually building up layer upon layer.

The cross-sectional area of the gap is quite large, and so is the amount of filler metal. The thicker the plate, the larger the gap, the amount of filler and the welding time. The major drawback of this technique is the amount of time required to complete the weld. As the thickness of the section increases, the volume of metal that must be deposited increases with the square of the depth **(Biswas et al. 2010)**.

In addition, distortions in the weld are related to the volume of weld metal. It is very important for large welded structures to quantitatively predict welding distortion during the assembly process. Generally, the major cause of geometrical error in the welded structure is local shrinkage due to rapid heating and cooling in the weld zone.

It results into: longitudinal shrinkage, transverse shrinkage and angular distortion. These three kinds of local deformations are strongly influenced by heat input, plate thickness and joint type **(Biswaset et al. 2010)**. The amount of shrinkage occurring in the weld determines the distortion. Also, residual stresses increase as the amount of weld metal increases. A large volume of weld metal increases therefore both distortions and the residual stresses, thus the cracking susceptibility. **(Nelson et al. 1967)**

NGW uses joint preparations with small groove angles. It is more economical thanks to reduced consumable requirements, shorter welding times and reduced inspection volume requirements (see Fig. 21).

As NGW can be automated, it enables to produce constant quality and reproducibility of mechanical properties. Since the subjectivity of bead placement that occurs in manual welding is eliminated, the weld results are more consistent with improved weld quality. In some cases there may also be a reduction in weld prep machining costs **(Henon, 2010)**. In addition, the reduced amount of weld metal leads to less shrinkage, less distortion and less residual stresses. One important consideration is also the use of low heat input, which is a natural characteristic of the NGW.

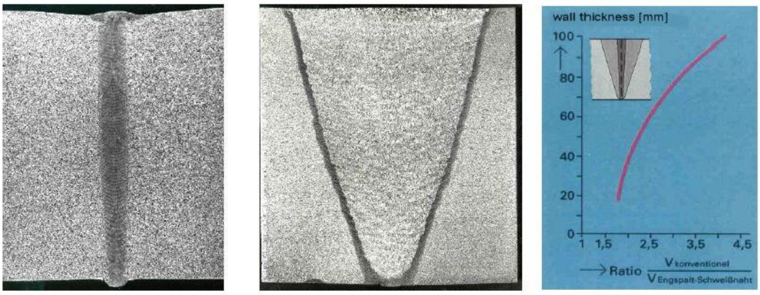

Narrow Gap Welding
material: stainless steel
thickness: 90mm

Conventional Weld
material: carbon steel
thickness: 90mm

Reduction of weld volume using GTA Narrow Gap Welding

Fig. 21 Reduction of the weld volume using GTA-NGW as compared to a conventional weld. The reduction is of about four times. ***(Aalto University, 2012)***

However, the mechanical properties of the welds produced by NGW have not yet been fully characterized. Variations in weld microstructure could cause non-uniform mechanical properties through the thickness direction.

As a result, the fatigue crack growth rate can show a strong spatial dependence both at room and at high temperature in the fusion zone. It depends on both dendrite alignment and residual stress distribution in the weld. The fatigue crack growth rates are greatest at the boundary between the inner weld deposit and the outer weld deposit where the dendrites are well aligned and high tensile residual stress exists. **(Jang et al. 2010)**

Another drawback is associated with the higher tendency of NGW to form weld defects and to the greater difficulty in repairing these defects in a narrow joint. Arc oscillation can reduce the susceptibility to defect formation and improve productivity in mechanized GTAW. Usually, a mechanical device is used to swing the arc. Alternatively, arc oscillation can be achieved by means of a variable magnetic field from an electromagnet attached to a relatively small torch.

NGW techniques are commonly associated with high deposition rate GMAW and SAW. However, NG-GTAW can be used in special applications, such as (i) critical structures, where the quality and the performance of the welded joint are key factors and (ii) materials that are traditionally welded with GTAW (SS and nickel-base alloys).

An important parameter for NGW is to have a good lateral melting whilst keeping low heat input. The key parameters to insure sidewall fusion are oscillation of the tungsten electrode to the side wall, wire position, rate of wire feed and hot wire current **(Henon, 2010)**. Base metal fusion, both lateral and axial, increases with heat input. For a constant level of heat input, lateral fusion increases with current. An increase in gap width makes it easier for the arc to reach the bottom of the joint. But it reduces heat transfer to the lateral walls of the joint. Therefore, axial fusion increases, but lateral fusion decreases with gap width. The wire feed speed does not affect lateral fusion though it decreases axial fusion. Arc oscillation increases the height reached by the arc in the joint wall and, therefore, affects the shape of the bead. **(Modenesi et al. 1995)**

It is not possible to have a direct view of the narrow groove during welding, thus leading and trailing cameras are needed for most applications. Torches should be designed to survive exposure to long term UV and high temperatures. **(Henon, 2010)**

As it has been seen before, DMWs are among the main failure locations in NPPs, and particularly the RPV nozzles and safe-end welds are critical. For this reason, the evolution of the weld design, and notably the recent use of NGW without buttering layer in modern PWR designs, has to be studied extensively.

4. Metallurgy of typical ferritic-austenitic DMW

4.1. Overview

Dissimilar metal welds between austenitic stainless steel and ferritic steel containing low amounts of carbon are extensively utilized in many high-temperature applications in energy conversion systems. In central power stations, the parts of the boilers that are subjected to lower temperature are made of ferritic steel for economic reasons. The other parts, operating at higher temperatures, are constructed with austenitic stainless steel. **(Celik et al. 1999)**

It has been seen that LAS and SS components are commonly welded together using Ni-base filler metals. Nickel-base filler metals are usually used for service temperature higher than 350-400°C **(Karlsson, 1995)**. It results in a DMW with two interfaces: the ferritic/austenitic interface and the austenitic/austenitic interface. A usual example of such a weld is the welding of a safe-end at the RPV nozzle. The RPV is made of LAS for mechanical and economic reasons. It is cladded with SS for corrosion resistance. The safe-end facilitates the posterior pipe welding (Figs. 22 and 23). An optical view of such a weld is given in Fig. 24.

The major issue with these welds is the difference in chemical composition between the alloys, especially for the ferritic/austenitic fusion line. The carbon content is much higher in the LAS than in the Ni-base alloys. The difference in carbon activity leads to carbon diffusion and metallurgical changes. This is particularly true when the weld is subjected to a PWHT. The main issue is to avoid cracking in the HAZ and UMZ or PMZ, where complex microstructures can develop **(Karlsson, 1995)**.

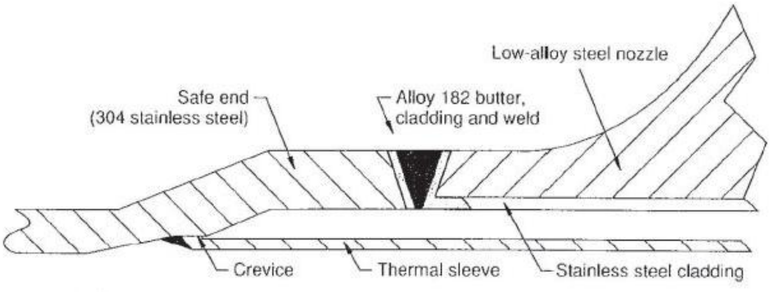

(a) Old configuration

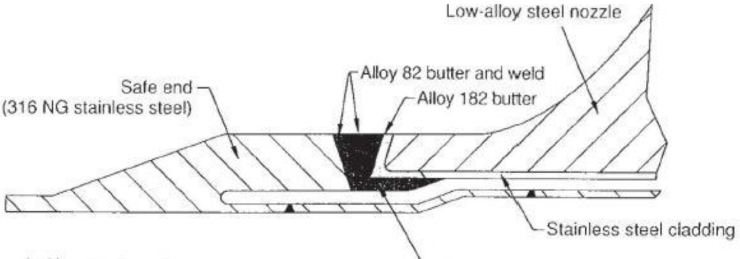

(b) New configuration

Fig.22 Cross-section of a RPV nozzle and safe-end in a BWR ***(Shah et al. 1993)***

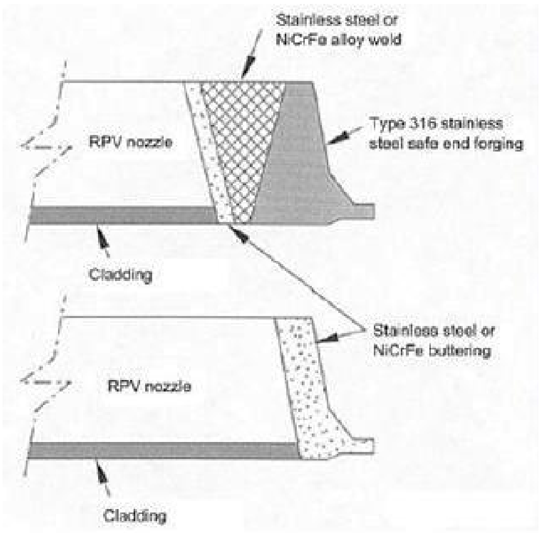

Fig. 23 Closer view of the weld between the RPV nozzle and the safe-end. It presents the LAS of the RPV and its SS cladding, the Ni-base buttering, the Ni-base weld metal (Ni-Fe-Cr alloys) and the austenitic SS of the safe-end. ***(Shah et al. 1993)***

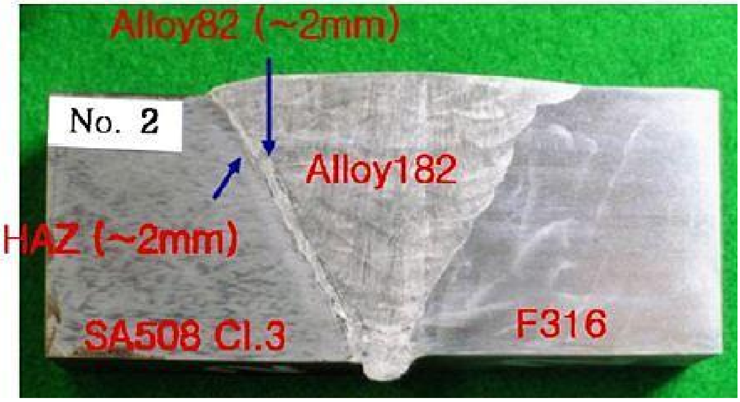

Fig. 24 Mock-up weld representing a usual weld between the ferritic LAS (SA508-3) of a RPV nozzle and the austenitic SS (SS316) of its safe-end, using Ni-base alloys as buttering and weld metals (respectively, Inconel 82 and 182). ***(Jang et al. 2008)***

4.2. Ferritic/austenitic interface

4.2.1. Ferritic HAZ

4.2.1.1. Microstructure

Figure 25 a) shows an optical view of the SA 508 Cl.3 base material. It consists mainly of upper bainite. However, when moving from the base material to the fusion line, the microstructures in the HAZ change significantly. Figure 25 b) shows grain refining and formation of small amount of martensite. Figure 25 c) shows the microstructure of the HAZ closer to the FL, with large prior austenite grains and higher amounts of martensite.

The microstructure in the HAZ is affected by the chemical composition, the welding condition and the temperature of the PWHT **(Seifert et al. 2005)**. The HAZ varies according to the distance from the fusion zone, as the experienced temperatures decrease. It is composed of a coarse-grain region above 1100°C, a grain refined region between 900-1100°C, a partially grain refined region between 700-900°C and finally a tempered or base material region below 700°C. The most sensitive region is the coarse grain zone close to the fusion line. **(Hong et al. 2000)**

With temperatures up to 1350°C, the microstructure consists mainly of martensite. Up to 900°C, bainite will form together with martensite because of slow cooling from lower austenite region. Thus, the martensite fraction decreases, and bainite or martensite islands are formed. For 750 and 600°C, the microstructures are not changed much and there is a minor tempering effect. **(Hong et al. 2000)**

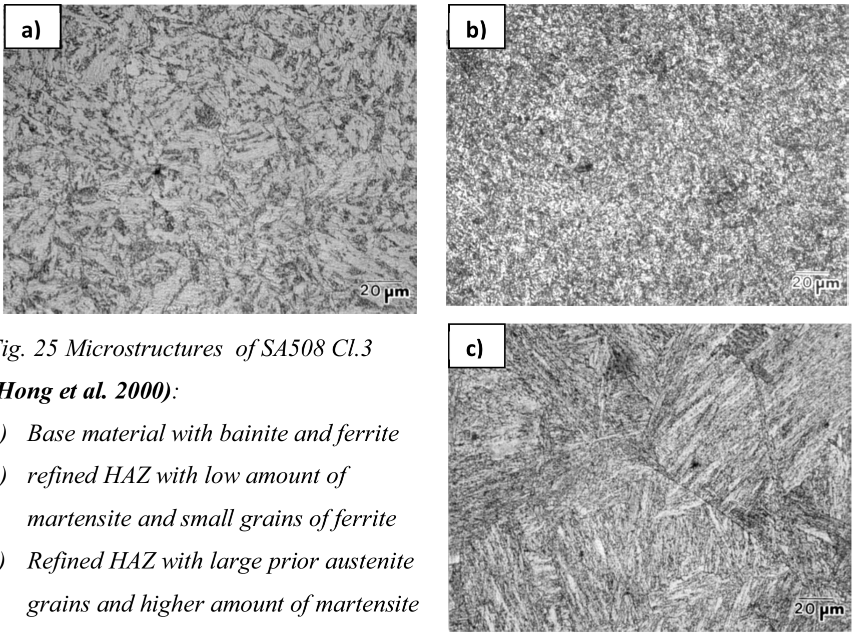

*Fig. 25 Microstructures of SA508 Cl.3 **(Hong et al. 2000)**:*

a) Base material with bainite and ferrite
b) refined HAZ with low amount of martensite and small grains of ferrite
c) Refined HAZ with large prior austenite grains and higher amount of martensite

The same changes in the microstructures (progressive grain refining then grain coarsening) are observed for SA508 Cl.1 in Figure 26 a). Figure 26 b) reveals a carbon-depletion zone along the fusion line after PWHT **(Kim et al. 2009)**. PWHT promotes the formation of a carbon-depleted zone (CDZ) and a fully austenitic zone (FAZ) at the opposite sides immediately adjacent to the fusion boundary. The CDZ manifests the loss of carbon as it diffuses from the HAZ towards the fusion boundary, leading to a columnar ferrite microstructure. **(Laukkanen et al. 2007)**

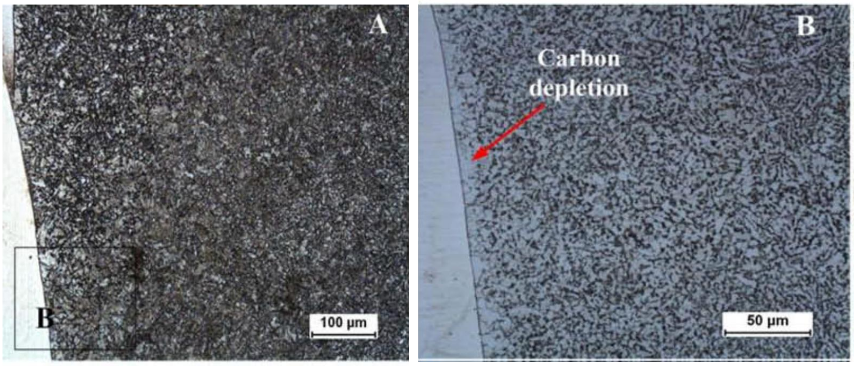

Fig. 26 HAZ microstructure of SA508 Cl.1 for an Inconel 182/SA508 Cl.1 interface: a) Global view showing grain refining then grain coarsening when moving to the fusion line. b) Grain coarsening area and carbon-depleted layer along the fusion line. ***(Kim et al. 2009)***

4.2.1.2. Issues

As seen before, the key point is to keep sufficient strength and toughness around the weld to ensure the integrity of the RPV. Hardness and strength increase together with the amount of martensite, but fracture toughness decreases. The micro-hardness near the fusion line is higher than that in the bulk metal. The peak hardness in the HAZ of LAS is generally less than 300 HV. It is a result of the microstructure change in the HAZ in LAS. With PWHT, the martensite is tempered. Thus, it is more the carbide fraction that becomes the key factor to fracture toughness after PWHT. **(Hong et al. 2000)**

A complex microstructure with varying chemical composition can evolve in the transition region between Alloy 182 weld metal and LAS due to mixing and diffusion of alloying elements and carbon migration. The SCC in the transition region plays an important role in the overall SCC behavior of a DMW. Notably, the reduced chromium and nickel content in the transition region due to dilution effects tend to increase its corrosion and SCC susceptibility with respect to the bulk weld metal. However, studies indicate that a SCC crack propagating in the dilution zone of

Alloy 182 tends to cease its propagation at the fusion line. It is usual that SCC stops in the LAS-HAZ or at latest in the LAS base metal. **(Seifert et al. 2005)**

The mechanically weak point is often the microstructures formed in the UMZ or PMZ. It is due to the composition gradient in these zones. The coarse-grained heat affected zone (CGHAZ) is a critical region for the performance of the weld. Degradation of toughness is attributed to the formation of this coarse upper-bainitic CGHAZ microstructure, as well as a narrow martensitic layer as a result of carbon diffusion from the LAS to the austenitic weld **(Laukkanen et al. 2007)**. Most problems are related to the formation of the carbon-depleted area in HAZ of the carbon steel and to the corresponding carbon-enriched band in the weld transition zone. The carbon depletion in the HAZ leads to loss of creep strength in DMWs at elevated temperatures. The carbon accumulation in the weld transition zone results in formation of extremely hard and brittle microstructures that are susceptible to hydrogen-assisted cracking. It explains why a majority of the transition joint failures, in austenitic/ferritic steel joints occur in the HAZ of the ferritic LAS, adjacent to the weld interface **(Celik et al. 1999)**.

There is a high diffusivity of chromium in the ferrite, and a low diffusivity of carbon in the austenite. Austenitic nickel-base weld metals can have a positive influence since they reduce the carbon migration. But PWHT results in carbon migration and carbide precipitation, associated with carbon depletion in the ferritic steel. Thus, high hardness can still be present in the weld metal near the fusion line, even with Ni-base fillers. This can be a problem during welding and in service. **(Karlsson, 1995)**

4.2.1.3. Influence of alloying elements

The two major factors affecting the mechanical properties of LAS are grain refinement and carbide control. Grain refinement can be obtained by pinning the GBs and controlling the austenitization temperature. Carbide control relies on the addition of alloying elements. **(Hong et al. 2001)**

Ni addition increases the martensite fraction by increasing the hardenability of steels. The size of martensite features is smaller than that of the bainite features. Thus, Ni additions to the LAS results in a refinement of the microstructure of the matrix. A refinement of the microstructure can improve significantly the impact toughness through an increase of boundaries acting as obstacle to crack propagation. Also, Ni improves the toughness of LAS as it increases the stacking fault energy. High stacking fault energy facilitates cross slip, which results in toughness improvement from increasing dislocation density. And last, higher Ni content will increases the amount of retained austenite, resulting in a complex path for crack propagation in the ferrite matrix. **(Lee et al. 2011)**

The Cr content does not affect the microstructure of the matrix, but it influences the precipitation of carbides. They are mostly Cr_7C_3 and $Cr_{23}C_6$. Their size decreases with an increase of Cr content. The precipitation of finer carbides with higher Cr content is thought to result from an increase of nucleation sites for Cr-rich carbide. Fracture toughness is controlled by the critical size of carbides that can cause cleavage fracture. An increase of Cr content improves the fracture toughness by reducing the amount of critical size carbide. **(Lee et al. 2011)**

C and Mn decrease the impact toughness because of the precipitation of coarse carbides, but they are needed to maintain strength. Mn decreases stress-relief cracking susceptibility. It explains that SA508 Cl.3 is more resistant to stress-relief cracking than SA508 Cl.2. Mo is strong carbide former that promotes fine needle-type M_2C carbides. It also contributes to solid-solution strengthening in the ferrite matrix. **(Hong et al. 2001)**

The welding properties are however affected by the alloying elements. Decrease in C and Mn contents prevents the formation of carbides. Increasing Ni prevents the reduction in hardenability. The addition of Mo protects from strength reduction and promotes fine carbides. **(Hong et al. 2001)**

4.2.2. Formation of hard and soft zones at the interface

Considering the effect of chromium on the migration of carbon, numerous studies have been made on the formation of hard and soft zones at the interface between two alloys of different chromium content. They pointed out the influence of PWHT.

PWHT of DMWs between Cr–Mo steels differing in Cr content or between a Cr–Mo steel and an austenitic stainless steel often result in the formation of a carbon-depleted soft zone in the low Cr side and carbide precipitates in the high Cr side **(Sudha et al. 2002)**. Some decarburization can also occur during welding **(DuPont et al. 2010)**. Following the same mechanism, carbon migration from the SA508 base metal (lower Cr content) to the Inconel 52 weld metal (higher Cr content) occurs during PWHT. It results in the formation of a CDZ with an entirely ferritic structure in the HAZ. A much lower diffusion of carbon in the nickel-base alloy results in the precipitation of carbides at the fusion interface. **(Chung et al. 2011)**

The role of chromium in the carbon migration across the weld interface has been studied extensively. Numerous studies have been conducted about the weld interface between two Cr-Mo steels of different carbon content. As shown in Figures 27 and 28 for a weld between a 9Cr-1Mo steel and a 2,25Cr-1Mo steel, the width of these zones and their hardness are influenced by the time of exposure at elevated temperature. A measurable increase in the width and a decrease in the hardness of the soft and hard zones with aging times are observed.

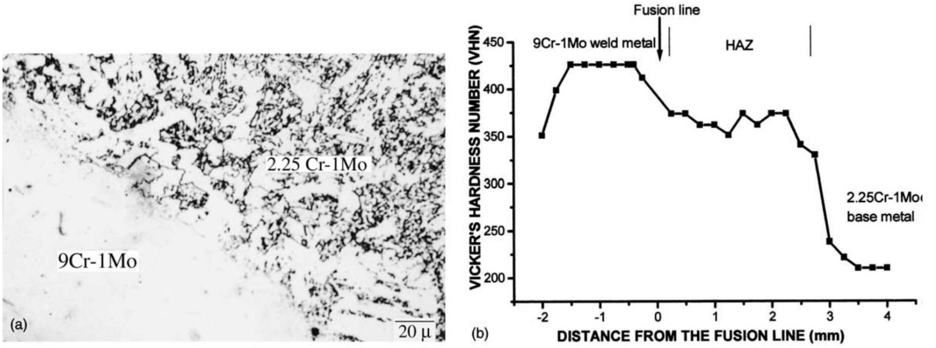

Fig. 27 As-welded interface between 9Cr-1Mo/2,25Cr-1Mo steels: a) Microstructure of the weld interface, b) Hardness profile taken across the weld interface. ***(Sudha et al. 2002)***

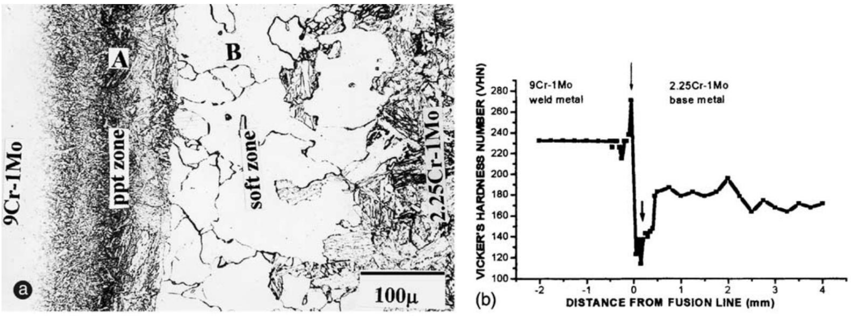

Fig. 28 Post-weld heat treated interface between 9Cr-1Mo/2,25Cr-1Mo steels: a) Microstructure of the weld interface, b) Hardness profile taken across the weld interface. ***(Sudha et al. 2002)***

For the heat treated sample, the hardness profile shows a high hardness peak in the high-chromium side (271 VHN). On the low-chromium side, a hardness drop is noted. It is associated with a lightly etched band of ferrite. Such bands are more rarely observed in as-welded samples. They correspond to a CDZ.

The microstructures near the weld interface are quite complicated. They consist of CDZ, carbides, martensite and Type II boundaries. The failure mechanism in ferritic-austenitic DMWs is mainly the nucleation and propagation of creep-fatigue cracks. It occurs around carbides close to the fusion line between the ferritic steel and the nickel-base weld metal. **(Chung et al. 2011)**

4.2.2.1. Carbon-depleted and carbon-enriched zones

A redistribution of carbon and nitrogen can be observed during welding, PWHT or in service at high temperatures. It can cause the formation of carbon-depleted zones (CDZ) in low-alloy steels, and on the contrary, the formation of carbon-enriched zones (CEZ) in high-alloy steels. It occurs at a close distance of the fusion zone. **(Foret et al. 2006)**

Carbon depletion usually results in a layer of coarse ferritic grains in the LAS HAZ, without any carbide precipitates. It can be explained in terms of the diffusion of carbon from low-chromium to high-chromium side. The difference in Cr content results in different carbon activities. It acts as the driving force for the diffusion of carbon. Carbides dissolve into the matrix, and carbon migrates to the high-Cr side of the weld. The reduced amount of remaining carbon leads from a ferrite–bainite structure to sole ferrite grains in the CDZ. **(Sudha et al. 2002)**

It is also necessary to examine the occurrence of carbides or nitro-carbides not only in the CDZ, but also in the carbon-enriched (hard) zone of high-alloy steel. Just beyond the interface, on the austenitic side of the fusion line, the C concentration is significantly enriched to the point where the solubility limit of C in austenite is exceeded. This leads to formation of carbides within this region. They are typically dark etched, and often observed after PWHT or aging in service **(DuPont et al. 2010)**. The carbon concentration is maximal at the precipitate rich-zone. For high-Cr alloys, the simultaneous enrichment of Cr and C in the hard zone suggests the formation of Cr-rich carbides. Studies of the precipitates in hard zone confirmed that they are mostly Cr-rich $M_{23}C_6$ carbides. **(Sudha et al. 2002)**

The CDZ is a preferential zone for plastic deformation to occur. Grain growth can also be observed in this soft zone due to the absence of pinning effect of carbides in the ferrite matrix **(Sudha et al. 2002)**. Thus, the effect of CDZ on mechanical properties must be considered, considering especially the creep characteristics. The appearance of the CDZ and CEZ can lead to Type IIIa creep cracking **(Foret et al. 2006)**. Such zones make the weld susceptible for cyclic stresses.

The possible methods of suppressing the occurrence and development of this structural instability are (i) the use of a diffusion barrier, e.g. a nickel-base alloy and (ii) lower PWHT temperatures and times. **(Foret et al. 2006)**

4.2.2.2. Carbon diffusion

The appearance of the above zones is due to an activity driven carbon diffusion. Carbon diffuses due to (1) difference in the concentration of C on either side of the weld interface and (2) difference in carbon activity. The activity of carbon in the low chromium side is higher than in the higher chromium side according to the following equation:

$$a_C = N_C(\exp(N_A \varepsilon_C^A + N_B \varepsilon_C^B))$$

where $\mathbf{a_C}$ is the activity of carbon, $\mathbf{N_A}$, $\mathbf{N_B}$ and $\mathbf{N_C}$ are the number of **A**, **B** (constituent atoms) and carbon atoms present in the alloy. $\boldsymbol{\varepsilon_C^A}$ and $\boldsymbol{\varepsilon_C^B}$ represent the Wagner interaction parameters in ferrite. $\boldsymbol{\varepsilon_C^{Cr}}$ is negative for chromium, hence activity of carbon on low-Cr side is greater than that of the high-Cr side. **(Sudha et al. 2002)**

The carbon behavior is controlled by the steel and weld metal composition, and by the PWHT temperature and duration. Also, the microstructure variations are dependent on the carbon content, the cooling rate, and the segregation of alloying elements **(Celik et al. 1999)**. Width and hardness of these zones vary with the time and intensity of heat exposure. The hardness of the hard and soft zones decreases when the time of heat treatment increases. The width of the hard zone remains almost constant. However, the soft zone shows a significant increase in width. Changes in both width and hardness slow down considerably for long aging times. **(Sudha et al. 2002)**

The microstructure of the weld interface depends on the temperature and on the amount of redistributed carbon. At higher temperatures, the matrices of the two alloys are completely austenitic. Thus, the differences in activities are smaller. In addition, carbon diffusion is reduced in austenite compared to ferrite. The carbon redistribution is then much lower. If, however, the matrix remains ferritic, the redistribution of carbon is considerable. With increasing temperature in the ferrite region, the amount of redistributed carbon increases. **(Foret et al. 2006)**

It has been observed that the diffusion of carbon in the soft zones is much higher than in the hard zone. Exposed to high temperatures, carbon diffuses from the low-chromium side of the weld interface due to the activity gradient. As a result, the precipitates on this side start dissolving leading to a change of structure from bainite to ferrite. The diffusion of carbon in a ferrite matrix which is almost devoid of carbides explains the higher rate of diffusion in the soft zone. On the contrary, the high amount of carbides in the hard zone explains the lower rate of carbon diffusion **(Sudha et al. 2008)**. Another explanation could be that the depletion of chromium in the weld metal due to the formation of carbides balances the local carbon activity. **(Sudha et al. 2002)**

Further, the formation of carbides in the hard zone sets in a local gradient in carbon concentration between the CEZ and bulk weld metal. It leads to diffusion of carbon in the weld metal away from the interface, increasing the thickness of the hard zone. As the diffusion of carbon continues, the carbon activity on the LAS side decreases and the growth rate of the zones slows down considerably with treatment time. The apparent D(c) values evaluated very close to the interface show that carbon diffusion in soft zone is much higher (2.85×10^{-9} m^2/s) than in the hard zone ($\sim 2.95 \times 10^{-13}$ m^2/s). This can be explained based on the fact that in the soft zone carbon diffuses in ferrite matrix, which is almost free of carbides. The formation of high number density of carbides in the diffusion path of carbon inhibits its diffusion in the high-Cr side. **(Sudha et al. 2010)**

4.2.2.3. Type II boundaries

As seen before, Type I boundaries are normal boundaries roughly perpendicular to the weld interface as a result of epitaxial growth. They are the result of the extension of HAZ grain boundaries at the fusion line. They develop in DMWs.

Type II boundaries are grain boundaries that run about parallel to the weld interface at a very short distance into the weld metal (less than 100 μm away from the fusion line) (see Fig. 29). They form mainly in DMWs where the base and weld metals have different crystal structures, e.g. ferritic (bcc) base metal and austenitic (fcc) weld metal. The development of such boundary has been attributed to the differences in the crystal structure between the materials. **(Srinivasan et al. 2006)**

Type II boundaries result from a change in the primary mode of solidification. Primary solidification in the base metal occurs as ferrite (bcc). In the weld metal, it occurs as austenite (fcc). At high temperature, some base metals will undergo an allotropic δ-ferrite to γ-austenite transformation. In that case, the fusion line becomes an austenite (fcc) boundary between the base metal (fcc) and the weld metal (also fcc) in the austenitic temperature range.

Since both sides have an austenitic lattice, the austenitic boundary can migrate easily into the weld metal. This migration is mainly the result of the composition gradients within the transition region between base and weld metals. Other factors are: temperature gradients and strain energy (resulting from the difference in lattice parameters and thermal expansion between the base and weld metal). These parameters control the migration of the austenitic boundary and, thus, the distance at which the Type II boundaries will be from the fusion line **(Lippold et al. 2000)**. Both types of boundaries are austenitic grain boundaries. They form in the weld metal. But they present differences in composition. The composition of Type I boundaries depends on the distance from the weld interface. The composition of Type II boundaries remains more or less the same. They have generally lower Ni and Cr contents due to dilution effect from the base metal to the weld metal.

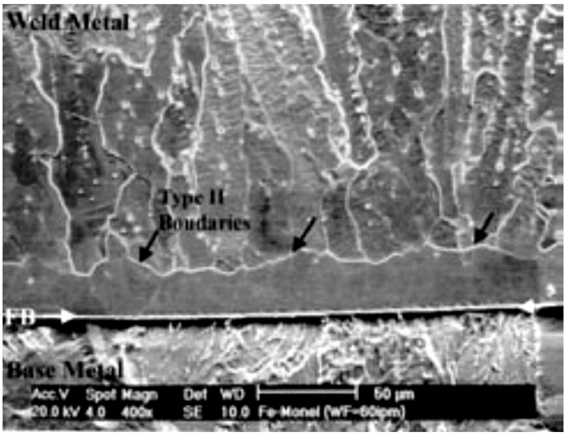

Fig. 29 Micrograph showing Type II boundaries adjacent to the weld interface of an Alloy 52/SA508 weld. ***(Lippold et al. 2000)***

The alloying elements in the transition zone vary with the distance from the weld interface. As the Ni and Cr contents lower, the susceptibility to SCC increases. The presence of Type II boundaries can cause IGC and significantly reduce the SCC resistance of the weld. Additionally, the structural discontinuity at the interface increases the SCC susceptibility of the weld interface specimen. **(Chung et al. 2011)**

4.2.2.4. Martensitic layer

The presence of martensite/austenite mixtures at the weld interface is often observed due to the non-uniform distribution of alloying elements within the transition zone **(Chung et al. 2011)**. Typically, a narrow martensitic layer approximately 10 to 20 µm wide develops along the weld interface.

It is the result of the wide difference in composition between base and weld metals. It can be predicted by a Schaeffler Constitution Diagram with the chromium and nickel equivalent for ferritic and austenitic materials. The transition composition is often situated in the martensitic range. This transition takes place generally over a short distance, resulting in a narrow martensitic band along the fusion line. Cracking usually occurs in this region, which also contains the Type II boundaries.

Martensite appears mostly in high dilution regions. Locally increased dilution near the fusion boundary is the result of a stagnant layer in the weld pool at the contact of the solid base metal. The martensitic region can form in the same way as the usual unmixed zones, but it does not have the same composition as the base metal. **(Lippold et al. 1999)**

In the transition zone, the variation in composition leads to a change in the martensite start temperatures M_s (see Fig. 30). It affects the width of the martensitic layer. The M_s temperature can be calculated according to the following formula in mass% **(Chung et al. 2011)**:

$$M_s(°\mathrm{C}) = 540 - (497 \cdot \mathrm{wt\%C} + 6{,}3 \cdot \mathrm{wt\%Mn} + 36{,}3 \cdot \mathrm{wt\%Ni} + 10{,}8 \cdot \mathrm{wt\%Cr} + 46{,}6 \cdot \mathrm{wt\%Mo})$$

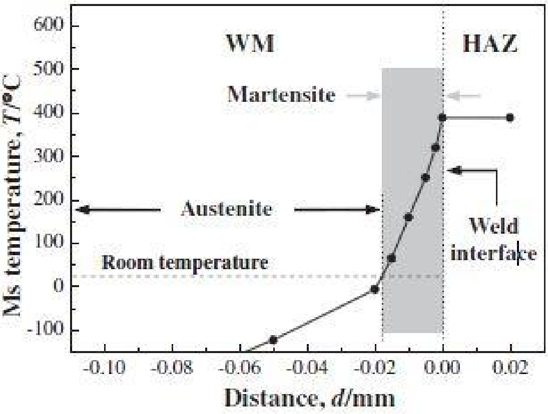

Fig. 30 Calculated M_s temperature profile across the weld interface of Inconel 52/SA508 weld. ***(Chung et al. 2011)***

Figure 31 shows a hardness peak in the ferritic steel side of the fusion line. This is due to the martensitic structure. With PWHT, the martensite is tempered and the hardness is much lower. **(Sireesha et al. 2005)**

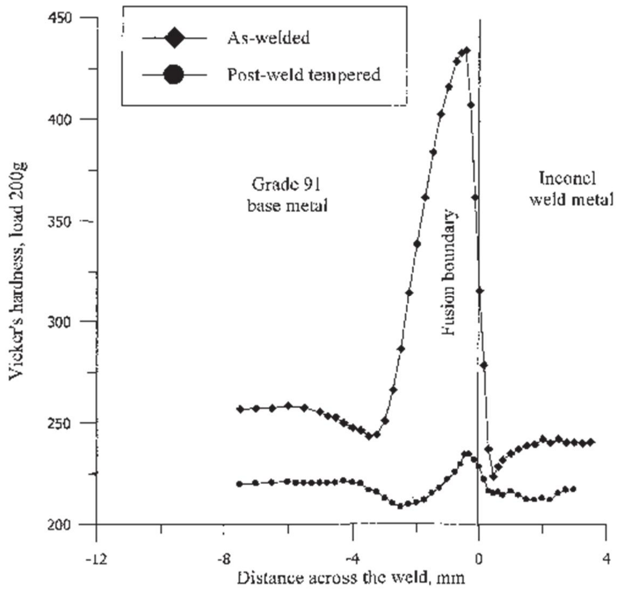

Fig. 31 Hardness peak due to a martensitic layer close to the LAS/Inconel 182 interface, and influence of PWHT. ***(Sireesha et al. 2005)***

The formation of martensite leads to high hardness and loss of ductility. The HAZ hardness can be decreased considerably after PWHT. However, a highly localized hardness peak can evolve just inside the interface on the weld metal side of the weld. As seen before, the localized increase in hardness is due to the nucleation and growth of carbides after carbon diffusion. **(DuPont et al. 2010)**

4.2.3. Effect of diffusion barriers

The main parameter to control the formation of hard and soft zones at the interface is carbon diffusion. Since the activity of carbon is mainly dependent upon the chromium concentration, the major alloying element considered is Cr.

Several methods are possible to prevent the formation of hard and soft zones:

- Joining alloys with graded Cr composition.
- Adding elements with high carbon affinity (as Nb or Ti) in the LAS side.
- Using buttering as diffusion barrier to carbon.

The use of buttering layers is based on the interaction between carbon and the main constituent element of the buttering alloy. Copper and nickel, for example, have a positive interaction parameter with carbon. It results in a repulsive interaction. As a consequence, the activation energy is much higher and the diffusion of carbon is significantly reduced.

As the element with the maximum value of interaction parameter is the most effective diffusion barrier, copper should be the best choice. However, nickel is usually preferred because of its good weldability. Also, its similar thermal expansion coefficient and melting point compared to ferritic and austenitic steels make it the usual choice of buttering alloy **(Sudha et al. 2008).** Figure 32 shows the effect of a simulated Ni interlayer between two Cr-Mo steels of different chromium contents (2,25Cr-1Mo and 9Cr-1Mo).

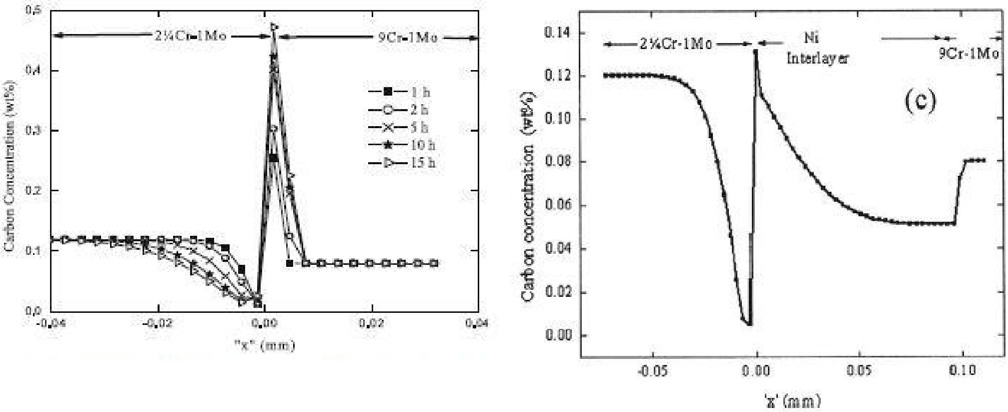

Fig. 32 Simulated effect of a pure Ni buttering layer on the carbon concentration profile at the 9Cr-1Mo/2,25Cr-1Mo weld interface: a) without buttering layer and b) with a simulated Ni buttering layer. PWHT at 1023 K has been applied for 15 h. ***(Sudha et al. 2008)***

Also, the use of over-alloyed Ni-base filler metals is useful as over-alloying will compensate for segregation in the weld metal. It makes sure that sufficient corrosion resistance remains in the depleted region. Although C diffusion occurs in welds made with Ni-base alloys, the problem is substantially reduced to the point where a decarburized layer is very small or not observed at all on the ferritic side of the joint.

The large Ni concentration of the weld metal is responsible for a reduction in the chemical potential gradient of carbon across the fusion line. **(DuPont et al. 2010)**

4.3. Austenitic-austenitic interface

Another usual type of weld interface in LWRs is the austenitic/austenitic DMW. It happens commonly when welding two nickel-base alloys or SS with nickel-base fillers. In that case, both sides of the fusion line are austenitic, with very low carbon contents. Thus, the carbon-related issues described before are no longer a major concern. However, carbon is not the only element having influence on the structural integrity of the welds. Thus, the weldability of nickel-base alloys and the long-time behavior of these welds are still to be considered.

4.3.1. Weldability of Ni-base alloys

In DMWs, a filler metal must be compatible with the different properties of the base metals. One major condition is that it has to accept dilution from the base metals without forming defects or increasing susceptibility to cracking. The weldability of Ni-base alloys, as well as their resulting mechanical properties, is largely dependent on their solidification behavior which in turn depends on solute redistribution of alloying elements.

Solid-solution strengthened Ni-Cr-Fe fillers are widely used. They produce fcc single-phase welds of high strength, resisting structural changes and with intermediate expansion properties (comparing to those of ferritic LAS and austenitic base metals). **(Payne, 1969)**

4.3.1.1. Solidification cracking

Studies identify the predominant mode of cracking in alloys 82, 182, 52, 152 and 52M as weld metal solidification cracking (also called hot cracking). Hot cracking is caused by a combination of low strength and low ductility of the material at high temperatures and tensile stress. During solidification at high temperatures, the material is brittle near and below the solidus temperature.

The formation of ferrite as the primary phase during solidification usually reduces the cracking susceptibility **(Masumoto et al. 1972)**. Hot cracking is thus a major problem in the welding of austenitic alloys. It is associated with low melting point eutectics such as FeS, TiC and NbC or Laves phase, which extend the solidification temperature range **(McCracken et al. 2011)**. Hot cracking is reduced with small solidification temperature ranges. The formation of hot cracks is usually explained by the presence of a liquid film under tensile stress at GBs **(Kim et al. 2002)**. Associated with the thermal stress of welding, it can lead to cracking. The presence of the liquid is often related to the segregation of impurities. It depends on the chemical composition of the alloy. In addition, constitutional liquation can result from the presence of silicon, sulfides, borides and intermetallic compounds **(Gooch et al. 1980)**.

4.3.1.2. Influence of alloying elements

The content of alloying elements affects the solidification temperature range. It also changes the extent and morphology of the low melting secondary phases. In addition, dilution will modify the chemical composition in the transition zone, thus modifying the solidification behavior **(DuPont et al. 1996)**. The compositions of nickel-base alloys change according to the expected service conditions of the components:

- Chromium is used to develop corrosion resistance.
- Aluminium, titanium and niobium promote strengthening precipitates.
- Molybdenum, chromium, cobalt and iron increase the strength of the austenitic matrix by solid-solution hardening. They also affect the lattice parameter and the coherency between the primary matrix and the precipitates.
- Most elements form carbides or nitrides.

Typically, the strengthening mechanism of an alloying element depends on its ability to stay in solid solution and the difference of its atomic size compared to that of nickel. It means usually that the element has to have similar electronic and crystal structure relative to nickel while keeping different atomic radii. Fe, Cr and Co have similar atomic size to that of Ni and show high solubility in Ni. They will stay in solid solution. Al, Ti, Nb and Mo show an interesting combination of good solubility in Ni while having significantly different atomic size. They can be used as good solid-solution strengtheners. On the other hand, Al and Ti are known to form γ'-Ni_3 (Ti, Al) precipitates for precipitation-strengthened Ni-base alloys. Among alloying elements, carbon has by far the highest atomic size difference as compared to Ni and the lowest solubility in Ni. **(DuPont et al. 2009)**

Of importance is that the atomic size and crystal structure of the alloying elements will also affect their segregation behavior and thus the weldability of Ni-base alloys. Elements with similar atomic radii to that of Ni have equilibrium distribution ratio k close to one, meaning that they segregate little to the liquid during solidification. Noticeable elements with close-to-1 k value are Fe, Cr, Co and Al. They will stay in solid solution and not segregate. Al is also a deoxidation element. A problem may arise for Al that may form Al oxides even in Ni-base filler metal wires. These oxides dissolve only at high temperatures and they can gather at the centerline of the weld. They have been observed for example on solidification crack surfaces of Alloy 52 during the SINI project.

The degree of segregation increases with decreasing k values. It leads to steep concentration gradients between dendrite cores (lower solute content) and interdendritic regions (higher solute content). A possible detrimental consequence is preferential corrosion attack of dendrite cores. In addition, intermetallic topologically closed pack (TCP) phases such as Laves phases form in highly alloyed materials at the end of solidification due to segregation or during welding and long term service. They are present in the interdendritic regions due to eutectic-like reaction associated with segregation. They can promote loss in strength and corrosion resistance due to depletion of alloying elements from the matrix. In addition, they have complex crystal structures with limited slip systems, leading to high hardness and brittle premature failure. **(DuPont et al. 2009)**

The C/Nb ratio is of particular importance as it controls the formation of low-melting Laves phase. The carbide/Laves phase content ratio increases with an increase of the

C/Nb ratio. It affects the liquation cracking susceptibility as an increase of Nb content will promote the formation of Laves phase. Brittle Laves phase will increase cracking susceptibility. In addition, hot cracking susceptibility depends on the solidification temperature range. As the Laves phase formation temperature increases, the solidification temperature range is decreased. It thus reduces the sensitive region width. Dilution increases the C/Nb ratio, and decreases the low melting phases because of chemical mixing. The Laves phase temperature increases with dilution, thus the solidification temperature range is decreased. As a consequence, hot cracking susceptibility is decreased by increased dilution. **(Yoon et al. 2002)**

Other trace elements can also be present. Their presence in nickel-base alloys is controlled closely because they can have huge effect on properties as the components are used in extreme conditions **(Richards et al. 2000)**. Their effects on the weldability and HAZ liquation cracking are a concern. They mostly segregate to GBs. The two segregation mechanisms are equilibrium segregation and non-equilibrium segregation:

- Equilibrium segregation is the movement of solute atoms to GBs to reduce the free energy of the system.
- Non-equilibrium segregation is more extended into the grain, where solute atoms can interact with vacancies to form solute-vacancy complex.

With increasing temperatures, equilibrium segregation decreases. Non-equilibrium segregation increases because of an increase in vacancy concentration. Rapid cooling can eliminate non-equilibrium segregation as there is too little time for diffusion. Heat treatments will also influence segregation, affecting grain growth, and the GB area per volume available for segregation. **(Huang et al. 1997)**

Sulphur is a dangerous element for nickel-base alloys. Its low solubility in nickel leads to the formation of an eutectic liquid film at GBs. The formation of Ni_3S_2 brittle particles at GBs is detrimental. It can form chromium sulphides and sulphocarbides M_2SC that promote cracking. **(Wallace et al. 1975)**

There is little knowledge about the influence of phosphorous. Its solubility in nickel is low, and a low melting eutectic is present. This promotes segregation and low temperature liquid film at GBs. Thus, phosphorous has a detrimental effect on hot cracking susceptibility. It may, however, have beneficial effects on creep resistance. **(Wallace et al. 1976)**

Carbon is used as a deoxidizer and desulphurizer. It improves the fluidity of the liquid alloys. It can prevent sulphur to form liquid films at GBs during solidification. Low carbon content may lead to creep susceptibility and insufficient deoxidation and desulphurization **(Holt et al. 1976)**. However, carbon influences mechanical properties by forming primary and secondary carbides. Higher carbon contents are detrimental because of weld cracking and GB embrittlement. After deoxidization and desulphurization, residual carbon can form primary MC carbides (mainly TiC and NbC) at high temperature. They are often located at GBs and appear as discrete precipitates. They can be a factor of liquation cracking in the HAZ, but the influence of carbon on weldability remains minor **(Huang et al. 1997)**. They can also act as obstacle against fatigue crack propagation. Primary carbides dissolve above 750°C and will form secondary carbides $M_{23}C_6$. These are primarily chromium carbides. They may present two morphologies: discrete particles along GBs that have beneficial effects on creep and stress rupture, or continuous films or cellular precipitates, causing embrittlement. Other carbides M_6C and M_7C_3 may also form depending on the content of chromium, tungsten and molybdenum. **(Holt et al. 1976)**

Nitrogen is a strengthening element that gives good corrosion resistance over a wide temperature range. It has been used to compensate the loss in mechanical properties induced by the reduction of carbon content in SS grades (304L, 316L). Nitrogen is an austenite stabilizer and it has an important impact on the solidification cracking behavior, as the austenite increases the susceptibility to hot cracking. In addition, it enhances the segregation of impurity element (P, S and Si) at GBs, creating low melting eutectics. **(Srinivasan et al. 2010)**

Trace elements often cause GB embrittlement, but additions of beneficial elements can counteract it. Boron and zirconium are used to improve high-temperature strength and ductility. Their effect is mostly beneficial for mechanical properties, especially creep resistance. The mechanism is related to the stabilization of GB constituents. Like other trace elements with low solubility in nickel, they segregate to GBs where they fill vacancies. They, thus, reduce the diffusion of other elements at

GBs. Like carbon, they prevent sulphur and phosphorous from collecting in GBs and forming brittle films **(Davies et al. 1969)**. Their effect is probably to tie up sulphur, preventing it from segregating at GBs **(Wallace et al. 1976)**. However, the presence of borides along with Laves phase in crack regions shows that boron segregation and constitutional liquation can contribute to HAZ cracking **(Huang et al. 1997)**.

The effects of gases (hydrogen, nitrogen and oxygen) are also to be considered for high-temperature properties. Oxygen and nitrogen can cause GB hardening and embrittlement of intermetallics such as NiAl, Ni_3Al and Ni_3Ti. Nitrogen reacts with Ti to form TiN, which in turn acts as nucleation sites for MC carbide precipitation **(Holt et al. 1976)**. Hydrogen embrittlement is known to affect nickel-base alloys. It has been attributed to an increase in hydrogen concentration at GBs. It helps crack nucleation by reducing surface energy due to hydrogen adsorption and crack propagation by high-pressure hydrogen in the crack **(Richards et al. 2000)**.

Dilution from the base metals has an influence on the cracking susceptibility, especially the dilution of Fe from the steel base metal to the nickel-base weld metal. The maximum solubility of Nb in Fe is lower than in Ni, thus Nb segregation to the liquid increases with Fe content. Higher Nb segregation and forming of NbC low melting eutectic extend the solidification temperature range. High S-Si amount in base metal promotes dilution and hot cracking **(McCracken et al. 2011)**. In addition, dilution of Fe in the weld metal will affect its coefficient of thermal expansion. Thus, dilution control is essential to reduce hot cracking susceptibility. For Ni-Cr-Fe fillers such as Inconel 82/182 and 52/152, dilution with Fe and Cr should be limited to 25-30% and 10-20%, respectively, to avoid hot cracking. Dilution of Si can also cause hot cracking. **(Payne, 1969)**

To be noted is that the micro-segregation of impurities usually increases with increasing cooling rate. Thus, the formation of low-melting point liquid films shall increase. However, in the primary austenitic solidification mode, increased cooling rate makes the material less susceptible to hot cracking. An explanation is the relation between the cooling rate and the solidification structures. After dendrites are formed, they start to coarsen and interlock. A liquid film is trapped between the interlocking dendrites. For a slow cooling rate, columnar dendrites are formed. This leads to coarse grains between which micro-cavities can easily propagate. For high cooling rate, equi-axed dendrites are formed, leading to fine grains. This makes difficult the propagation of micro-cavities, reducing the cracking susceptibility. **(Kim et al. 2002)**

4.3.1.3. Comparison between Ni-base filler metals

Inconel 82 and 182 show good weldability but are sensitive to PWSCC. Thus, Inconel 52 and 152 have been developed to replace them. Studies have shown that alloys 52 and 152 show better hot cracking resistance than alloys 82 and 182, respectively **(Bruemmer et al. 2009)**. However, they suffer from a phenomenon known as ductility dip cracking (DDC) or cold cracking. Inconel 52M is supposed to have better cold cracking resistance and it has led to a new DDC resistant Inconel family **(Smith et al. 2008)**.

The only significant defects present in Inconel 152, 52 and 52M are IG cracks. The fewest cracks are present in the alloy 152, and the greatest number of weld cracks is found in the alloy 52M **(Bruemmer et al. 2009)**. Theses cracks are related to secondary phase precipitates. Among them, TiN is the prevalent feature leading to weld cracks. The presence of these cracks may have significant impact during the in-service life. They can act as stress concentrators or be a preferential corrosion site. This makes them particularly susceptible to SCC. **(Bruemmer et al. 2009)**

Inconel 52MSS is a high-Cr filler metal with higher Nb and Mo addition. It was developed to resist DDC. Higher Nb contents lead to a better resistance to DCC. However, Nb increases the solidification cracking susceptibility. With higher Nb content, an NbC eutectic reaction at the end of the solidification expands the solidification temperature range, increasing solidification cracking susceptibility. Laves phase may also form due to the segregation of Nb. **(Alexandrov et al. 2009)**

4.3.2. Microstructures

4.3.2.1. Weld metal

All the weld metals considered in this study have an fcc austenitic solid solution structure. They can take into solution Ni, Cu, Cr, and Fe to the levels corresponding to the dilution from base metals. As a result, the weld should have a normal dendritic structure of a single-phase material. It has been noticed, however, that Inconel 52 weld microstructure can contain dynamically recrystallized zones, which may improve SCC growth through a dendritic structure. **(Moss et al. 2012)**

The weld metal microstructure of Inconel 82 filler metal is fully austenitic. This weld metal contains 3% niobium. As seen before, Nb has a tendency to increase the solidification temperature range. Thus, the substructure tends to change from cellular to columnar dendritic, as the degree of constitutional undercooling is increased **(Naffakh et al. 2009)**. The subgrain structure near the centerline of the fusion zone middle layer is cellular and columnar dendritic in the Inconel 52 weld, and dominantly columnar with Nb-rich precipitates in the Inconel 82 weld **(Kuo et al. 2002)**. The hardness of the Inconel 82 welds is on average higher than that of the Inconel 52 welds. This is because the Inconel 82 FZ has a denser dendritic structure and because of the formation of abundant niobium-enriched precipitates **(Kuo et al. 2002)**. In comparison, the Inconel 52 weld metal has coarse dendrites and no niobium-enriched precipitates. It exhibits superior corrosion resistance than Inconel 82 but has a lower tensile strength **(Lee et al. 2001)**. As a consequence, rupture occurs in the base metal for Inconel 82 welds, and in the fusion zone for Inconel 52 welds.

The weld metal can present inclusions and precipitates, such as titanium nitrides, carbonitrides and carbides (usually chromium carbides) **(Payne, 1969)**. Some Nb inclusions, Nb and Ti carbides can be localized in the interdendritic regions. The precipitation is increased with PWHT **(Soares et al. 2007)**. The presence of iron in nickel-base alloys lowers the Nb solubility in austenite phase. The ability of Nb to remain in solution is then limited and its partitioning to interdendritic regions in the weld metal is increased **(Naffakh et al. 2009)**. As seen in Figure 33, continuous NbC (shiny precipitates) and distributed TiC precipitates (dark particles) form in the interdendritic regions **(Naffakh et al. 2009)**. In Inconel 52, precipitates are distributed in the interdendritic regions and also at the GBs. They are mostly TiN and TiC and their number is lower than in the Inconel 82 welds. **(Kuo et al. 2002)**

The scale of the solidification structure is governed by the cooling rate, which is equivalent to GR, where G is the temperature gradient and R is the solidification rate. As is well known, a higher GR (fast cooling rate) contributes to a finer subgrain structure. **(Kuo et al. 2002)**

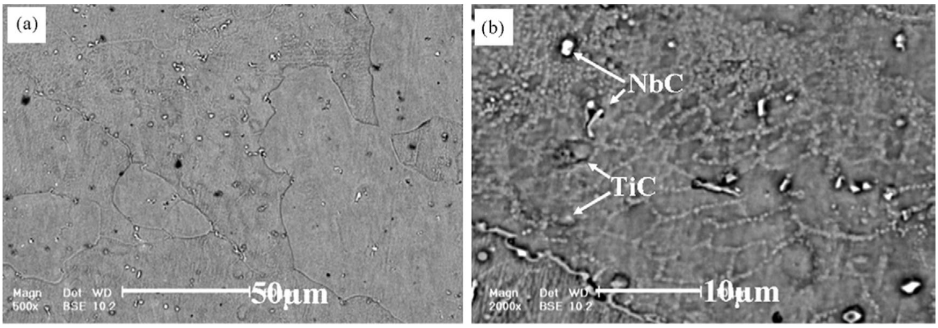

Fig. 33 Microstructure of Inconel 82 weld metal: (a) weld metal and (b) interior of weld with higher magnification. ***(Naffakh et al. 2009)***

Within the weld metal, the root hardness is usually higher than the crown hardness. This is a consequence of the residual stress induced in the weldment during welding and cooling. If the residual stress is greater than the yielding stress, especially during post-welding cooling, plastic deformation results and the weld is thereby hardened. Moreover, the cooling rate in the root is faster, promoting a finer microstructure and a higher hardness in the FZ root than in the FZ crown. **(Kuo et al. 2002)**

The microstructures of Alloys 182 and 82 are similar to that of wrought Alloys 600 and 690. Under thermal treatments, Cr–rich carbides can precipitate at both inter-dendrite and intra-dendrite GBs **(McNeil et al. 2001)**. Chromium depletion occurs at the GBs with such carbides. The precipitate phases are predominantly $M_{23}C_6$ and TiC carbides. During the welding process, only the $M_{23}C_6$ carbide precipitates because of the rapid cooling of the weld metal from fusion temperature. Nucleation of M_7C_3 carbides requires long periods at relatively high temperatures, whereas nucleation of

$M_{23}C_6$ is quite rapid and cannot be avoided even during water quenching from solution treatment temperatures.

The greater susceptibility of Alloy 182 to SCC than Alloy 82 has been attributed to differences in Cr depletion observed in the two alloys because of differences in their composition. Alloy 182 contains higher concentrations of C and Fe and a lower concentration of Cr, all of which enhance Cr depletion during carbide precipitation. **(McNeil et al. 2001)**

4.3.2.2. Base metal

The microstructure of Alloys 600 and 690 typically consists of either a semi-continuous or continuous carbide precipitates at the grain boundaries and some intragranular carbide. The precipitate phases are Cr–rich M_7C_3 and $M_{23}C_6$ carbides and Ti(C, N) carbo-nitrides **(Webb et al. 1995)**. In general, the microstructures depend on the thermo-mechanical processing histories and the solubility of C in the material **(Server et al. 1987)**. The optical microstructure of the Alloy 690 base metal (Fig. 34 a) shows random grain orientation. No texture is observed. It also includes small golden TiN compounds **(Wu et al. 1999)**. It clearly indicates a single austenitic phase with many annealing twins formed after heat treatment. Carbides in the form of particles are dispersed in matrix and particularly at grain boundaries.

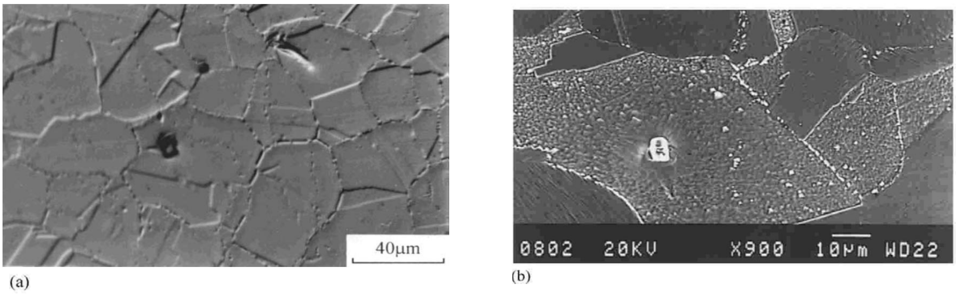

Fig. 34 a) Optical and b) SEM microstructure of Alloy 690, showing fine dispersed carbides and coarse TiN compounds. ***(Kuo et al. 2002)***

As seen in the SEM image of Alloy 690 (Fig. 34 b), two types of precipitates are present:

- The more numerous precipitates have a size of about 0.5 µm and are $M_{23}C_6$ carbides. These white carbides precipitate in the matrix and at grain boundaries, and consist mostly of $Cr_{23}C_6$.
- The less numerous precipitates have a size of about 2- 8 µm and are dispersed randomly. They appear golden in color, with a rectangular shape, under optical microscopy. They are identified as TiN. **(Kuo et al. 2002)**

Another feature of Alloy 690 microstructures is banding. Two kind of banding can be observed: carbide banding (see Fig. 35) and grain size banding (see Fig. 36). The extent of banding is related to the manufacturing history and the type of Alloy 690 product form. **(Willis et al. 2011)**

Three main product forms are available: plate, billet and extruded. Carbide and grain size banding are commonly observed in billets and plates. The reason is that prior GB carbides dissolve at higher temperatures. If the working temperatures are too low, these carbides are not dissolved and retain at the prior GBs. It can create bands of fine grains adjacent to coarser grains. In billets, banding is more pronounced near the center. The difference is that in billets, banding can be observed only in longitudinal cuts, whereas it is invisible in transversal cuts. In plates, banding is planar and, thus, visible in all directions. Extrusion of Alloy 690 gives usually an ideal microstructure, with equi-axed grain structure in all directions and without banding.

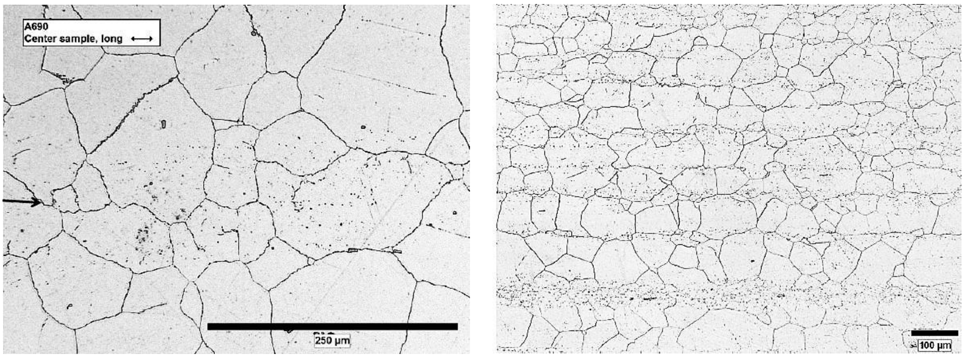

Fig. 35 Longitudinal sections of a) an Alloy 690 billet and b) an Alloy 690 plate showing carbide banding. ***(Willis et al. 2011)***

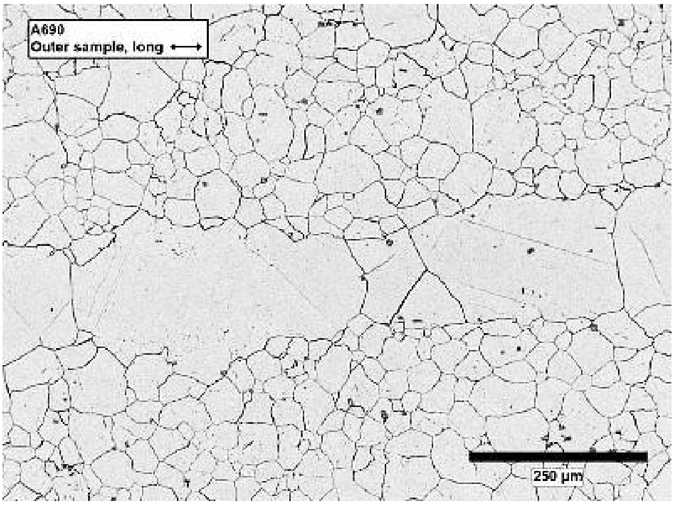

Fig. 36 Grain size banding and isolated coarse grains in an Alloy 690 billet. ***(Willis et al. 2011)***

It is an issue since an inhomogeneous microstructure will retain more residual strain. It is known that the SCC susceptibility is strongly dependent on the amount of residual strain present in the material. Coarse grains can also disturb ultrasonic testing of the materials.

Annealing heat treatments help to minimize the effects of cold work, but banding can remain an issue if the annealing temperature is too low. To be noted is that the annealing temperature must be chosen in order to homogenize the microstructure without increasing too much the grain size and without promoting sensitization at GBs. Results of heat treatments on the carbide precipitation are shown in Figure 37.

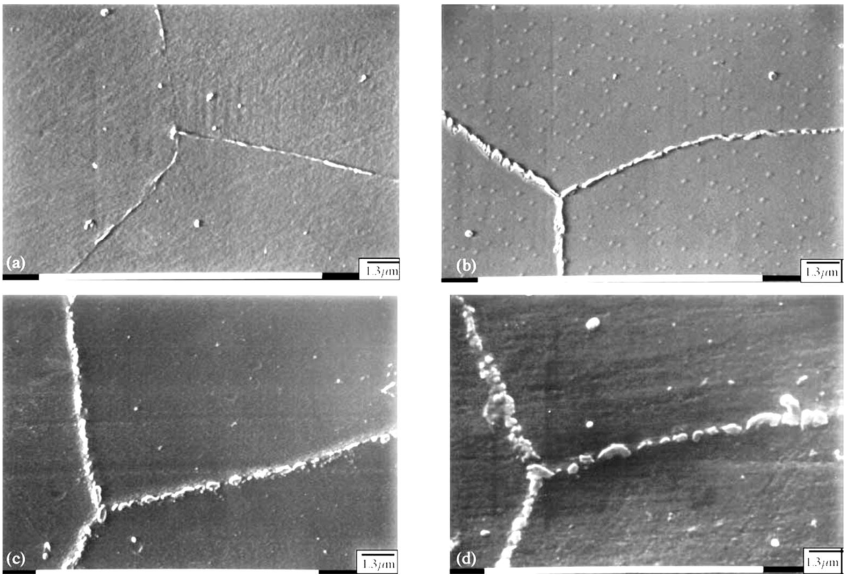

Fig. 37 Carbide morphology of Alloy 690 a) solution annealed at 1150°C for 1 h, b) solution annealed at 1150°C for 1 h then thermally treated 700°C for 1 h, c) as-received and d) solution annealed at 1150°C for 1 h then thermally treated at 800°C for 1 h. ***(Hong et al. 2005)***

The microstructure of Alloy 690 is affected by the temperature and duration of the heat treatment. Grain size increases and hardness decreases with increasing the temperature and the duration of solution annealing. The difference between GB and matrix microhardness is due to the strain energy of the GB, resulting from inclusions or precipitates at GBs. The sizes and discontinuity of carbides increases with temperature and duration of the thermal treatment. Solution annealing alone affects the grain size of the material, whereas the low temperature heat treatment precipitates carbides in the GB region and barely affects the grain size. The size of the carbides increases with the temperature and duration of the low-temperature heat treatment. **(Hong et al. 2005)**

Materials with greater GB coverage of carbides are resistant to SCC in high–temperature high–purity water. Also, materials with M_7C_3 carbides are more resistant to SCC than those with $M_{23}C_6$ carbides **(Webb et al. 1995)**. The favorable microstructure may be developed by thermal treatments that promote extensive precipitation of intergranular carbides. The resistance to SCC of this favorable microstructure does not seem to depend on Cr depletion that accompanies formation of Cr–rich carbides. The greater resistance of Alloy 690 to SCC than that of Alloy 600 is attributed to the differences in the C solubility and carbide precipitation kinetics of these alloys. **(Server et al. 1987)**

Alloy 690 shows a HAZ with typical coarse grains due to grain growth **(Kuo et al. 2002)**. However, it can be difficult to distinguish between Alloy 690 base metal and the austenitic weld metal since the microstructures at the interface are complex.

4.3.2.3. Interface

Austenitic/austenitic fusion lines show fewer changes as compared to the ferritic/austenitic interfaces. This is mostly due to the limited carbon diffusion. However, typical DMW microstructures can be observed.

The interface of a weld between Inconel 625 weld metal and austenitic SS 304 base metal reveals the presence of an unmixed zone (Fig. 38).

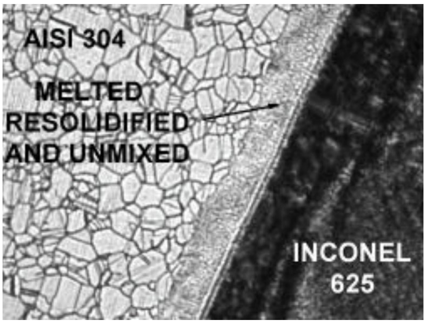

Fig. 38 UMZ at the austenitic SS 304/Inconel 625 interface. ***(Soares et al. 2007)***

The interface between Inconel 82 weld metal and Inconel 657 base metal also shows an unmixed zone and a partially melted zone (Fig. 39). The partially melted zone on the Inconel 657 side of the joint is wider than that on the other side. The tendency of dendritic boundaries to melt in Inconel 657 is attributed to the enrichment of Nb at GBs. **(Naffakh et al. 2009)**

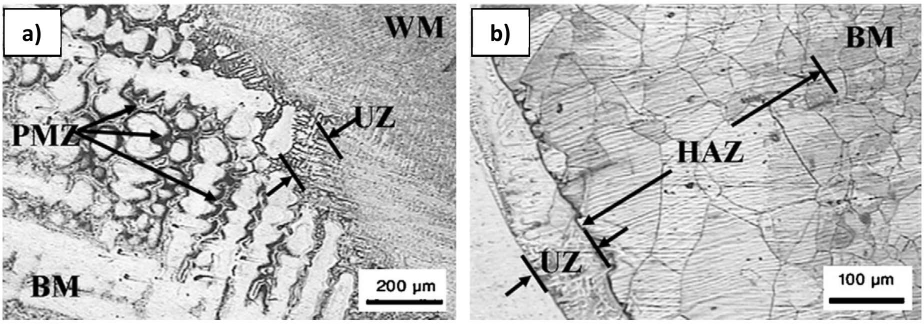

Fig. 39 Weld interfaces with weld metal Inconel 82 and base metals a) Inconel 657 and b) 310 SS. ***(Naffakh et al. 2009)***

As welded, there is evidence of grain boundary thickening and liquation in the HAZ. With PWHT there is more evidence of GB thickening and liquation, and formation of Type II boundaries (see Fig. 40). **(Soares et al. 2007)**

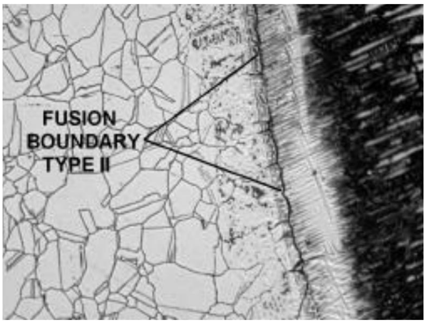

Fig. 40 HAZ of SS 304 with formation of Type II boundaries at the interface with Inconel 625 weld metal. ***(Soares et al. 2007)***

It can be difficult to distinguish between Alloy 690 base material, HAZ, PMZ and UMZ. It is, however, of major importance as it is in these complex microstructures that a lot of residual strain is present, increasing the susceptibility to SCC.

An approximation of Alloy 690 interface (see Fig. 41) can be based on a grain size change from the base metal to the thermal HAZ to PMZ to UMZ. Further, the transition from the UMZ to the weld metal is indicated by carbides precipitated along the dendrite cores as the PMZ region with elongated grains has few particles on its boundaries. Cr_3C is the major precipitate, along with TiC particles. **(Moss et al. 2012)**

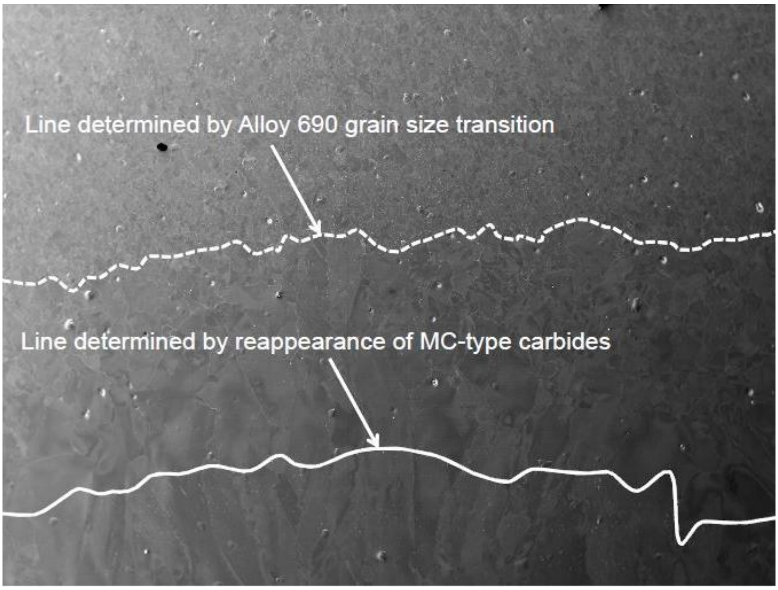

Fig. 41 Alloy 690 interfaces between base material, HAZ, PMZ+UMZ and weld metal, based on grain size transition and carbide precipitation. ***(Moss et al. 2012)***

4.3.3. Long-term behavior of Ni-base alloys

Since Alloy 690 has always been considered very resistant to corrosion and SCC, most research has been conducted about fretting wear, which is purely mechanical and occurs as the result of a low amplitude motion between contacting components.

In fact, in view of mechanical properties, steam generator with Alloy 690 would be inferior to the one with Inconel 600. Because of the thermal conductivity of Alloy 690, the length of the tube can be increased by 10% during the temperature cycles. Consequently, mechanical damage such as fretting or fatigue is likely to occur more than pure corrosion damage. **(Hong et al. 2005)**

However, if operating experience and testing continue to show excellent behavior of Alloy 690/52/152 materials in resistance to PWSCC under normal PWR conditions **(Fyfitch et al. 2012)**, they are not immune to SCC, and cracks can grow at moderate or high rates in PWR primary water under certain conditions (see Fig. 42). Issues rise especially with the effect of residual strains at the weld interfaces and within the base metal as a result of the cold work and manufacturing history. Another common thought is that GB carbides in nickel-base alloys are always beneficial to SCC resistance. **(Andresen et al. 2012)**

Examples of SCC have been reported in flowing coolant in locations, that is to say not obviously subject to O_2 or anion contamination. They were all associated with high levels of cold work. The distribution of the residual strains is usually:

- 40 – 50% in the weld metal
- 20% in the UMZ and PMZ
- ~15% in the HAZ
- 8 – 10% away from weld (within the base material). **(Andresen et al. 2012)**

4.3.3.1. SCC behavior of Alloy 690

Figure 42 shows that Alloy 690 and its weld metal are still susceptible to SCC in PWR water chemistry, especially in the vicinity of the welds. This is mainly related to tensile residual stresses.

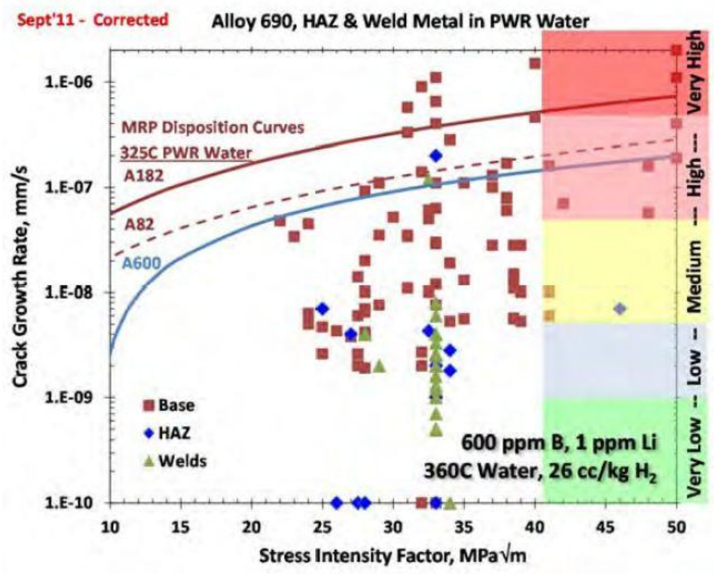

Fig. 42 Graph showing the SCC behavior of Alloy 690 base material, HAZ and weld metals Inconel 52, 152 in PWR water. Cracks can grow under certain conditions. ***(Andresen et al. 2012)***

Even in the base material (no influence of the weld), Alloy 690 plates retain up to 10% of residual strain. As shown before, this is due to the manufacturing history and the consequent inhomogeneous microstructures. A consequence is that the samples for mechanical testing have to be chosen according to this inhomogeneity. Orientation is relevant to SCC in weld HAZ.

Figure 43 shows different samples issued from an Alloy 690 plate, which presents a banded microstructure.

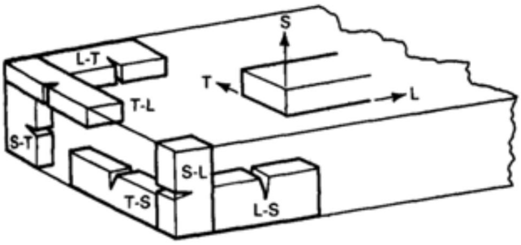

Fig. 43 Alloy 690 plate with planar banding and samples for mechanical testing with different orientation. They present, thus, different microstructures and SCC behavior. ***(Andresen et al. 2012)***

The L-T orientation (good) shows very homogeneous microstructure, and low crack growth rate (CGR) during testing. The S-T orientation shows medium CGR due to very homogeneous microstructure 1D cold rolled. High CGR is present in the S-L orientation due to inhomogeneous microstructure in the direction of the notch. The composition and microstructural banding affects grain size and grain boundary carbide decoration, thus the mechanical properties, retaining of residual stresses and SCC behavior. **(Andresen et al. 2012)**

The residual stresses that can be already in the base material (due to an improper annealing treatment or to deformations) will be magnified during welding in the vicinity of the weld. Measurements show that the highest residual strains are in the UMZ and PMZ regions of Alloy 690/Inconel 52, 152 weld interfaces (see Fig. 44). This is mostly due to the complex microstructures that form in these areas. **(Moss et al. 2012)**

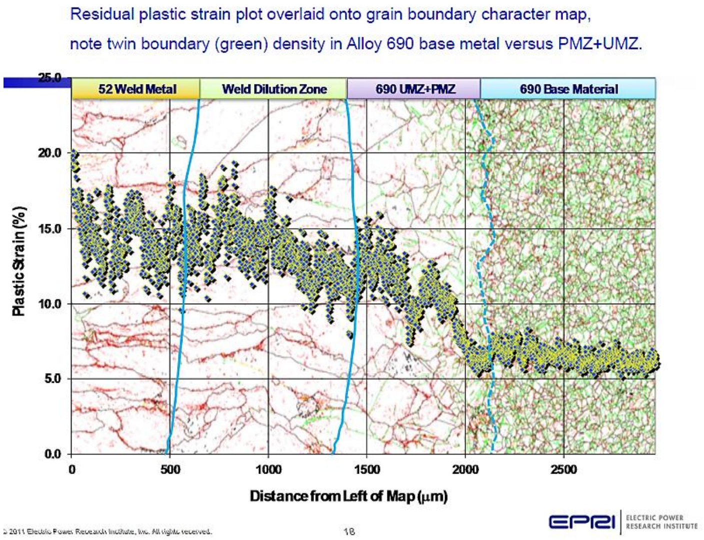
Residual plastic strain plot overlaid onto grain boundary character map, note twin boundary (green) density in Alloy 690 base metal versus PMZ+UMZ.

Fig. 44 Map of the several zones at an Alloy 690/Inconel 52 weld interface and the corresponding residual strain measurement. Residual strains increase in the UMZ+PMZ of Alloy 690. The higher residual strains are found in the weld metal. ***(Moss et al. 2012)***

This leads to concern for higher CGR in the HAZ than in the base material due to the altered microstructures and residual strains **(Fyfitch et al. 2012)**. This is especially true for interfaces with LAS or carbon steels, which show high CGRs **(Andresen et**

al. 2012). First results show small correlation between CGR and dilution effects, but show a reduced resistance to PWRSCC at high levels of cold work **(Fyfitch et al. 2012)**. This research is the focus of an international effort to achieve closure of many knowledge gaps associated with Alloy 690/52/152 materials.

4.3.3.2. Chromium depletion

The nickel-base alloys have evolved for many years to meet more demanding in-service requirements. But even if they show excellent mechanical and anti-corrosion properties, their behavior may evolve after long-term exposure to extreme LWR conditions. Of major importance is to observe the correlation between the thermal cycles experienced by Alloy 690 during welding and the corresponding corrosion resistance changes.

Ni-base alloys are homogenized by high-temperature annealing. Their high chromium concentration destabilizes the solution by generating chromium carbides of type Cr_3C_2, Cr_7C_3, $Cr_{23}C_6$ and intermetallic phases. The consequence of the intergranular precipitation of these phases is to create a chromium-depleted zone near the grain boundaries, which increases the susceptibility to IGSCC. The depleted zones get wider as the temperature and/or the aging duration is higher.

Alloy 690 is one of the most sensitive to the phenomenon of chromium carbide precipitation at the grain boundaries and the subsequent chromium depletion during aging at the LWR operating temperatures. **(Sahlaoui et al. 2002)**

Figure 45 a) shows the accumulation of precipitates at the GBs as compared with the grain interior. Figure 45 b) and c) present the EDS analysis results for the white particles at the GBs and in the grain interior, respectively:

- The original Cr content of the Alloy 690 weldment is 29.45 wt%.
- The particles at the GBs have a Cr content of 31.06 wt%.
- Those within the grain have a Cr content of 29.29 wt%.

Thus, the particles formed at the grain boundaries are chromium carbides and the lower chromium content close to the GBs suggests chromium depletion. As a result, these regions of the weldment become anodic relative to the base metal and are preferentially attacked when exposed to a highly corrosive oxidizing environment.

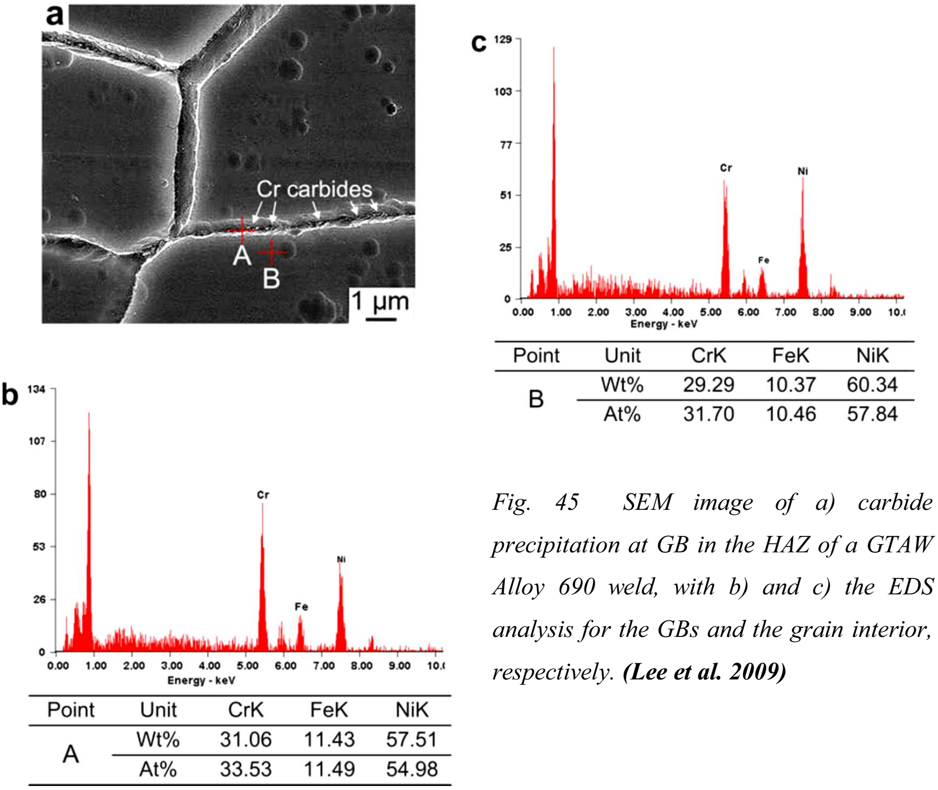

Point	Unit	CrK	FeK	NiK
B	Wt%	29.29	10.37	60.34
	At%	31.70	10.46	57.84

Point	Unit	CrK	FeK	NiK
A	Wt%	31.06	11.43	57.51
	At%	33.53	11.49	54.98

Fig. 45 SEM image of a) carbide precipitation at GB in the HAZ of a GTAW Alloy 690 weld, with b) and c) the EDS analysis for the GBs and the grain interior, respectively. ***(Lee et al. 2009)***

4.3.3.3. Ductility dip cracking

Ductility dip cracking (DDC) has often been referred to as “micro-fissuring”. It was not before the 90s that DDC was discriminated from solidification cracking. It can also be called cold cracking.

It refers to a solid-state high temperature cracking. This cracking is isolated from liquid phase and has no relation to hot or liquation cracking **(Findlan et al. 2004)**. It has been observed in multi-pass welding of thick section of nickel-base alloys. DDC results from the deterioration of the ductility at austenitic GBs at high temperature. Studies suggest that GBs exhibit less high-temperature ductility than the grain interiors. When exposed to strain at elevated temperature, the ductility limit of the GB is exceeded and cracking occurs. It can be stopped as the stress is reduced at the crack tip. The energy released is absorbed in recrystallization. Clusters of fine recrystallized grains are found at crack tips **(Kiser, 2003)**. DDC is mainly the result of the difference between inter- and intra-granular strength. It is related to GB segregation during cooling, which is mostly influenced by the content of S and P of the weld metal. **(Nishimoto et al. 2006)**

Inconel 52 and 152 are resistant to PWSCC, but they are susceptible to DDC. Inconel 52M and 152M have been developed for improved DDC resistance. They have been used widely for overlays, but are thought to be insufficient for higher restraints **(Kiser et al. 2003)**. Inconel 52MSS was developed with higher Nb and Mo content. These elements have shown to improve DDC resistance. Earlier alloys 52 and 52M have straight GBs. This is due to $M_{23}C_6$ carbides that form at low temperatures and are ineffective to pin the migrated GBs. Inconel 52MSS has serpentine GBs. Mo and Nb segregate in the interdendritic regions, and precipitate as MC (mostly NbC) carbides at higher temperatures. They are therefore effective to pin the GBs, creating serpentine GBs that resist sliding and thus improve DCC resistance. **(Kiser et al. 2010)**

Alloy 690 has proved to be susceptible to DDC, especially for thick component welding **(Davé et al. 2004; Lippold et al. 2004)**. In Alloy 690, the cracking decreases with the decrease of impurities. O, C and S are degrading GB ductility. However, adding GB elements such as zirconium and boron seems to be able of suppressing DDC. Lanthanum has good affinity for P and S. It can be used to reduce the segregation of impurities at GBs as it forms La phosphides, sulphides and oxides. Another point is that it slightly decreases the grain size, thus, reducing the intensity of segregation. **(Nishimoto et al. 2006)**

4.3.3.4. Hydrogen embrittlement

Nickel-base alloys are more resistant to hydrogen embrittlement than ferritic steels. However, due to the slow diffusivity of hydrogen in nickel, hydrogen embrittlement must be taken into account. Hydrogen has played an important role in the PWSCC susceptibility of Inconel 600. The most accepted cracking mechanisms are:

- Hydrogen-induced softening
- Hydrogen-induced decohesion, related to hydrogen segregation at GBs.
- Strain-induced hydrogen redistribution. It results from the trapping of hydrogen at GBs, which involves the transport of hydrogen by moving dislocations.

Hydrogen will form micro-voids in the material. This creates stress up to levels where the metal has reduced ductility and tensile strength up to the point where cracks can develop. The loss of ductility and the resultant cracking are dependent on the temperature and on the strain rate. At high temperatures, a strong correlation exits between the carrying capacity of dislocations and the ductility loss **(Brass et al. 2004)**. Research indicates that high residual strains and hydrogen trapping lower the ductility of Ni-Cr-Mn-Nb weld metal when dissolved hydrogen concentrations are greater than 5 wt.ppm. Shielding gas mixtures with 1% hydrogen additions can result in hydrogen concentrations greater than 5 wt. ppm in the weld metal and reduce ductility via hydrogen embrittlement. In addition, recrystallization decreases the resistance to hydrogen embrittlement. Recrystallized grains lower strength and localize deformation **(Young et al. 2002)**. The interaction between hydrogen and the microstructure (trapping sites) also influences the hydrogen embrittlement sensitivity.

Cracking along DMWs has often been associated with the exposure to hydrogen in service. But cracking has also occurred before any exposure to hydrogen in service. For the welding of austenitic alloys, argon-hydrogen mixture is often used as a shielding gas. It helps making the shielding atmosphere reducing and it increases the arc voltage. **(Young et al. 2002)**

4.3.4. Grain boundary engineering

It has been seen that most of the ageing and failure mechanisms are related to the segregation of alloying elements at GBs. Also, the methods to counteract these mechanisms are based on the segregation of other elements at GBs. For example, it is noted that the DDC susceptibility increases with high-angle GBs relative to the stress direction **(Kiser et al. 2010)**. In addition, the presence of borides in crack regions shows that boron segregation and constitutional liquation can contribute to HAZ cracking. It has been observed that boron segregates more to high-angle GBs than to twin or low-angle GBs. Subsequently, the high-angle GBs show more liquation **(Huang et al. 1997)**. In addition to that, B segregation has beneficial effects concerning creep resistance. It has brought the idea that modifying precisely the nature of the GBs can prevent deleterious segregation and improve beneficial segregation.

This is especially true for Alloy 690. It is generally accepted that the precipitation of intergranular chromium carbides by thermal treatments improves its IGSCC resistance in primary water. The precipitation of chromium carbides is strongly influenced by the GB character. The distribution of $M_{23}C_6$ precipitates in austenitic alloys is sensitive to the degree of GB misorientation **(Lim et al. 2004)**. Alloy 690 has low stacking fault energy. Thus, it presents extensive amount of twins (see Fig. 46 a). A twin can strongly affect the precipitation behavior of the intergranular chromium carbides, since an abrupt change of the misorientation occurs, when the twin boundary impinges on a grain boundary **(Lim et al. 2004)**.

The intergranular chromium carbides develop by thermal treatment on most of the grain boundaries except some special boundaries, such as the coherent twin boundaries (see Fig. 46 b). Precipitation is dependent on the grain boundary energy, mobility and diffusivity, which depends in turn on the grain boundary structure. Therefore, it can be preferentially initiated on the GBs with a particular misorientation relationship and grain boundary structure. **(Hirth et al. 1998)**

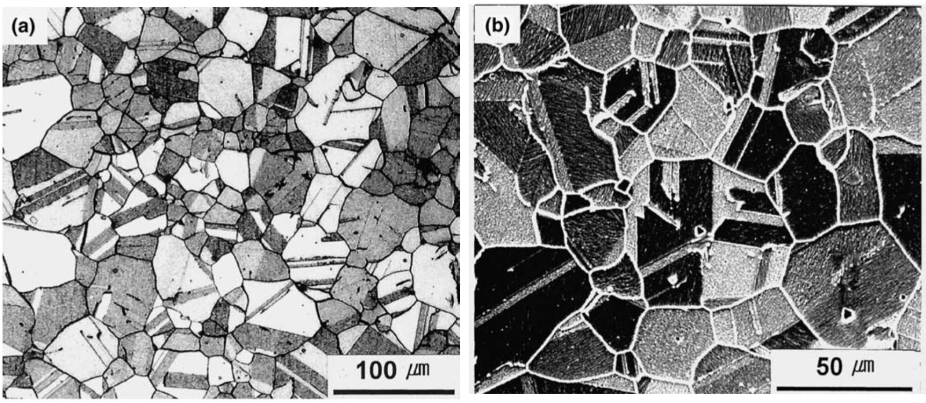

Fig. 46 a) Optical microstructure of heat-treated Alloy 690 and b) corresponding Cr-carbide precipitation at GBs. The extent of precipitation is much lower for coherent twins. ***(Lim et al. 2004)***

The precipitation of the intergranular carbides is retarded on the low angle boundaries, in comparison with that on the random high angle grain boundaries **(Lim et al. 2004)**. Minor elements tend to segregate less at low angle GBs, reducing the susceptibility to hot cracking and IG cracking. In addition, creep, fatigue and weldability can be improved by grain boundary engineering **(Lehockey et al. 1998)**. Grain boundary engineering (GBE) will process the metal by cold rolling or tensile strain creating small deformation, followed by annealing. It has been demonstrated for Inconel 625 and 600. **(Was et al. 1996)**

An example of GBE is given below. It consists of creating clusters of grains. As seen in Fig. 47, the non-GBE sample has a much higher density of random grain boundaries than that of the GBE sample. The assembly of grains encircled by random grain boundaries is called a grain-cluster. All the grains inside these kinds of clusters have special orientation relations. The highly twinned large size grain-cluster microstructure plays the key role in enhancing the intergranular corrosion resistance **(Xia et al. 2011)**:

- The large grain-cluster can arrest the penetration of intergranular corrosion.
- The large grain-cluster can protect the underlying microstructure.

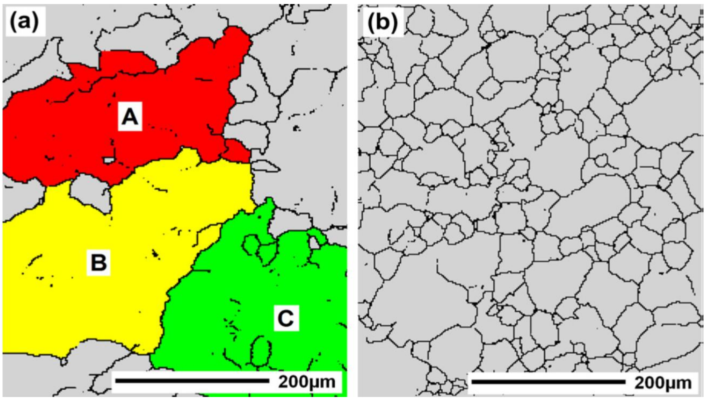

Fig. 47 Grain boundary network of Alloy 690 with a) GBE and b) non-GBE. See the grain clusters in the GBE alloy. ***(Xia et al. 2011)***

5. Experimental research work

DMWs show complex interfaces due to metallurgical changes activated by high temperatures and composition gradients. The aim of this study was to provide a first understanding of these interfaces for several samples representing new DMW features present in LWRs. Materials characterization involves three fundamental questions: what is the elemental composition, what are the crystal and local structures, and what types of defects are present.

The characterization methods employed were microstructural characterization and hardness measurements. These are the usual first tests run in material science and in the characterization of welds. They provide the basic knowledge about the characteristics of the materials and the interfaces, and orientate the future research.

5.1. Microstructural characterization

The properties of a material are directly related to its microstructure. With microscopy, it is possible to observe the key parameters such as grain size, nature of grain boundaries, nature of primary phases, distribution and morphology of secondary phases and precipitates. It is then possible to determine the solidification history as well as the main contributors to failure.

After an appropriate sample preparation, optical microscopy enables to observe microstructural features to a resolution up to 2 µm. For higher resolutions up to 0,5 µm, it is possible to use electron microscopy. The use of electrons to illuminate the sample increases the resolving power as they have a shorter wave length as compared to photons. Electron-back-scattered microscopy helps to distinguish better between the different phases as the emerging beam depends on the chemical composition of the material.

In this study, optical characterization has been conducted with a Nikon Epiphot 200, associated to the image treatment software NIS-Elements F.2.30.

5.2. Hardness measurements

Optical microscopy points out the interesting zones of the weldment. After that, hardness measurements give the first idea of the mechanical properties.

Surface contacts between materials are dependent on their mechanical properties. Different indentation and impression tests are available to measure such mechanical properties from a contact of known geometry. Hardness gives a relative idea of these properties rather than an intrinsic value. However, it can be correlated to tensile strength for many metals, and is an indicator of wear resistance and ductility.

Indentation hardness measures the resistance of a material to plastic deformation. A prescribed load is applied to an indenter in contact with a specimen and the area of the residual impression is measured by optical imaging after the load is removed, hardness is then obtained through dividing the load by this area. The value will depend on the type of test. The most common hardness tests are the Vickers test, the Rockwell test, the Knoop test and the Brinell test. The difference mainly relates to the shape of the indenters. Conversion tables can be established between these tests for some materials, but there is usually no simple link between different hardness tests.

The Vickers hardness test uses a square-based pyramid indenter. The load is applied without impact, and held in place for 10 or 15 seconds. The Vickers indenter usually produces a geometrically similar indentation at all test forces, except for very low loads. The hardness measure will be the same as long as the material being tested is quite homogeneous. **(ASTM E384 - 11e1)**

The distance between two successive indentations has to be sufficient to avoid that strain hardening resulting from the first indentation affects the new measurement. Usually, it is considered that a distance three times higher than the diagonal of the indentation is sufficient.

The size of the indentation depends on the force applied to the indenter. It determines therefore the scale of the hardness test:

- Macroindentation tests: loads from 10N to 1000N
- Microindentation tests: loads from 10mN to 10N
- Nanoindentation tests: loads from 10µN to 10 mN

In a conventional micro- or macro-hardness test, penetration depths of the order of 10^1–10^3 µm and forces in the range 10^{-2}–10^2 N occur. In a nano-hardness test, both are significantly smaller (<10 mN and < 10 µm, respectively) (**Mukhopadhyay et al. 2006)**. An issue rises for very low loads, as the elastic response of the material becomes as important as the plastic response **(ASTM E384 - 11e1)**.

Microindentation allows the evaluation of specific phases or constituents and regions or gradients too small for macroindentation hardness testing. Nanoindentation allows the evaluation of GB regions and specific grains. The technique was developed in the early 1970s, motivated by modern applications, such as thin films, microelectronics and biomaterials. Compared to other methods of mechanical testing in the sub-micron range, nanoindentation has a relatively simple setup and specimen preparation. Furthermore, it is commonly perceived as relatively non-destructive. **(Ravichandran et al. 2008)**

For the indentations at nano-scale, the remaining area is difficult to be measured with the traditional optical microscopy because of a too low resolution. Atomic force microscopy techniques can be used but the determination of the nano-indentation hardness usually uses a depth-sensing indentation. A diamond tip with a geometry known to high precision (commonly, a Berkovich tip, see Fig. 48 a) is pressed into the specimen until a given maximum depth or load are reached, and then removed. Synchronously, the load and the displacement of the indenter are recorded. Hardness and elastic modulus of the material can be extracted from such a load–depth curve (see Fig. 48 b). It uses a model for the deformation of an elastic half space by an elastic punch which relates the contact area at peak load to the elastic modulus and estimates the contact area from the indenter shape function. This analysis is usually made using the Oliver and Pharr method. (**Qian et al. 2005)**

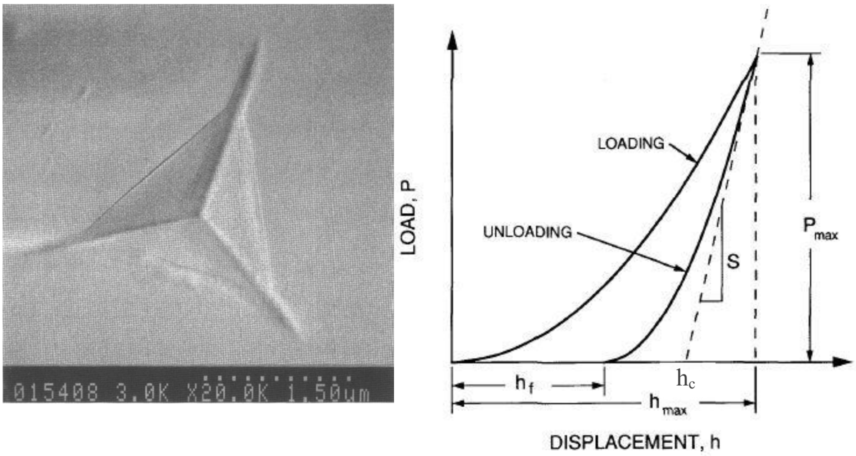

Fig. 48 a) Indentation mark of a Berkovich tip and b) schematic representation of load-displacement data for an indentation experiment. The quantities shown are P_{max}: the peak indentation load; h_{max}: the indenter displacement at peak load; h_f: the final depth of the contact impression after unloading; S: the initial unloading stiffness; and h_c: the contact depth. ***(Oliver et al. 1992)***

Figure 49 shows an illustration of an indentation by a rigid cone into a linearly elastic solid. It also shows the contact depth h_c.

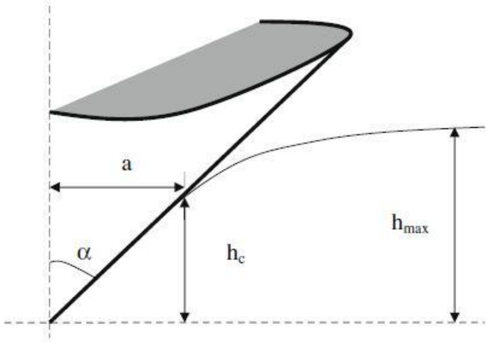

Fig. 49 Indentation of a rigid cone into a linearly elastic solid. It shows: h_{max}*: the depth at peak load;* h_c*: the contact depth; a: the indenter radius at the contact depth; α: the angle of the indenter. For a Berkovich indenter, α = 70,3°.* ***(Ravichandran et al. 2008)***

The usual model assumes that:

- Deformation upon unloading is purely elastic
- The compliance of the sample and of the non-rigid indenter tip can be combined as springs in series with a reduced modulus, defined as in (1)

$$\frac{1}{E_r} = \frac{(1-\nu^2)}{E} + \frac{(1-\nu_i^2)}{E_i} \qquad (1)$$

  where E_r is the reduced modulus, E and ν are Young's modulus and Poisson's ratio for the specimen and E_i and ν_i are the same parameters for the indenter.

- The contact can be modeled using an analytical model for contact between a rigid indenter of defined shape with a homogeneous isotropic elastic half space using equation (2)

$$S = \frac{dP}{dh} = \frac{2}{\sqrt{\pi}} E_r \sqrt{A} \qquad (2)$$

  where S is the experimentally measured stiffness of the upper portion of the unloading data, E_r is the reduced modulus, and A is the projected area of the elastic contact. This equation applies to tips with a wide range of shapes. E_r and E can, thus, be calculated by knowing S and A.

The Oliver and Pharr method is based on the notion that, at peak load, the material conforms to the shape of the indenter to some depth; if this depth can be established from the load-displacement data, the projected area of contact can be estimated directly from the indenter shape function with (3). The function F has to be determined experimentally prior to analysis:

$$A = F(h_c) \qquad (3)$$

where A is the projected area of contact and h_c is the contact depth.

The contact depth h_c is determined from the load-displacement data. In the Oliver and Pharr method, it is assumed that the unloading data is well described by a power law relation like (4)

$$P = \alpha(h - h_f)^m \qquad (4)$$

where α, m and h_f are constants of the material. The initial unloading slope S is then found by analytically differentiating this expression and evaluating the derivative at the peak load and displacement. Knowing S enables to know the contact depth h_c from the load-displacement data and, thus, the value of the projected area A. It is then possible to calculate E_r and E.

In addition to the modulus, the data can be used to determine the hardness, defined as the mean pressure the material will support under load. With this definition, the hardness H is computed from equation (5)

$$H = \frac{P_{\max}}{A} \qquad (5)$$

where A is the projected area of contact at peak load P_{max}. To be noted is that this definition is different from the conventional definition in which the area is determined by direct measurement of the size of the residual hardness impression. The values can, thus, be different. **(Oliver et al. 1992)**

During this study, microhardness tests were conducted using a Buehler Micromet 2104 with a Vickers indenter. Nanoindentation was done with a CSM Instruments Ultra nanoindentation tester with a Berkovich tip.

5.3. Sample presentation

Totally 8 samples were characterized: two were from a dissimilar metal narrow-gap weld (DM-NGW) mock-up manufactured in project and six samples were mock-up welds provided by EPRI.

5.3.1. Alloy 52 mock-up

This mock-up represents the typical new design for RPV nozzle/safe-end weld in the modern PWR design. The weld is made between the RPV LAS SA 508 and SS 304. The LAS is cladded with a first layer of 309L stainless steel (over alloyed) and a second layer of 308L. The filler metal is Inconel 52. The welding technique is TIG welding, using a 70%He + 30%Ar shielding gas (see Fig. 50).

Cross-section cuts are then made of the weld. They provide a view of all the materials and HAZ (see Fig. 51). A first cut from the NG-GTAW weld has not been post-weld heat treated and is called “As-welded” (AW). The other has been Heat-treated (HT) following the cycle presented in Figure 52. It consists of heating and maintaining the sample at 550°C for 20 h, then increasing shortly the temperature to 610°C for 10 h. It is the same PWHT done for the actual welds in PWR.

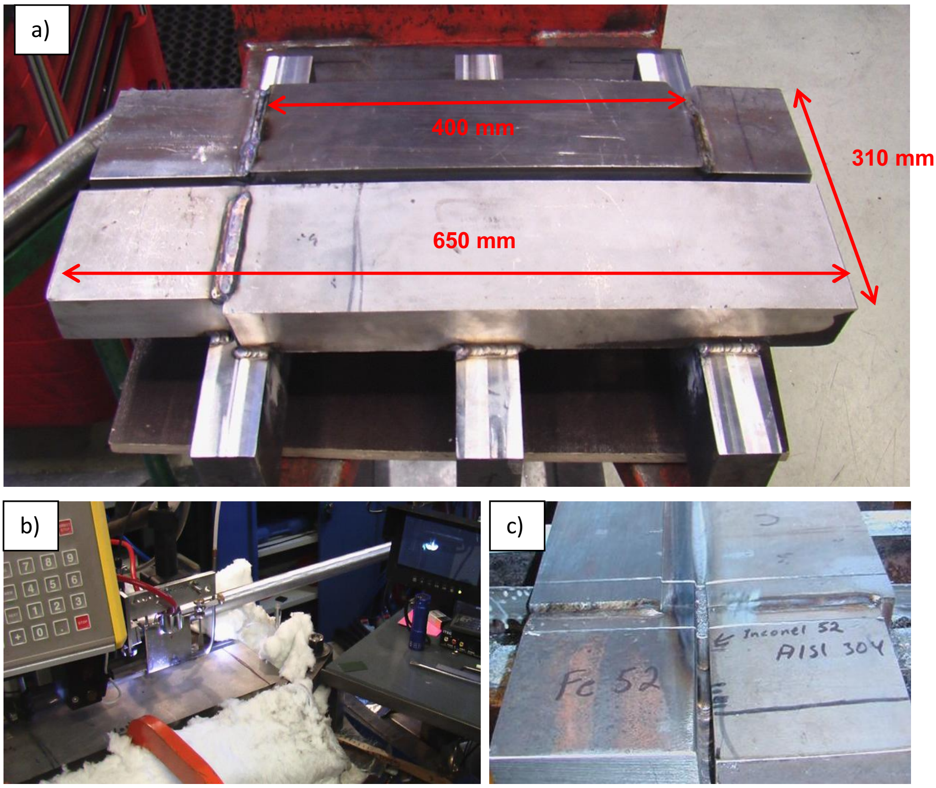

Fig. 50 Views of the Alloy 52 mock-up weld manufacturing, with a) the two base metal plates, b) the NG-GTAW welding torch in process (note the leading camera needed to see inside the groove) and c) the final weld.

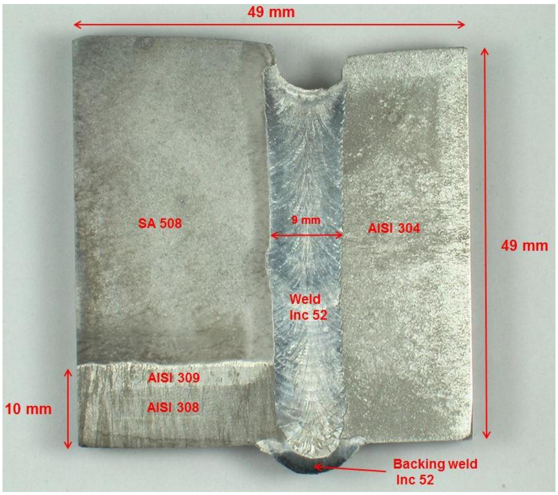

Fig. 51 Cross-section of the NG-GTAW weld. It has been etched to reveal better the macrostructure: materials, weld passes in Inconel 52 weld metal and HAZ of SA508 and SS304.

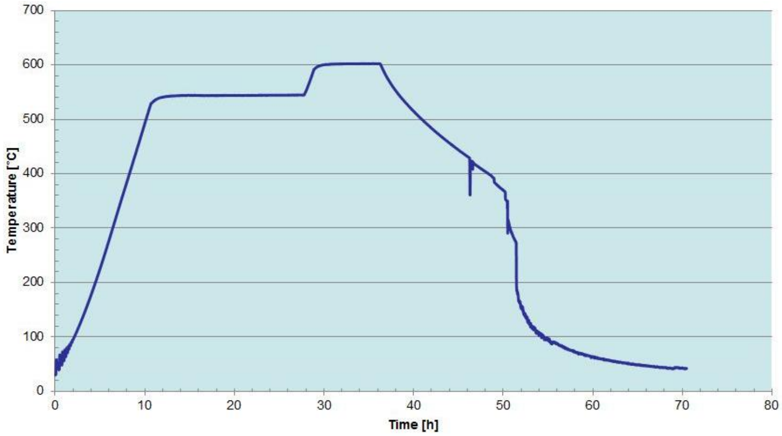

Fig. 52 Cycle of temperatures for the post-weld heat treatment done on the Alloy 52 mock-up sample.

For the AW cross-section, five samples were then cut using electro-discharge wire cutting (EDWC). They represent the main zones of interest (see Fig. 53). The same was done for the HT cross-section (see Fig. 54).

- Sample 1: SA 508/Inconel 52 interface
- Sample 2: Interface between SA 508, its SS cladding and Inconel 52
- Sample 3: Same as Sample 1. It was to be used for other tests if needed
- Sample 4: Inconel 52/SS 304 interface
- Sample 5: SA 508/Inconel 52/SS 304. It is destined to TEM analysis.

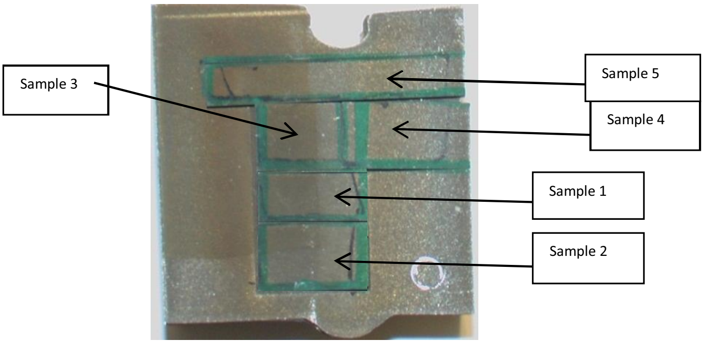

Fig. 53 Cutting of the samples from the cross-section of the AW Alloy 52 mock-up.

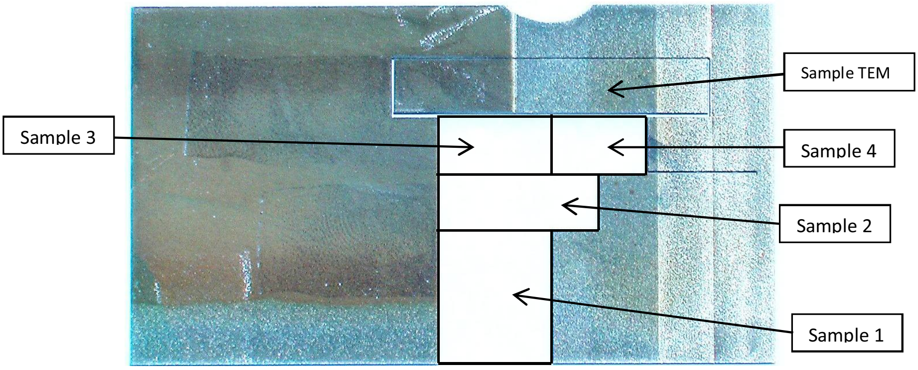

Fig. 54 Cutting of the samples from the HT cross-section.

- Sample 1: SA508 and SS cladding/Inconel 52 interface
- Sample 2: SA508/Inconel 52 interface
- Sample 3: SA508/Inconel 52 interface
- Sample 4: Inconel 52/SS304 interface
- Sample 5: SA508/Inconel 52/SS304. Sample for TEM characterization.

The samples characterized in this study were the sample 1 from the AW cross-section and the sample 3 from the HT cross-section. They both show the interface between SA508/Inconel 52 as well as the HAZ of the LAS.

5.3.2. EPRI samples

These samples have been made out of mock-up welds previously studied by EPRI. They all show different weld designs involving Alloy 690 for nuclear applications. They are much broader samples than the Alloy 52 mock-up ones.

5.3.2.1. CIEMAT samples

The two CIEMAT samples are both based on the same weld design: two plates of Alloy 690 (50 mm thick, 400 mm long) are welded with a half-V groove (30°) (see Fig. 55).

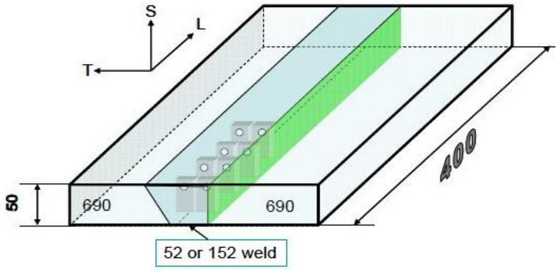

Fig. 55 Weld design for the CIEMAT samples: two Alloy 690 plates welded with a half-V groove. The weld metal is either Inconel 52 or 152, and the welding technique is either GTAW or SMAW, respectively.

The plates are hot-rolled plates produced by Aubert&Duval and processed by Industeel (Arcelor group). They have been hot-rolled, solution-annealed at 1070°C for 17 min followed by water cooling and tempered at 710°C for 10 h followed by air cooling. The samples are cross-sections from the weldment, showing the Alloy 690/Inconel 52 or 152/Alloy 690 interfaces.

- Sample #02477: CIEMAT weld HT WP547 GTAW (see Fig. 56)
  It was made with automatic TIG Welding using an Inconel 52 wire. It was heat-treated at 615°C for 16 h.

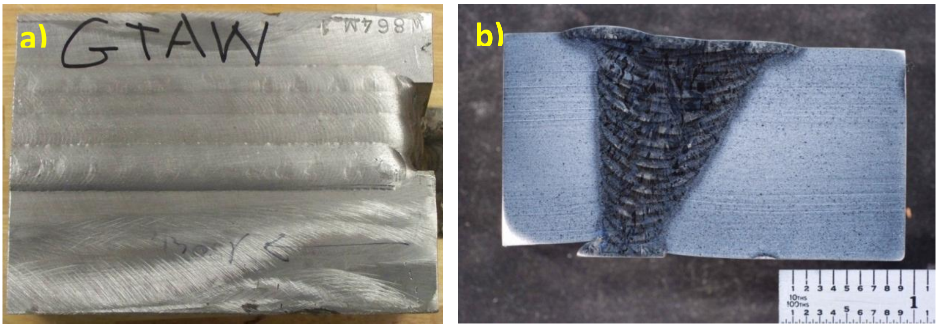

Fig. 56 Views of the sample CIEMAT GTAW: a) broad weld from above and b) the sample which is a transversal cut of the weld.

- Sample #02477: CIEMAT weld HT WP547 SMAW (see Fig. 57)
  It was made with manual metal arc welding (thicker weld passes), using Inconel 152 as filler metal. It was heat-treated at 615°C for 16 h.

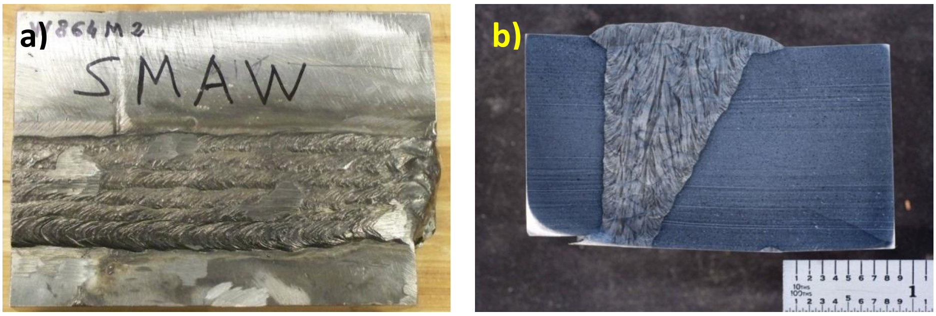

Fig. 57 Views of the sample CIEMAT SMAW: a) broad weld from above and b) the final sample that has been cut transverse from the weld.

5.3.2.2. Sample #02530: MHI plate

Two plates of SA508 Gr2 and Alloy 690 are welded using SMAW and Inconel 152 weld metal, and a buttering layer on the LAS side. The sample is a cross-section of the weld (see Figs. 58 and 59). The Alloy 690 plate was manufactured by ThyssenKrupp VDM. It has been hot rolled, solution annealed at 1030°C for 1 h and stabilization annealed at 716°C for 16 h.

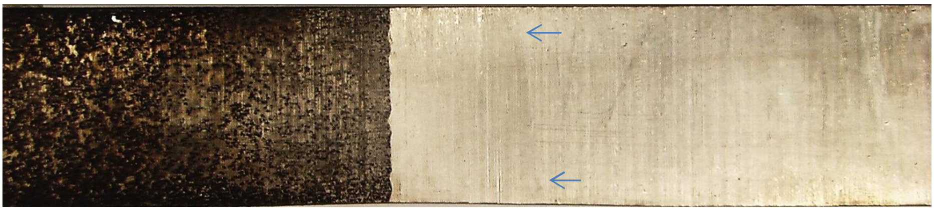

Fig. 58 Global view of the weld, showing the SA508 plate (dark), the weld metal and the Alloy 690 plate (arrows mark the interface between Inconel 152 weld metal and Alloy 690 base metal).

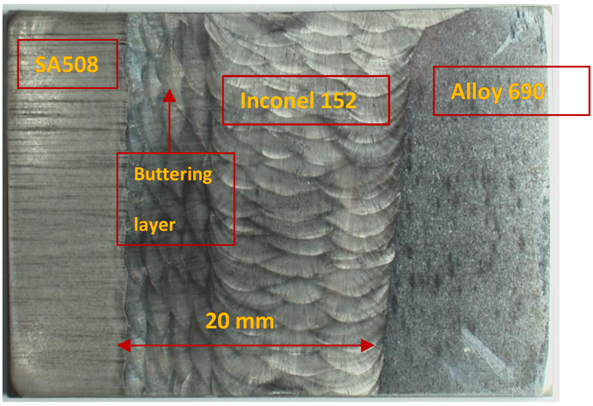

Fig. 59 MHI plate sample. Cross-section of the weldment. It has been etched to reveal the macrostructure: SA508, weld-passes in Inconel 152, Alloy 690. The different orientation of the weld-passes reveals the buttering layer on the SA508 side of the weld. It is made to limit the diffusion at the interface.

The weld was PWHT at 515°C for 20 min then 715°C for 10 h.

5.3.2.3. *Sample #02435: GTAW 19508A*

It is a narrow-gap weld between two plates of Alloy 690 using Inconel 52M weld metal and Inconel 52M overlay (see Fig. 60). It was not PWHT. The sample is a cross-section of the weldment (see Fig. 61). Figure 62 shows the details of the welding parameters used for this weld.

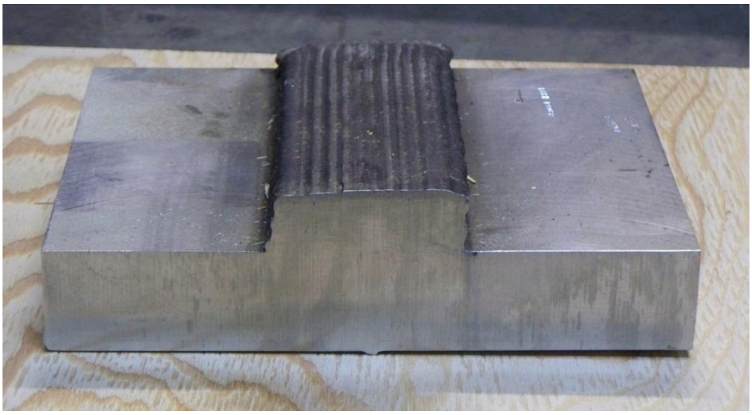

Fig. 60 Global view of the GTAW 19508A weld, showing the two plates and the weld overlay.

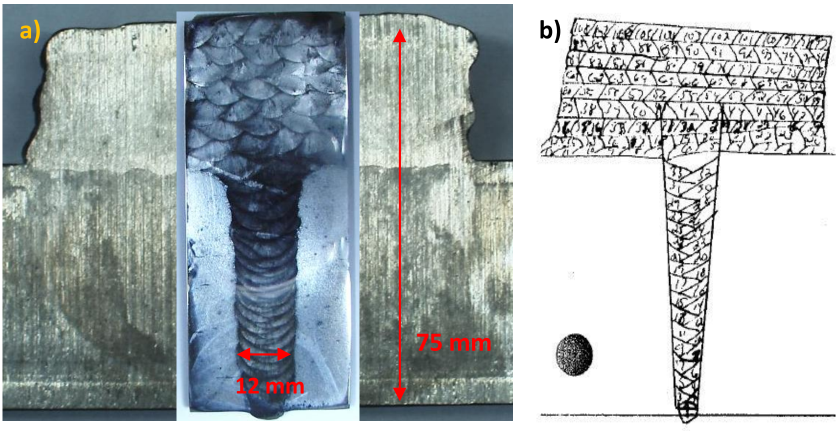

Fig. 61 GTAW 19508A sample, cut from a cross-section of the weldment: a) the sample has been etched to reveal the weld passes corresponding to b) the scheme of the weld passes.

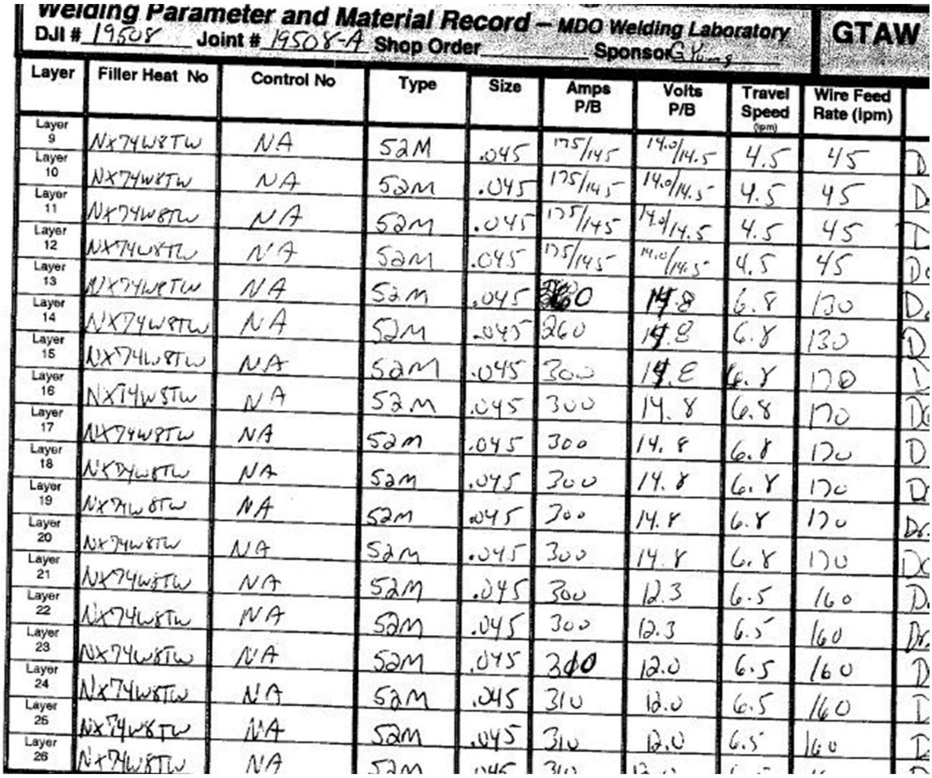

Welding Parameter and Material Record – MDO Welding Laboratory **GTAW**

DJI # 19508 Joint # 19508-A Shop Order ________ Sponsor G Y[illegible]

Layer	Filler Heat No	Control No	Type	Size	Amps P/B	Volts P/B	Travel Speed (ipm)	Wire Feed Rate (ipm)
Layer 9	NX74W8TW	NA	52M	.045	175/145	14.0/14.5	4.5	45
Layer 10	NX74W8TW	NA	52M	.045	175/145	14.0/14.5	4.5	45
Layer 11	NX74W8TW	NA	52M	.045	175/145	14.0/14.5	4.5	45
Layer 12	NX74W8TW	NA	52M	.045	175/145	14.0/14.5	4.5	45
Layer 13	NX74W8TW	NA	52M	.045	260	14.8	6.8	130
Layer 14	NX74W8TW	NA	52M	.045	260	14.8	6.8	130
Layer 15	NX74W8TW	NA	52M	.045	300	14.8	6.8	170
Layer 16	NX74W8TW	NA	52M	.045	300	14.8	6.8	170
Layer 17	NX74W8TW	NA	52M	.045	300	14.8	6.8	170
Layer 18	NX74W8TW	NA	52M	.045	300	14.8	6.8	170
Layer 19	NX74W8TW	NA	52M	.045	300	14.8	6.8	170
Layer 20	NX74W8TW	NA	52M	.045	300	14.8	6.8	170
Layer 21	NX74W8TW	NA	52M	.045	300	12.3	6.5	160
Layer 22	NX74W8TW	NA	52M	.045	300	12.3	6.5	160
Layer 23	NX74W8TW	NA	52M	.045	300	12.0	6.5	160
Layer 24	NX74W8TW	NA	52M	.045	310	12.0	6.5	160
Layer 25	NX74W8TW	NA	52M	.045	310	12.0	6.5	160
Layer 26	NX74W8TW	NA	52M					

Fig. 62 Welding parameters for the GTAW 19508A sample. Different heat inputs are used for layers 9-12, layers 13-14, layers 15-20 and layers 21-26 in the NGW.

The heat input Q (kJ/cm) can be calculated from these parameters, according to the following equation:

$$Q = \frac{V \times I \times 60}{S \times 1000} \times Efficiency$$

with I = welding current (A), V = arc voltage (V), S = travel speed (cm/min). The efficiency depends on the welding technique. Usually, it is 0.75, 0.9 and 0.6-0.8 for shielded metal arc, gas metal arc welding and submerged arc welding, and gas tungsten arc welding, respectively.

For pulsed welding, I (or V) = I (or V) peak x %time peak + I (or V) back x %time back.

Considering here a 50% peak + 50% background pulse for the layers 9-12, and an GTAW efficiency of 0,7, four different heat inputs have been used for this weld:

- layers 9-12: Q= 7 kJ/cm
- layers 13-14: Q= 9,5 kJ/cm
- layers 15-20: Q=10,9 kJ/cm
- layers 21-26: Q= 9,3 kJ/cm

For the layers 13-14 and 21-26, the heat input is almost the same, but higher current and lower voltage is used for the layers 21-26, resulting in larger weld pool and lower penetration. Associated to higher wire feed rate, this combination should give large but thin weld passes, which are good for NGW, as it requires good side penetration and melting the overlapping passes.

5.3.2.4. Sample #02540 ENSA weld mock-up

An Alloy 690 plate is welded to a carbon steel plate with GTAW using Inconel 52 weld metal and Inconel 52M buttering. No PWHT was applied. The Alloy 690 plate has been manufactured by Faulenbach Schmiedetechnik GmbH. It has been forged, solution annealed at 1036°C for 1 h followed by water cooling and tempered at 720°C for 8 h followed by air cooling.

Figure 63 shows several views of the broad weld configuration and Figure 64 shows the sample cut from the weld and etched.

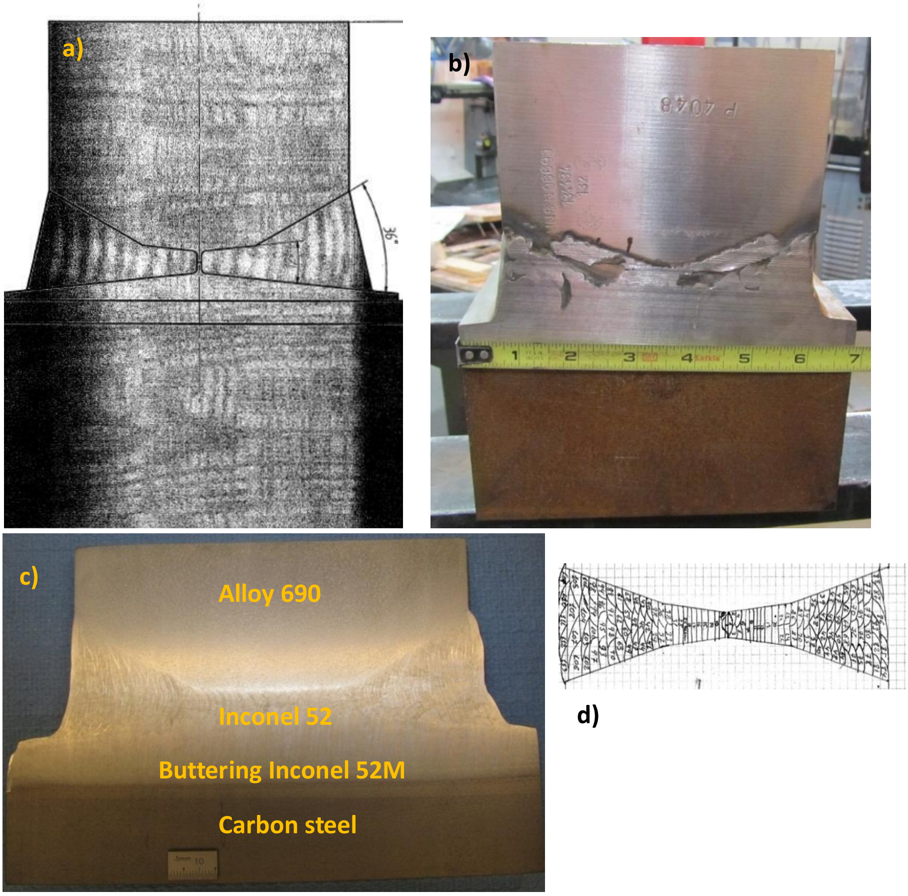

Fig. 63 Views of the ENSA weld mock-up with a) schematic of the grooves and components, b) view of the broad sample, c) view of the weld polished and etched and d) schematic of the weld passes.

Fig. 64 View of the sample cut from the weld and prepared for characterization.

5.3.2.5. Sample #02432 PG&E mock-up

This is a CRDM mock-up weld. An Alloy 690 pipe is welded using an Inconel 52M J-groove weld to a 308L cladded SA533 Gr.B plate. No information was available concerning the welding technique and the origin of the Alloy 690 pipe. It is supposed, however, that the pipe was extruded. Figure 65 shows several views of the sample.

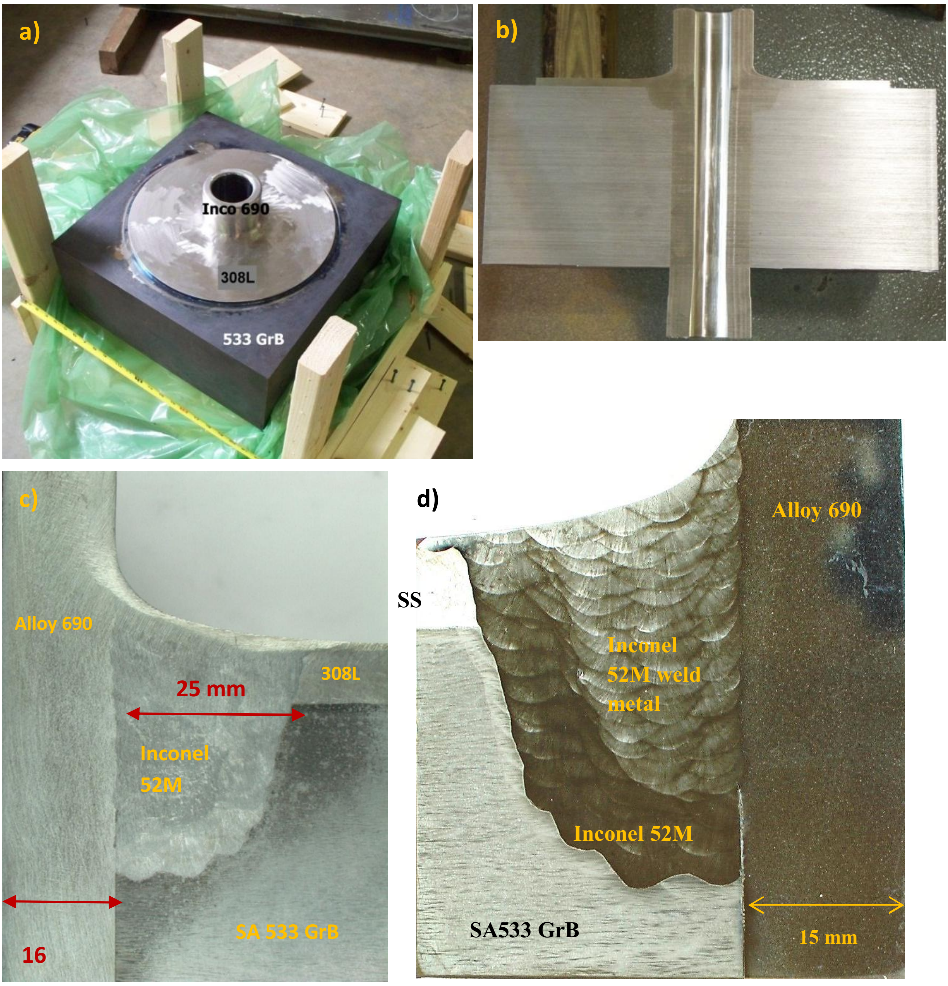

Fig. 65 Views of the sample PG&E mock-up with a) broad sample showing the Alloy 690 pipe inside the LAS SA533 GrB plate with the SS 308L cladding, b) the sample cut in half, c) a closer view of the sample cut in four showing Inconel 52M weld metal and d) the sample cut, polished and etched.

The pipe has probably been put into the LAS plate with the shrink-fitting technique. It uses the thermal expansion of both materials to make the joint. The Inconel 52M J-groove weld ensures that the cladding remains intact and protects the joint between the Alloy 690 pipe and the LAS plate. It can be seen that there is a lack of fusion in between the pipe and the J-groove weld buttering.

5.4. Sample preparation

Sample preparation is necessary to reveal the microstructure of the samples. In addition, the surface roughness affects significantly the results of all the hardness tests, especially for nanoindentation and EBSD mapping. All specimens have some degree of surface roughness. The rougher the surface, the more variable will the results be. A suitable choice of maximum load will be required to suit the surface roughness of the specimen. A usual rule is that the surface roughness of a sample should not be more than 5% of the indentation depth. In addition, the surface of the specimen must be free from grease, finger prints, dust, and preferably free of oxide layers. Ultrasonic cleaning may be required. Any polishing compound residue has to be removed. Even washing with acetone can sometimes leave an oily film on the surface which affects the results.

The Alloy 52 NG mock-up samples were first put into a conductive polymer matrix adapted to SEM observation. All samples were then grinded to remove the residual strain resulting from cutting. It was assumed that a four time 90° rotation on a 320 grinder is enough to remove any remains of strains. Then, the grinding was done using 800, 1200, 2400 grit papers, each time with one 90° rotation. Finally, samples were polished using 3 μm and 1 μm diamond paste. The samples were rinsed each time with ethanol to remove particles and to avoid corrosion of the LAS when present.

After the polishing, the samples were etched using a 2% Nital solution to reveal the microstructure of the LAS. After the optical characterization of the LAS, the samples were polished again and etched with aqua regia (60% HCl + 30% HNO_3) to reveal the microstructure of the Inconel alloys and SS.

6. Results

The results are presented for each sample separately, beginning by the microstructure characterization of the different zones of interest and following by the hardness tests. A comparison between the samples is made further.

The main features observed are the SA 508 HAZ, the interface between SA 508 and Inconel weld metals, the microstructures of Inconel weld metals and of Alloy 690 base metal.

6.1. Alloy 52 mock-up AW sample 1

This sample shows the interface between the RPV LAS SA508 and Inconel 52 weld metal in the as-welded condition.

6.1.1. Microstructures

6.1.1.1. LAS microstructure

Figure 66 shows the microstructures of the SA508 HAZ and base material. It shows the characteristics of the HAZ of a LAS, with the four distinct regions: i) grain coarsening near the fusion line, ii) grain refining when moving away from the fusion line, iii) partial grain refining and iv) base material further away from the interface.

The microstructure of the base material is upper bainite. When going closer to the fusion line, the material experiences higher temperatures during welding. Thus, a higher fraction of austenite forms. After cooling, the austenite turns into a fine distribution of ferrite grains and bainite. Along the fusion line, the temperature is at its highest. It triggers the growth of austenite grains and forms the grain coarsening zone.

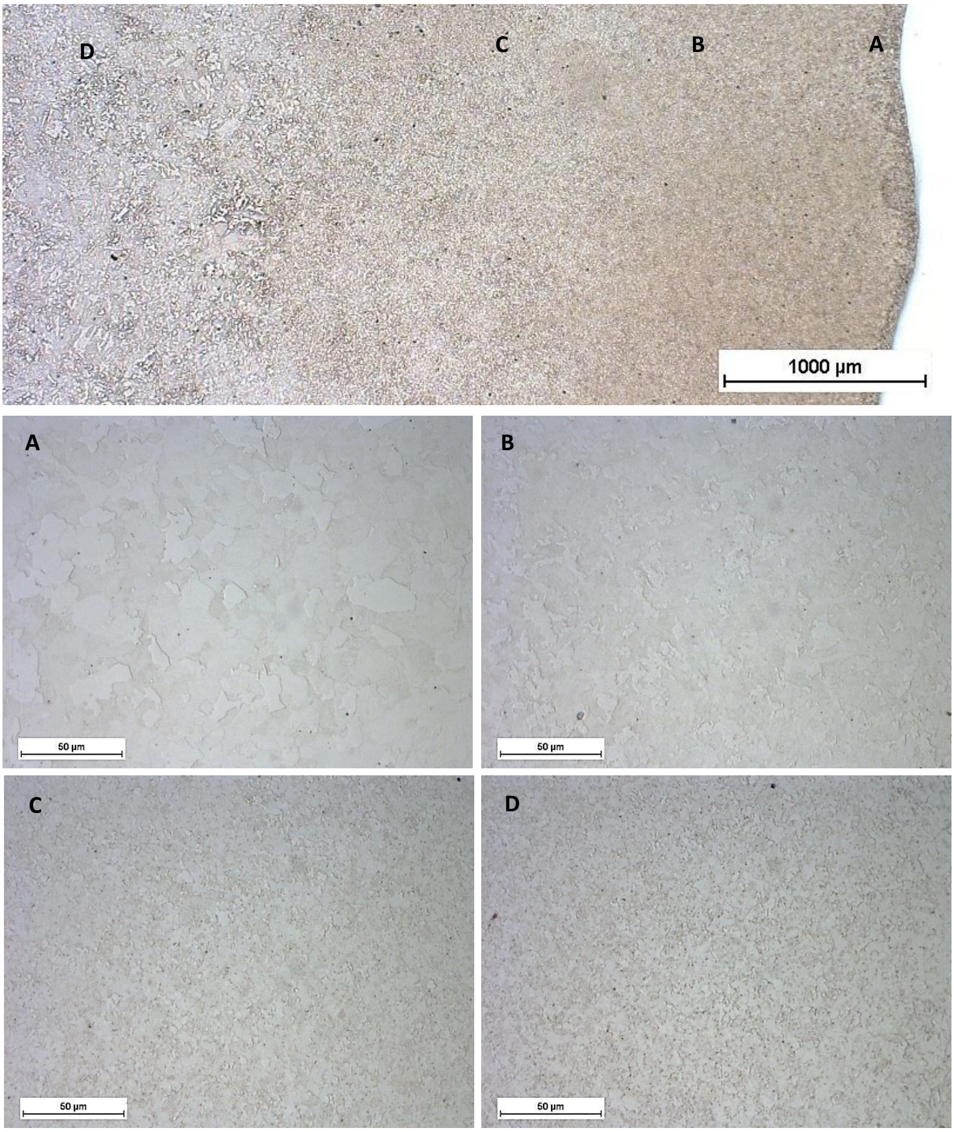

Fig. 66Microstructures of the SA508 HAZ and base material: A) Grain coarsening, B) grain refining, C) partial grain refining and D) base material.

6.1.1.2. Fusion line

Figure 67 a) shows the fusion line between SA508 and Inconel 52 when etched with Nital. Only the LAS is affected. A carbon-depleted zone (CDZ) can be observed. As seen in the literature review, carbon migrates at high temperature to the weld metal due to composition gradients. As a result, sole ferrite grains form from the austenite. It is about 0.01-0.02 mm wide zone.

Figure 67 b) shows the Inconel side of the fusion line. The GBs seem mainly Type I. It seems that a layer of about 0.05 mm is free of precipitates along the fusion line. It can be an unmixed-zone (UMZ) in which precipitates are dissolved, according to the literature. The columnar dendritic structure starts after this layer.

Figure 67 c) shows what seems to be a Type II boundary along the fusion line. It is, however, closer to the interface (about 0.01 mm) than usual Type II boundaries (0.1 mm).

It is rather difficult to say if the grains are continuous across the interface since the two materials react differently to the etchants. Since the interface is ferritic/austenitic, discontinuity is to be expected.

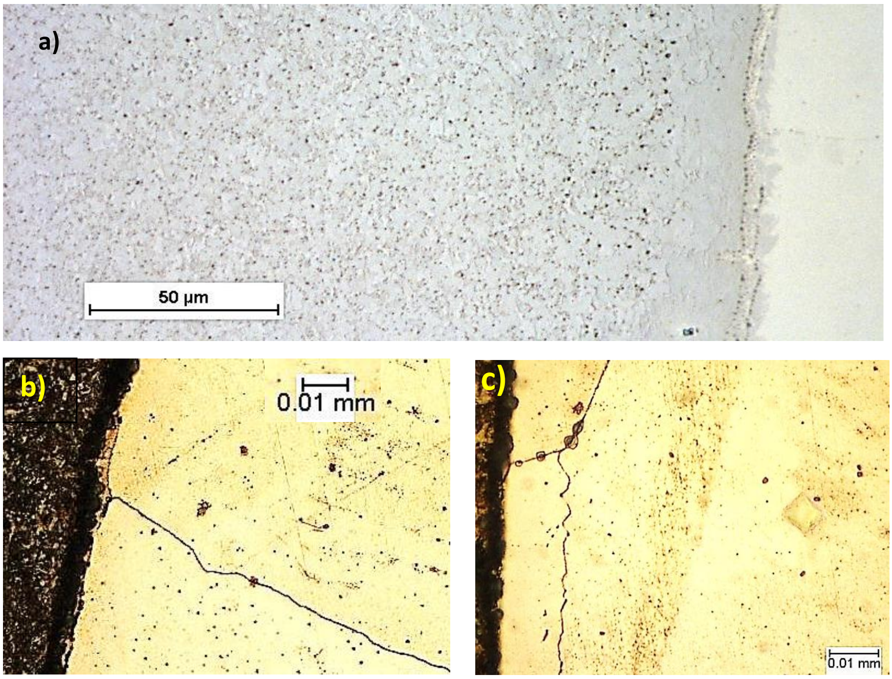

Fig. 67 Microstructure of the SA508/Inconel 52 fusion line, with: a) CDZ in the LAS side, b) a layer free of precipitates on the weld metal side along the fusion line and c) a possible Type II boundary.

6.1.1.3. Inconel 52 weld metal

Figure 68 shows a global view of the Inconel 52 weld metal and the weld passes.

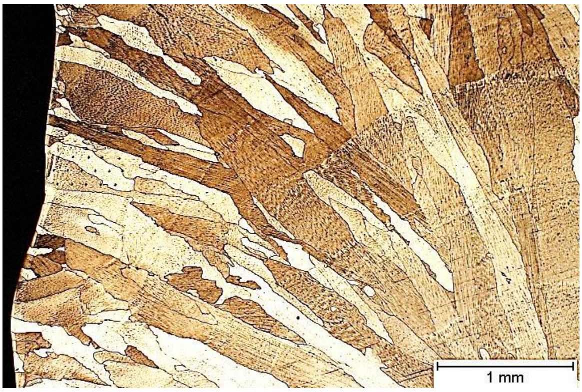

Fig. 68 Weld metal Inconel 52. The grains start to grow perpendicular to the interface, and then their orientation follows the heat gradient in the weld passes.

Figure 69 a) shows the microstructure of the Inconel 52 weld metal. It consists of columnar dendrites. The primary arm spacing is of about 0.01 mm (see Fig. 56 b).

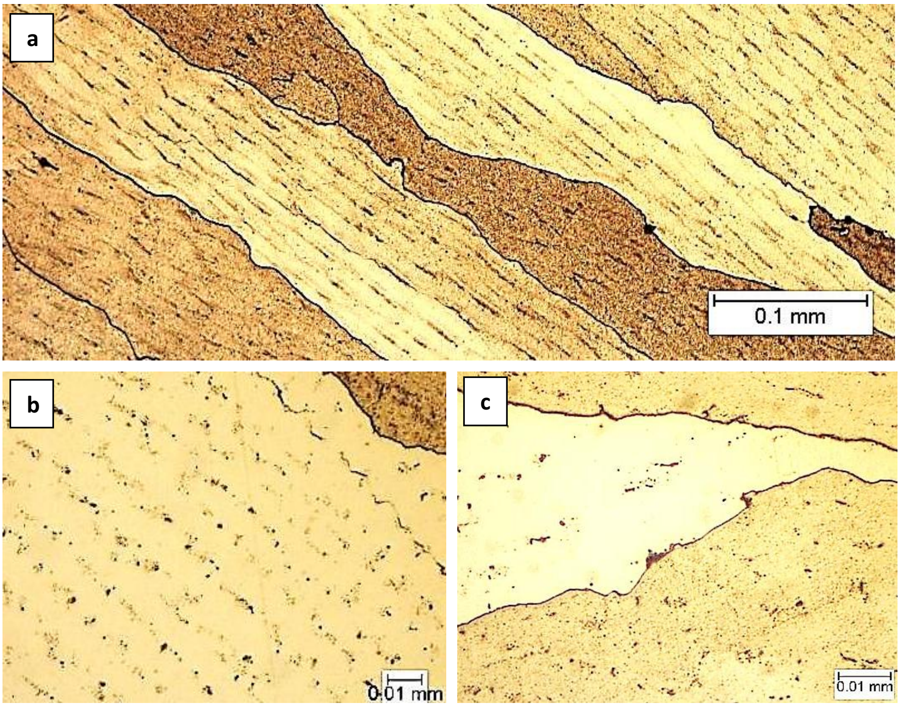

Fig. 69 Microstructure of the Inconel 52 weld metal, with: a) global view of the columnar dendrite grains, b) primary arm spacing and c) a closer view.

6.1.2. Microhardness

Tests were conducted across the sample, normal to the interface, with a 1 mm step and a 0.5 kg load. It is aimed at characterizing the influence of the SA508 HAZ. Figure 70 shows the results of the testing. Microhardness tests were done to characterize further the hardness at the interface. They were done with a 0.2 mm step and a 0.1 kg load. The results are shown in Figure 71 and a view of the indents in Figure 72.

Hardness increases from about 190-200 HV in the SA508 base material to 270 HV in the HAZ. It then drops to 230 HV in the coarse-grain layer and to about 210-220 HV in the weld metal.

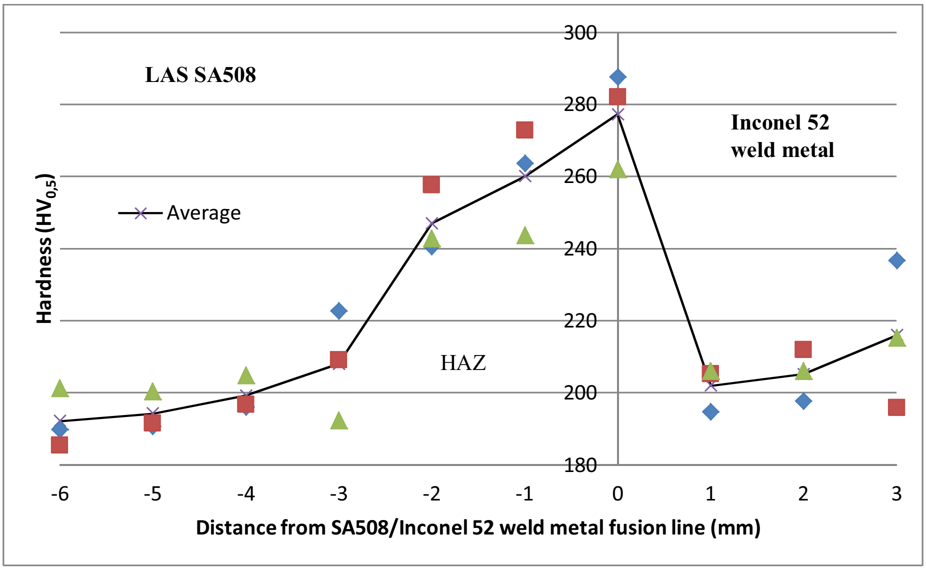

Fig. 70 Hardness profile across the sample. The hardness increases progressively in the LAS HAZ due to grain refining.

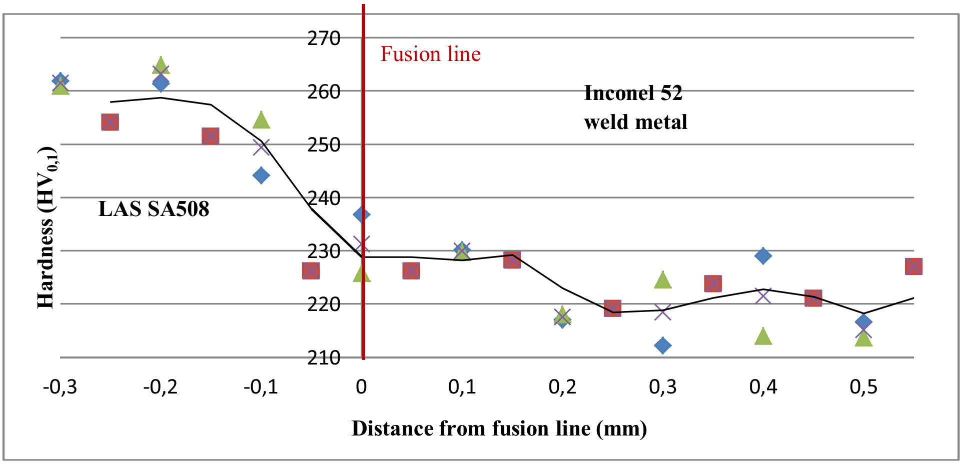

Fig. 71 Hardness profile across the fusion line. The black line is the average from the 3-line measurements. The hardness decreases in the LAS at the fusion line because of the coarse-grain layer and CDZ.

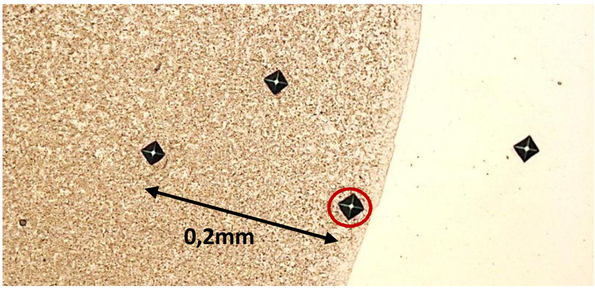

Fig. 72 Microscopic view of second line loadings, and the position of the X = -0,05 mm loading near the fusion line.

Nanoindentation tests were conducted to determine the influence of the CDZ on the mechanical properties. The typical test is made with a 3 line staggered matrix, where indents are separated by 30 µm steps in order to avoid deformation effects of the surrounding indentations. The second layer is moved 15 µm forward in order to cover more space and be sure to indent the supposed carbon-depleted layer observed before.

The parameters were:

- Acquisition rate: 10 Hz
- Maximum load: 20 mN
- (Un)Loading rate: 30 mN/min
- Pause: 15 s

- Loading: linear

It was assumed that the value from the staggered second line can be used to complete those of both first and third line. The results of one test are shown in Figure 73 and the corresponding indents in Figure 74.

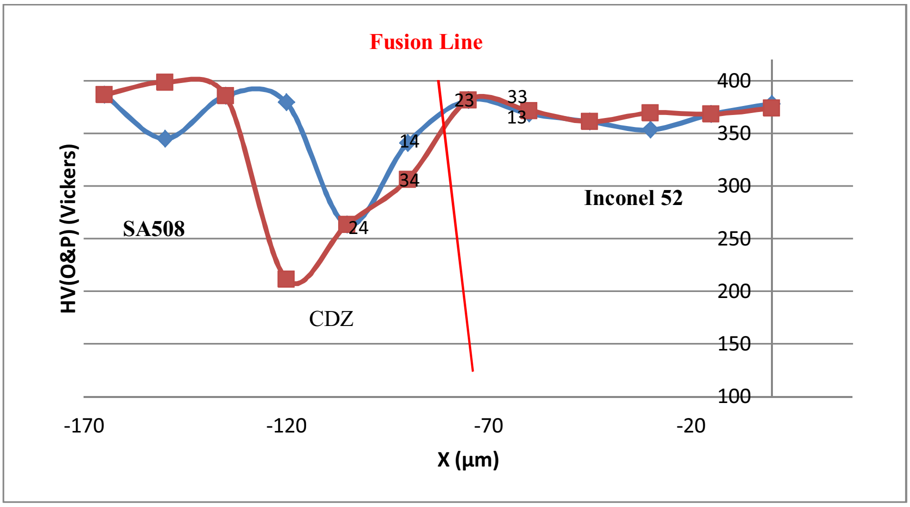

Fig. 73 Nanohardness profile across SA508/Inconel 52 interface.

In Figure 73, the fusion line is represented by relating the indentation abscissa and the position of the fusion line relatively to the indentations on the picture below. A drop in hardness can be seen. The hardness values do not correspond to the microhardness values of the Vickers tests, which is normal. The values are calculated with the Oliver&Pharr method.

It thus shows that the soft layer is in the carbon steel, and is about 40 µm thick. This is more than what can be seen on the pictures, where the carbon-depleted layer seems to be about 10-20 µm thick.

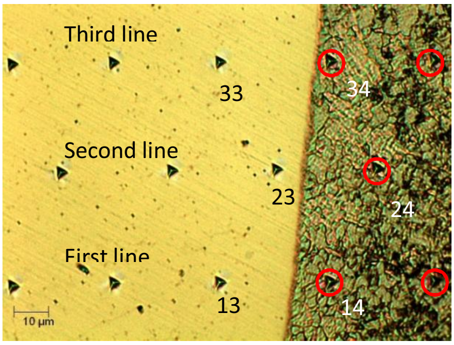

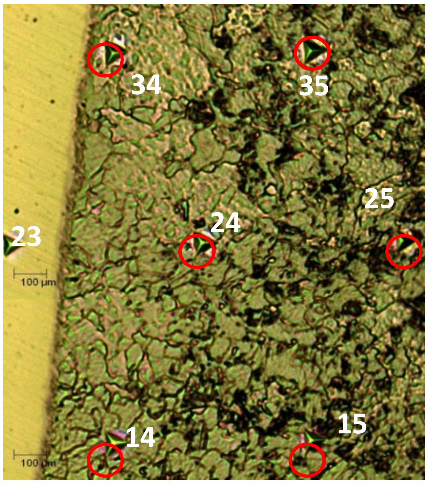

Fig. 74 View of the indentation across the CDZ in the LAS SA508 side of the weld (dark-etched).

6.2. Alloy 52 mock-up HT sample 3

As for the previous sample, it shows the interface between the LAS SA508 and Inconel 52 weld metal. This sample is taken from the cut that has been PWHT.

6.2.1. Microstructures

The microstructures show the HAZ of SA508, then the fusion between SA508 and Inconel 52 weld metal and finally the Inconel 52 weld metal.

6.2.1.1. LAS microstructure

Figure 75 shows the microstructure of the SA508 HAZ after PWHT. The features seem the same as in the AW sample, with partial grain refining, grain refining and grain coarsening when going from the base material to the fusion line. PWHT does not seem to affect the HAZ microstructures.

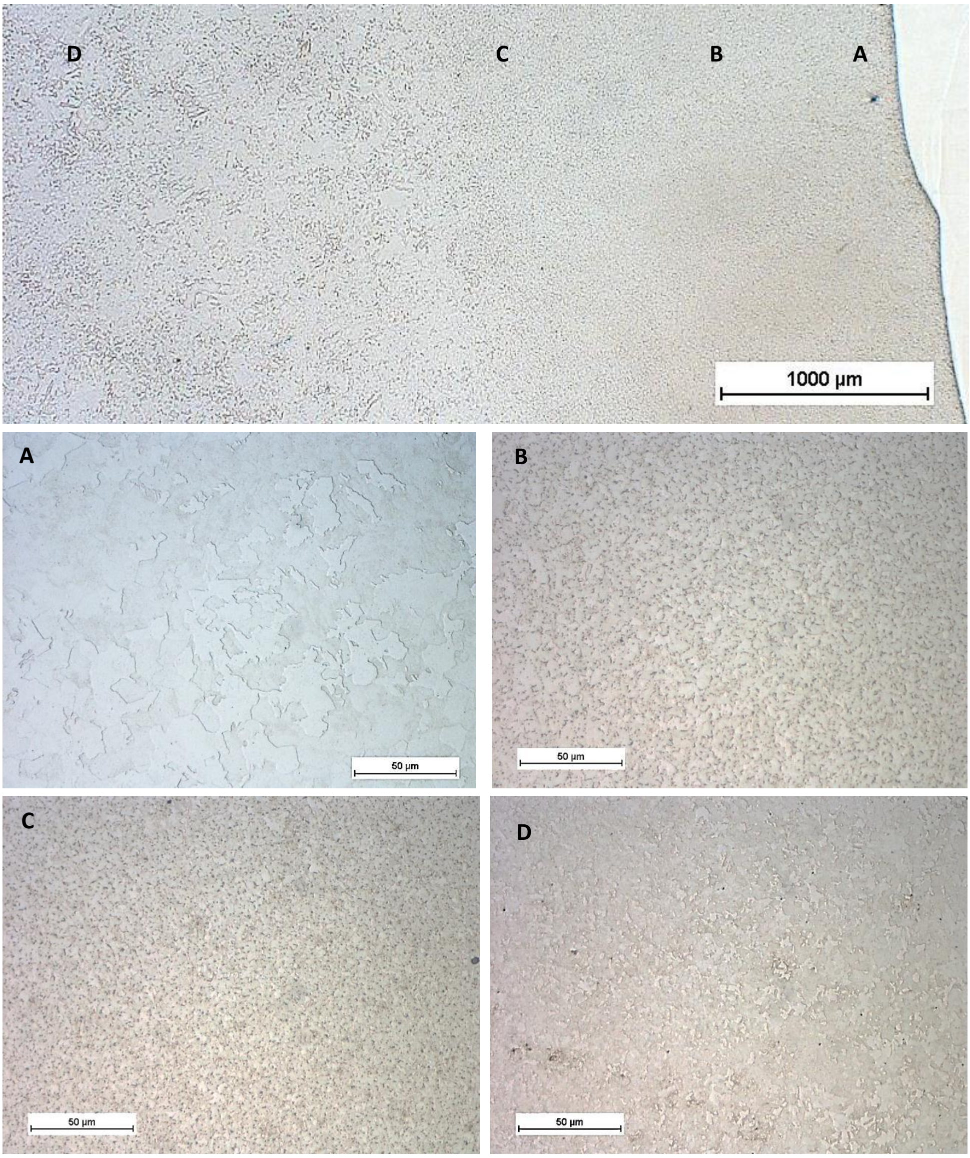

Fig. 75 Global view of the HT LAS microstructure: A) grain coarsening, B) grain refining, C) partial grain refining and D) base material.

6.2.1.2. Fusion line

PWHT affects, however, the microstructure at the interface, as shown in Figure 76.

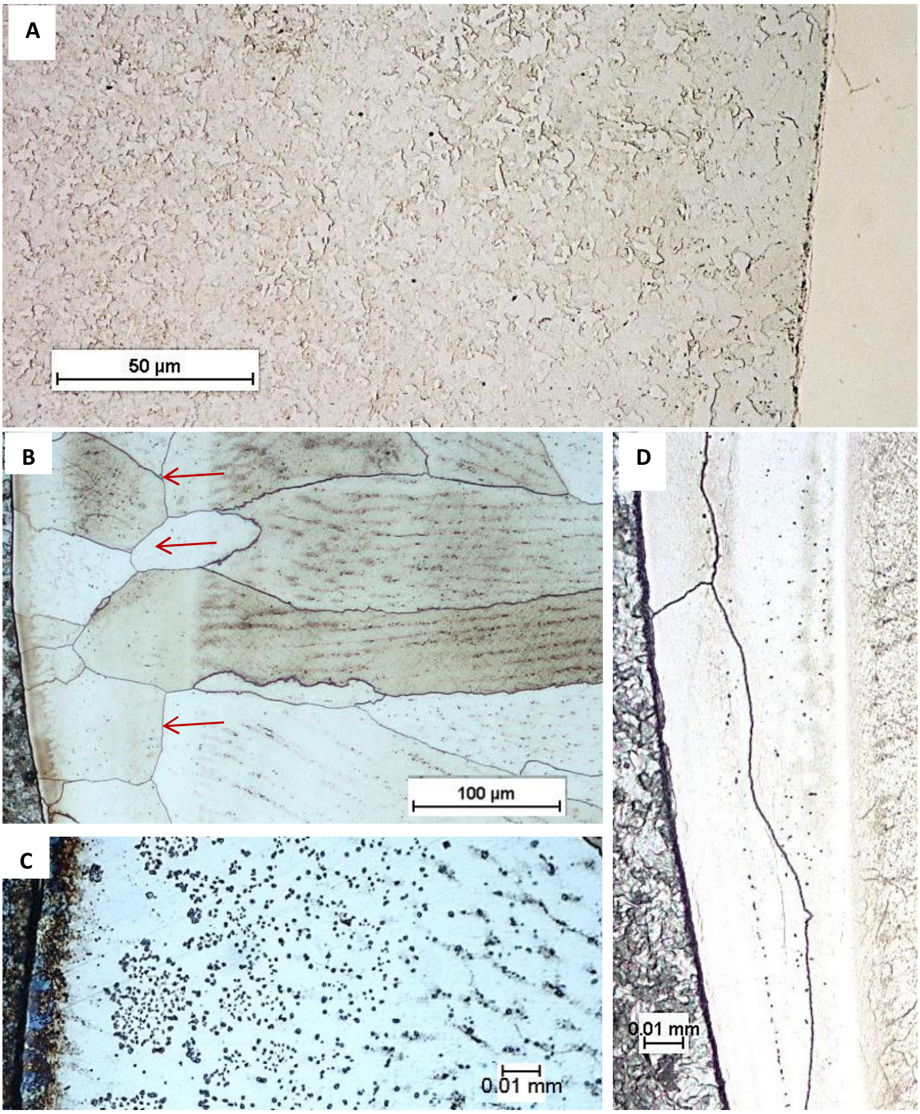

Fig. 76 Microstructure of the PWHT SA508/Inconel 52 interface: a) CDZ on the SA508 side and the dark etched fusion line, b) Inconel 52 weld metal along the fusion line, c) extensive precipitation in the weld metal close to the fusion line and d) a Type II boundary.

Figure 76 a) shows the interface when only the LAS is etched by Nital. A CDZ can be observed and it is much wider than in the AW condition. It is about 0.1 mm wide. In addition, the fusion line itself is much darker etched than in the AW sample, probably due to a higher carbon content.

Figure 76 b) and c) show that many precipitates have formed in the weld metal side of the fusion line at approximately 50 μm from the interface. Their composition is not known, yet, but they are probably chromium carbides. In addition, Type II boundaries appear in the Inconel 52 weld metal at about 100 μm from the fusion line.

Figure 76 d) shows what looks like a Type II boundary. It is, however, much closer to the interface (about 10 μm) than what is reported in the literature (about 100 μm).

6.2.1.3. Inconel 52 weld metal

Figure 77 shows a global view of the Inconel 52 weld metal after PWHT. The direction of the grains does not change.

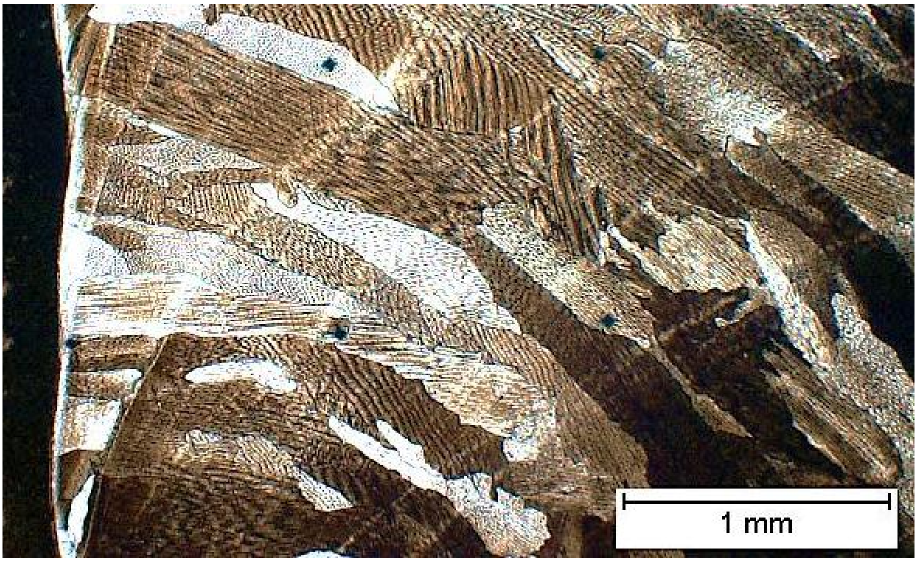

Fig. 77 Global view of the Inconel 52 weld metal after PWHT.

Figure 78 shows closer views of the weld metal microstructure. The previous columnar dendrites seem to have evolved in a cellular structure during the heat treatment.

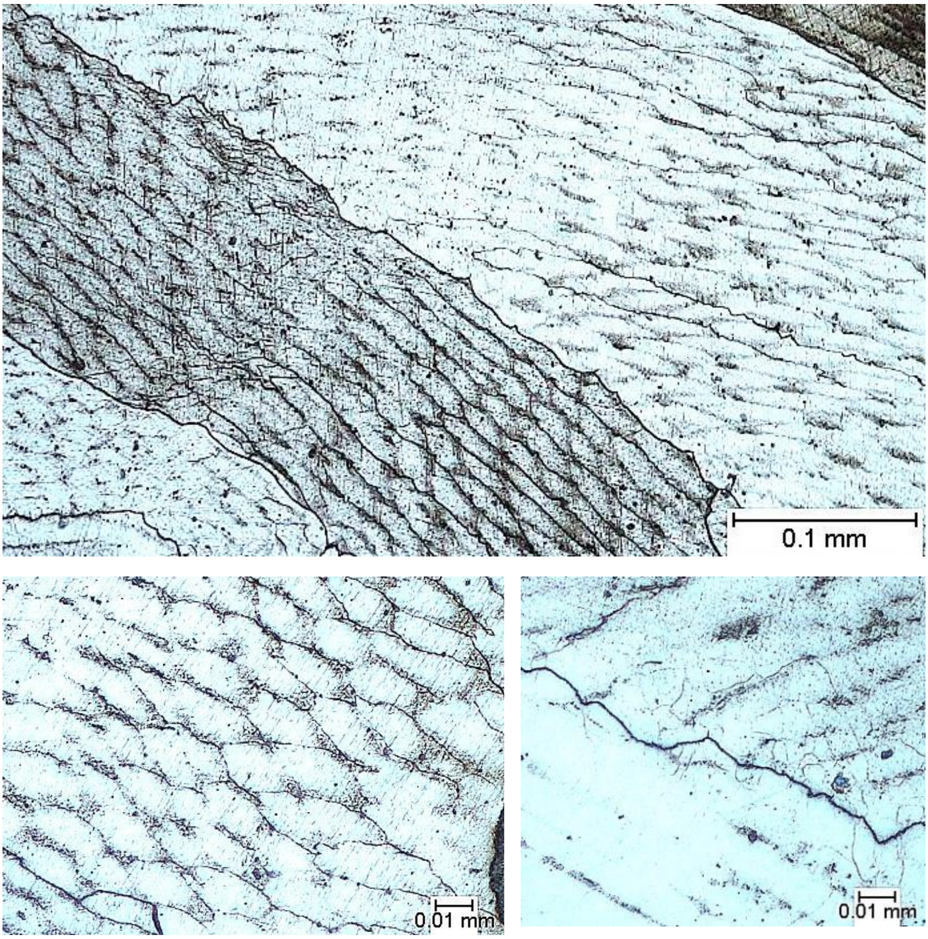

Fig. 78 Microstructures of Inconel 52 weld metal after PWHT: a) several grains, b) close view of the cellular structure and c) close view of a solidification GB.

6.2.2. Microhardness

For the first tests, the step was 1 mm and the load 0.5 kg. The results are shown in Figure 79. Hardness is about 170 HV in the SA508 base material. It then increases in the LAS HAZ due to grain refining to about 240 HV and drops to 210-220 HV in the weld metal. These hardness values are lower than in the AW sample. It comes probably from tempering and grain coarsening.

It is interesting to note that the values at the fusion line are very scattered. They correspond to the three positions across the fusion line: the lower is on the SA508 side and must correspond to the grain-coarsening zone (210 HV), the intermediate value is precisely on the fusion line (240 HV) and the highest is on the Inconel 52 side (260 HV). This is related to the extensive precipitates present after PWHT.

Tests with 0,1 mm step and 0,1 kg load were conducted. The results are shown in Figure 80 and confirm the previous ones. After the hardness reaches a maximum (250-270 HV) in the refined microstructure of the SA508 HAZ, it decreases in the grain-coarsening layer and the CDZ layer along the fusion line (to about 190–200 HV). When reaching the austenite side of the weld, however, the hardness increases drastically (up to 340 HV) and then drops (230 HV) before returning to the value of the weld metal (240 HV).

This phenomenon has been extensively observed at ferritic/austenitic interfaces of DMWs. As seen before, a common mechanism is the migration of carbon driven by the difference in chromium content between the LAS and the Ni-base alloy. This leads to the formation of the CDZ on the SA508 side and to chromium carbides on the Inconel 52 side. It happens quite close to the interface (0.1 mm) due to the low diffusivity of carbon in nickel.

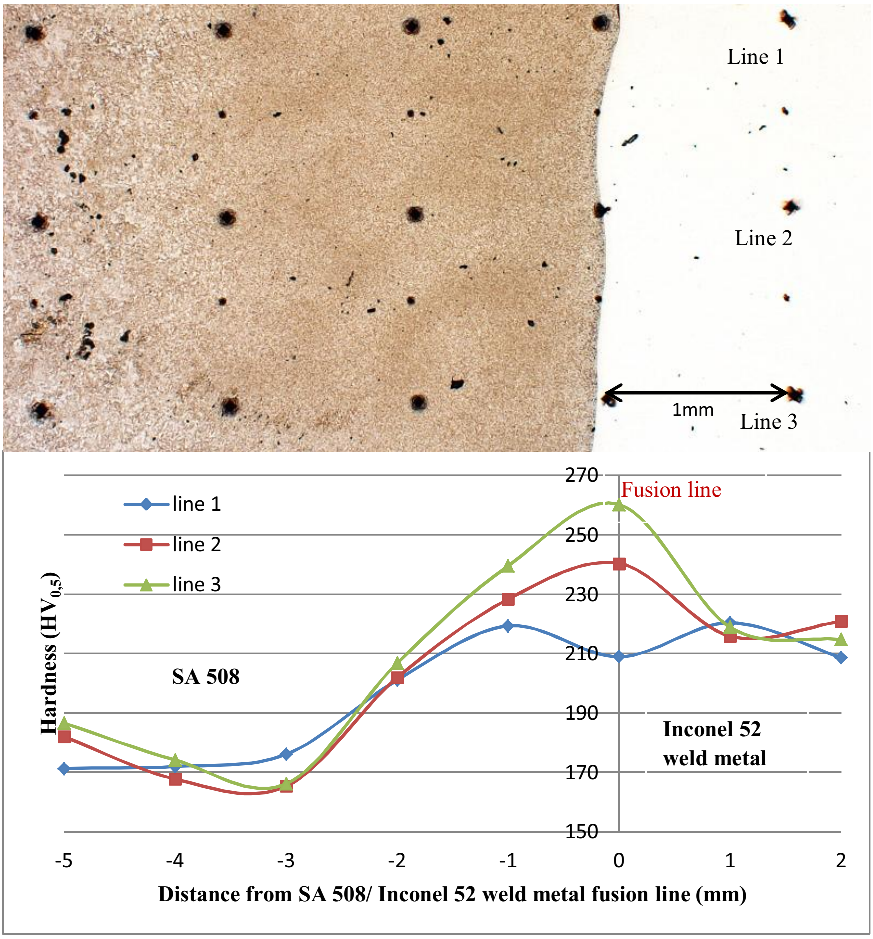

Fig. 79 Microhardness profile across the HT SA508/Inconel 52 interface and the corresponding indentations. It shows the increasing hardness in the LAS HAZ and the rapid change in hardness just across the fusion line.

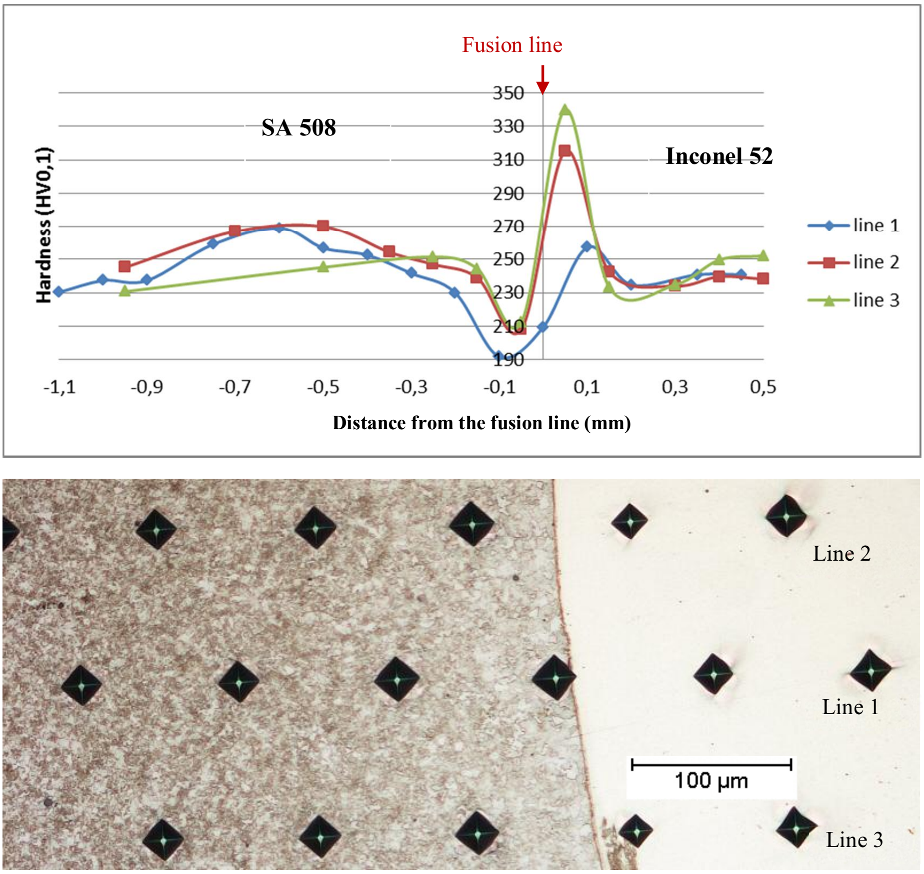

Fig. 80 Microhardness profile across the PWHT SA508/Inconel 52 interface and the corresponding view of the indentations. A drop is seen on the LAS side of the interface while a peak appears on the weld metal side.

6.2.3. Nanoindentation

Nanoindentation tests were performed to further characterize the narrow zone across the fusion line where such hardness changes appear after PWHT. The results are shown in Fig. 81.

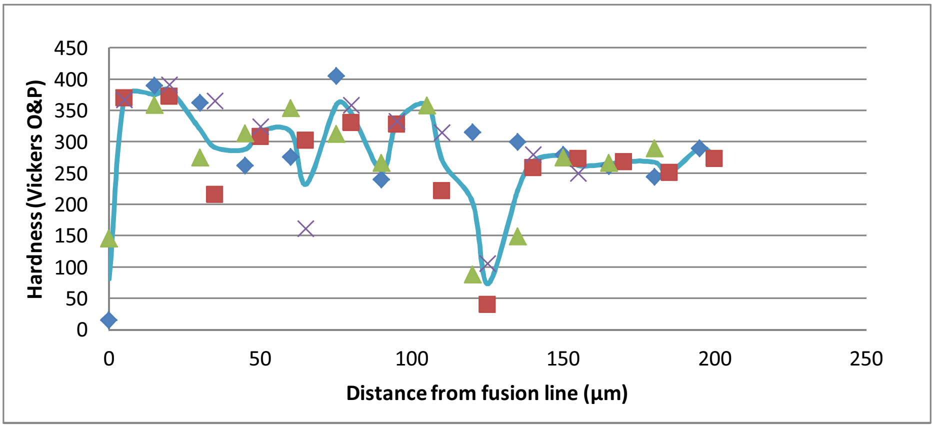

Fig. 81 Nanohardness profile from the fusion line in the Inconel 52 weld. No hardness peak is visible.

The results show no visible hardness peak near the fusion line. Hardness seems to decrease progressively from 400 to 250 HV (Oliver&Pharr method). A sharp drop to 100 HV is seen at about 0.125 mm from the fusion line.

Figure 82 shows the corresponding nanoindentation in Inconel 52 weld metal close to the fusion line and across the precipitates.

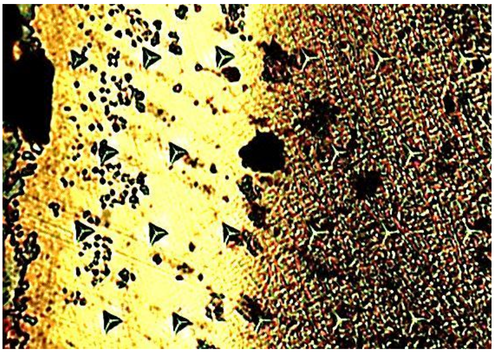

Fig. 82 Nanoindentations in Inconel 52 weld metal across the precipitates.

It is possible that the nanoindentations are too small compared to the microstructures responsible of the hardness peak seen before. Another possibility is that aqua regia etches more the weld metal close to the fusion line due to a change in composition and that the difference in depth affects the nanoindentation results.

6.3. CIEMAT GTAW

Two Alloy 690 plates are welded with GTAW with Inconel 52 weld metal.

6.3.1. Microstructures

Figure 83 shows a global view of the weld, with Alloy 690 base metal, Inconel 52 weld metal and the interface. Several weld passes can also be seen.

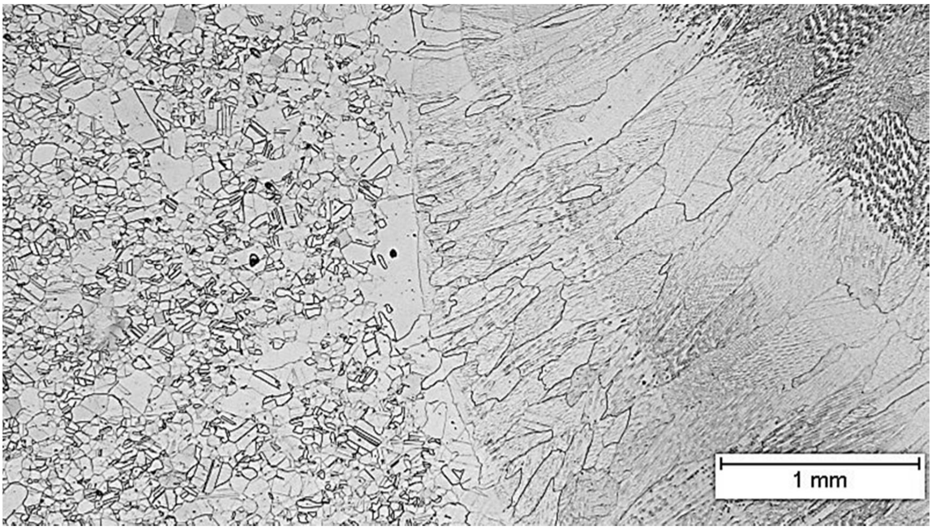

Fig. 83 Global view of the Alloy 690/Inconel 52 interface.

6.3.1.1. Alloy 690

The microstructure of Alloy 690 base material is seen in Figure 84. It is characteristic of an austenitic alloy, with extensive twins due to the low stacking fault energy of the alloy. Fine black precipitates are present both inside the grains and at GBs. They are carbides according to the literature. Bigger particles are present, with rectangular shapes and golden color. They have been identified as TiN particles in numerous studies. Some grain size banding can already be seen.

Figure 85 shows the microstructure of Alloy 690 near the fusion line. No changes are visible in the HAZ. Grain growth occurs very close to the fusion line.

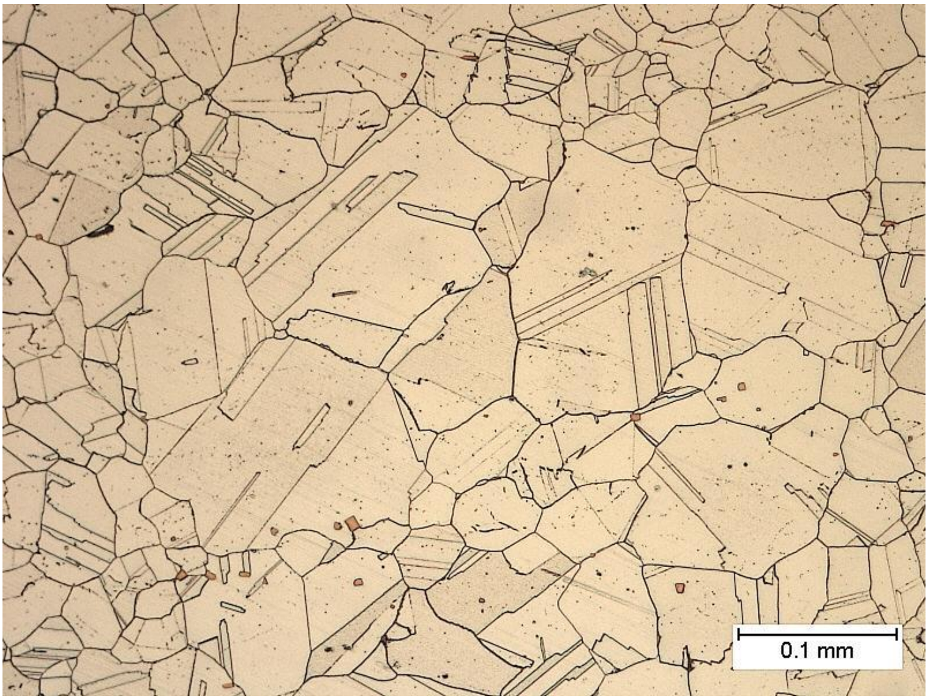

Fig. 84 Microstructure of Alloy 690 base material, with twin boundaries, fine carbide precipitates and golden TiN particles.

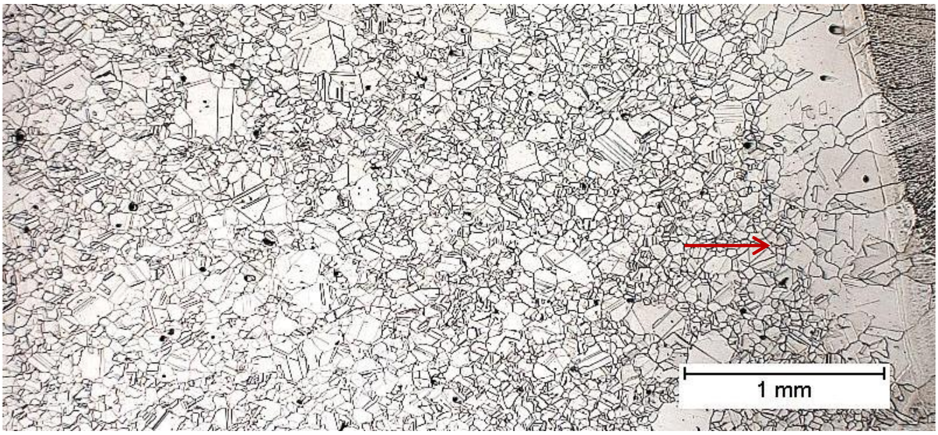

Fig. 85 Microstructure of Alloy 690 HAZ near the fusion line. Important grain growth (red arrows) occurs along the fusion line.

As seen before, the Alloy 690 product form is here a plate, which is the reason to banding structures. Figures 86 and 87 show some of the numerous carbide banding structures present in the plate.

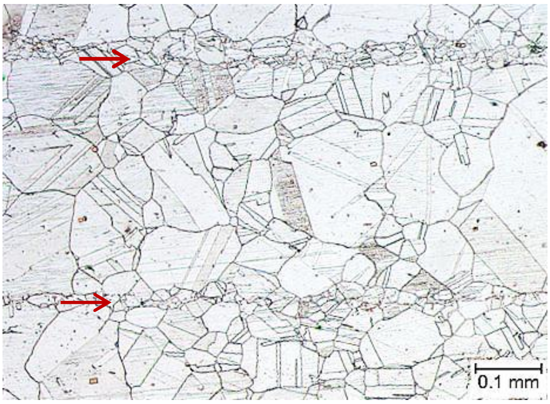

Fig. 86 Carbide banding in Alloy 690 plate.

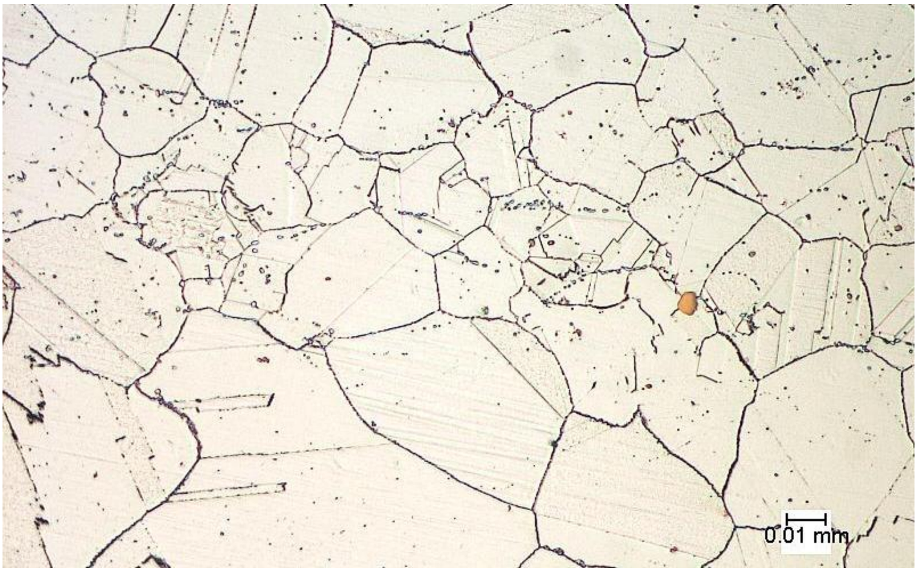

Fig. 87 Closer view of carbide banding. Carbides are clearly visible inside the grains and at the GBs. They pin the prior GBs during the manufacturing, preventing homogeneous grain growth.

6.3.1.2. *Fusion line*

Figure 88 shows the austenitic-austenitic interface between Alloy 690 and Inconel 52. No grain growth is visible in Alloy 690 until the grains at the fusion line. The grain growth in the weld metal seems epitaxial, which is plausible according to the literature concerning an austenitic-austenitic interface. EBSD analysis will help in determining if there is continuity in the grain orientation at the interface.

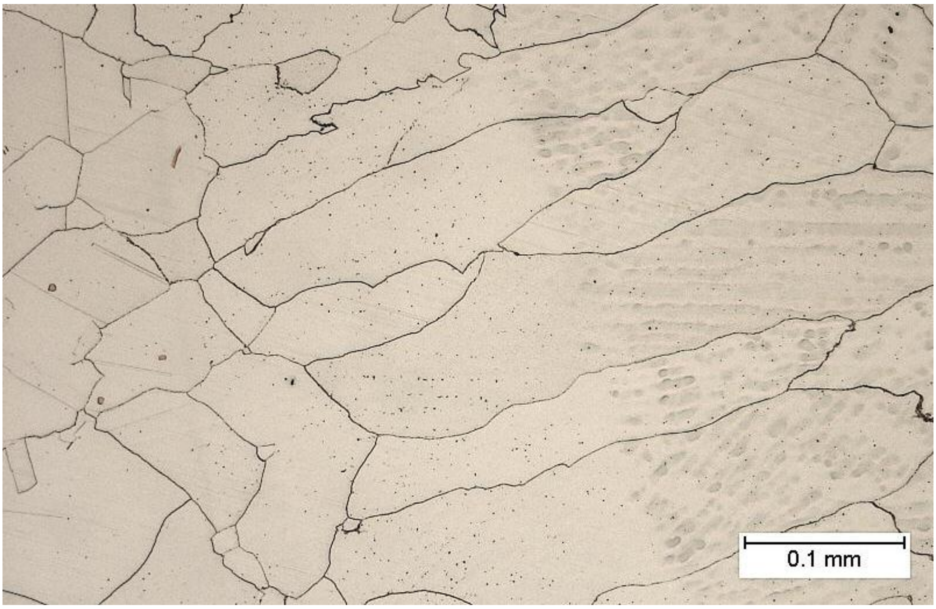

Fig. 88 Alloy 690/ Inconel 52 weld metal interface with epitaxial growth of the weld metal grains.

6.3.1.3. *Inconel 52 weld metal*

Figure 89 shows a view of several weld passes in the Inconel 52 weld metal. The passes are about 2 mm thick. The grains are continuous between the successive weld passes.

Figure 90 shows the columnar dendritic structure of Inconel 52 weld metal. Precipitation occurs in the interdendritic regions. The primary arm spacing is about 0.01 mm.

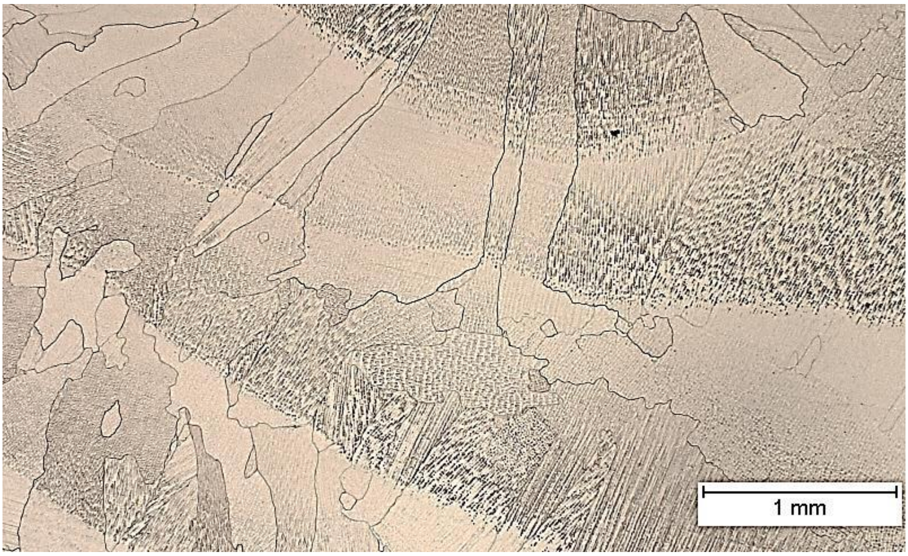

Fig. 89 Weld passes in Inconel 52 weld metal.

Fig. 90 Columnar dendrites in the Inconel 52 weld metal. The GB is clearly visible at the intersection between two different dendrite orientations.

6.3.2. Microhardness

A hardness map was made across the sample (see Fig. 91). Even if no HAZ was visible with optical microscopy, there is an increase in hardness in Alloy 690 from 180 – 190 HV in the base material to 210 – 220 HV at the fusion line.

The values within the weld metal are quite scattered. The influence of weld passes was investigated, but no correlation was found. However, the average hardness values were all similar and the average hardness in the weld metal is 207 HV.

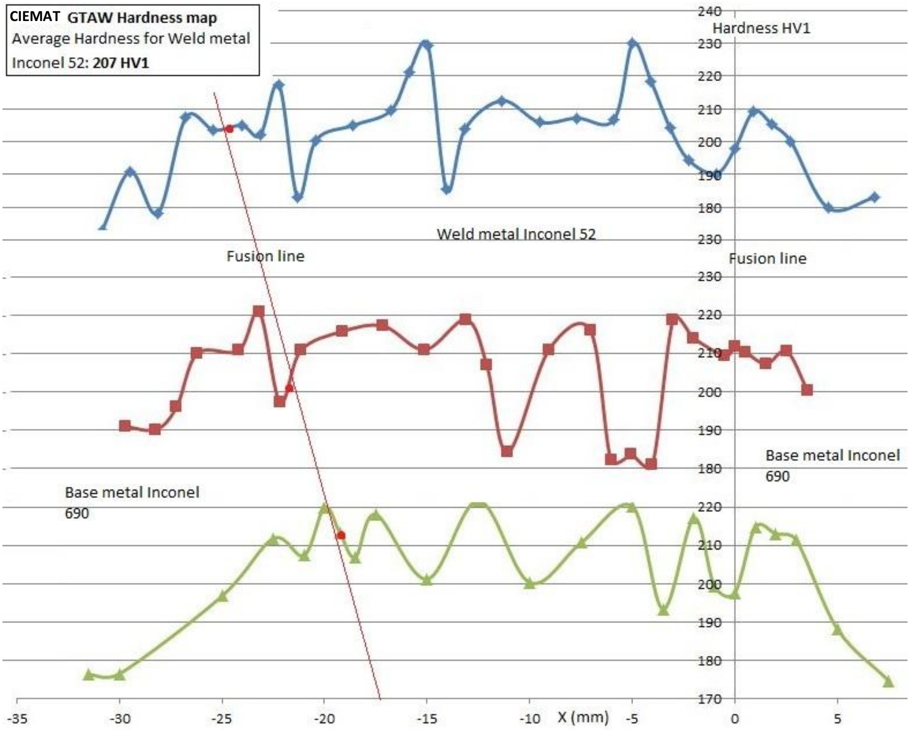

Fig. 91 Hardness map of the samples. There is a hardness increase in the Alloy 690 HAZ and the average Inconel 52 weld metal hardness is 207 HV.

6.4. CIEMAT SMAW

With the same weld configuration as the previous sample, it presents a weld between two Alloy 690 plates with Inconel 152 weld metal.

6.4.1. Microstructures

Figure 92 shows a global view of the Inconel 152 weld passes. They are thicker (about 5 mm) than in the previous CIEMAT sample because manual arc welding has been used here.

Fig. 92 Weld passes in the Inconel 152 weld metal.

6.4.1.1. Alloy 690

Figure 93 shows the Alloy 690 base material microstructure. Here again, twining is present. Fine carbide precipitates are found within the grains, and golden TiN particles are at GBs. The same kind of carbide banding than in CIEMAT GTAW is present in this sample.

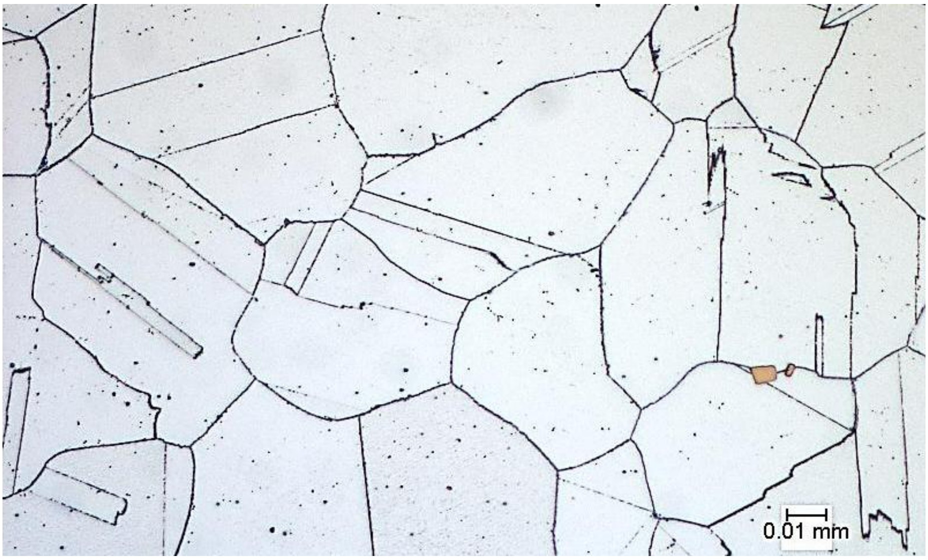

Fig. 93 Microstructure of Alloy 690 base material for sample CIEMAT SMAW.

6.4.1.2. Fusion line

As seen in Figure 94, the fusion line is similar to the previous one. Grain growth in the weld metal is epitaxial and no visible HAZ is present in the Alloy 690 side. However, extensive precipitation occurs in the weld metal, as can also be seen in Figure 95. The nature of the precipitates is not known, yet. They can be NbC according to the literature.

Fig. 94 Fusion line between Alloy 690 and Inconel 152. More precipitates are present in the weld metal than in Inconel 52.

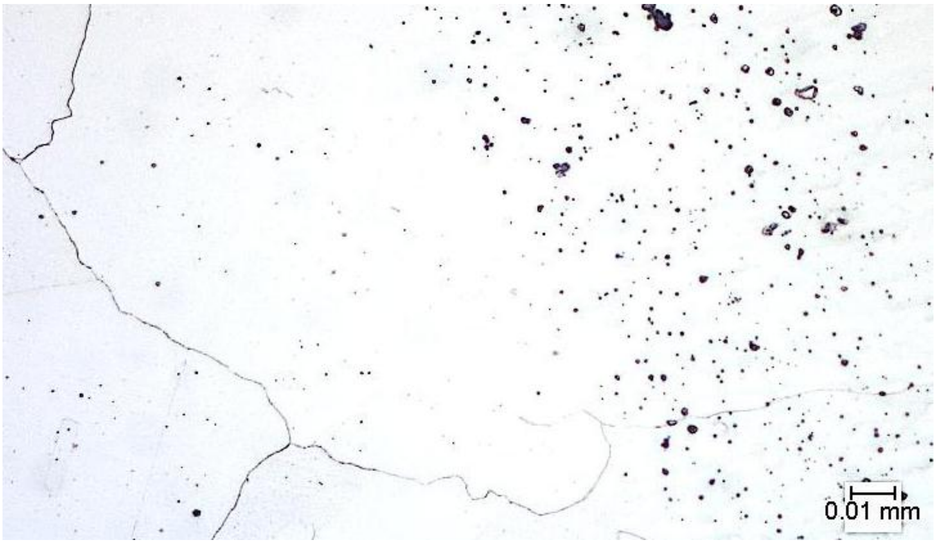

Fig. 95 Closer view of the precipitation occurring in the dendritic microstructure of the Inconel 152 weld metal. It is hard to determine the different zones: Alloy 690 PMZ+UMZ and beginning of Inconel 152 weld metal.

6.4.1.3. Inconel 152 weld metal

Figure 96 shows the microstructure between two weld passes in Inconel 52 weld metal. The dendrite structure is much finer in the beginning of the weld pass.

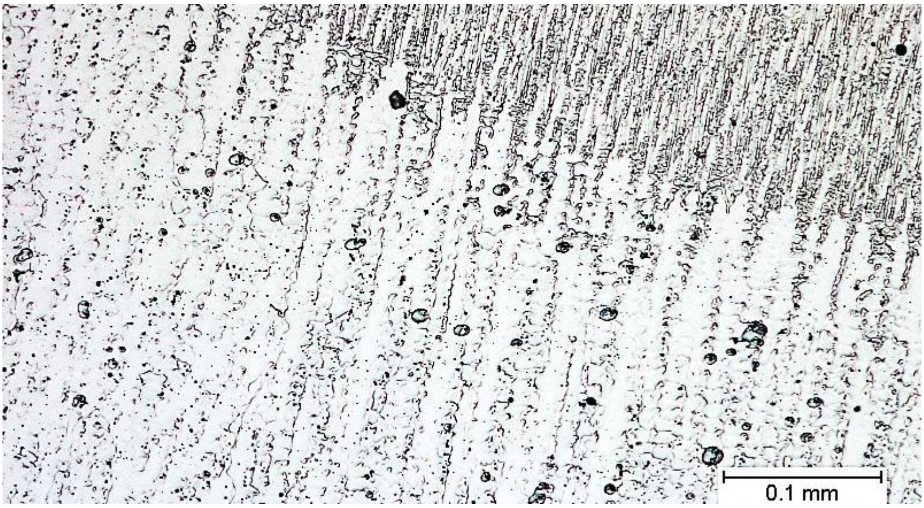

Fig. 96 Transition between two weld passes in Inconel 152 weld metal.

The primary arm spacing in Inconel 152 weld metal in CIEMAT SMAW is much smaller compared to the one in Inconel 52 of the CIEMAT GTAW sample. It is about 0.003 mm near the fusion line (three times smaller).

6.4.2. Microhardness

A hardness map was made across the sample (see Fig. 97). As previously, although no HAZ is clearly visible in Alloy 690, hardness increases from 170 HV in the base material to about 210 HV at the fusion line. The hardness values in the weld metal are more stable than in the previous sample. The average hardness in the weld metal is 224 HV. It is higher than for the Inconel 52 in the CIEMAT GTAW sample.

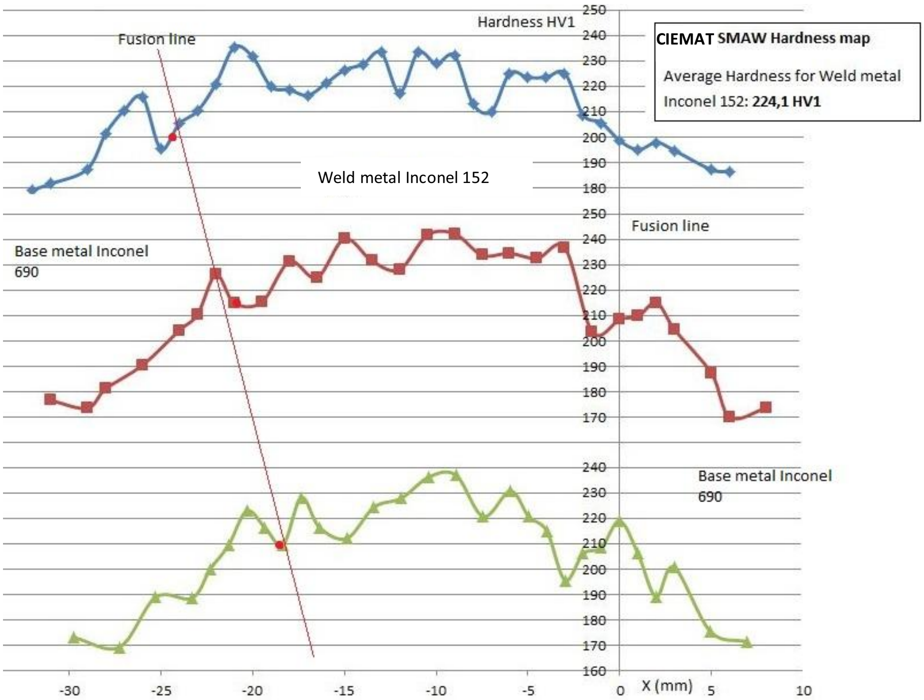

Fig. 97 Hardness map for the CIEMAT SMAW sample, showing hardness increase in the Alloy 690 from the base material to the fusion line. Average weld hardness is 224 HV.

6.5. MHI plate

A LAS SA508 plate and an Alloy 690 plate are welded with Inconel 152 weld metal and an Inconel 152 buttering layer.

6.5.1. Microstructures

Two different interfaces are present: one between ferritic SA508 and austenitic Inconel 152 buttering, one between Inconel 152 weld metal and Alloy 690 base metal. The last interface could be between the buttering layer and the weld metal. The same material is used but the direction of the weld passes changes.

6.5.1.1. SA508 HAZ

Figure 98 shows the microstructure of SA508 HAZ near the SA508/Inconel 152 buttering layer interface. The features are characteristic of a LAS HAZ, as previously for the Alloy 52 mock-up samples.

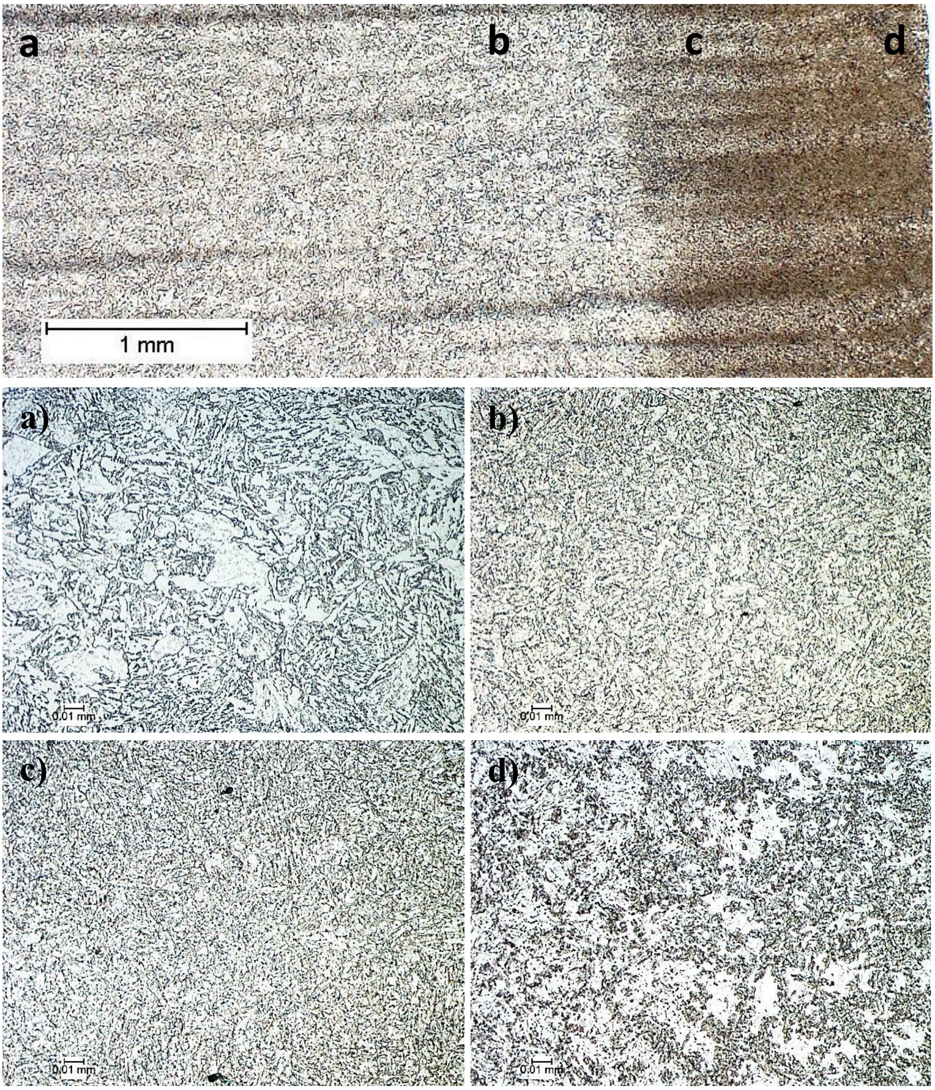

Fig. 98 SA508 HAZ: a) grain coarsening, b) grain refining, c) partial grain refining and d) base material.

Carbide banding is visible in the SA508 plate.

6.5.1.2. Fusion line LAS/Inconel 152

Figure 99 gives a closer view of SA508 steel at the interface with Inconel 152 weld metal.

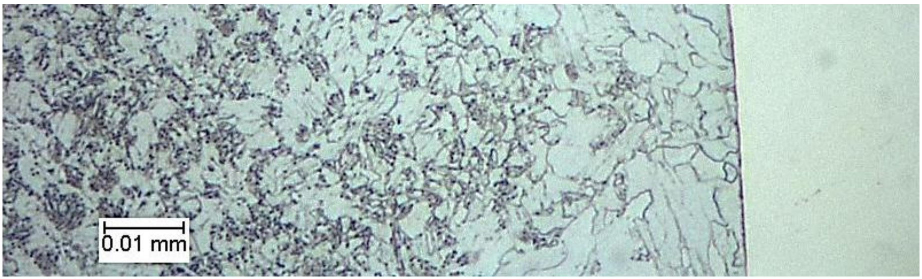

Fig. 99 SA508 side of the SA508/Inconel 152 interface with.

It was observed that Widmannstätten ferrite is sometimes present along the fusion line, as shown in Figure 100. Carbon depletion occurs at the fusion line. As seen in Figure 99, the CDZ is about 0.05 mm wide.

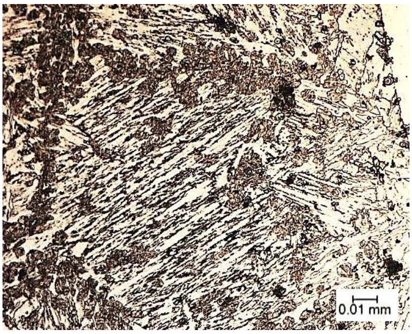

Fig. 100 Widmannstätten ferrite along the fusion line.

Figure 101 shows a carbon-enriched region at the fusion line, dark-etched. Such regions appear mostly where the carbide banding of the LAS plate reaches the fusion line.

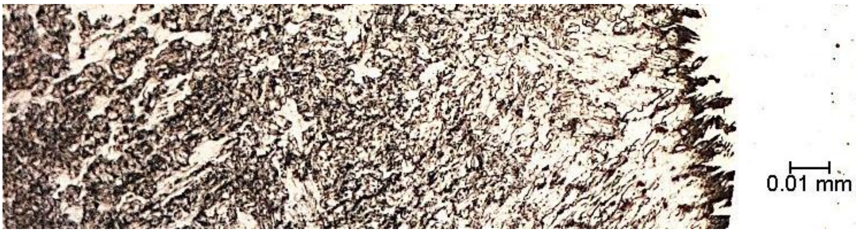

Fig. 101 Dark-etched carbon-enriched layer on the fusion line between SA508 and Inconel 152.

These carbon-rich regions at the interface seem to be martensite. They appear mostly where the carbide banding of the LAS reaches the fusion line. The fusion line outside these bands is mostly free of such features.

Figure 102 shows the microstructure of the interface on the Inconel 152 side. Type II boundaries are clearly visible. They are about 0.05 mm from the fusion line. Extensive precipitation occurs at these boundaries and in the Inconel 152 weld metal in general.

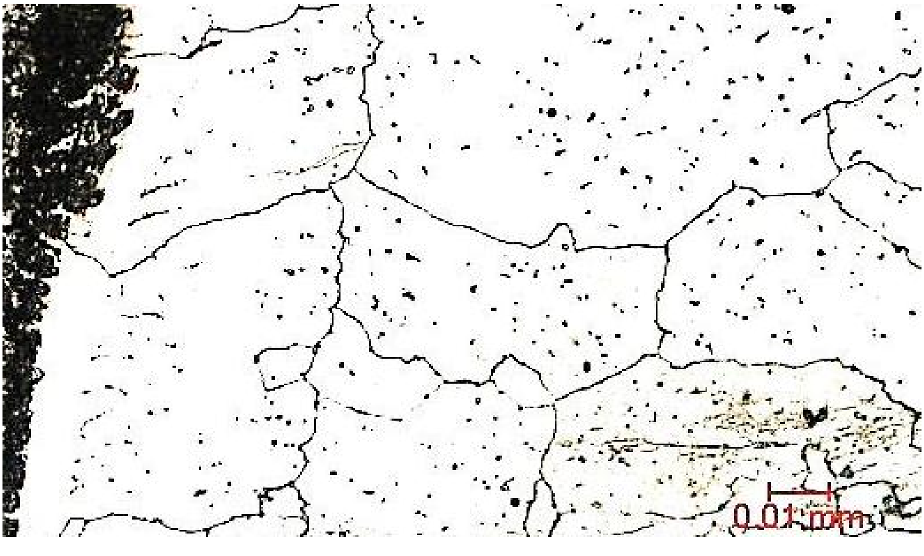

Fig. 102 Type II boundaries on the weld metal side of the SA508/Inconel 152 interface.

The carbon-enriched layer can be seen at the fusion line. Moreover, there is little precipitation occurring in the weld metal between the fusion line and the Type II boundaries (compared, for example, to the SA508/Inconel 52 interface of the Alloy 52 mock-up samples). Carbon diffusivity may be less in Inconel 152 than in Inconel

52. It would explain that more carbides precipitate in the Inconel 152 weld metal than in the Inconel 52. Also, it explains the carbon-enriched layer at the fusion line between SA508 and Inconel 152, since carbon will diffuse very little in the weld metal.

6.5.1.3. Fusion line Inconel 152/Alloy 690

Figure 103 shows the Inconel 152/Alloy 690 interface. No HAZ is visible on the Alloy 690 side. Extensive precipitation occurs in the weld metal. There seems to be continuity between the grains from the base and weld metals. The growth mechanism is epitaxial.

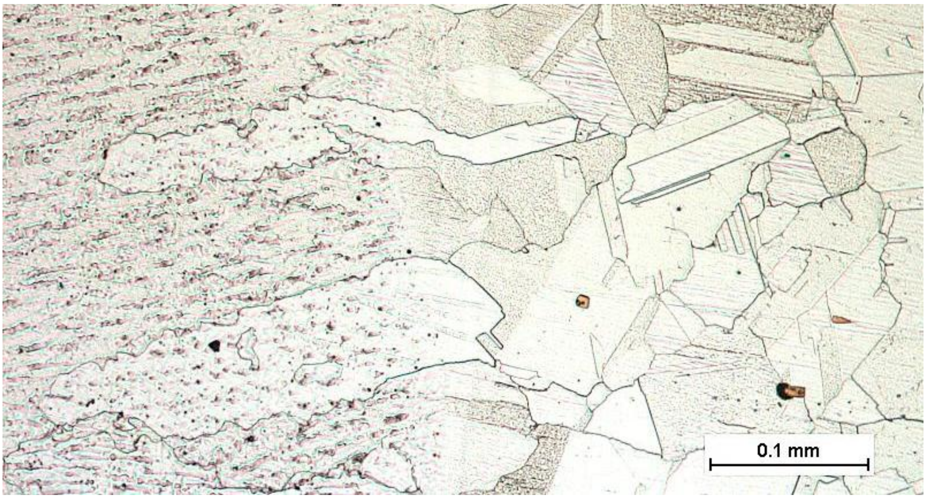

Fig. 103 Inconel 152/Alloy 690 interface.

6.5.2. Microhardness

A hardness map has been made for the sample on the Inconel 152/Alloy 690 side (see Fig. 104). Hardness increases in the HAZ from the Alloy 690 base material (190 HV) to the fusion line (230 HV). The average weld hardness is 239 HV. It is higher than the average hardness in the Inconel 152 weld metal of the CIEMAT SMAW sample. It may be due to carbon diffusion from the SA508 side.

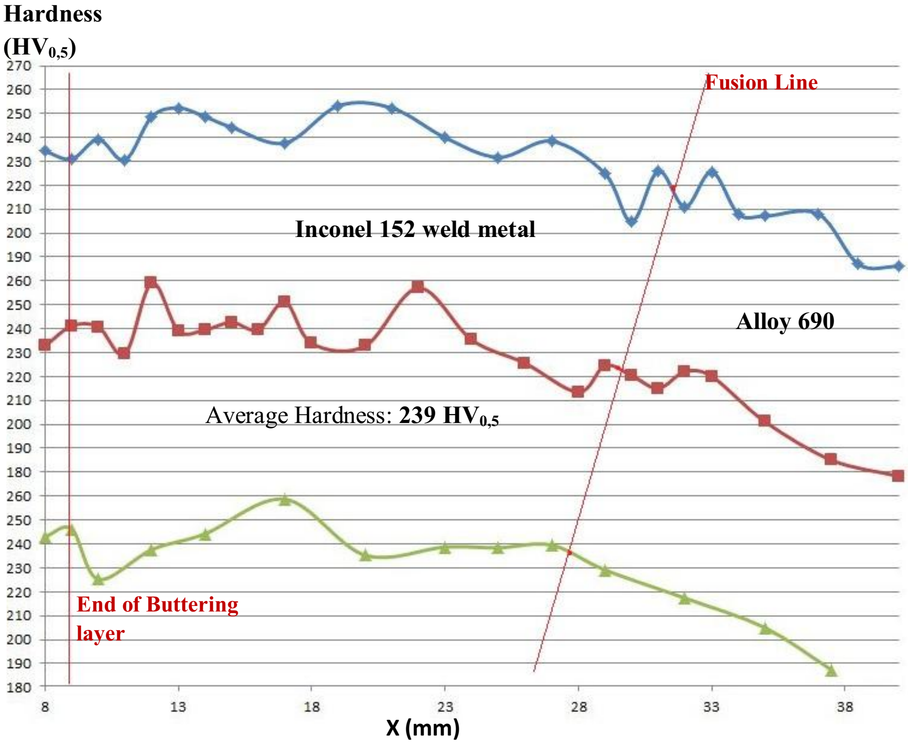

Fig. 104 Hardness map of the Inconel 152/Alloy 690 side of the sample. Hardness increases in the Alloy 690 HAZ. The average weld hardness is 239 HV.

Hardness tests were also conducted on the straight SA508/Inconel 152 buttering layer side (see Fig. 105). Hardness increases in the SA508 HAZ from 200 HV (base material) to 240-260 HV at the fusion line. After a drop in Inconel 152 (220 HV), hardness progressively increases in the buttering layer and reaches a peak at the interface between the buttering and the weld (250 HV at 7-8 mm from the SA508/buttering fusion line).

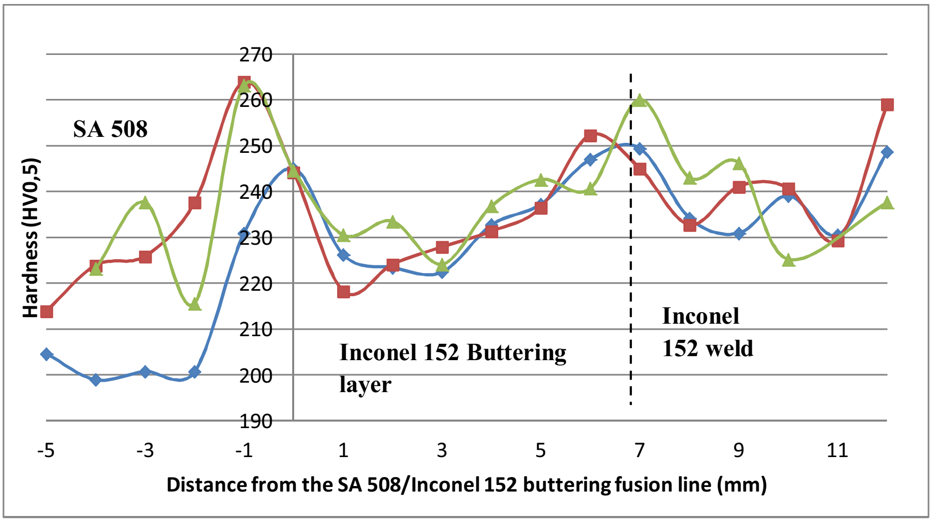

Fig. 105 Hardness profile across the SA508/Inconel 152 buttering and in the buttering layer. It shows a peak in the SA508 HAZ, and another at the buttering layer/weld metal interface.

Microhardness was then measured across the SA508/Inconel 152 buttering layer interface to better characterize it. The results are shown in Figure 106. The values in the buttering layer are all similar (220-230 HV) and correspond to the previous tests. However, the hardness values in SA508 are very scattered. All the lines follow the same profile but with different values (with hardness peaks ranging from 270 to 420 HV). Thus, the influence of the HAZ is still visible, but another parameter affects the hardness. At the same distance from the fusion line, hardness increases from Line 1 to Line 3 when carbide banding is more important, and decreases from Line 3 to 5 when carbide banding decreases.

The influence of banding was investigated. Figure 107 shows a detailed microstructure of the bands and Figure 108 shows the hardness profile across several bands.

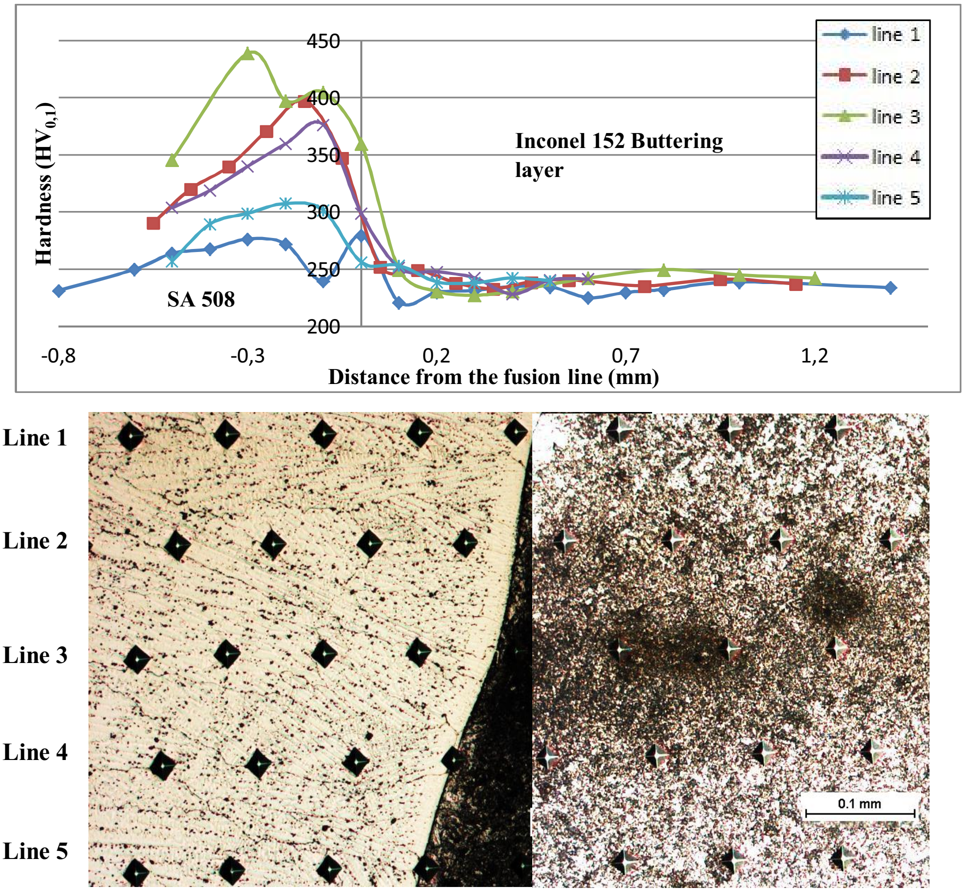

Fig. 106 Microhardness profile across the SA508/Inconel 152 buttering layer. Hardness always follows the same profile in the LAS HAZ, but with different amplitudes.

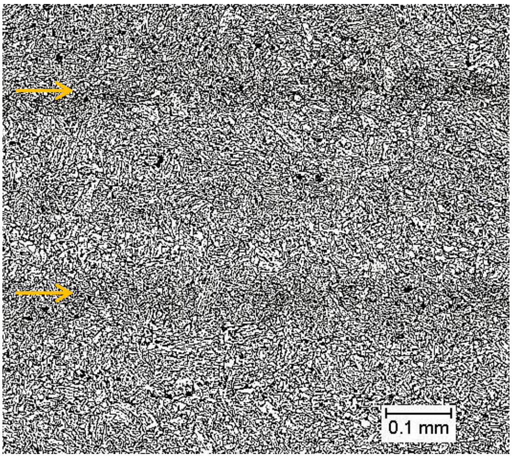

Fig. 107 Banded microstructure in SA508 with dark- and light-etched bands.

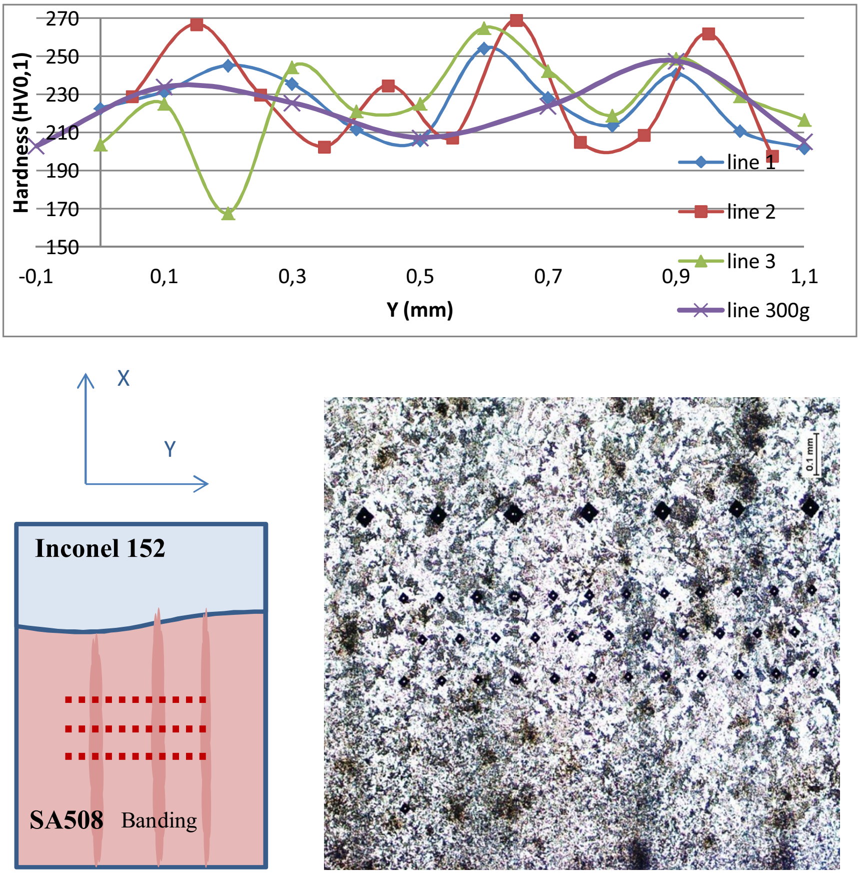

Fig. 108 Hardness profile across several bands in SA 508 steel; three lines with 100 g load and one with 300 g load. Hardness increases significantly when measured inside the dark-etched band.

The measurements with 300 g load were done to make sure that the hardness variations with smaller loads are not artefacts.

The dark-etched bands contain much more precipitates than the bright ones. The influence of banding was notable in the microhardness tests due to the lower loads and smaller steps. The difference in hardness due to the banding can reach 70 HV.

6.6. GTAW 19508A

Two Alloy 690 plates are welded with NG-GTAW with Inconel 52M weld metal.

6.6.1. Microstructures

6.6.1.1. Alloy 690

Figure 109 shows a global view of the Alloy 690/Inconel 52M interface. Grain growth is clearly visible for the first time in this study in the Alloy 690 HAZ along the fusion line. Figure 110 gives a closer view. The HAZ is about 0.3 mm wide.

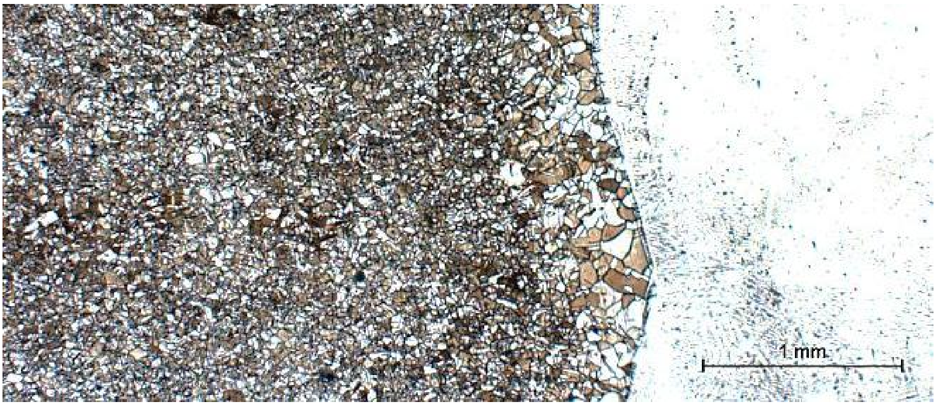

Fig. 109 Microstructure of the Alloy 690/Inconel 52M interface. The Alloy 690 HAZ is clearly visible.

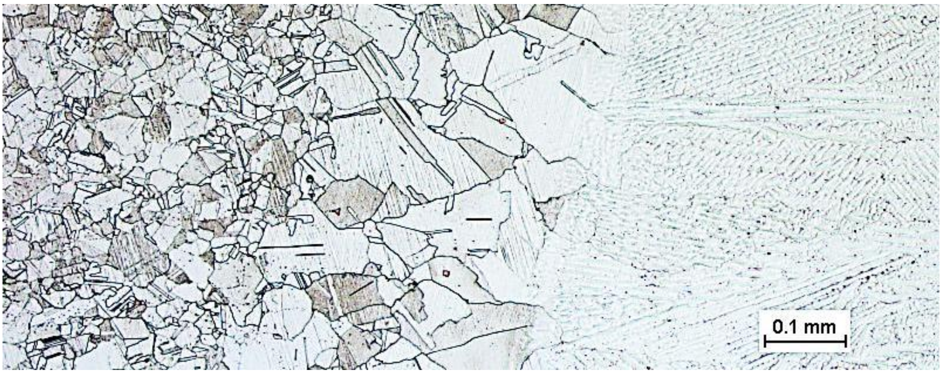

Fig. 110 HAZ of Alloy 690 at the fusion line with Inconel 52M weld metal.

6.6.1.2. *Alloy 690/Inconel 52M interface*

Figure 111 shows a close view of the Alloy 690/Inconel 52M weld metal interface. There is continuity between the grains from base to weld metal and the growth is epitaxial.

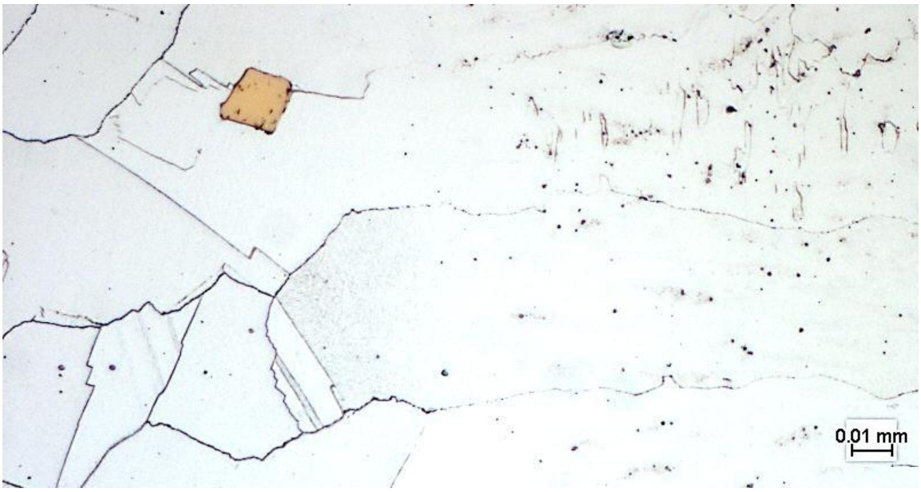

Fig. 111 Alloy 690/Inconel 52M weld metal interface, showing the growth of the weld metal grains from those of the base metal. Note the golden rectangular TiN particle.

6.6.1.3. *Inconel 52M weld metal*

Figure 112 shows the microstructure of the Inconel 52M weld metal. The dendritic structure is cellular. To be noted is that the GBs seem less straight than for Inconel 52, 152. It is probably due to the higher amount of alloying elements of Inconel 52M that creates more interdendritic segregation which pin the GBs when they migrate.

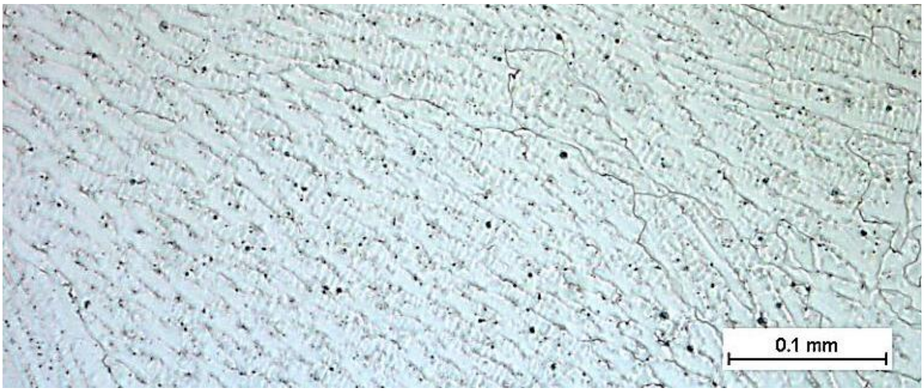

Fig. 112 Inconel 52M weld metal microstructure.

6.6.2. Microhardness

The hardness profile was measured across this NGW (see Fig. 113). The average hardness in the Inconel 52M weld metal is 252 HV. This is higher than the average hardness of the Inconel 52 and 152 welds of the previous samples. It has been reported in the literature that Inconel 52M weld has more alloying elements and finer microstructures than that of Inconel 52 and 152. It explains the higher hardness.

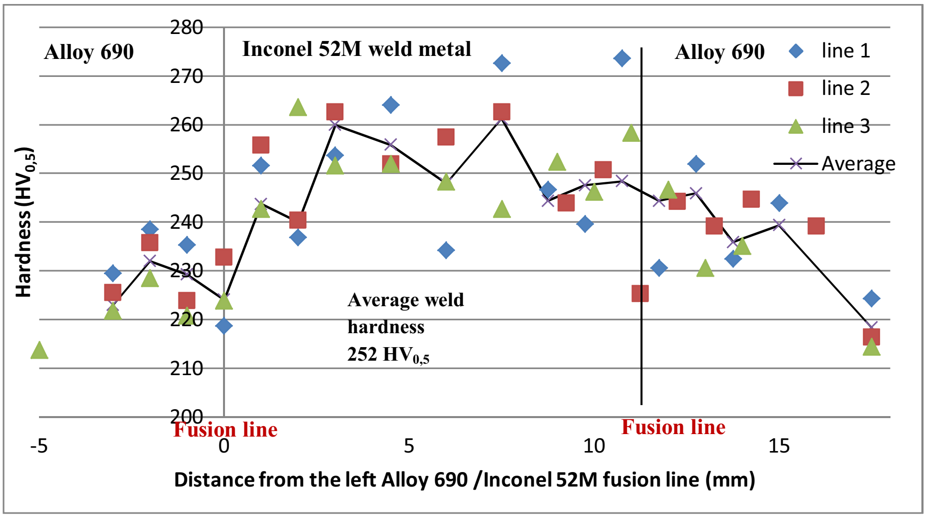

Fig. 113 Hardness profile across the Alloy 690/Inconel 52M/Alloy 690 weld.

There is a hardness increase in the HAZ of Alloy 690, which was confirmed in the microhardness measurements across an Alloy 690/Inconel 52M interface. Figure 114 shows the microhardness profile and the corresponding indentations in the HAZ and across the fusion line.

Hardness increases from 230 HV in the Alloy 690 base material, and reaches a peak in the HAZ (270 HV at 0.7 mm from the fusion line). Hardness then decreases in layer of coarse grains along the fusion line (240 HV) and increases again in the weld metal.

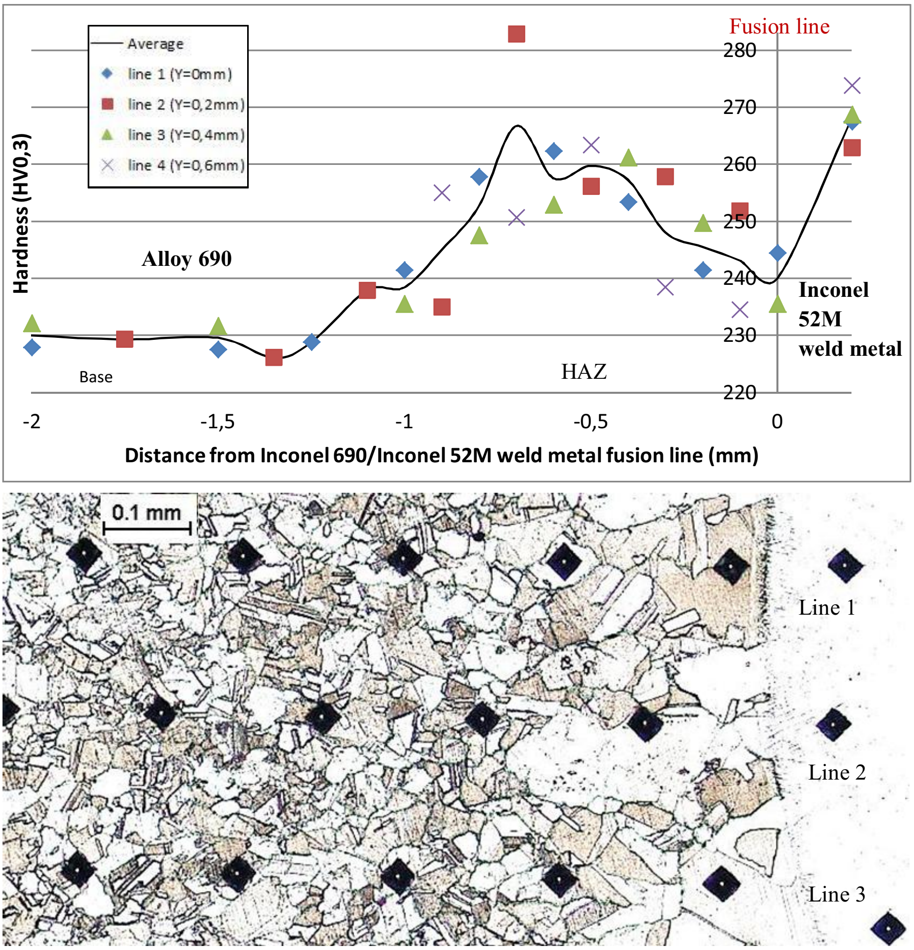

Fig. 114 Hardness profile in the Alloy 690 HAZ and at the fusion line with Inconel 52M. Hardness increases in the HAZ from the base material but decreases due to grain growth along the fusion line.

6.7. ENSA weld mock-up

A carbon steel plate is welded to a forged Alloy 690 plate with the several Inconel 52M buttering layers and the Inconel 52 weld metal.

6.7.1. Microstructures

The microstructural characterization focuses here on the LAS HAZ, the interface between the LAS and the Inconel 52M buttering layer and Alloy 690 microstructure.

6.7.1.1. LAS HAZ and interface with the buttering

Figure 116 shows the LAS HAZ. It presents the same features as in the previous samples: base material, partial grain refining, grain refining and grain coarsening along the fusion line. To be noted is that carbide banding is present in the plate, but it is now parallel to the fusion line, as opposed to the MHI sample.

Figure 117 shows the fusion line between the LAS and the Inconel 52M buttering. As previously, a CDZ forms in the LAS side. It is 70 µm wide.

Figure 118 shows the interface between the LAS and the Inconel 52M buttering layer. Type II boundaries form at about 50-100 µm from the fusion line. A dark-etched layer appears all along the fusion line in the Inconel 52M. It may be a martensitic layer or a PMZ.

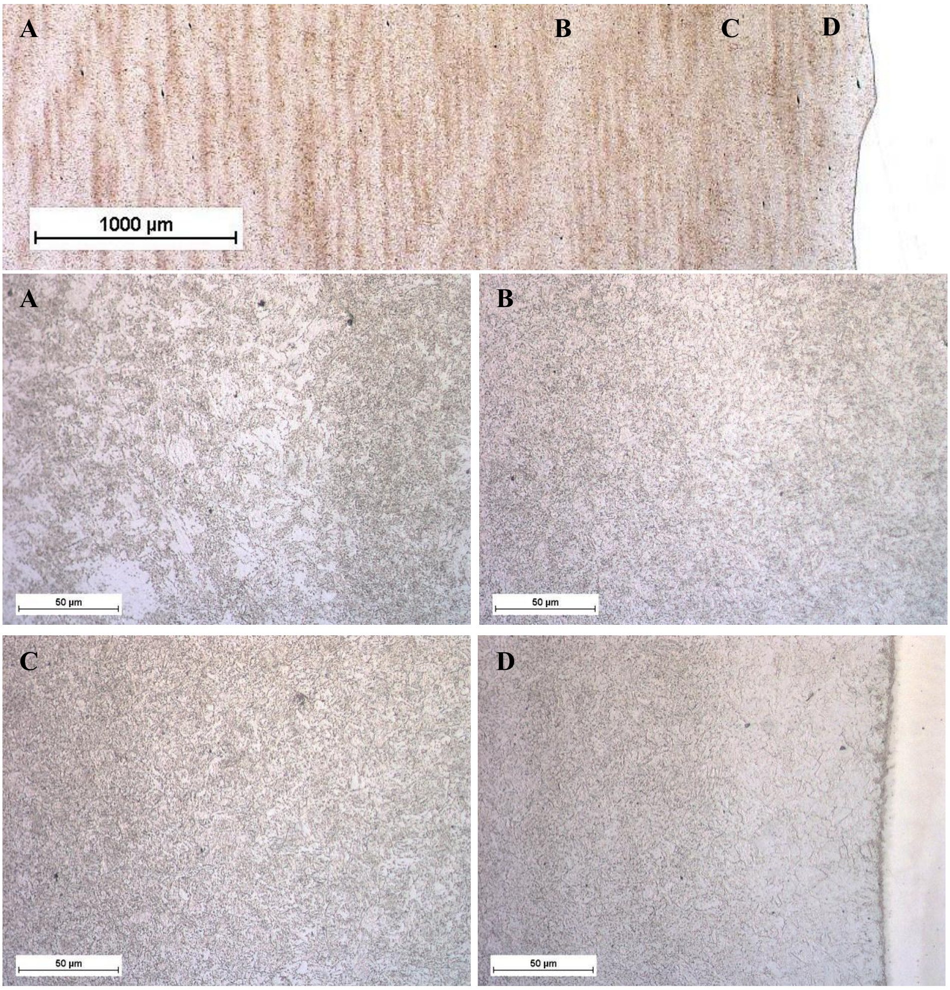

Fig. 116 LAS HAZ with A) base material, B) partial grain refining, C) grain refining and D) grain coarsening along the fusion line.

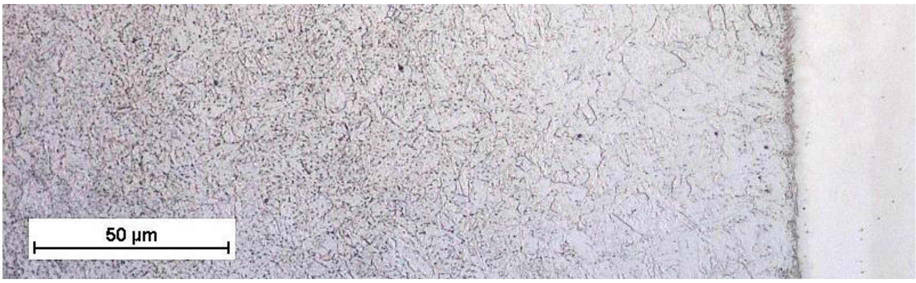

Fig. 117 CDZ in the LAS side of the LAS/Inconel 52M buttering layer interface.

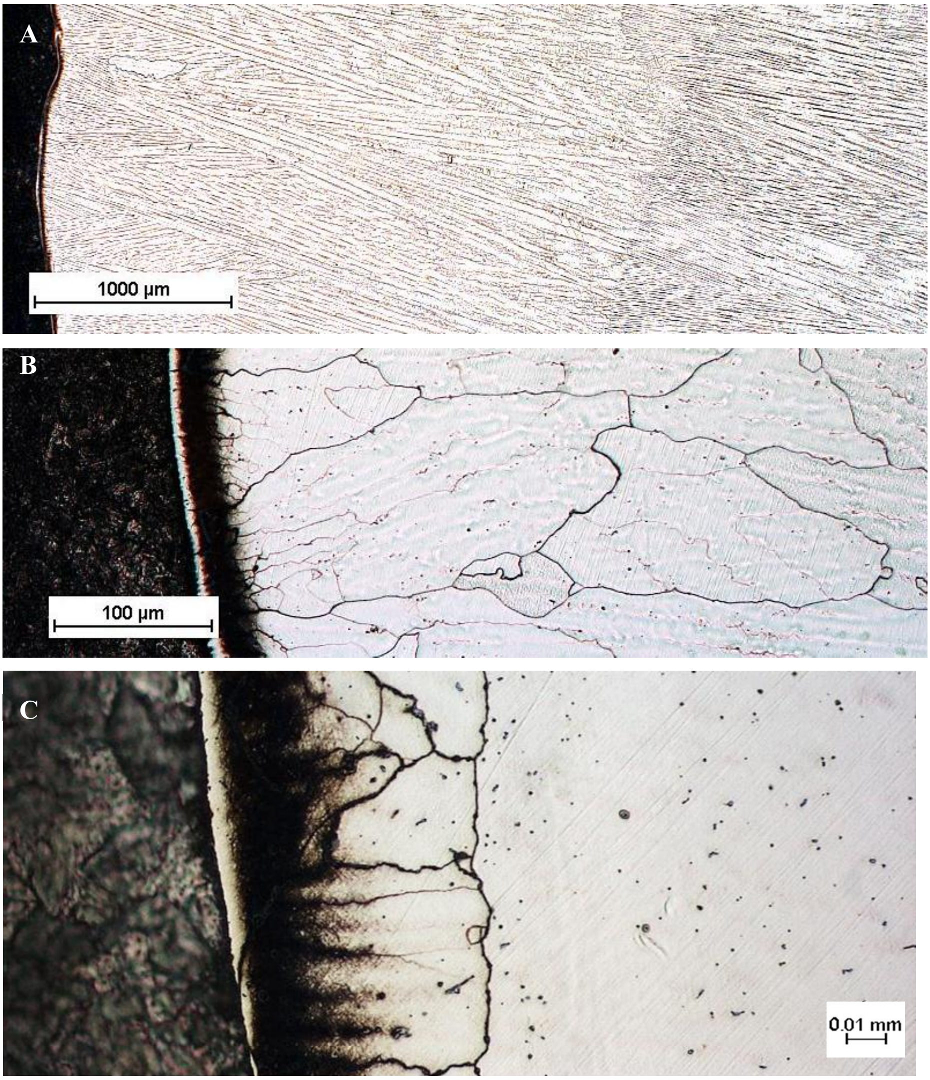

Fig. 118 a) Broad view, b) closer view of the LAS/Inconel 52 M buttering fusion lines and c) Type II boundary at 10 µm from the fusion line.

It is not clear if the dark layer is an artifact from the etching or if it results from carbide or martensite.

6.7.1.2. Forged Alloy 690 microstructure

Figures 119 and 120 show the microstructure of Alloy 690. It shows a lot of carbide banding in all directions. The microstructure is the most inhomogeneous among all the samples for Alloy 690, with extensive carbide banding and arrays, and very inhomogeneous grain size distribution.

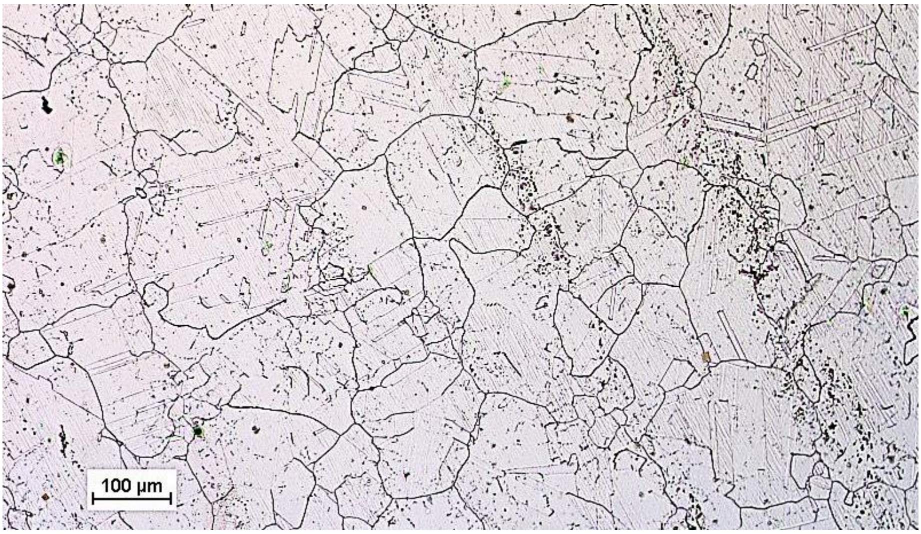

Fig. 119 Carbide banding in forged Alloy 690 plate.

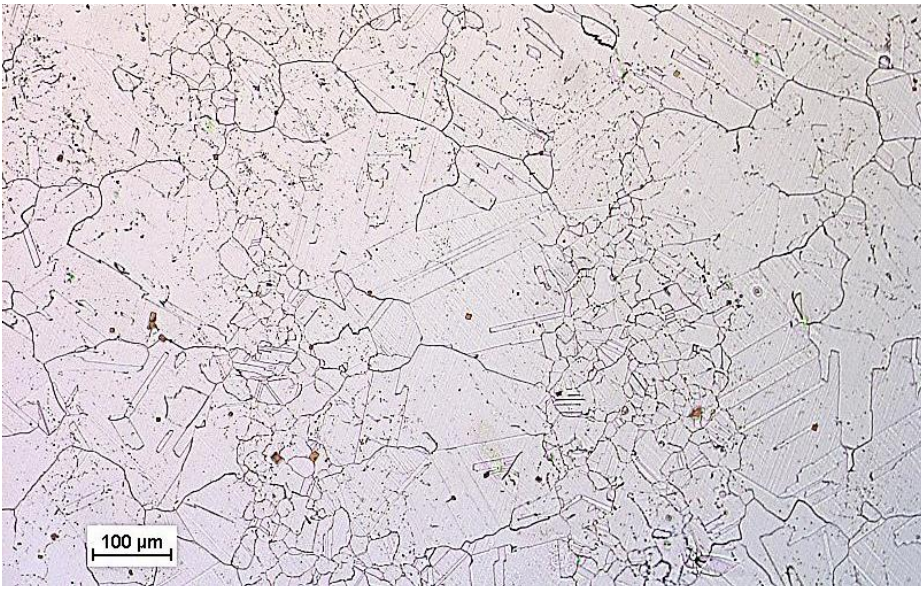

Fig. 120 Very inhomogeneous microstructure in forged Alloy 690 plate. Fine grains are associated with carbides arrays, with bigger grains in-between.

6.7.2. Microhardness

Figure 121 shows the location of the 3 different hardness measurement locations across the sample.

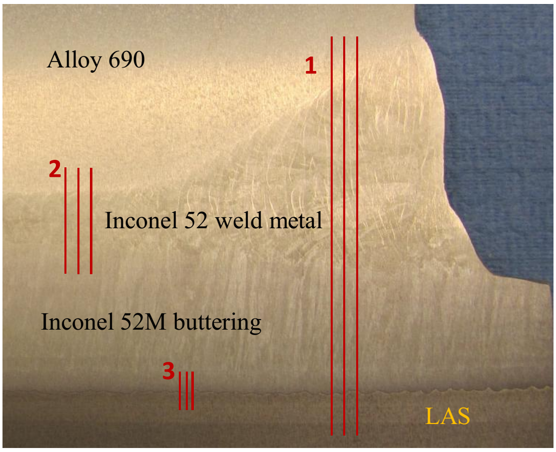

Fig. 121 Schematic of the hardness measurements for the ENSA weld mock-up.

The first measurement is made across all the materials in the sample and the V-groove Inconel 52 weld. The second is across the Inconel 52 NGW and Alloy 690 HAZ. The third is made at the fusion line between LAS and Inconel 52M buttering.

Figures 122, 123 and 124 show the results of the first, second and third measurements, respectively.

Figure 122 shows that hardness increases in the LAS HAZ with a hardness peak at the fusion line (260 HV) and a drop in the Inconel 52M buttering. Hardness increases in the buttering from the LAS to the weld metal. Despite carbon diffusion from the LAS side, it is probably due to the major influence of residual strains that increase towards the weld metal. Inside the Inconel 52 weld metal, hardness decrease towards the Alloy 690 side. The average weld hardness is 215 HV.

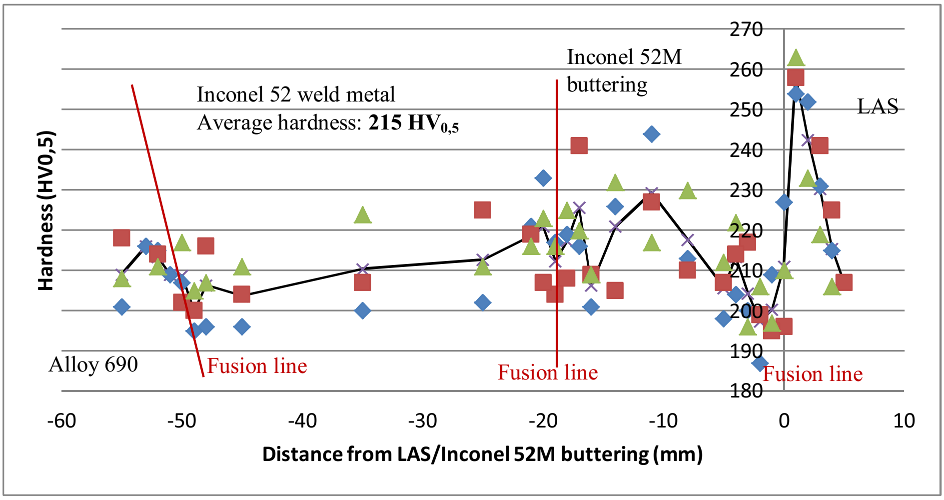

Fig. 122 Hardness measurement from location 1: across LAS, Inconel 52M buttering, Inconel 52 weld metal and Alloy 690 base metal. The black line shows the average from the 3-line measurements. It shows a hardness peak in the LAS HAZ, hardness drop in the buttering (190 HV) along the fusion line, and then increase in the buttering towards the weld metal. Slow hardness decrease in the weld metal towards the Alloy 690 side.

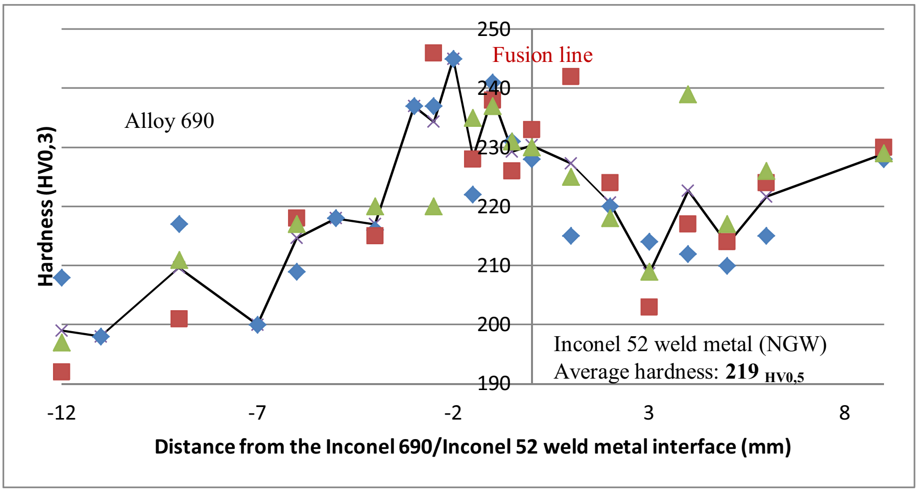

Fig. 123 Hardness measurement from location 2: Alloy 690 HAZ and Inconel 52 NGW. The black line shows the average from the 3-line measurements.Hardness increases in the Alloy 690 HAZ due to residual strain, then decreases due to grain coarsening. The average weld metal hardness is 219 HV.

Figure 123 shows the hardness profile in Alloy 690 HAZ and Inconel 52 weld metal in the narrow-gap weld. Hardness increases in the Alloy 690 HAZ, without noticeable change in the microstructure. It is probably due to increasing residual strains when going closer to the fusion line. Closer to the fusion line, hardness starts to decrease in Alloy 690 due to grain coarsening. In the Inconel 52 weld metal, hardness increases towards the edge of the narrow-gap weld and is lower in the center of the weld. The average hardness is, however, slightly higher (219 HV) than that of the V-groove weld (215 HV).

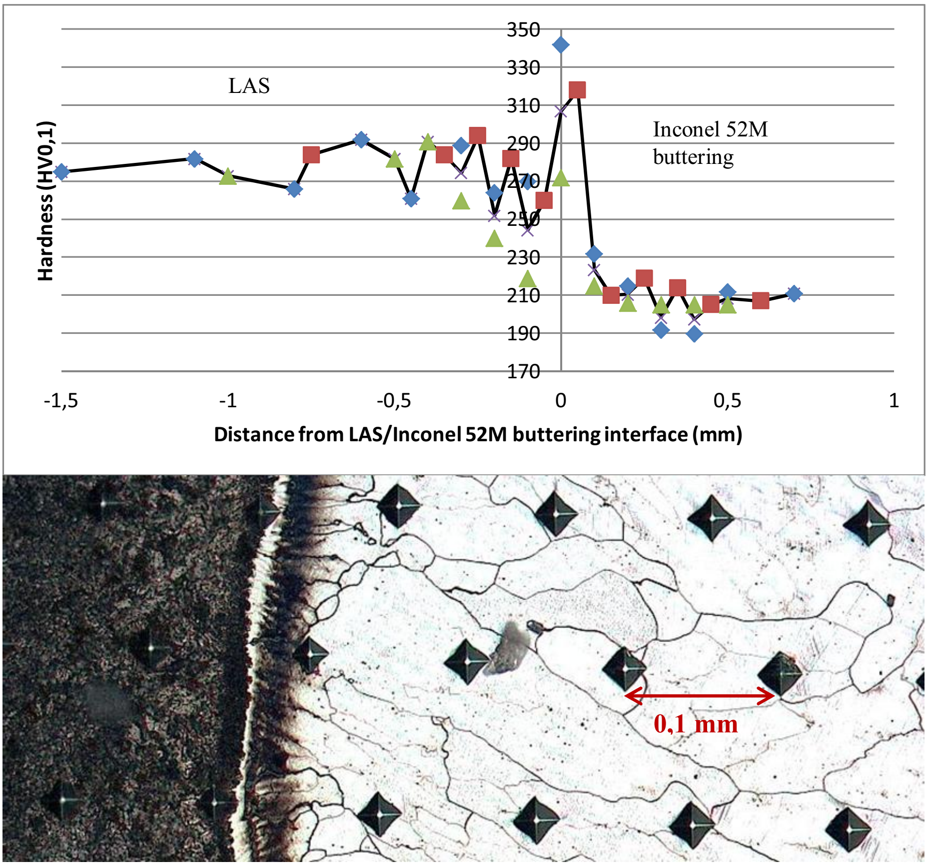

Fig. 124 Hardness measurement from location 3 and corresponding indentations: LAS HAZ and interface with Inconel 52M buttering. The black line shows the average from the 3-line measurements. A hardness peak is present on the Inconel 52M side.

Figure 124 shows a closer view of the LAS/Inconel 52M buttering. The hardness in the LAS HAZ remains high (290 HV). It is because the measures are very close to the fusion line, showing therefore only the hardness peak in the LAS from Figure

122. LAS hardness would decreases if going further from the fusion line into the LAS base material. The scatter in the values in the LAS side is due to the carbide banding parallel to the fusion line. When entering the Inconel 52M buttering, another hardness peak is present (320 HV). It corresponds to the dark layer at approximately 10 µm from the fusion line. Further study will investigate the nature of this layer. Hardness then decreases in the buttering to reach the first values seen in Figure 122 (190 HV).

6.8. PG&E mock-up

An extruded Alloy 690 pipe is welded to a SA533 Gr.B plate with the heat-shrink technique and an Inconel 52M J-groove weld. A SS308L cladding is on the SA533 Gr.B plate around the pipe. An Inconel 52M buttering is on the LAS side. There is a lack of fusion between the pipe and the weld metal of the buttering layer.

6.8.1. Microstructures

Many materials and interfaces are present. The LAS SA533 Gr.B HAZ is present, as well as the fusion line between the SA533 Gr.B and the Inconel 52M buttering. Then, the interface between the Inconel 52M buttering, the SS cladding and the LAS is shown to see the difference between the austenitic/austenitic and ferritic/austenitic fusion lines. Finally, the microstructure of the Inconel 52M weld metal, the interface between Inconel 52M weld metal and Alloy 690 base metal, and the microstructure of the extruded Alloy 690 base material are examined.

6.8.1.1. LAS HAZ and fusion lines

Figure 126 shows the SA533 Gr.B HAZ. The same features as for other ferritic LAS HAZ (base material, partial grain refining, grain refining and grain coarsening) are observed. Banding is present in all the material.

Figure 127 A) shows a closer view of the carbide banding, and its influence on the fusion line microstructures is seen in Figures 127 B) and C). Outside the banding structure (Fig. 127 B) a CDZ is clearly visible in the LAS side. It is about 50 µm wide. When a carbide banding reaches the fusion line (Fig. 127 C), the CDZ is harder to see. In addition, the fusion line microstructure changes: a dark-etched layer appears to grow on the Inconel 52M side. It is similar to the features observed in the MHI plate sample. It is not clear, yet, if it is martensite or PMZ. It seems, however, to be related to the higher carbon content in the carbide banding.

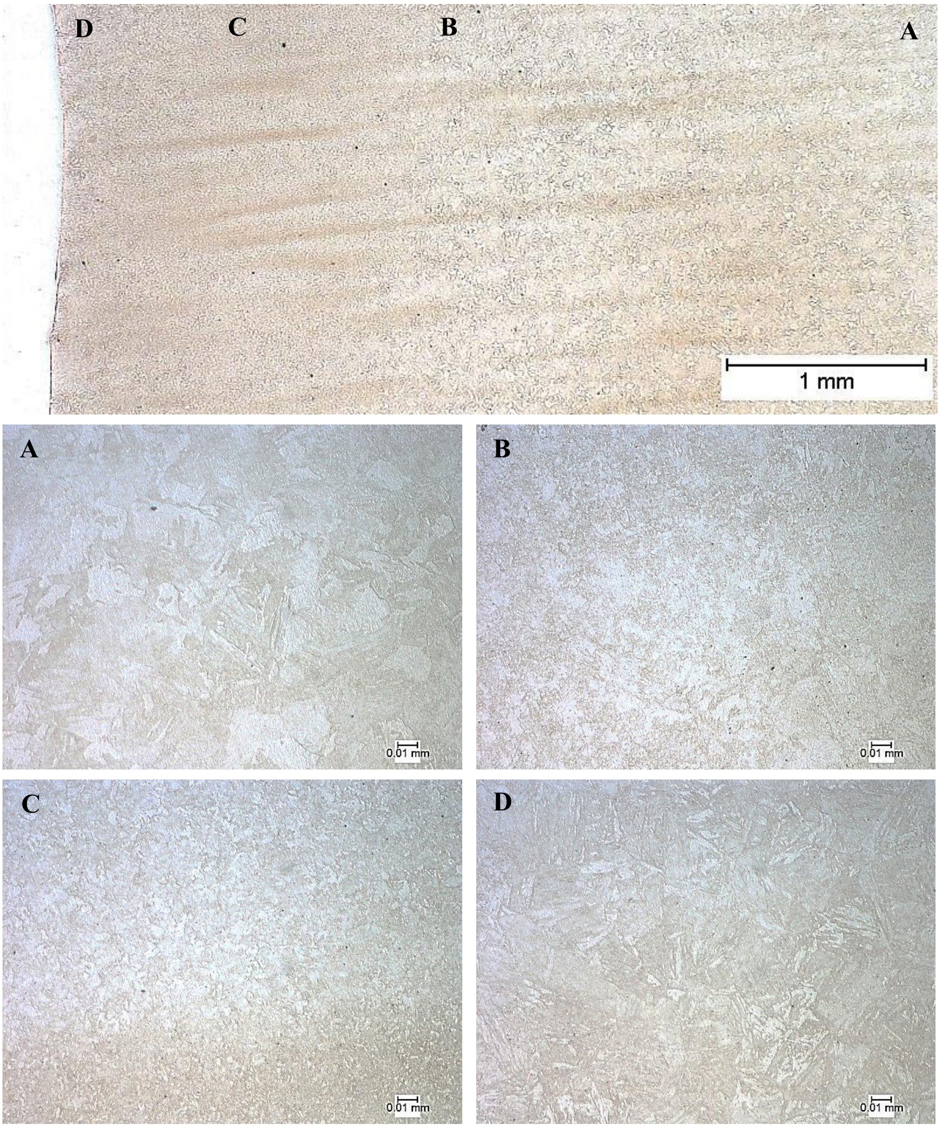

Fig. 126 SA533 Gr.B HAZ with A) base material, B) partial grain refining, C) grain refining and D) grain coarsening.

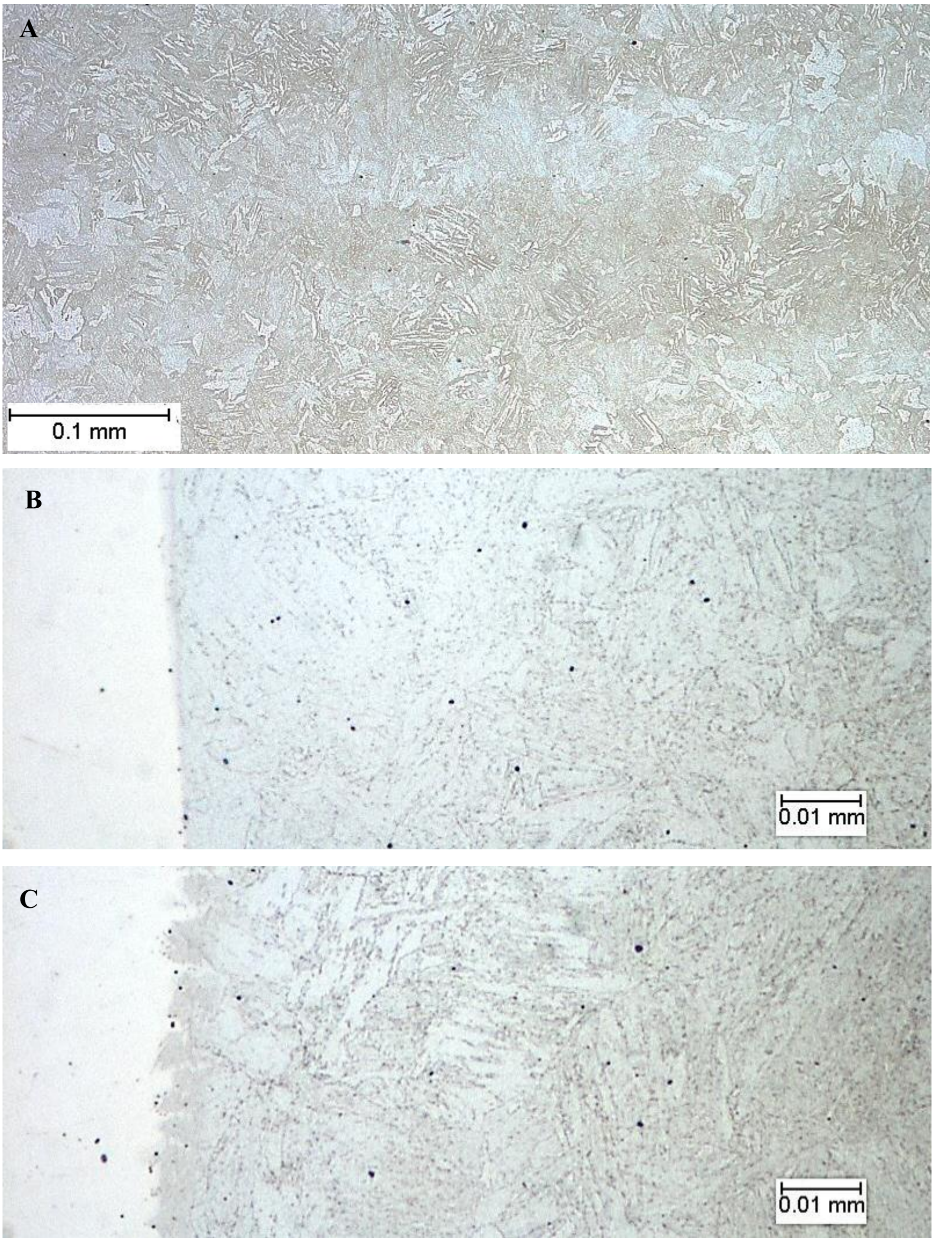

Fig. 127 SA533 Gr.B / Inconel 52M buttering fusion line and the influence of LAS carbide banding. A) Carbide banding in the LAS, B) fusion line and CDZ in the LAS side without carbide banding, C) same fusion line when carbide banding reaches the weld metal.

6.8.1.2. *Inconel 52M weld metal and fusion lines*

Figure 128 shows a global view of the Inconel 52M buttering/SA 533 Gr.B interface and Figure 129 shows a closer view of the dendritic microstructure of Inconel 52M weld metal.

Fig. 128 Inconel 52M buttering layer and interface with SA 533 Gr.B.

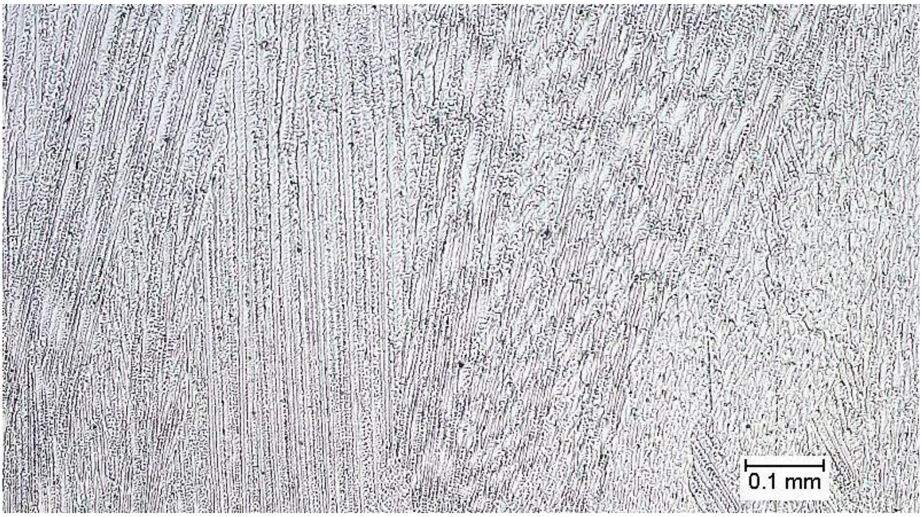

Fig. 129 Inconel 52M weld metal microstructure.

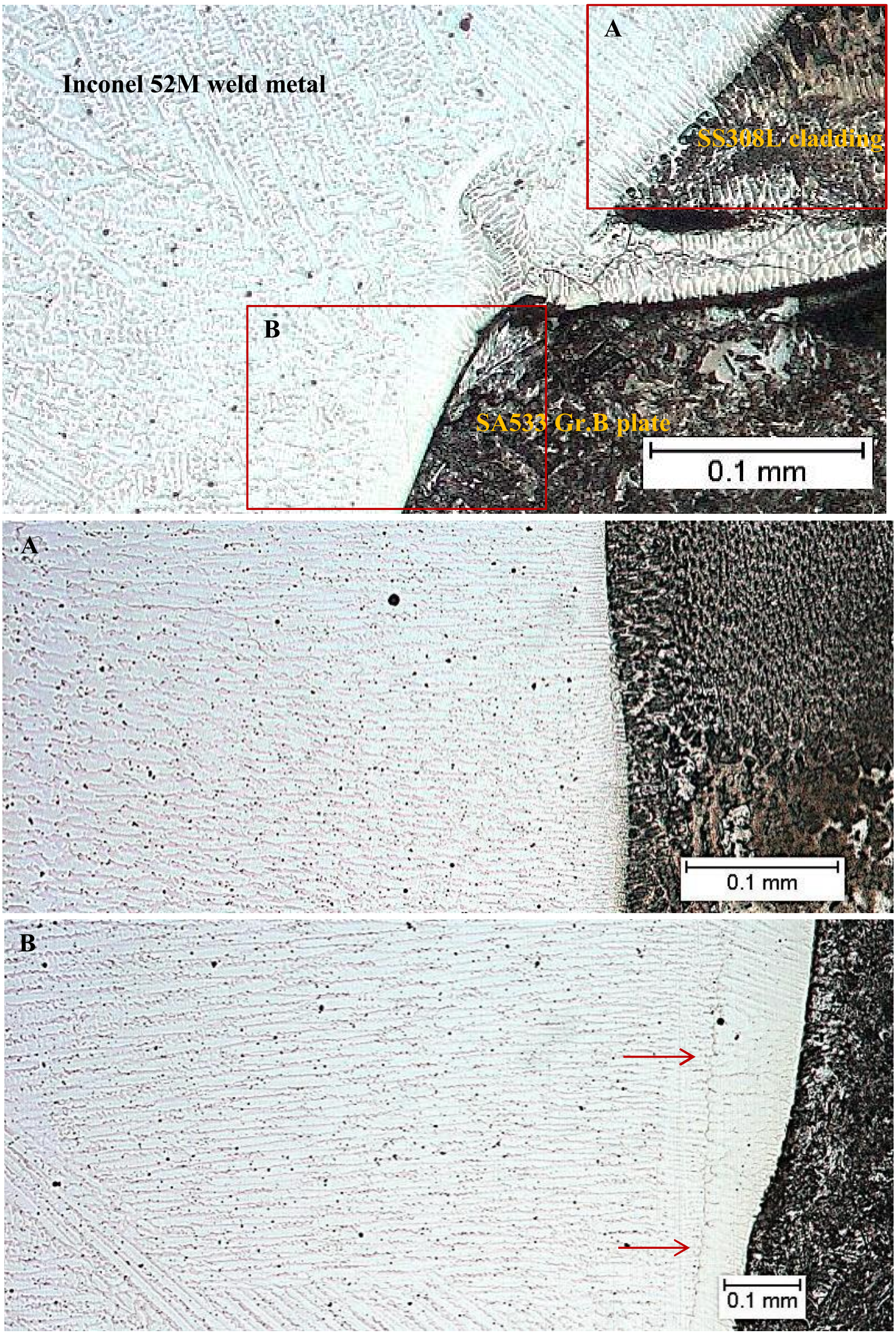

Fig. 130 Fusion line between the Inconel 52M weld metal, the LAS plate and the SS cladding. The first picture shows the place where the cladding starts on the LAS plate, with some weld metal penetration between them. The next pictures show close view of the Inconel 52M interface with A) SS308L and B) SA533 Gr.B.

Figure 130 shows the difference of interfaces with the Inconel 52M buttering for SS308L (Fig. 130 A) and SA 533 Gr.B (Fig. 130 B). The SS308L/Inconel 52M interface is austenitic/austenitic and appears quite continuous: the dendritic structure of the buttering starts from the fusion line. On the other hand, the SA 533 Gr.B/Inconel 52M interface is ferritic/austenitic. The dendritic structure of the buttering seems to appear further away from the fusion line (20-30 µm). In addition, Type II boundaries form in the Inconel 52M side at 100 µm distance from the fusion line. As seen in the literature, it is typical for a ferritic/austenitic interface and results from the migration of this boundary after austenization of the ferritic side. Figure 131 gives a closer view of these two interfaces.

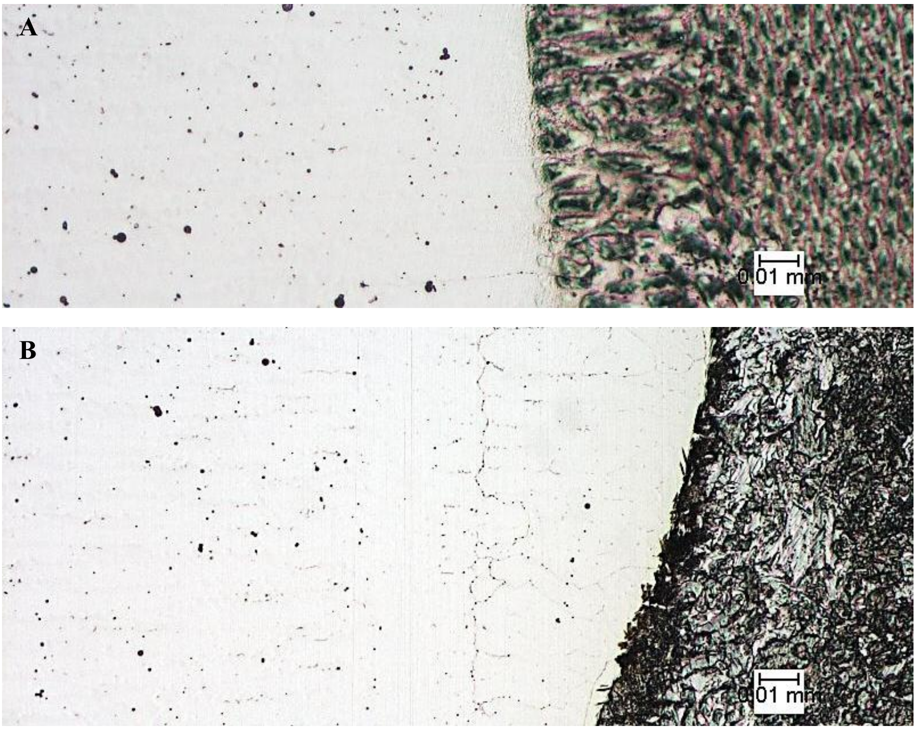

Fig. 131 Comparison between the two Inconel 52M interfaces: A) with SS308L and B) with SA533 Gr.B.

6.8.1.3. Alloy 690

For other samples, the Alloy 690 product was a hot-rolled plate or a forged bar. Extensive carbide banding was present in all samples, associated with inhomogeneous grain size distribution. The Alloy 690 pipe of the PG&E mock-up has been extruded. In addition to the longitudinal cut from the mock-up, a transverse cut was made from the pipe to study the microstructures in both directions. They were found to be identical.

Figure 132 shows a global view of the longitudinal Alloy 690 microstructure. No banding is observed. Bigger grains are present, but homogeneously distributed.

Figure 133 gives a closer view of the longitudinal microstructure. It is homogeneous, and no carbide banding is present. It is according to the literature: the extruded Alloy 690 product form is the closest to an ideal and homogeneous microstructure.

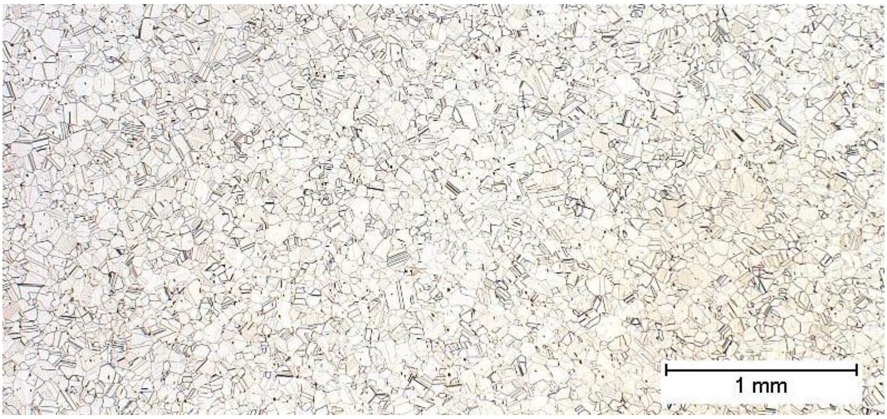

Fig. 132 Global view of the extruded Inconel 690 pipe. No banding is visible.

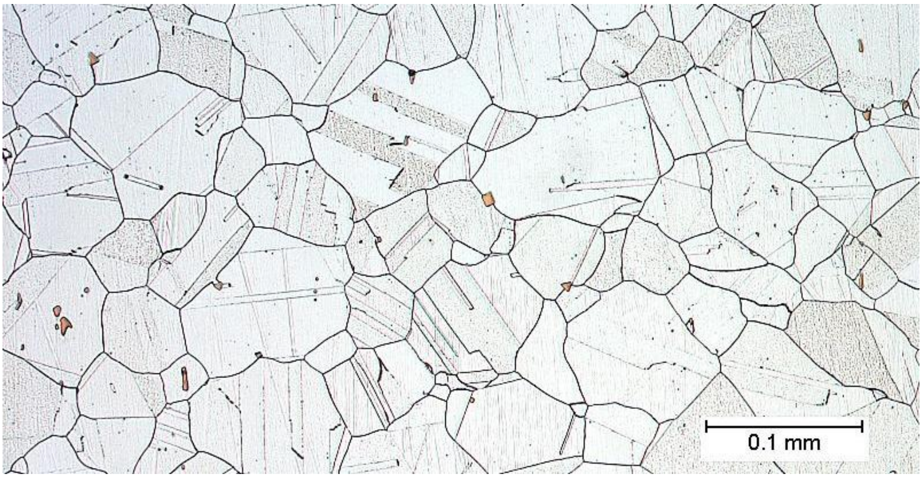

Fig. 133 Extruded Inconel 690 microstructure. It is the most homogeneous microstructure among in this study. No carbide banding is visible and the grain size distribution remains homogeneous.

6.8.2. Microhardness

Hardness measurements were conducted across all the samples to cover the SA 533 Gr.B, the Inconel 52M buttering, the Inconel 52M weld metal and the Alloy 690 pipe. Figure 134 shows the global hardness profile across the sample and a schematic of the hardness measurements. Figures 135 and 136 give a closer view of the hardness profiles at the LAS/Inconel 52M buttering and in the Inconel 52M weld metal, respectively.

Hardness increases in the LAS HAZ and reaches a peak (250 HV) before decreasing at the fusion line with the buttering. It increases in the Inconel 52M buttering towards the weld metal, due to increasing residual strains, and reaches a new peak at the Inconel 52M buttering/Inconel 52M weld metal interface (270 HV). Hardness is lower in the center of the Inconel 52M weld metal, and increases towards the two sides of the weld. Hardness increases in the Alloy 690 HAZ due to residual strains, and reaches a peak at the Inconel 52M weld metal/Alloy 690 base metal interface (260 HV).

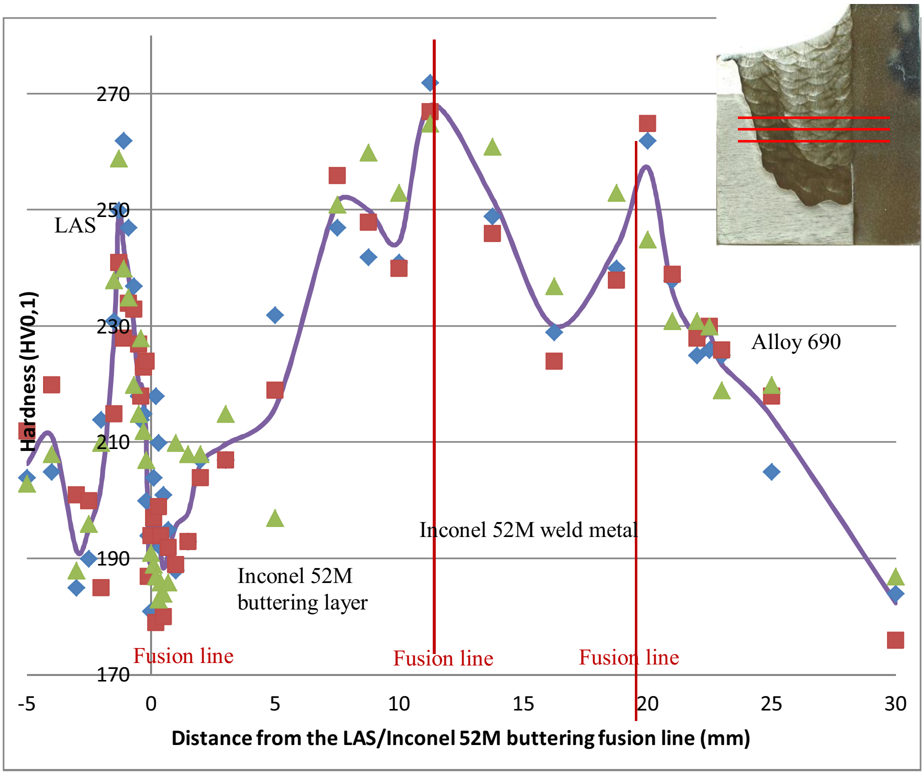

Fig. 134 Hardness profile across the PG&E sample. The purple line shows the average between the 3-line measurements. Hardness increases in the LAS HAZ and in the Alloy 690 HAZ. It increases in the buttering layer towards the weld metal. It is lower in the center of the weld and increases at the interfaces with the buttering and Alloy 690.

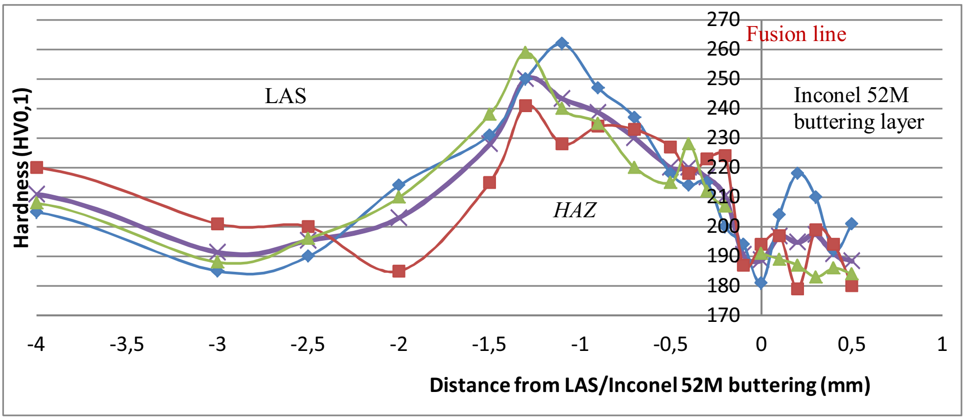

Fig. 135 Hardness profile across the SA 533 Gr.B/Inconel 52M buttering interface. Hardness increases in the LAS HAZ and reaches a peak. It then decreases due to grain coarsening.

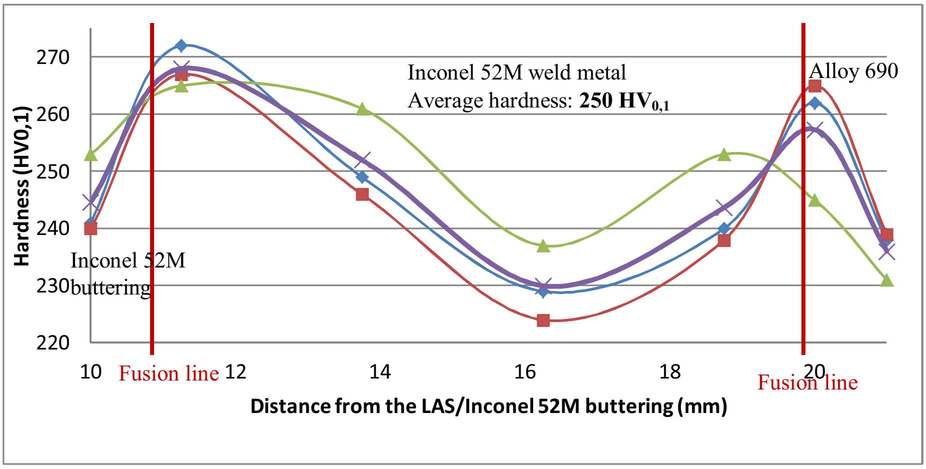

Fig. 136 Hardness profile across the Inconel 52M weld metal and the interfaces with Inconel 52M buttering and Alloy 690 base metal. Hardness is higher at the interfaces and decreases towards the center of the weld. The average weld hardness is 250 HV.

Figure 135 shows some hardness increase in the buttering, about 0-500 µm from the LAS/Inconel 52M buttering fusion line. It can be due to Type II boundaries and carbide precipitations.

Figure 136 shows that hardness increases in the Inconel 52M weld metal towards the interfaces with the buttering and Alloy 690 base metal. It is probably due to increasing residual strains at the interfaces. The average Inconel 52M weld metal hardness is 250 HV. This corresponds to the value measured for the Inconel 52M weld metal in the GTAW 1950A sample.

6.9. Discussion

Among the weld configurations and different materials that have been studied, three main subjects can be highlighted: the ferritic/austenitic interface between LAS and Ni-base weld metal, the behavior of different Ni-base weld metal and the microstructures of Alloy 690. A comparison between the samples will show the difference in behavior and characteristics of these materials and interfaces.

6.9.1. LAS HAZ and interface with Ni-base weld metal

Several samples display a fusion line between a LAS (SA508 or SA533 Gr.B) and Ni-base filler metals: Alloy 52 mock-up as-welded, heat-treated, MHI plate, ENSA weld mock-up and PG&E mock-up. In all cases, a hardness peak (260-290 HV) is present in the LAS HAZ, due to grain refining. Higher hardness can be reached locally due to carbide banding (400 HV in the MHI plate). Hardness decreases closer to the fusion line due to grain coarsening and carbon depletion. A comparison between Alloy 52 mock-up AW and HT shows that PWHT does not affect significantly the SA508 HAZ: no visible changes are seen in the microstructures. However, hardness is slightly lower in the PWHT sample, due to tempering and grain growth. In all case, the grain refining was important and the grain size decreased drastically in the HAZ. The very small grains were quite hard to etch and observe with optical microscopy. SEM analysis will give better results.

The consequences of PWHT are visible at the fusion lines. The CDZ is about ten times wider in the Alloy 52 mock-up after PWHT (100 μm) than in the AW condition (10 μm). Worth noting, however, is that a CDZ is already present in the AW condition. In addition, the fusion line etched with Nital is darker in the PWHT sample, may be due to higher carbon migration. The MHI plate has also been PWHT; the CDZ is about 50 μm, thus, intermediate between those of Alloy 52 mock-up AW and PWHT. The same CDZ width is found in the PG&E mock-up and the ENSA mock-up CDZ is about 70 μm.

There are almost no precipitates visible in the Inconel 52 side of the Alloy 52 mock-up in the AW condition, but an extensive precipitation occurs during PWHT. From the literature review, it is assumed that the precipitates are chromium carbides. They form as a result of the carbon migration from the LAS to the weld metal, due to the difference in the chromium content and are precipitated at high temperatures. As a result, a hardness peak (350 HV) is present in the Inconel 52 weld metal near the fusion line. It corresponds to the location of the carbides (50 μm from the fusion line). A hardness peak is also visible in the ENSA mock-up Inconel 52M buttering, but it has lower amplitude (310 HV) and it corresponds to a dark-etched layer very close to the fusion line (less than 10 µm). No such hardness peak is present in the MHI plate, but some scatter in the values and hardness increases occur in the PG&E mock-up Inconel 52M buttering at 100-200 µm from the fusion line. It corresponds to the location of Type II boundaries, which can be associated with precipitates. Types II boundaries form in the ENSA mock-up and in the MHI plate at about 50 µm from the fusion line in Inconel 52M and Inconel 152, respectively. In the PWHT Alloy 52 mock-up, they form closer to the fusion line, at about 10 µm from the fusion line in Inconel 52.

Numerous wide dark-etched carbon-rich zones are present on the fusion line in the MHI plate. A first possibility is that carbon diffuses less in Inconel 152 than in Inconel 52. Therefore, carbon migration from the LAS is stopped closer to the fusion boundary in the MHI plate than in the Alloy 52 mock-up samples. In addition, it explains that more precipitates form in the Inconel 152 weld metal than in Inconel 52. However, such bands are also visible in the PG&E mock-up with the Inconel 52M buttering. As for the MHI plate, the PG&E mock-up LAS is affected by carbide banding. It has been observed that the dark-etched bands tend to appear where the carbide banding of the LAS reaches the fusion line. It is not clear at the moment if these zones are martensite or PMZ.

6.9.2. Ni-base weld metals and buttering layers

Inconel 52M, 52 and 152 have been used for the samples in different or similar conditions. Several comparisons can be made.

For the CIEMAT samples, the hardness value of the Inconel 52 weld metal of the CIEMAT GTAW (207 HV) was lower than that of the Inconel 152 weld metal in the CIEMAT SMAW sample (224 HV). This is attributed to a finer microstructure (the primary dendrite arm spacing was three times smaller for Inconel 152) and to a higher amount of precipitates in Inconel 152. In both cases, hardness increases when a LAS is present as base metal: the hardness in Inconel 52 weld metal was higher for the Alloy 52 mock-up samples and ENSA weld mock-up (210-220 HV and 215 HV, respectively) and the hardness in Inconel 152 weld metal was higher in the MHI plate sample (239 HV). This is probably related to carbon diffusion and iron dilution from the LAS to the weld metal. The highest hardness was found for Inconel 52M weld metal in the GTAW 19508B sample and PG&E mock-up (250 HV). It has been attributed to the finer microstructure of Inconel 52M compared to Inconel 52 and 152, and may be the change from straight to serpentine GBs. In all cases, hardness tends to increase at the interfaces, where residual strains are the highest.

The trend for the Inconel 152 and 52M buttering layers is that hardness increases from the LAS side to the Ni-base weld metal side. It is, thus, assumed that the main contributor to the hardness is not the carbon content but the residual strains, which increase towards the weld metal interface.

6.9.3. Alloy 690

Alloy 690 was present in several conditions, with different filler metals and weld designs. Its microstructure was always according to the literature, austenitic grains with high amount of twin boundaries, fine carbides in the grain interiors and TiN particles at GBs.

Three Alloy 690 product forms were present in the samples: hot-rolled plate, forged bar and extruded pipe. They show sensibly different microstructures. Hot-rolled plates show extensive carbide banding, associated with smaller grain size. The banding and the small grain size are, however, quite localized. The bands are not wider than 50 µm. In the forged Alloy 690, carbide banding and grain size distribution are also present. The difference in grain size is higher, and the width of the carbide banding is higher than 100 µm. In addition, the direction of the banding is less clear. It makes this microstructure the most inhomogeneous. The extruded pipe shows no carbide or grain size banding, and its microstructure is the most homogeneous. This is according to the literature.

Alloy 690 HAZ showed no visible grain refining. Grain growth was visible along the fusion line. The hardness of Alloy 690 base material was around 180-200 HV. The HAZ always showed an increase in hardness from Alloy 690 base metal to the fusion line. The increase was always between 40-70 HV and is related to the increase in residual strains towards the weld interface. Hardness decrease was observed at the fusion line, related to grain growth.

Conclusions

In this study, a literature review was conducted concerning the behavior of Ni-base alloys and LAS in DMWs for new possible nuclear applications. It was centered on the metallurgical changes occurring with PWHT at the interface of ferritic/austenitic DMWs, on the weldability of Inconel filler metals and on the NG-GTAW technique that is now used in NPPs. In addition, the microstructures of several Alloy 690 product forms were studied. Of importance was the characterization of a NG-GTAW mock-up using Inconel 52 filler metal and no buttering layer to join the RPV nozzle to its safe-end. This design is now used in the construction of new PWR reactors.

Eight samples were characterized. The Alloy 52 mock-up manufactured in project was studied in the as-welded condition and after PWHT. It showed that PWHT resulted in an increase in the CDZ width in the LAS side and in an extensive chromium carbide precipitation in the weld metal. It was responsible for a sharp hardness peak in the weld metal, just near the fusion line. Samples from EPRI were characterized, showing different weld configurations involving Alloy 690 as base metal and Inconel 52M, 52 and 152 as filler metals. Differences in the behavior of the filler metals were observed. The higher hardness was found in Inconel 52M, 152 and 52, respectively. Inconel 152 showed a different behavior concerning carbon migration than Inconel 52. The microstructure of Alloy 690 was characterized and was found to correspond to the literature review and to depend on the type of product form. Hardness always increased from the base material to the fusion line, certainly due to residual strains.

The time available for this study allowed optical microscopy observations and hardness measurements (macro-, micro- and nano-) to characterize the samples. This is thus the beginning in the study of the samples. Other techniques will be used later, such as SEM observations, EBSD mapping, EDS profiles, tensile and fracture toughness tests, to further understand the behavior of the welds. Notably, the EBSD study of residual strains and their correlation with hardness and SCC behavior in

Alloy 690 should be investigated, as well as the nature of precipitates and microstructures at the interfaces.

References

Aalto University (2012) Kon-67.5100 Postgraduate Seminar on Engineering Materials, Otaniemi, March - April 2012.

Ahluwalia K., King C. (2007) Materials reliability program: review of stress corrosion cracking of alloys 182 and 82 in PWR primary water service (MRP-220). Technical report 1007832. EPRI, Palo Alto, CA, October 2007.

Akbari D, Farahani M, Soltani N. (2012) Effects of the weld groove shape and geometry on residual stresses in dissimilar butt-welded pipes. The Journal of Strain Analysis for Engineering Design. Vol. 47. 2. P. 73- 82.

Albert S. K., Gill T. P. S., Tyagi A. K., Mannan S. L., Kulkami S. D., Rodriguez P. (1997) Soft zone formation in dissimilar welds between two Cr-Mo steels. Welding Journal. Vol. 76. 3. P. 135–142.

Alexandrov B.T., Hope A.T., Sowards J.W., Lippold J.C. (2009) Weldability studies of high-Cr, Ni-base filler metals for power generation applications. IX-2313-09-Rev3.

Anand R., Sudha C., Karthikeyan T., Terrance A.L.E., Saroja S., Vijayalakshmi M. (2008) Metal interlayers to prevent ‘hard zone’ formation in dissimilar weldments of Cr-Mo steels – A comparison between Cu, Co and Ni. Transactions of the Indian Institute of Metals. Vol. 61. P. 483-486.

Andresen P., Morra M., Ahluwalia K. (2012) SCC of Alloy 690 and its weld metals. EPRI International BWR and PWR Materials Reliability Conference and Exhibit Show, National Harbor, Maryland, July 16-19. P. 321-361.

ASTM E384 - 11e1. Standard test method for Knoop and Vickers hardness of materials. ICS number code 19.060.

Bamford W., Hall J. (2005) Cracking of alloy 600 nozzle and welds in PWRs: review of cracking events and repair service experience. Proceedings of the 12th International Conference on Environmental Degradation of Materials in Nuclear Power System–Water Reactors–TMS, Salt Lake City, 2000. Eds. Allen T.R., King P.J., Nelson L. USA: The Minerals, Metals and Materials Society. P. 959–965.

Becker A.A., Hyde T.H., Sun W. (2001) Creep crack growth in welds: a damage mechanics approach to predicting initiation and growth of circumferential cracks. International Journal of Pressure Vessels and Piping. Vol. 78. P. 765-771.

Biswas P., Mandal N.R., Vasu P., Padasalag S.B. (2010) Analysis of welding distortion due to narrow-gap welding of upper port plug. Fusion Engineering and Design. Vol. 85. P. 780–788.

Boursier J., Vaillant F, Yrieix B. (2004) A review of PWSCC behavior of nickel weld metals containing 15 to 30% chromium. Proceedings of ASME/JSME

Pressure Vessels and Piping Conference, San Diego, California, USA, 25-29 July 2004. Ed. Tahara T. PVP. Vol. 490. P. 109-121.

Brass A.M., Chêne J. (2004) Role of temperature and strain rate on the hydrogen-induced intergranular rupture in alloy 600. Metallurgical and Materials Transactions A. Vol. 35A. P. 457- 464.

Brooks J.A., Lippold J.C. (1993) Selection of Wrought Austenitic Stainless Steels. ASM Handbook. Vol. 6. Welding, Brazing, and Soldering. P. 456 - 470.

Bruemmer S.M., Toloczko M.B., Olszta M.J., Seffens R., Efsing P. (2009) Characterization of defects in alloy 152, 52 and 52M welds. Proceedings of the 14th international conference on environmental degradation of materials in nuclear power systems, August 23-27, Virginia Beach, Virginia, USA. P. 319 - 332.

Bundy J. (2012) Six ways to prevent weld failures. Welding Journal. Vol. 91. P. 30 - 32.

Celik A., Alsaran A. (1999) Mechanical and structural properties of similar and dissimilar steel joints. Materials Characterization. Vol. 43. P. 311–318.

Chatterjee S., Abinandanan T.A., Chattopadhyay K. (2006) Microstructure development during dissimilar welding: case of laser welding of Ti with Ni involving intermetallic phase formation. Journal of Materials Sciences. Vol. 41. P. 643–652.

Chung W.C., Huang J.Y., Tsay L.W., Chen C. (2011) Microstructure and stress corrosion cracking behavior of the weld metal in Alloy 52-SA508 dissimilar welds. Materials Transactions. Vol. 52. P. 12 -19.

Coleman M. C., Kimmins S. T., Smith D. J. (1993) An overview of creep failure associated with heat affected zones of ferritic weldments. Creep and Fracture of Engineering Materials and Structures. Swansea, UK, 28 March – 2 April. P. 681-694.

Crum J.R., Scarberry R.C. (1982) Corrosion testing of Inconel alloy 690 for PWR steam generators. Journal of Materials for Energy Systems. Vol. 4. P. 125-130.

Danko J.C. (1992) Stress-corrosion cracking of weldments in boiling water reactor service. Ed. Jones R.H. Stress-Corrosion Cracking, ASM International, Ohio. P. 345–354.

Davé V.R., Cola M.J., Kumar M., Schwartz A.J., Hussen G.N.A. (2004) Grain boundary character in Alloy 690 and ductility-dip cracking susceptibility. Welding Journal. Vol. 83. P. 1-5.

Davies R.G., Johnston T.L. (1969) Ordered alloys. Proceedings of the 3rd International Bolton Landing Conference AIME 447. Ed. Keat B.H. et al. New York, Claitors Publishing Division.

Deng D., Murakawa H., Liang W. (2008) Numerical and experimental investigations on welding residual stress in multi-pass butt-welded austenitic stainless steel pipe. Computational Materials Science. Vol. 42. P. 234–244.

DuPont J.N. (1996) Solidification of an alloy 625 weld overlay. Metallurgical and Materials Transactions A. Vol. 27A. P. 3612 - 3620.

DuPont J.N., Lippold J.C., Kiser S.D. (2009) Welding metallurgy and weldability of nickel-base alloys. Ed. John Wiley and Sons, Inc. ISBN 978-0-470-08714-5.

DuPont J.N., Mizia R.E. (2010) Review of dissimilar metal welding for the NGNP helical-coil steam generator. INL/EXT-10-18459.

Engelhard G., Habip L.M., Pellkofer D., Schmidt J., Weber J. (2000) Optimization of residual welding stresses in austenitic steel piping: proof-testing and numerical simulation of welding and post-welding processes. Nuclear Engineering and Design. Vol. 198. P. 141–151.

Findlan S., Newton B., Kiser S.D. (2004) Successful structural weld metal build-ups on P-3 Gr-3 Pipe coupon made with Inconel filler metal 52M. EPRI Nuclear Conference, San Destin.

Foret R., Zlamal B., Sopousek J. (2006) Structural stability of dissimilar weld between two Cr-Mo-V steels. Supplement to the Welding Journal. Vol. 85. 10. P. 211-217.

Frederick G., Mcllree A. (2006) Materials reliability program: selection of materials and fabrication of weldments for investigation of PWSCC susceptibility in the alloy 600 and 690 weld heat affected zones (MRP-161). Technical report 1011805. EPRI, Palo Alto, CA.

Fyfitch S., Ahluwalia K. (2012) Current status of knowledge gaps and testing for Alloy 690 and its weld metals. EPRI International BWR and PWR Materials Reliability Conference and Exhibit Show, National Harbor, Maryland, July 16-19. P. 362-384.

Gandhi T., Aidun D.K. (2005) Effect of enhanced convection on the microstructure of dissimilar welds. Trends in Welding Research: Proceedings of the 7th International Conference, May 16-20, Pine Mountain, Georgia, USA. Ed. David S.A. P. 731- 736.

Gooch T.G., Honeycombe J. (1980) Welding variables and microfissuring in austenitic stainless steel weld metal. Welding Journal. Vol. 59. P. 233-241.

Hänninen H. (2009) Material development in new reactor designs –Gen III and SCWR concept, 20th International Conference on Structural Mechanics in Reactor Technology (SMiRT), August 9-14, 2009, Dipoli Congress Centre, Espoo, Finland. P. 1-30.

Henon B.K. (2010) Hot wire narrow groove welding and cladding with nickel-based alloys. Focus on Nuclear Power Generation. Arc Machines, Inc.

Hickling J., Ahluwalia A. (2004) Advanced testing techniques to measure the PWSCC resistance of alloy 690 and its weld metals. Technical Report 1011202. EPRI, Palo Alto, CA.

Hirth S., Gottstein G. (1998) Misorientation effects on discontinuous precipitation in Al-Ag-Ga. Acta Metallurgica. Vol. 46. P. 3975-3984.

Holt R.T., Wallace W. (1976) Impurities and trace elements in nickel-base super alloys. International Metals Reviews. Vol. 21. 1. P. 1-24.

Hong J.H., Kim S., Kang S.Y., Oh S.J., Kwon S.J., Lee S., Kim J.H. (2000) Correlation of the microstructure and fracture toughness of the heat-affected zones of an SA 508 steel. Metallurgical and Materials Transactions A. Vol. 31A. P. 1107-1120.

Hong J.H., Kim S., Lee S., Lee H.C., Oh S.J. (2001) Effects of alloying elements on mechanical and fracture properties of base metals and simulated heat-affected zones of SA 508 steels. Metallurgical and Materials Transactions A. Vol. 32A. P. 903-912.

Hong J.K., Kim I.S., Park C.Y., Kim E.S. (2005) Microstructural effects on the fretting wear of Alloy 690 steam generator tube. Wear. Vol. 259.P. 349–355.

Horn R. M., Andresen P. L., Hickling J. (2002) BWR Alloy 182 stress corrosion cracking. Proceedings of the 5th International Symposium on Contribution of Materials Investigation to the Resolution of Problems Encountered in Pressurized Water Reactors, Fontevraud, France, 23–27 September 2002. P. 55- 60.

Huang X., Chaturvedi M.C., Richards N.L., Jackmann J. (1997) The effect of grain boundary segregation of boron in cast alloy 718 on HAZ microfissuring – a SIMS analysis. Acta Materialia. Vol. 45. P. 3095-3107.

Hyde T.H., Sun W., Becker A.A. (2001) Creep crack growth in welds: a damage mechanics approach to predicting initiation and growth of circumferential cracks. International Journal of Pressure Vessels and Piping. Vol. 78. P. 765-771.

IAEA Nuclear Energy Serie (2005) Assessment and management of ageing of major nuclear power plant components important to safety: BWR pressure vessel internals. TECDOC-1471.

IAEA Nuclear Energy Serie (2011) Stress corrosion cracking in light water reactors: good practices and lessons learned. International Atomic Energy Agency, Vienna, 2011. No. NP-T-3.13. P. 3-16.

Jang C., Cho P.Y., Kim M., Oh S.J., Yang S.J. (2010) Effects of microstructure and residual stress on fatigue crack growth of stainless steel narrow gap welds. Materials and Design. Vol. 31. P. 1862–1870.

Jang C., Lee J., Jong Sung Kim J.S., Jin T.E. (2008) Mechanical property variation within Inconel 82/182 dissimilar metal weld between low alloy steel and 316 stainless steel. International Journal of Pressure Vessels and Piping. Vol. 85. P. 635–646.

Kaneshima Y., Totsuka N., Nakajima N. (2005) Effect of strain rate on primary water stress corrosion cracking fracture mode and crack growth rate of nickel alloy and austenitic stainless steel. Corrosion. Vol. 61. 3. P. 219–229.

Karlsson L. (1995) Welding of dissimilar metals. Welding in the World. Vol. 36. P. 125-132.

Kerr H.W., Katoh M. (1987) Investigation of heat affected zone cracking of GTA welds of Al-Mg-Si alloys using the Varestraint test. Welding Journal. Vol. 66. 9. P. 251-259.

Kim J.T., Kwon H.K., Chang H.S., Park Y.W. (1997) Improvement of impact toughness of the SA 508 class 3 steel for nuclear pressure vessel through steel-making and heat-treatment practices. Nuclear Engineering and Design. Vol. 174. P. 51–58.

Kim J.W., Lee K., Kim J.S., Byun T.S. (2009) Local mechanical properties of Alloy 82/182 dissimilar weld joint between SA508Gr.1a and F316 SS at RT and 320 °C. Journal of Nuclear Materials. Vol. 384. P. 212–221.

Kim S.K., Lee Y.D., Hansson K., Fredriksson H. (2002) Influence of cooling rate on the hot cracking formation of nickel rich alloys. ISIJ International. Vol. 42. P. 512-519.

King C.P. (2003) Materials reliability program PWSCC of alloy 600 type materials in non-steam generator tubing applications – survey report through June 2002: part 1: PWSCC in components other than CRDM/CEDM penetrations (MRP-87). Technical report 1007832. EPRI, Palo Alto, CA.

Kirk-Othmer Encyclopedia of Chemical Technology (2005) Chapter 9.8. Nickel–Iron–Chromium, Nickel and Nickel Alloys.

Kiser S.D. (2003) Nuclear welding just became easier with Inconel filler metal 52M and Inconel welding electrode 152M. Focus on Nuclear Power Generation. P. 18-21.

Kiser S.D., Zhang R., Baker B.D. (2010) A new Ni-Cr-Fe welding product Inconel FM52MSS provides optimum resistance to PWSCC and DDC. Special Metals Welding Products Company.

Klueh R. L., King J. F. (1982) Austenitic–ferritic weld joint failures. Welding Journal. Vol. 61. P. 302–311.

Klueh R.L., Harries D.R. (2001) High-chromium Ferritic and Martensitic Steels for Nuclear Applications. ASTM International. ISBN 0-8031-2090-7.

Kotecki D. J., Rajan V. B. (1996) Submerged arc fillet welds between mild steel and stainless steel. Proceedings of the Conference on Advanced Welding Technologies: Joining High-Performance Materials, USA: Edison Welding Institute, Columbus, Ohio. P. 33–58.

Kou S. (2003) Welding Metallurgy, 2nd edition. Ed. John Wiley and Sons, Inc. P. 243-263. ISBN 0-471-433491-4

Kuo T., Lee H. (2002) Effects of filler metal composition on joining properties of alloy 690 weldments. Materials Science and Engineering. Vol. 338. P. 202- 212.

Laukkanen A., Nevasmaa P., Ehrnsten U., Rintamaa R. (2007) Characteristics relevant to ductile failure of bimetallic welds and evaluation of transferability of fracture properties. Nuclear Engineering and Design. Vol. 237. P. 1–15.

Lee H.T., Wu J.L. (2009) Correlation between corrosion resistance properties and thermal cycles experienced by gas tungsten arc welding and laser beam welding Alloy 690 butt weldments. Corrosion Science. Vol. 51. P. 733–743.

Lee H.T., Jeng S.L (2001) Characteristics of dissimilar welding of alloy 690 to 304L stainless steel. Science and Technology of Welding & Joining, Vol. 6. 4. P. 225-234.

Lee K.H., Park S.G., Kim M.C., Lee B.S., Wee D.M. (2011) Characterization of transition behavior in SA508 Gr.4N Ni–Cr–Mo low alloy steels with microstructural alteration by Ni and Cr contents. Materials Science and Engineering. Vol. 529. P. 156– 163.

Lehockey E.M., Palumbo G. Lin P. (1998) Improving the weldability and service performance of nickel- and iron-based super-alloys by grain boundary engineering. Metallic Material Transactions A. Vol. 29A. P. 3069-3079.

Lim Y.S, Kim J.S, Kim H.P., Cho H.D. (2004) The effect of grain boundary misorientation on the intergranular $M_{23}C_6$ carbide precipitation in thermally treated Alloy 690. Journal of Nuclear Materials. Vol. 335. P. 108–114.

Lippold J. C., Mills M. J., Nelson T. W. (1999) Nature and evolution of the fusion boundary in ferritic-austenitic dissimilar weld metals, Part 1 - Nucleation and growth. Supplement to the Welding Journal. Vol. 78. P. 329-337.

Lippold J. C., Mills M. J., Nelson T. W. (2000) Nature and evolution of the fusion boundary in ferritic-austenitic dissimilar weld metals, Part 2 - On-cooling transformations. Supplement to the Welding Journal. Vol. 79. P. 267-277.r

Lippold J.C., Collins M.G., Ramirez A.J. (2004) An investigation of ductility-dip cracking in nickel-base filler materials - Part III. Welding Journal. Vol. 83. P. 39-49.

Lippold J.C., Rowe M.D., Nelson T.W. (1999) Hydrogen-induced cracking along the fusion boundary of dissimilar metal welds. Welding Research Supplement. Vol. 78. 2. P. 31-37.

Lundin C. D., Khan K. K., Yang D. (1990) Effect of carbon migration on the metallurgical structure and mechanical properties of Cr-Mo weldments. Proceedings of the Conference on Recent Trends in Welding Science and Technology, Gatlinburg, May 14–18, 1989. ASM International, Materials Park, OH. P. 291–296.

Masumoto I., Takami K., Kutsuna M. (1972) Hot cracking of austenitic stainless steel weld metal. Journal of the Japan Welding Society. Vol. 41. P. 1306-1314.

McCracken S.L., Smith R.E. (2011) Behavior and hot cracking susceptibility of filler metal 52M (ERNiCrFe-7A) overlays on cast austenitic stainless steel base materials. Ed. Lippold J. et al. Hot Cracking Phenomena in Welds III. P. 333-352.

McNeil M. B., Chopra O. K., Soppet W. K., Shack W. J. (2001) Effects of alloy chemistry, cold work, and water chemistry on corrosion fatigue and stress corrosion cracking of nickel alloys and welds. Division of Engineering Technology. Office of Nuclear Regulatory Research. NUREG/CR–6721. ANL–01/07.

Messler R.W. (1999) Principles of Welding, Processes, Physics, Chemistry and Metallurgy. Ed. John Wiley and Sons, Inc.

Modenesi P.J., Starling C.M.D., Marques P.V. (1995) Statistical modeling of narrow-gap GTA welding with magnetic arc oscillation. Journal of Materials Processing Technology. Vol. 51. P. 37- 49.

Moss T., Was G. (2012) Accelerated stress corrosion crack initiation testing of Alloys 600 and 690. EPRI International BWR and PWR Materials Reliability Conference and Exhibit Show, National Harbor, Maryland, July 16-19. P. 385-407.

Mukhopadhyay N. K., Paufler P. (2006) Micro- and nanoindentation techniques for mechanical characterization of materials. International Materials Reviews. Vol. 51. P. 209-245.

Naffakh H., Shamanian M., Ashrafizadeh F. (2009) Dissimilar welding of AISI 310 austenitic stainless steel to nickel-based alloy Inconel 657. Journal of Materials Processing Technology. Vol. 209. P. 3628–3639.

Nelson J.W., Lewis W.J. (1967) Process for narrow gap welding. United States Patent Office. Patent 3328556.

Nishimoto K., Saida K., Okauchi H. (2006) Microcracking susceptibility in multi-pass weld metal of Alloy 690 alloy. Part 1 – Microcracking susceptibility in reheated weld metal. Science and Technology of Welding and Joining. Vol. 11. 4. P. 455- 461.

Oliver W.C., Pharr G.M. (1992) An improved technique for determining hardness and elastic modulus using load and displacement sensing indentation experiments. Journal of Materials Research. Vol. 7. 6. P. 1565-1583.

Page R.A. (1983) Stress corrosion cracking of Alloys 600 and. 690 and N°82 and 182 weld metals in high temperature water. Corrosion. Vol. 39. 10. P. 409 – 421.

Page R.A., McMinn A. (1988) Stress corrosion cracking resistance of alloys 600 and 690 and compatible weld metals in BWRs. Final Report. EPRI. NP-5882M. Project 1566-1.

Payne B.E. (1969) Nickel-base welding consumables for dissimilar metal welding applications. Metal Construction. Vol. 1. 12. P. 79-87.

Perrin I.J., Hayhurst D.R. (1999) Continuum damage mechanics analyses of type IV creep failure in ferritic steel cross weld specimens. International Journal of Pressure Vessels and Piping. Vol. 76. P. 599–617.

Qian L., Ming Li M., Zhou Z., Yang H., Shi X. (2005) Comparison of nano-indentation hardness to microhardness. Surface and Coatings Technology. Vol. 195. P. 264–271.

Rajan T.V., Sharma C.P. (2004) Heat treatment: principles and techniques. PHI Learning Pvt. Ltd. 2004. P. 357–359. ISBN 812030716X.

Ravichandran G., Poon B., Rittel D. (2008) An analysis of nanoindentation in linearly elastic solids. International Journal of Solids and Structures. Vol. 45. P. 6018–6033.

Rebak R. B., Szklarska-Smialowska Z. (1996) The mechanism of stress corrosion cracking of alloy 600 in high temperature water. Corrosion Science. Vol. 38. P. 971-988. ISSN 0010-938X.

Richards N.L., Chaturvedi M.C. (2000) Effect of minor elements on weldability of nickel-base superalloys. International Materials Reviews. Vol. 45. P.109-129. ISSN 0950-6608.

Roberts D. I., Ryder R. H., Viswanathan R. (1985) Performance of dissimilar welds in service. Journal of Pressure Vessel Technology. Vol. 107. P. 247–254.

Ryder R. H., Dahms C. F. (1990) Design criteria for dissimilar metal welds. Welding Research Council Bull. Vol. 350. P. 1–11.

Sahlaoui H., Sidhom H., Philibert J. (2002) Prediction of chromium depleted-zone evolution during aging of Ni–Cr–Fe alloys. Acta Materialia. Vol. 50. P. 1383–1392.

Scott P.M. (2007) An overview of materials degradation by stress corrosion in PWRs. Eds. Feron D., Olive J.M., Corrosion issues in light water reactors: stress corrosion cracking, Woodhead, England. P. 3–24.

Segle P., Andersson P., Samuelson L. (1998) Proceedings of the International HIDA Conference: Creep and Fatigue Crack Growth in High Temperature Plant, 15–17 April 1998, Paris, France. P. 2–17.

Segle P., Tu S., Gong J. (2004) Creep damage and fracture of weldments at high temperature. International Journal of Pressure Vessels and Piping. Vol. 81. P. 199–209.

Seifert H. P., Ritter S., Shoji T., Peng Q. J., Takeda Y., Lu Z. P. (2008) Environmentally-assisted cracking behavior in the transition region of an Alloy 182/SA 508 Cl.2 dissimilar metal weld joint in simulated boiling water reactor normal water chemistry environment. Journal of Nuclear Materials. Vol. 378. P. 197–210.

Seifert H.P., Peng Q., Shoji T., Ritter S. (2005) SCC behavior in the transition region of an Alloy 182-SA508 Cl.2 dissimilar metal weld joint under simulated BWR-NWC conditions. Proceedings of the 12th International Conference on Environmental Degradation of Materials in Nuclear Power System – Water Reactors. Eds. Allen T.R., King P.J., Nelson L. The Minerals, Metals and Materials Society, 2005.

Server J. M., Crum J. R., Mankins W. L. (1987) Carbide precipitation and the effect of thermal treatments on the SCC behavior of Inconel Alloy 690. Proceedings of the 3rd International Symposium on Environmental Degradation of Materials in Nuclear Power Systems-Water Reactors, Warrendale, PA. The Metallurgical Society, P. 581–586.

Shah V., MacDonald P. (1993) Aging and life extension of major light water reactor components. Elsevier, The Netherlands. ISBN 0444894489. P. 941.

Shah V.N., Natesan K., Majumdar S., Shankar P.S. (2006) Preliminary materials selection issues for the next generation nuclear plant reactor pressure vessel. Nuclear Engineering Division, Argonne National Laboratory.

Siefert J.A., Tanzosh J.M., Newell W.F. (2011) EPRI P87: a promising new filler metal for dissimilar metal welding. Welding Journal. Vol. 90. 3. P. 30-34.

Sireesha M., Albert K., Shankar V., Sundaresan S. (2000) A comparative evaluation of welding consumables for dissimilar welds between 316LN austenitic stainless steel and Alloy 800. Journal of Nuclear Materials. Vol. 279. P. 65-76.

Sireesha M., Shaju K. Alert, Sundaresan S. (2005) Influence of high-temperature exposure on the microstructure and mechanical properties of dissimilar metal welds between modified 9Cr-1Mo steel and Alloy 800. Metallurgical and Materials Transactions A. Vol. 36A. P. 1495-1506.

Smith R. (2008) Experiences with hot cracking in Alloy 52M overlays. Proceedings of Welding and Repair Technology for Power Plants, 8th International EPRI Conference, June 18-20, Sanibel Island, FL.

Soares B., De Abreu Mendonça Schvartzman M.M., Reis da Costa Campos W. (2007) Characterization of the dissimilar welding - austenitic stainless steel with nickel alloy filler metal. International Nuclear Atlantic Conference. ISBN 978-85-99141-02-1.

Srinivasan G., Divya M., Albert S.K., Bhaduri A.K. (2010) Study of hot cracking behavior of nitrogen-enhanced austenitic stainless steels using Varestraint and hot ductility tests. Welding in the World. Vol. 54. P. 322-332.

Srinivasan P.B., Sivan V., Muthupandi V., Dietzel W. (2006) An assessment of impact strength and corrosion behavior of shielded metal arc welded dissimilar weldments between UNS31803 and IS2062 steels. Materials and Design. Vol. 27. 3. P. 182-191.

Staehle R., Gorman J.A. (2003) Quantitative assssmen of submodes of stress corrosion cracking on the secondary side of steam grenerator tubing in pressurized water reactors. Corrosion. Vol. 59. 11. P. 417-426.

Sudha C., Anand R., Karthikeyan T., Terrance A.L.E., Saroja S., Vijayalakshmi M. (2008) Microstructure and microchemistry of hard zone in dissimilar weldments of Cr-Mo steels. Transactions of the Indian Institute of Metals. Vol. 61. P. 483-486.

Sudha C., Anand R., Saroja S., Vijayalakshmi M. (2010) Evaluation of concentration dependant diffusion coefficients of carbon in a dissimilar joint of ferritic steels. Transactions of the Indian Institute of Metals. Vol. 63. P. 739-744.

Sudha C., Anand R., Saroja S.C., Terrance A. L. E., Vijayalakshmi M. (2008) Simulation of carbon diffusion profile in dissimilar weldment of ferritic steels using diffusion coefficients evaluated by Den Broeder's method. Physical Metallurgy Division. Metallurgy and Materials Group, Indira Gandhi Centre for Atomic Research. P. 13 – 15.

Sudha C., Terrance A.L.E., Albert S.K., Vijayalakshmi M. (2002) Systematic study of formation of soft and hard zones in the dissimilar weldments of Cr–Mo steels. Journal of Nuclear Materials. Vol. 302. P. 193–205.

Tipping P.G. (2011) Understanding operational effects on materials used in NPPs. Technical paper. Nuclear Exchange. May, 2011. ISSN 1877-2765. P. 16-20.

Tu S.T., Yoon K.B. (1999) The influence of material mismatch an the evaluation of time-dependent fracture mechanics parameters. Engineering Fracture Mechanics. Vol. 64. 6. P. 765-780.

Turner P. W., Estes C. L. (1964) Dilution in multi-pass welding of AISI 4130 to type 304 stainless steel. Welding Journal. Vol. 43. 12. P. 541-550.

Vaillant F., Boursier J., Legras L., Yrieix B., Lemaire E., Champredonde J., Amzallag C. (2007) ATEM & SEM study of the oxides developed in SCC cracks and at the surface of nickel-based alloys exposed in primary water. Proceedings of the 13th International Conference on Environmental Degradation of Materials in Nuclear Power System—Water reactors. Whistler, British Columbia, August 19–23, 2007. P. 423-434.

Wallace W., Holt R.T., Whelan E.P. (1975) Properties of 713LC compacts, hot isostatically pressed at supersolidus temperatures. Journal of Testing Evaluation. Vol. 3. ISSN: 1945-7553. P. 113-120.

Wang H.T., Wang G.Z., Xuan F.Z., Tu S.T. (2011) Numerical investigation of ductile crack growth behavior in a dissimilar metal welded joint. Nuclear Engineering and Design. Vol. 241. P. 3234– 3243.

Was G., Thaveeprungsriporn V. (1996) Grain boundary properties of Ni-16Cr-9Fe at 360 °C. Scripta Metallurgica et Materialia. Vol. 35. 1. P. 1-8.

Webb G. L., Burke M. G. (1995) Stress corrosion cracking behavior of Alloy 600 in high–temperature water. Proceedings of the 7th International Symposium on Environmental Degradation of Materials in Nuclear Power Systems-Water Reactors, NACE International, Houston, TX. P. 41–55.

Willis E., Morra M., Sandusky D. (2011) Microstructural studies of Alloy 690 product forms. Alloy 690/52/152 PWSCC research collaboration meeting, EPRI. P. 1-34.

Wu W., Tsai C.H. (1999) Hot cracking susceptibility of fillers 52 and 82 in Alloy 690 welding. Metallurgical and Materials Transactions A. Vol. 30A. P. 417- 426.

Xia S., Li H., Liu T.G., Zhou B.X. (2011) Applying grain boundary engineering to Alloy 690 tube for enhancing intergranular corrosion resistance. Journal of Nuclear Materials. Vol. 416. P. 303–310.

Yoon B.H., Ahn Y.S. Lee C.H. (2002) The effect of dilution on HAZ liquation cracking in PTAW Ni-base superalloys overlay deposit. ISIJ International. Vol. 42. P. 178-183.

Young G.A., Battige C.K., Lewis N., Penik M.A. (2002) Factors affecting the hydrogen embrittlement resistance of Ni-Cr-Mn-Nb welds. Proceedings of the 6th International Trends in Welding Research Conference. 15-19 April 2002, Pine Mountain, GA, ASM International. P. 666-671.

Yu G.P., Yao H.C. (1990) The relation between the resistance of IGA and IGSCC and chromium depletion of Alloy 690. Corrosion. Vol. 46. P. 391- 402.

Zumelzu E., Cabetas C. (1996) Study of welding such dissimilar materials as AISI 304 stainless steel and DHP copper in a sea water environment: Influence of weld metal on corrosion. Journal of Material Processing Technology. Vol. 57. P. 246–252.

Aalto-ST 5/2013

ISBN 978-952-60-5065-2
ISBN 978-952-60-5066-9 (pdf)
ISSN-L 1799-4896
ISSN 1799-4896
ISSN 1799-490X (pdf)

Aalto University
School of Engineering
Department of Engineering Design and Production
www.aalto.fi

BUSINESS +
ECONOMY

ART +
DESIGN +
ARCHITECTURE

SCIENCE +
TECHNOLOGY

CROSSOVER

DOCTORAL
DISSERTATIONS